UNIVERSITÉ SORBONNE PARIS NORD
INSTITUT GALILÉE
LABORATOIRE DE PHYSIQUE DES LASERS

**Thèse présentée par**

**Rishabh Sharma**

**Pour obtenir le grade de**

**Docteur de l'Université Sorbonne Paris Nord**

**Sujet :**

# Production, fast rotation and non-destructive imaging of a superfluid in a bubble trap

**Soutenue le 31 janvier 2025 devant le jury composé de :**

| | | |
|---|---|---|
| **M.** | **Thomas Bourdel** | **Rapporteur** |
| **Mme** | **Kali Wilson** | **Rapporteuse** |
| **M.** | **Jakob Reichel** | **Examinateur** |
| **M.** | **Giacomo Roati** | **Examinateur** |
| **M.** | **Athanasios Laliotis** | **Examinateur** |
| **M.** | **Romain Dubessy** | **Co-directeur de thèse** |
| **Mme** | **Hélène PERRIN** | **Directrice de thèse** |

# Contents

**Acknowledgements** **7**

**General Introduction** **9**

**I Preliminaries** **15**

**1 Bose-Einstein condensate, superfluidity and collective modes** **17**
1.1 Bose-Einstein condensate . . . 17
1.1.1 Saturation of excited states . . . 17
1.1.2 Ideal Bose gas in a 3D harmonic trap . . . 18
1.1.3 Ideal Bose gas in 2D . . . 19
1.1.4 Interactions in Bose gases . . . 20
1.2 Superfluid dynamics of a Bose gas . . . 23
1.2.1 Hydrodynamic formulation . . . 23
1.2.2 The Bogoliubov approach . . . 24
1.2.3 Vortex formation in a weakly interacting Bose gas . . . 26
1.3 2D regime and BKT transition . . . 27
1.3.1 Experimental realisation of 2D Bose gases . . . 27
1.3.2 BKT transition . . . 28
1.4 Collective modes of the trapped condensate . . . 29
1.4.1 In-plane collective modes in the 3D regime . . . 29
1.4.2 Collective modes in the quasi-2D gas . . . 30

**2 Radio-frequency Dressed Trapping Potential** **31**
2.1 Rf-dressed atoms in adiabatic potentials . . . 32
2.1.1 Trapping of atoms in an inhomogeneous magnetic field . . . 32
2.1.2 Description of rf field . . . 33
2.1.3 Rf dressed adiabatic potential . . . 35
2.1.4 Local Rabi coupling . . . 37
2.2 Dressed quadrupole trap . . . 37
2.2.1 Circular Polarisation . . . 38

2.2.2 Elliptical Polarisation . . . 40
2.2.3 Determination of local Rabi coupling in the experiment . . . 42
2.3 Conclusion . . . 43

**II Thermal melting of a vortex lattice 45**

**3 Experimental setup: first version 47**
3.1 Overview of the experimental apparatus . . . 48
3.1.1 2D-MOT . . . 49
3.1.2 3D-MOT and magnetic transport . . . 50
3.1.3 Science Cell . . . 51
3.2 Compensation coils . . . 52
3.3 Initial laser configuration . . . 52
3.3.1 Master laser . . . 52
3.3.2 Cooling laser . . . 53
3.3.3 Repumper laser . . . 53
3.3.4 Off resonant repumper laser . . . 53
3.3.5 Blue detuned (532 nm) high power laser for a plugged quadrupole trap 53
3.4 Experimental sequence . . . 54
3.5 Radiofrequency sources . . . 58
3.5.1 Antennas for dressing . . . 58
3.5.2 Other rf antennas . . . 59
3.6 Imaging system . . . 59
3.6.1 Absorption imaging . . . 59
3.6.2 Horizontal imaging setup . . . 61
3.6.3 Vertical imaging setup . . . 62
3.7 Conclusion . . . 63

**4 Thermal melting of a vortex lattice in a quasi 2D Bose gas 65**
4.1 KTHNY theory . . . 66
4.1.1 Two-step melting of 2D crystals . . . 66
4.1.2 Prediction of Gifford and Baym . . . 67
4.1.3 Correlation functions . . . 67
4.1.3.1 Pair correlation function . . . 68
4.1.3.2 Orientational correlation function . . . 68
4.2 Rotating superfluid in a bubble trap . . . 69
4.2.1 Potential in the rotating frame . . . 69
4.2.2 Experimental details and protocol for rotation . . . 70
4.2.3 Spin-up evaporation . . . 72
4.2.4 Measurement of the effective rotation frequency $\Omega$ . . . 73
4.3 Detection of vortices and Delaunay triangulation . . . 75
4.4 Analysis of results by correlation functions . . . 77
4.4.1 Characterization of translational order . . . 77
4.4.2 Characterization of orientational order . . . 79
4.5 Evidence of thermal melting through Fourier analysis . . . 82
4.6 Conclusion . . . 84

**III Improved experimental setup 85**

**5 Bose-Einstein condensation in a hybrid dimple trap 87**
5.1 Hybrid dimple trap . . . 88
5.1.1 Optical setup . . . 88
5.1.2 Thermodynamic properties . . . 89
5.2 Characterisation of the hybrid dimple trap . . . 92
5.2.1 Position of the focal point $z_c$ . . . 92
5.2.2 Oscillation frequencies . . . 93
5.2.3 Alignment of the dimple beam . . . 93
5.2.4 Experimental determination of $z_H$ . . . 94
5.2.5 Measurements of the oscillation frequencies . . . 95
5.2.6 Position of the focus of the dimple beam ($z_c$) and its waist . . . 97
5.3 Production of the condensate in a hybrid dimple trap . . . 97
5.3.1 Transfer to the hybrid trap and final evaporative cooling . . . 97
5.4 Transfer to the bubble trap . . . 102
5.4.1 Transfer from hybrid dimple trap . . . 103
5.4.2 Transfer from the dimple trap . . . 105
5.4.3 Lifetime of atoms and heating rate in the bubble trap . . . 107
5.4.4 Optimisation of the excitation of the center-of-mass motion . . . 108
5.5 Conclusion . . . 109

**6 New laser system 111**
6.1 Need of a new laser system . . . 111
6.2 Upgraded laser chain . . . 111
6.3 Master laser . . . 112
6.3.1 Optical setup and locking scheme . . . 112
6.4 New NarrowDiode lasers from Radiant Dyes . . . 115
6.4.1 Controllers for lasers . . . 116
6.5 Optical setup with new lasers . . . 117
6.5.1 Frequency beatnote between the $F = 1$ laser and the master laser . . . 118
6.5.2 Frequency beatnote between the $F = 2$ laser and the master laser . . . 120
6.5.3 Frequency beatnote between the $F = 2$ laser and the cooling laser . . . 122
6.6 Problems encountered on the updated setup . . . 124
6.7 Conclusion . . . 127

**7 Non-destructive imaging 129**
7.1 Theory of non-destructive imaging . . . 129
7.2 Different available techniques . . . 131
7.3 Shadowgraph imaging . . . 133
7.3.1 Alignment of the camera . . . 135
7.3.1.1 Focal point . . . 135
7.3.1.2 Determination of the distance of propagation ($d$) . . . 136
7.3.2 Measurement of Thomas-Fermi radius . . . 138
7.3.3 Effect of the EMCCD gain . . . 141
7.4 Acquisition of multiple images . . . 142
7.4.1 Residual atomic losses . . . 142
7.4.2 Choice of the optimal imaging parameters . . . 143

7.5 Conclusion . . . . . 146

**Conclusion** **147**

**Appendices** **149**

**A Useful quantities for the thermal melting of a vortex lattice** **151**
A.1 Vortex pair number $\overline{P_v}$ for continuous uniform vortex density $n_v$ . . . . . 151
A.2 Estimation of $T_c^0$ and $T_{\mathrm{BKT}}$ . . . . . 152

**Bibliography** **153**
Mots-clefs : . . . . . 165
Keywords: . . . . . 165

# Acknowledgements

Je tiens à remercier ici toutes les personnes qui m'ont apporté un soutien constant, de près ou de loin, au cours des trois dernières années de ma thèse de doctorat au LPL.

Tout d'abord, je tiens à remercier les membres du jury de ma soutenance de thèse. Merci à Thomas Bourdel et Kali Wilson pour avoir accepté d'être le rapporteur et la rapporteuse de ma thèse et pour l'avoir lue attentivement. Merci à Jakob Reichel, Giacomo Roati, et Athanasios Laliotis pour avoir accepté de faire partie de mon jury et pour avoir montré leur intérêt pour mon travail.

Je commencerai maintenant par remercier Hélène Perrin, ma directrice de thèse, de m'avoir accepté comme doctorant dans son équipe BEC au LPL, d'avoir dirigé mon travail, d'avoir toujours été disponible pour des discussions scientifiques malgré une charge de travail très importante, et de s'être constamment assurée de mon bien-être tout au long de ma thèse et pendant la période de rédaction. Je te remercie de m'avoir accordé ton temps chaque fois que j'en avais le plus besoin et de corriger mes petites fautes de français.

Je remercie Romain Dubessy, mon co-directeur de thèse, d'avoir été présent au laboratoire pour m'encadrer sur l'expérience de rubidium. Ces trois années de thèse n'auraient pas été les mêmes sans ta présence. Je te remercie d'avoir toujours été calme et posé lors des discussions et d'avoir été là pour comprendre et soutenir mes idées sur l'expérience. Je te souhaite bonne chance pour ce nouveau chapitre de ta vie en tant que professeur à Marseille.

Je remercie Laurent Longchambon d'avoir été présent sur l'expérience chaque fois que tu le pouvais, malgré la lourde charge d'enseignement. Merci pour tes explications pédagogiques sur les observations expérimentales que nous avons faites lors des longues heures d'acquisition de données. Je remercie Thomas Badr, l'ingénieur dans notre groupe, pour son soutien constant sur l'expérience de rubidium. C'est toujours un mystère pour moi de comprendre comment tu parviens à être aussi activement impliqué dans les deux expériences (rubidium et sodium) du groupe. Ta contribution au développement de l'imagerie non-destructive sur l'expérience de rubidium, qui constitue la partie principale de ma thèse, a été immense. Je remercie Aurélien Perrin de n'avoir jamais manqué l'occasion de faire des remarques utiles et des suggestions sur l'expérience au rubidium lors des réunions hebdomadaires du groupe.

Enfin, je tiens à remercier les autres doctorants et post-docs de l'équipe avec qui j'ai passé la majeure partie de mon temps pendant ma thèse. Je tiens à remercier David de m'avoir accueilli sur l'expérience. Ton travail sur l'implémentation de Labscript sur l'expérience a rendu ma routine quotidienne plus agréable et même amusante. Je remercie Matthieu qui a désormais pris la relève sur l'expérience et je te remercie encore plus d'être un bon

professeur d'escalade. Merci à Manon pour être toujours la première personne à comprendre mes blagues et à rire, tandis que les autres ont du mal à les comprendre. Merci à Bastien pour les discussions drôles, dans et hors du laboratoire. Je souhaite bon courage à toi et Matthieu pour la suite de vos thèses. Je tiens à souhaiter bon courage à Zhibin, qui a récemment rejoint notre groupe en tant que post-doctorant. Bien que nous ayons passé peu de temps ensemble au laboratoire, je suis vraiment heureux d'avoir fait ta connaissance, et ta présence lors de nos réunions des doctorants et post-docs en dehors du laboratoire a toujours été très agréable.

Je tiens aussi à remercier les membres de l'atelier de mécanique, ainsi que les membres de l'atelier d'électronique, pour leur assistance sur notre expérience. Je remercie aussi les personnels administratifs du laboratoire pour garantir le bon fonctionnement du laboratoire. Je remercie Stéphane Simonazzi pour pour son soutien technique lors de la mise en place du matériel le jour de ma soutenance de thèse. Je remercie également Anne Amy-Klein, la directrice du laboratoire, nos diverses discussions qui étaient aussi intéressantes les unes que les autres.

Je n'aurais pas pu terminer ma thèse sans le soutien de certaines personnes précieuses en dehors du laboratoire. À ce titre, je tiens à remercier tous mes amis, mais plus particulièrement Pascal, qui m'a vraiment aidé à évoluer en tant que personne dès la première semaine de mon arrivée en France. Ton influence a été immense et je suis vraiment reconnaissant d'avoir fait ta connaissance. Je voudrais également remercier Alexandre d'avoir été la première personne à m'envoyer ses vœux chaleureux et ses encouragements pour ma soutenance.

Je vais maintenant clore cette thèse en exprimant ma gratitude envers ma famille. Je tiens à remercier mes parents et ma petite sœur pour leur soutien constant tout au long de mon parcours académique. Un grand merci à ma mère pour avoir toujours été présente et à mes côtés chaque fois que j'avais le plus besoin de toi.

# General Introduction

Bose-Einstein condensate is a state of matter that exists at very low temperatures and was predicted in 1924 by Einstein [1, 2]. Einstein had extended the ideas of Satyendra Nath Bose [3] on the statistical behaviour of bosons, showing that, at a temperature $T$ lower than a critical temperature $T_c$, a group of bosons could occupy the same quantum state, forming a single macroscopic quantum entity. The concept of Bose-Einstein condensate remained theoretical for a long time. However, this theoretical concept was later taken into consideration by London after the experiment performed by Kapitza [4], Allen and Misener [5] to cool down liquid helium below 2.17 K where they observed that the viscosity of liquid helium suddenly dropped to zero during the cooling process resulting in a transition from liquid phase to superfluid phase. London [6] related this transition to the Bose-Einstein condensation as the cooling temperature in the experiment was much closer to the critical temperature required for an ideal gas with the same density to reach the Bose-Einstein condensation.

The first experimental observation of a Bose-Einstein condensate in a dilute gas in the mid-1990s opened a new frontier in the study of the dynamics of a superfluid and has led to a rapid expansion of research in ultracold atomic physics. For this initial accomplishment, Wolfgang Ketterle [7] and Eric Cornell and Carl Wieman [8] were awarded the Nobel Prize in Physics in 2001. This milestone would not have been achieved without the advancements in realization and experimental development of laser cooling and magneto-optical trapping of atoms, that led Claude Cohen-Tannoudji, Steven Chu and William D. Phillips to win the Nobel prize in physics in 1997 [9–11].

The field of ultracold atomic physics has grown at an unprecedented pace, with experimental techniques advancing rapidly to allow for more sophisticated and precise control over quantum gases. One significant achievement was the ability to load ultracold atoms into optical lattices [12] formed by intersecting laser beams that create a periodic potential for the atoms. This allowed for the study of atomic systems in highly controlled, artificially engineered potentials, enabling researchers to manipulate individual atoms and observe quantum effects at the single-particle level [13–15].

The lower atomic density and weaker interactions in dilute gases make them ideal for theoretical models like the Gross-Pitaevskii equation which describes very well the system by taking into account the interactions through a mean-field theory. Moreover, the ability to manipulate these quantum gases with extreme precision using optical lattices, magnetic fields, and laser cooling techniques has revolutionized the study of superfluidity and quantum systems more generally. The ability to create and control BECs using laser cooling [16,

17], optical dipole trap [18], magnetic trap [19] and evaporative cooling [20, 21] techniques have enabled researchers to cool down atoms to temperatures as low as 100 nK to achieve quantum degeneracy [22, 23] and observe superfluid behaviour. One of the most intriguing characteristics of a superfluid [24] is that it is non-viscous. Moreover a superfluid flow is irrotational as its velocity is proportional to the gradient of the phase. Any attempt to set a superfluid into rotation will result in the nucleation of quantized vortices [25–28].

Alongside advances in experimental techniques, the study of superfluidity itself has progressed significantly. Early experiments on superfluidity in dilute gases demonstrated well-known effects like the collective modes [29–31], which were confirmed only a few years after the first creation of dilute BECs. There have been significant advancements in the study of rotating superfluids. The observation of quantized vortices [32, 33] and vortex lattices [34] both key features of rotating superfluids has provided valuable insight into the quantum dynamics of these systems. The study of rotating superfluids has also led to the discovery of phenomena analogous to the Quantum Hall Effect [35], with research showing that superfluids in rotating systems can exhibit behaviour similar to that seen in two-dimensional electron gases subjected to strong magnetic fields.

Another exciting development has been the study of low-dimensional superfluids. In systems with reduced dimensionality, quantum fluctuations play a more prominent role, which can drastically alter the system's behaviour. In two-dimensional systems, for example, a quasi-long range order is expected at a low temperature which eventually disappears as the temperature exceeds its critical value and this results in a transition from a superfluid state to a normal fluid state. This mechanism is called the Berezinskii-Kosterlitz-Thouless (BKT) transition [36, 37]. This transition, which occurs in the presence of thermal fluctuations, is a unique feature of two-dimensional systems and has provided new insights into the interplay between quantum effects and phase transitions [38, 39]. Other recent advancements in the study of low-dimensional superfluids have underscored their potential for simulating complex many-body systems. Very recently, Neely et al. [40] developed a "vortex matter" simulator designed to emulate the two-dimensional one-component plasma (2D OCP) by manipulating quantised vortices within a quasi-2D superfluid. Although their work has not yet been published, this approach aims to explore phase transitions such as the melting of the Wigner crystal, and phenomena like the Kosterlitz-Thouless-Halperin-Nelson-Young (KTHNY) transition and topological edge states analogous to those observed in the fractional quantum Hall effect. Such emerging experimental platforms complement and extend earlier theoretical and experimental efforts, including those presented in this thesis, helping to bridge the gap between models and real-world observations and offering deeper insights into superfluid behaviour in reduced dimensions. In order to produce experimentally a 2D quantum gas, we have to confine it tightly along one direction in space and in this way, the dynamics is frozen along that confined axis. It is possible to realise this trapping configuration using magnetic fields [41], which is the case in our experiment.

I did my PhD thesis on the ultracold atoms experiment using an isotope of rubidium, $^{87}$Rb which is bosonic. In our experiment, we prepare the BEC in the 3D regime. However, it enters the quasi-2D regime when we set the gas into rotation. For this purpose, we use a trap made of a static magnetic field and a radiofrequency field that has the geometry of a bubble and is anharmonic in nature which allows us to reach very large rotation rates. A part of my PhD thesis is focused on the observation of the thermal melting of the vortex lattice in a fast-rotating quasi-2D superfluid at the bottom of a bubble trap. The preliminary observations regarding this experiment were made during the PhD thesis of Matthieu de Goër

de Herve [42]. The melting scenario in 2D crystals was proposed by Kosterlitz, Thouless, Halperin, Nelson and Young [37, 43, 44], and was named KHTNY theory.

During the early days of my PhD thesis, we were working with the plugged quadrupole trap to produce the BEC [45]. We used a blue detuned (532 nm), 10 W Verdi laser, plug beam focused around the center of the quadrupole trap in order to prevent atoms reaching the trap center and getting lost due to Majorana losses [46] while performing evaporative cooling. This way of producing a BEC in the trap would lead to the excitation of the center of mass motion while transferring the ultracold sample to the bubble trap. To overcome this limitation, I worked on changing the trapping configuration with a quadrupole magnetic trap in our experiment to produce a BEC and make the smooth transfer to the bubble trap. This was made by replacing the plug beam with a red-detuned (1064 nm), 5 W Keopsys laser. This change required the characterization of the trap in terms of atom number, the temperature of the atomic cloud and the oscillation frequencies in the trap. The way of performing evaporative cooling in the new trap was changed and adapted to be optimal.

An upgrade of the 780 nm laser system in our experiment was required as the initial version had some limitations. One major limitation was related to the initial imaging setup. The initial imaging setup was absorption-based: we imaged the condensate using a resonant probe beam and this resulted in the complete destruction of the signal after a single measurement. Our motivation was to image the BEC several times during a single experimental sequence in order to create a movie of its evolution which was not possible using the absorption imaging method. To perform this imaging we needed a probe beam which could be detuned from the imaging transition in order to suppress the absorption during the imaging thus allowing us to make multiple measurements during the single experimental sequence. Therefore to have access to desirable detunings of the different laser beams required to carry on the experiment, we decided to change the laser system and implemented a locking scheme through beatnotes between the lasers.

Finally, the new non-destructive imaging system in our experiment was implemented. This way of imaging the atomic cloud makes the process much faster and less prone to experimental fluctuations.

This PhD thesis consists of seven chapters divided into three parts and is organized as follows:

- The first part named **Preliminaries** consists of two chapters:

  **Chapter** 1: This chapter aims to present the necessary theoretical elements required to understand the experimental content of this PhD thesis. I start by presenting the theory of Bose-Einstein condensate and the possibility of the occurrence of this transition for an ideal gas in 3D and 2D regimes. Then I consider the presence of weak interactions among the particles and use the time-dependent and time-independent Gross-Pitaevskii equations (GPEs) to explain the true ground state of the system in which the BEC transition will occur. Then I relate the time-dependent GPE equation to the hydrodynamic equations of a superfluid to introduce the concept of vortex formation in a superfluid. Next, I introduce the method to undergo the 2D regime experimentally and the BKT transition that can occur in this regime leading to the superfluid transition of a quantum gas. Finally, I present the collective modes of trapped quantum gas in 3D and 2D regimes respectively.

  **Chapter** 2: This chapter is devoted to the concept of adiabatic potentials for atoms dressed by the radiofrequency field. The content of this chapter is closely based on the

published work of Hélène Perrin and Barry Garraway [47]. In this chapter, I explain the principle of a bubble trap and its geometry depending on the polarization of the radiofrequency field.

- The second part named **Thermal melting of a vortex lattice** consists of two chapters:

  **Chapter** 3: This chapter represents the experimental setup along with the laser configuration that I worked on at the beginning of my PhD thesis. I start by explaining the main part of the experiment, i.e., 2D-MOT, 3D-MOT and a science cell in which we produce a BEC. I then present the initial laser configuration in our experiment and the process we used to produce a BEC and its transfer to the bubble trap. Finally, I explain the limitations of the experiment setup with the initial laser configuration and the motivation to change the laser system in order to achieve better stability and to be able to perform desired experiments.

  **Chapter** 4: This chapter presents the experimental work done to make the first-ever observation of the thermal melting of a vortex lattice in a fast-rotating quasi-2D superfluid Bose gas [48]. I start this chapter by explaining the theory of thermal melting in 2D crystals and how our experimental system was ideal to observe this melting scenario. I then describe the experimental sequence in order to put a superfluid into rotation to form a vortex lattice. Lastly, I present the experimental results and compare them with the theoretical predictions to conclude the presence of a melting transition.

- The third part named **Improved experimental setup** consists of three chapters:

  **Chapter** 5: This chapter presents the installation and the characterization of the newly installed red-detuned (1064 nm), 5 W laser from Keopsys to create a hybrid dimple trapping configuration with the quadrupole magnetic trap. This chapter describes the motivation behind the installation of this trapping configuration, the complete characterization process of the trap and the evaporation process to produce a BEC in this trap [49]. I explain two possible ways of performing evaporation either using a radiofrequency field or optically by reducing the trap depth of the dimple laser. Then, I explain the transfer process of atoms to the bubble trap depending on the performed evaporation in the hybrid trap and compare their respective performances. Finally, I conclude the chapter by discussing the optimization of the excitations of the center of mass motion of the atoms after the transfer process.

  **Chapter** 6: This chapter presents the upgraded version of the 780 nm laser system in our experiment. I start this chapter by presenting the organization of the upgraded laser system. I give information about the two newly installed Narrowdiode lasers from Radiant Dyes and their need in our experiment. I explain the locking of a master laser in our experiment using a saturated absorption scheme and then the locking scheme for other lasers through beatnotes with the master laser. Finally, I detail the problems we experienced with the two newly installed Narrowdiode lasers from Radiant Dyes and how we solved those problems.

  **Chapter** 7: This is the final chapter of this PhD thesis describing the non-destructive imaging technique that we have recently implemented in our experiment. I start this chapter by explaining the need for this imaging method in our experiment and its working principle. Then, I present some of the available techniques to be able to perform non-destructive imaging. Then, I explain the motivation behind choosing the

shadowgraph imaging method out of all other available techniques for our experiment. I provide the theoretical details of the shadowgraph imaging method followed by the experimental characterization performed to implement this method in our experiment. I then explain the method used to compute the atomic density for this imaging method. Finally, I discuss the experimental destructiveness of the measurements depending on the different values of the imaging parameters and compare them with the theoretical models.

Finally, I end this PhD thesis by presenting a general conclusion.

# Part I

# Preliminaries

# Chapter 1

# Bose-Einstein condensate, superfluidity and collective modes

This chapter aims to provide details about the basic concepts of Bose-Einstein condensation and superfluidity. I will first start by describing the mechanism of Bose-Einstein condensation, its physics at rest with and without interactions and its out-of-equilibrium behaviour. To understand the out-of-equilibrium behaviour, I will first discuss the formulation of hydrodynamic equations of the superfluid from the time-dependent Gross-Pitaevskii equation (GPE). I will then investigate the Bogoliubov excitation spectrum in the case of small elementary excitations. Then, I will show that the consequence of rotating a superfluid leads to the formation of vortices. In the end, I will discuss the experimental realisation of a 2D Bose gas and the BKT transition in that regime and finally, I will conclude the chapter by describing the excitations of collective modes in the 3D and quasi-2D regime.

## 1.1 Bose-Einstein condensate

### 1.1.1 Saturation of excited states

The phenomenon of Bose-Einstein condensation is best described in the grand canonical ensemble, where both energy and atom number can fluctuate, their average value being fixed by the knowledge of the temperature $T$ and the chemical potential $\mu$. To understand this phenomenon well, we will start by considering an ideal Bose gas with a number $N$ of bosons at equilibrium at $T$ and $\mu$. In this case, we obtain the average number of particles in each energy level from Bose-Einstein statistics. In the grand canonical ensemble the average occupation of $i^{\text{th}}$ state with energy $E_i$ can be written under the form:

$$N_i = \frac{1}{e^{(E_i-\mu)/k_BT} - 1} \tag{1.1}$$

and the average total number of particles in all the energy levels can then be written as:

$$N = \sum_i N_i = \sum_i \frac{1}{e^{(E_i-\mu)/k_BT} - 1}. \tag{1.2}$$

$N_i$ should be positive which means that $\mu$ should always be less than the energy of the ground state $E_0$. Defining the energy of the ground state $E_0 = 0$, we set the condition given by equation (1.3) i.e., $\mu$ can take the values between $-\infty$ and 0.

$$\mu < E_0 = 0. \tag{1.3}$$

We can decompose equation (1.2) into two parts, first for the ground state and second for all the excited states as:

$$N = N_0 + N_{\text{exc}}, \tag{1.4}$$

where

$$N_0 = \frac{Z}{1-Z}, \;\; N_{\text{exc}} = \sum_{i>0} \frac{Z}{e^{E_i/k_BT} - Z}. \tag{1.5}$$

$Z = \exp(\mu/k_BT)$ is called the fugacity. As $\mu$ is negative, the fugacity is a number between 0 and 1. There is thus an upper bound on the total population of the excited states:

$$N_{\text{exc}} < N_{\text{exc}}^{(\max)}(T) = \sum_{i>0} \frac{1}{e^{E_i/k_BT} - 1}, \tag{1.6}$$

provided that the infinite sum over $i$ converges. We can explain the mechanism of Bose-Einstein condensation through this upper bound. Indeed, if the system for a given temperature $T$, has a number of particles greater than $N_{\text{exc}}^{(\max)}(T)$, then at least $N - N_{\text{exc}}^{(\max)}(T)$ particles will accumulate in the ground state $i = 0$. However, in the thermodynamic limit i.e., where $N$ and the volume tend towards infinity at constant density, the convergence of the sum in equation (1.6) depends upon the dimension and the geometry of the trap. We will next see if the saturation of excited states survives the thermodynamic limit in the following cases: 3D harmonic trap, 2D uniform case and 2D harmonic trap.

### 1.1.2 Ideal Bose gas in a 3D harmonic trap

Let us consider $N$ particles trapped in a 3D anisotropic harmonic trap whose potential is expressed as:

$$V(x,y,z) = \frac{1}{2}M(\omega_x^2 x^2 + \omega_y^2 y^2 + \omega_z^2 z^2) \tag{1.7}$$

where $M$ is the atomic mass and $\omega_x, \omega_y$ and $\omega_z$ are the trapping frequencies in the $x$, $y$ and $z$ direction respectively. We can then write the energies of the single-particle states as:

$$E_{n_x,n_y,n_z} = n_x\hbar\omega_x + n_y\hbar\omega_y + n_z\hbar\omega_z \tag{1.8}$$

where $n_x, n_y$ and $n_z$ are non-negative integers and we have taken again the ground state as the origin of energies. Then, the equation (1.6) will have 3 sums for $n_x, n_y$ and $n_z$ respectively. In the semi-classical limit ($k_BT \gg \hbar\omega_{x,y,z}$), we can replace the sum in equation (1.6) by an integral allowing us to calculate the maximal population of the excited states [50]:

$$N_{\text{exc}}^{(\max)}(T) = \zeta(3)\left(\frac{k_BT}{\hbar\omega_{\text{ho}}}\right)^3, \tag{1.9}$$

where $\omega_{\rm ho} = (\omega_x\omega_y\omega_z)^{1/3}$ is the geometric mean of the trapping frequencies, $\zeta$ is the Riemann function and $\zeta(3)$=1.202. $N_{\rm exc}^{(\rm max)}(T)$ is a monotonic function that depends only on the temperature such that there is a critical temperature $T_c$ at which $N = N_{\rm exc}^{(\rm max)}(T_c)$. Therefore, the equation (1.9) can be rewritten as [50]:

$$k_B T_c = \hbar\omega_{\rm ho}\left(\frac{N}{\zeta(3)}\right)^{1/3} = 0.94\hbar\omega_{\rm ho}N^{1/3}. \tag{1.10}$$

Below the critical temperature, the population of the ground state is a macroscopic fraction of $N$ and we can represent the total number of particles $N$ as a sum of the particles in the excited states and particles in the ground state as shown in the equation (1.4). Dividing this equation by $N = N_{\rm exc}^{(\rm max)}(T_c)$, we can calculate the fraction of atoms in the ground state as:

$$\frac{N_0}{N} = 1 - \left(\frac{T}{T_c}\right)^3. \tag{1.11}$$

### 1.1.3 Ideal Bose gas in 2D

In this section, we will examine the convergence of the sum of equation (1.6) in the 2D regime to see if BEC transition can occur. We will first investigate the case of uniform Bose gas and then that of the Bose gas confined in a 2D harmonic trap.

#### Uniform case

Let us start by considering $N$ particles in a hard wall square 2D box of side length $L$ inside which the potential is zero. In the semi-classical limit ($k_B T \gg \frac{\hbar^2}{ML^2}$), we can replace the sum in equation (1.6) by an integral [51]:

$$N_{\rm exc} = \int_0^\infty \frac{\mathcal{D}(E)}{e^{(E-\mu)/k_B T}} dE. \tag{1.12}$$

The density of states is constant $\mathcal{D}(E) = ML^2/2\pi\hbar^2$, therefore

$$N_{\rm exc} = -\frac{L^2}{\lambda_T^2}\ln(1-Z), \tag{1.13}$$

where $\lambda_T = \frac{\hbar}{\sqrt{2\pi M k_B T}}$ is the thermal de-Broglie wavelength. In the thermodynamic limit ($N, L \to \infty$, with $\frac{N}{L^2}$ = constant) as $\mu \to 0$, the number of particles in the excited states $N_{\rm exc}$ diverges resulting in the absence of the saturation of the excited states. Therefore, there is no condensation for the uniform Bose gas in 2D at $T \neq 0$. We can also show from equation (1.13) that the expression of the phase space density is :

$$\mathcal{D} = -\ln(1-Z). \tag{1.14}$$

#### Harmonic trap

We now consider that the particles are confined in an isotropic 2D harmonic trap of frequency $\omega$. In this case, we can write the potential of the trap as:

$$V_{\rm trap} = \frac{1}{2}M\omega^2 r^2, \tag{1.15}$$

the density of states is $\mathcal{D}(E) = E/(\hbar\omega)^2$ and with equation (1.12) we can show that the saturation of the excited states occurs at

$$N_{\text{exc}}^{\max} = \frac{\pi^2}{6}\left(\frac{k_B T}{\hbar\omega}\right)^2. \tag{1.16}$$

Unlike the uniform case, the saturation of excited states survives here at the thermodynamic limit leading to the BEC transition [52]. The critical temperature for the BEC transition at a fixed number of atoms is given by:

$$k_B T_c = \hbar\omega \frac{\sqrt{6N}}{\pi}. \tag{1.17}$$

The phase space density in this case is:

$$\mathcal{D}(r) = -\ln\left(1 - e^{(\mu - \frac{1}{2}M\omega^2 r^2)/k_B T}\right). \tag{1.18}$$

From the above equation, we can note that the phase space density diverges at the center of the trap during condensation ($\mu = 0, r = 0$). The phase space density has the same form as in equation (1.14) provided that the chemical potential is replaced by a local chemical potential $\mu_{\text{loc}}$, reduced by the confinement potential:

$$\mu_{\text{loc}} = \mu - \frac{1}{2}M\omega^2 r^2. \tag{1.19}$$

Of course, this divergence is not physical and the maximum phase-space density will be limited by interactions, that need to be taken into account.

### 1.1.4 Interactions in Bose gases

Previously, I discussed the case of an ideal Bose gas and how the particles accumulate in the ground state below a certain critical temperature. However, with typical atomic gases used in the experiments, due to the presence of interactions the picture is not the same even if the interactions are weak as this modifies the condensate behaviour. If the interactions are present we can not simply say that the criterion for Bose-Einstein condensation is the accumulation of the particles in the ground state. In the presence of repulsive interactions, the atoms will accumulate in the different single-particle states to reduce the density and thus the true ground state in which the condensation occurs will be modified.

We can write the many-body Hamiltonian describing $N$ interacting bosons in an external potential $V_{\text{ext}}$ as [50]:

$$\begin{aligned}\hat{H} = &\int d\mathbf{r}\hat{\Psi}^\dagger(\mathbf{r})\left[-\frac{\hbar^2}{2M}\nabla^2 + V_{\text{ext}}(\mathbf{r})\right]\hat{\Psi}(\mathbf{r}) \\ &+ \frac{1}{2}\int d\mathbf{r}d\mathbf{r}'\hat{\Psi}^\dagger(\mathbf{r})\hat{\Psi}^\dagger(\mathbf{r}')V(\mathbf{r}-\mathbf{r}')\hat{\Psi}(\mathbf{r})\hat{\Psi}(\mathbf{r}')\end{aligned} \tag{1.20}$$

where $\hat{\Psi}^\dagger(\mathbf{r})$ and $\hat{\Psi}(\mathbf{r})$ are the boson field operators that create and annihilate the particle at a position $\mathbf{r}$ and $V(\mathbf{r}-\mathbf{r}')$ is the two-body interaction potential.

We can deduce the ground state and the thermodynamic properties of the system using equation (1.20). However, the calculation can be complicated for systems with a large number

of particles. To overcome this problem, the mean-field approach can be used so that we don't have to solve completely the many-body Hamiltonian. The many-body description for the Bose gas was first proposed by Bogoliubov. This approach implies separating the condensate part in the decomposition of the boson field operator in an appropriate basis. The boson field operator can be represented as:

$$\hat{\Psi}(\mathbf{r}) = \sum_i \Psi_i(\mathbf{r})\hat{a}_i \tag{1.21}$$

where $\Psi_i(\mathbf{r})$ are the single particle wave functions and $\hat{a}_i$ are the corresponding annihilation operators. We can write the number of particles in the single particle $i^{\text{th}}$ state as $N_i = \left\langle \hat{a}_i^\dagger \hat{a}_i \right\rangle$. As we have already seen the BEC occurs at $T < T_c$ when the population of the ground state becomes macroscopic, i.e., $N_0 \gg 1$. In this case, the operators $\hat{a}_0^\dagger$ and $\hat{a}_0$ relative to the ground state can be treated as c-numbers: $\hat{a}_0^\dagger = \hat{a}_0 = \sqrt{N_0}$ [50, 53]. The field operator can then be written as:

$$\hat{\Psi}(\mathbf{r}) = \sqrt{N_0}\Psi_0(\mathbf{r}) + \sum_{i\neq 0} \Psi_i(\mathbf{r})\hat{a}_i. \tag{1.22}$$

We can generalise this Bogoliubov description to the case of nonuniform and time-dependent configurations as [50]:

$$\hat{\Psi}(\mathbf{r}, t) = \psi(\mathbf{r}, t) + \hat{\Psi}'(\mathbf{r}, t), \tag{1.23}$$

where $\psi(\mathbf{r}, t)$ is a complex function also defined as the expectation value of the field operator. The modulus of this complex function gives the density of the condensate: $|\psi(\mathbf{r}, t)|^2 = n_0(\mathbf{r}, t)$. This function is the order parameter which characterizes the off-diagonal long-range behaviour of the one-particle density matrix and is usually known as the wave function of the condensate. We can also write the first-order correlation function as one-particle density matrix:

$$g_1(\mathbf{r}, \mathbf{r}', t) = \left\langle \hat{\Psi}^\dagger(\mathbf{r}, t)\hat{\Psi}(\mathbf{r}', t) \right\rangle. \tag{1.24}$$

Penrose and Onsager showed in 1956 [54] that in the presence of interactions the population of the ground state is given by:

$$\lim_{|\mathbf{r}-\mathbf{r}'|\to\infty} g_1(\mathbf{r}, \mathbf{r}', t) \tag{1.25}$$

where $g_1(\mathbf{r}, \mathbf{r}', t) = \psi^*(\mathbf{r}, t)\psi(\mathbf{r}', t)$. From the above equation (1.25), we can say that the existence of the BEC is possible when the first-order correlation function tends towards a non-zero limit at a large distance translating in a long-range order (LRO).

To deduce an equation for the condensate wave function $\psi(\mathbf{r}, t)$, we first have to apply the Heisenberg equation to the many-body Hamiltonian (equation 1.20) to describe the time evolution of the field operator $\hat{\Psi}(\mathbf{r}, t)$:

$$\begin{aligned} i\hbar\frac{\partial}{\partial t}\hat{\Psi}(\mathbf{r}, t) &= \left[\hat{\Psi}, \hat{H}\right] \\ &= \left[-\frac{\hbar^2}{2M}\nabla^2 + V_{\text{ext}}(\mathbf{r}) + \int d\mathbf{r}'\hat{\Psi}^\dagger(\mathbf{r}', t)V(\mathbf{r}' - \mathbf{r})\hat{\Psi}(\mathbf{r}', t)\right]\hat{\Psi}(\mathbf{r}, t). \end{aligned} \tag{1.26}$$

Then we have to replace $\hat{\Psi}$ by $\psi$ in order to derive the equation for the condensate wave function. In the ultracold temperature and dilute gas regime, we can obtain a proper expression for the interaction term $V(\mathbf{r}'-\mathbf{r})$ by saying that in this regime the only important interactions between the particles are low energy binary collisions (s-wave collisions). These interactions can be fully summarized by the single parameter called scattering length $a$ [53]. The effective interaction potential between the particles can thus be described by a Dirac potential with only one amplitude parameter [50]:

$$V_{\text{int}}(\mathbf{r}'-\mathbf{r}) = g_{\text{int}}\delta(\mathbf{r}'-\mathbf{r}) \tag{1.27}$$

where $\delta(\mathbf{r})$ is the Dirac distribution and $g_{\text{int}}$ is the interaction constant, which is related to the scattering length $a$. This interaction constant is written under the form:

$$g_{\text{int}} = \frac{4\pi\hbar^2 a}{M}. \tag{1.28}$$

By replacing $V(\mathbf{r}'-\mathbf{r})$ in equation (1.26) with the effective interaction potential (1.27), we get the following result:

$$i\hbar\frac{\partial}{\partial t}\psi(\mathbf{r},t) = \left(-\frac{\hbar^2}{2M}\nabla^2 + V_{\text{ext}}(\mathbf{r}) + g_{\text{int}}|\psi(\mathbf{r},t)|^2\right)\psi(\mathbf{r},t). \tag{1.29}$$

This equation is called the Gross-Pitaevskii equation (GPE) [50]. Here the first term corresponds to the kinetic energy of the condensate, the second term corresponds to the trapping energy and the third term to the interaction energy. Through this equation, one can deduce the different properties of the trapped condensate like its atomic density, its size and its dynamics.
To find the stationary solution of the equation (1.29), we can first write the condensate wave function as:

$$\psi(\mathbf{r},t) = \psi(\mathbf{r})\exp\left(-i\frac{\mu t}{\hbar}\right) \tag{1.30}$$

where $\mu$ is the chemical potential. Substituting the wave function equation (1.30) in the GPE (1.29), one gets the following stationary equation:

$$\mu\psi(\mathbf{r}) = \left(-\frac{\hbar^2}{2M}\nabla^2 + V_{\text{ext}}(\mathbf{r}) + g_{\text{int}}|\psi(\mathbf{r})|^2\right)\psi(\mathbf{r}). \tag{1.31}$$

This time-independent equation describes specifically the ground state of the system.

In the case of repulsive interactions, the kinetic energy term in the equation (1.31) becomes less important than the interaction term and can be neglected. This approximation is called the Thomas-Fermi approximation. Under this approximation, the density profile takes the following form:

$$n(\mathbf{r}) = |\psi(\mathbf{r})|^2 = \frac{\mu - V_{\text{ext}}(\mathbf{r})}{g_{\text{int}}}, \text{ for } \mu > V_{\text{ext}}(\mathbf{r}). \tag{1.32}$$

For a gas confined in a harmonic trap, the Thomas-Fermi condition writes $Na \gg a_{\text{ho}}$, where $a_{\text{ho}} = \sqrt{\hbar/M\omega_{\text{ho}}}$ is the length of the harmonic oscillator and the density distribution can be rewritten as:

$$n(\mathbf{r}) = n_0\left(1 - \frac{x^2}{R_x^2} - \frac{y^2}{R_y^2} - \frac{z^2}{R_z^2}\right) \tag{1.33}$$

where $n_0 = \mu/g_{\text{int}}$ is the maximum density at the center of the trap and $R_{x,y,z}$ are the Thomas-Fermi radii in $x, y$ and $z$ direction respectively and can be written as:

$$R_\alpha^2 = \frac{2\mu}{M\omega_\alpha^2};\ \text{for } \alpha = x, y, z. \tag{1.34}$$

We can express the relation between chemical potential $\mu$ of the 3D cloud trapped in a harmonic trap and the number of particles as [50]:

$$\mu = \frac{1}{2}M\omega_\alpha^2 R_\alpha^2 = \frac{\hbar\omega_{\text{ho}}}{2}\left(\frac{15Na}{a_{\text{ho}}}\right)^{2/5}. \tag{1.35}$$

One can note from the equation (1.33) that the density vanishes at the edge of the BEC, so here the kinetic energy term plays an important role as the interaction term becomes small. In this region, the Thomas-Fermi approximation does not hold. The length over which the kinetic energy term becomes more important is called the healing length $\xi$ and can be deduced by comparing the kinetic energy over the length $\xi$ with the chemical potential $\mu = g_{\text{int}}n_0$:

$$\xi = \sqrt{\frac{\hbar^2}{2M\mu}} = \frac{1}{\sqrt{8\pi a n_0}}. \tag{1.36}$$

## 1.2 Superfluid dynamics of a Bose gas

In the previous section, I have discussed the BEC at rest but in the upcoming sections, I will also talk about the superfluid dynamics of the condensate when putting it into rotation or while performing excitations to study collective modes etc. In the following section, I will thus provide some theoretical formulation necessary to describe the out-of-equilibrium dynamics of the condensate.

### 1.2.1 Hydrodynamic formulation

The time-dependent GPE (1.29) can be written equivalently as hydrodynamic equations of a superfluid with a continuity equation and an Euler-like equation. To do so, we first multiply the time-dependent GPE (1.29) by $\psi^*(\mathbf{r}, t)$ and subtract from it the complex conjugate of the resulting equation [55]:

$$i\hbar\left(\psi^*\frac{\partial}{\partial t}\psi + \psi\frac{\partial}{\partial t}\psi^*\right) = -\frac{\hbar^2}{2M}(\psi^*\nabla^2\psi - \psi\nabla^2\psi^*) \tag{1.37}$$

which can also be written as:

$$\frac{\partial}{\partial t}|\psi|^2 = -\nabla.\left[\frac{\hbar}{2Mi}(\psi^*\nabla\psi - \psi\nabla\psi^*)\right]. \tag{1.38}$$

As $|\psi|^2 = n$, the equation above can be written under the form of the continuity equation for a classical compressible fluid:

$$\frac{\partial n}{\partial t} + \nabla.(n\mathbf{v}) = 0 \tag{1.39}$$

where $\mathbf{v}$ is the velocity of the fluid and is defined as:

$$\mathbf{v} = \frac{\hbar}{2Mi|\psi|^2}(\psi^*\nabla\psi - \psi\nabla\psi^*). \tag{1.40}$$

Writing the wave function as a function of density and the phase: $\psi(\mathbf{r},t) = \sqrt{n(\mathbf{r},t)}e^{i\phi(\mathbf{r},t)}$ and inserting this expression of the wave function into the equation (1.40), we get:

$$\mathbf{v}(\mathbf{r},t) = \frac{\hbar}{M}\nabla\phi(\mathbf{r},t). \tag{1.41}$$

This is the expression for the local velocity of the superfluid which is proportional to the gradient of the phase. This means that the superfluid is irrotational, at least if the phase has no singularity.
Inserting the wave function depending on density and phase in the time-dependent GPE (1.29) leads to the following equation describing the evolution of the phase:

$$\hbar\frac{\partial\phi}{\partial t} + \frac{1}{2}M\mathbf{v}^2 - \frac{\hbar^2}{2M\sqrt{n}}\nabla^2(\sqrt{n}) + g_{\text{int}}n + V_{\text{ext}} = 0. \tag{1.42}$$

The above expression can also be written as the time derivative of the superfluid velocity using the relation (1.41) as:

$$\nabla\left(\frac{1}{2}M\mathbf{v}^2 - \frac{\hbar^2}{2M\sqrt{n}}\nabla^2(\sqrt{n}) + g_{\text{int}}n + V_{\text{ext}}\right) + M\frac{\partial\mathbf{v}}{\partial t} = 0. \tag{1.43}$$

The above equation is referred to as the Euler equation for quantum fluids [56]. The term containing $\hbar$ with the gradient of the density is called the 'quantum pressure' term and it tells that the importance of quantum effects is emphasized in nonuniform gases. The continuity equation (1.39) and the equation describing the evolution of the phase (1.42) provide the set of coupled equations which is equivalent to the time-dependent GPE (1.29). These hydrodynamic equations allow us to study the out-of-equilibrium dynamics such as the collective modes of the trapped BEC [57].

### 1.2.2 The Bogoliubov approach

#### Bogoliubov excitation spectrum

To describe the dynamics of a quantum fluid, it is important to characterise its excitations. Through the Bogoliubov approach, we can obtain the excitation spectrum of the Bose gas by considering a small perturbation from its equilibrium state and finding the solution of the time-dependent GPE. However, we can also use this approach with the hydrodynamic equations (1.39) and (1.43). Here we will look at the excitation spectrum of a uniform gas, i.e., without the trapping potential. In classical hydrodynamics the evolution of the density distribution of a fluid $n(\mathbf{r},t)$ in time is related to the time evolution of its velocity field $\mathbf{v}(\mathbf{r},t)$. In order to obtain the excitation spectrum, we will consider a small deviation from the stationary values of the density and the velocity fields ($n_0$ and $\mathbf{v}_0$) and expand the equation to first order. For a BEC at rest, the density $n_0$ is independent of $\mathbf{r}$ and the stationary value of the velocity field is zero ($\mathbf{v}_0 = \mathbf{0}$). In this case, we can write the following equations:

$$n(\mathbf{r},t) = n_0 + \delta n(\mathbf{r},t),\ \mathbf{v}(\mathbf{r},t) = \mathbf{0} + \mathbf{v}(\mathbf{r},t). \tag{1.44}$$

Since $\delta n$ and $\mathbf{v}$ must be real, they can be written as:

$$\delta n(\mathbf{r},t) = Ae^{i(\mathbf{k}.\mathbf{r}-\omega t)} + A^*e^{-i(\mathbf{k}.\mathbf{r}-\omega t)}, \tag{1.45}$$

$$\mathbf{v}(\mathbf{r},t) = \mathbf{k}\left[Be^{i(\mathbf{k}.\mathbf{r}-\omega t)} + B^*e^{-i(\mathbf{k}.\mathbf{r}-\omega t)}\right]. \tag{1.46}$$

Here we have considered the phase as: $\phi(\mathbf{r},t) = \frac{M}{i\hbar}\left[Be^{i(\mathbf{k}.\mathbf{r}-\omega t)} - B^* e^{-i(\mathbf{k}.\mathbf{r}-\omega t)}\right]$. Substituting these expressions for the density and velocity fluctuations in the continuity equation (1.39) and in the Euler equation describing the superfluid (1.43), we get the following set of equations to first order in $\delta n$ and $\mathbf{v}$:

$$\omega A + k^2 n_0 B = 0, \tag{1.47}$$

$$\omega n_0 B + \frac{g_{\rm int} n_0}{M} A + \frac{\hbar^2 k^2}{4M^2} A = 0. \tag{1.48}$$

We can now write these equations in the form of an eigenvalue equation:

$$\begin{pmatrix} \omega & k^2 \\ \frac{\hbar^2 k^2}{4M^2} + \frac{g_{\rm int} n_0}{M} & \omega \end{pmatrix} \begin{pmatrix} A \\ n_0 B \end{pmatrix} = 0. \tag{1.49}$$

By solving this eigenvalue equation we get the Bogoliubov excitation spectrum:

$$E_k = \sqrt{\frac{\hbar^2 k^2}{2M}\left(\frac{\hbar^2 k^2}{2M} + 2g_{\rm int} n_0\right)} = \frac{\hbar^2 k^2}{2M}\sqrt{1 + \frac{2}{(k\xi)^2}} \tag{1.50}$$

where $E_k$ is the energy of an elementary excitation of the system of momentum $\mathbf{k}$ and the energy spectrum is shown in Fig. 1.1.

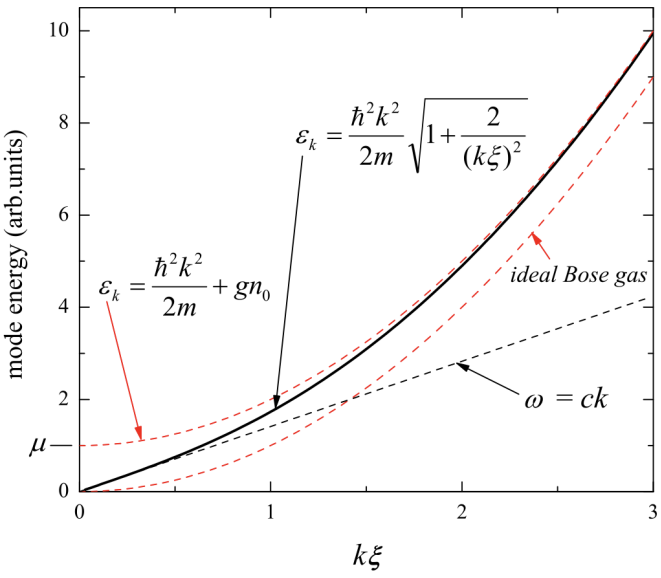



**Figure 1.1** — The plot represents the Bogoliubov excitation spectrum (black solid line), phonon regime (black dashed line) and free-particle regime (upper red dashed line). The figure is taken from [56].

In the low momentum limit where $\frac{\hbar^2 k^2}{2M} \ll 2g_{\rm int} n_0$ or $k\xi \ll 1$, the dispersion relation becomes:

$$E_k \simeq \sqrt{\frac{g_{\rm int} n_0}{M}}\hbar k = c\hbar k \tag{1.51}$$

where $c = \sqrt{g_{\text{int}} n_0/M}$ is the speed of sound. The dispersion relation is linear and takes the phonon-like form so the regime is called the phonon regime, plotted with a black dashed line in Fig. 1.1.
In the other case where $\frac{\hbar^2 k^2}{2M} \gg 2g_{\text{int}} n_0$, i.e., $k\xi \gg 1$, the dispersion relation becomes:

$$E_k = \frac{\hbar^2 k^2}{2M} + g_{\text{int}} n_0. \tag{1.52}$$

Here the dispersion relation approaches the free particle law with an offset $g_{\text{int}} n_0$ related to the interaction with the condensate and the regime is called the free particle regime, upper red dashed line in the Fig. 1.1. The transition between the phonon and free particle regime takes place when $\hbar^2 k^2/2M \sim g_{\text{int}} n_0 = Mc^2$, i.e., $k\xi = 1$.

### 1.2.3 Vortex formation in a weakly interacting Bose gas

The Bogoliubov spectrum does not give all possible excitations as it considers only small density fluctuations. Here, I will introduce another kind of excitation that appears in rotating condensates. Equation (1.41) relates the velocity of the superfluid to the gradient of the phase. It shows that the superfluid flow is irrotational ($\nabla \times \mathbf{v} = 0$) if the phase is not singular. As a consequence, the circulation of the velocity field around any closed path is zero meaning that the rotation of the superfluid is not expected to behave like a normal rigid body rotation. In a superfluid, the rotation is realised through the creation of quantised vortex lines in a 3D gas (points for a 2D gas). As we put a superfluid in rotation, we observe the emergence of vortices around which the variation of the phase is an integer multiple of $2\pi$. This results in the quantized circulation as noted by Onsager and Feynman [25, 58]:

$$\oint_C \mathbf{v}(\mathbf{r}, t).d\mathbf{l} = \oint_C \frac{\hbar}{M} \nabla\phi(\mathbf{r}, t).d\mathbf{l} = \ell \times 2\pi \frac{\hbar}{M},\ \ell \in \mathbb{Z}. \tag{1.53}$$

$\ell$ is the integer number called the winding number and $2\pi\hbar/M$ is the quantum of circulation. Vortices are particular solutions of the GPE (1.29) or of the hydrodynamic equations, characterised by their position and their charge or winding number $\ell$. In principle, any integer value is possible for $\ell$ but the configuration with $|\ell| > 1$ is unstable. A vortex with a phase winding larger than $2\pi$ spontaneously breaks into several vortices with a phase winding of $2\pi$ each [59, 60], which repel each other.
Consider the case $\ell = 1$ i.e., singly charged vortex centered in a uniform 2D gas of radius $R$ and density $n_0$, assuming that the potential is $V_{\text{ext}} = 0$ for $r < R$ and $V_{\text{ext}} = \infty$ for $r > R$, the superfluid flow around the vortex is equal to:

$$v_r = \frac{\hbar}{M} \nabla\phi = \frac{\hbar}{M} \frac{2\pi}{2\pi r} = \frac{\hbar}{Mr} \text{ for } r < R. \tag{1.54}$$

This equation would lead to a divergence of the velocity of the superfluid at the center of the vortex, which is impossible so the density at the center of the vortex must vanish. This happens on a region of typical radius $\xi$. If we model the vortex by a uniform density $n_0$ outside the vortex that drops abruptly to zero in a central region of radius $\xi$, the energy per unit length of a centered singly charged vortex in a 2D superfluid of radius $R$ can be estimated as:

$$E_1 = \int_\xi^R n_0 \frac{1}{2} M \left(\frac{\hbar}{Mr}\right)^2 2\pi r dr = \pi n_0 \frac{\hbar^2}{M} \ln\left(\frac{R}{\xi}\right). \tag{1.55}$$

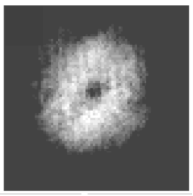


**Figure 1.2** — Experimental image of a singly charged vortex in a dilute BEC. Figure taken from [61].

We can also give the generalized expression for the energy in the case where $\ell > 1$ as:

$$E_\ell = \ell^2 \pi n_0 \frac{\hbar^2}{M} \ln\left(\frac{R}{|\ell|\xi}\right) = \ell^2 E_1 - \ell^2 \pi n_0 \frac{\hbar^2}{M} \ln|\ell| \simeq \ell^2 E_1. \tag{1.56}$$

The approximation made in the above equation holds if $R \gg \xi$ and $\ell$ is a few units. The energy $E_\ell$ increases with the size of the condensate but the relative change of the energy with respect to the ground state energy remains small in the thermodynamic limit. This expression shows indeed that $E_\ell > \ell E_1$, which favours the existence of $\ell$ vortices of charge 1 compared to a single vortex of charge $\ell$.
Fig.1.3 shows the pictures of a rotating superfluid taken after the time-of-flight (TOF) expansion as a function of the rotational frequency of the trap. We can see that the vortex number increases as the frequency of rotation increases. At the large rotation rate, when there are lots of vortices present in the superfluid, they tend to arrange in a regular triangular lattice with constant vortex density [25, 34] given by:

$$n_v = \frac{M\Omega}{\pi\hbar} \tag{1.57}$$

where $\Omega$ is the frequency of rotation.

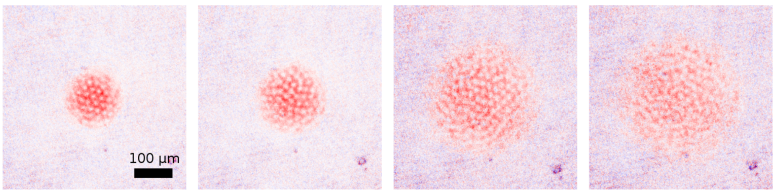



**Figure 1.3** — Images showing a vortex lattice in a rotating condensate as a function of the frequency of rotation. From left to right, the rotation frequency is 24, 25, 27 and 28 Hz and the trap frequency is 34 Hz. Figure taken from [42].

## 1.3 2D regime and BKT transition

### 1.3.1 Experimental realisation of 2D Bose gases

We consider here the case of a 2D Bose gas confined in an harmonic potential, such that it can undergo Bose-Einstein condensation. The experimental realisation of a 2D Bose gas is based on the use of a strongly anisotropic trap. Considering a condensate trapped in a

highly anisotropic harmonic trap ($\omega_z \gg \omega_r$) with temperature $T$ and chemical potential $\mu$, the criterion to reach the 2D regime is: $\mu, k_B T \ll \hbar\omega_z$, i.e., the chemical potential and the temperature of the gas should be much smaller than the energy of the first excited state in the vertical direction. This condition prevents the atoms from reaching the first excited state and in this way the motion is frozen along $z$, resulting in an effective 2D dynamics.
The chemical potential can be calculated in the Thomas-Fermi regime for a 2D Bose gas [50] and is expressed as follows:

$$\mu_{2\mathrm{D}} = 2\hbar\omega_r \left(\frac{Na}{\sqrt{2\pi}a_z}\right)^{1/2} \tag{1.58}$$

where $a_z = \sqrt{\hbar/(M\omega_z)}$ is the harmonic oscillator length in the vertical direction. In a 2D regime, the interaction between the atoms can still be described by Dirac potential but with a different interaction constant:

$$g_{2\mathrm{D}} = \frac{g_{\mathrm{int}}}{\sqrt{2\pi}a_z} = \frac{\hbar^2}{M}\widetilde{g} \tag{1.59}$$

where $\widetilde{g}$ is a dimensionless constant and is given by:

$$\widetilde{g} = \sqrt{8\pi}\frac{a}{a_z} \tag{1.60}$$

The interaction constant depends on the ratio of the scattering length and the harmonic oscillator's length in the vertical direction.
The 2D healing length is then defined as:

$$\xi^{2\mathrm{D}} = \frac{\hbar}{\sqrt{Mg_{2\mathrm{D}}n}} = \frac{1}{\sqrt{\widetilde{g}n}} \tag{1.61}$$

where $n$ is the 2D density.

In our experiment, we can reach a quasi-2D regime when the system is in rotation, i.e., the confinement energy in the vertical direction is comparable to the chemical potential $\mu_{2\mathrm{D}}$ and to the temperature ($\mu_{2\mathrm{D}}, k_B T \sim \hbar\omega_z$).

### 1.3.2 BKT transition

In the homogeneous case of the 2D system at some finite temperature, condensation is not possible in both ideal and repulsively interacting Bose gas due to thermal phase fluctuations. These fluctuations prevent the existence of the long-range order as the first-order correlation function $g_1$ represented in the equation (1.25) always tends to zero as $\mathbf{r} \to \infty$. However, the presence of repulsive interactions below a finite critical temperature $T_c$ leads to the suppression of the density fluctuations at a length scale larger than the healing length $\xi^{2\mathrm{D}}$ leading to the transition towards the superfluid state exhibiting a quasi-long range order. As the phase fluctuations prevent the establishment of LRO, only the superfluid transition occurs without the condensation. Above the critical temperature $T_c$ the quasi-long range order is destroyed resulting in a transition towards a normal fluid state. This mechanism was first described by Berezinskii [36], Kosterlitz and Thouless [37] and was named BKT transition. Later this transition in a trapped Bose gas was observed experimentally in 2006 [62]. The key point of BKT theory is that apart from the phonons, another source of phase fluctuations are the vortices. For simplicity, I consider only singly charged vortices of phase winding $\pm 2\pi$.

The two signs of phase winding corresponds to the two directions of rotation around the vortex. For $T < T_c$ the trapped gas has a finite superfluid density $n_s$ and the first-order correlation function $g_1(\mathbf{r})$ decays algebraically at large distance as [63]:

$$g_1(\mathbf{r}) \propto r^{-(n_s\lambda_T^2)^{-1}}. \tag{1.62}$$

Below $T_c$, vortices exist only in bound pairs formed by two vortices with opposite circulation resulting in a zero net charge. They thus have a limited effect on the first-order correlation function. The decay in this case is dominated by the phonons. As the temperature of the gas increases, the vortex-bound pairs start breaking up resulting in free individual vortices and at $T > T_c$, these free vortices proliferate resulting in the transition towards the normal fluid state and the decay of $g_1(\mathbf{r})$ becomes exponential.

## 1.4 Collective modes of the trapped condensate

A study of collective modes of a harmonically trapped condensate can be performed using a similar approach as that of Bogoliubov for linearizing the hydrodynamic equations. Through this study, we can get important information about different properties of a trapped quantum gas for example if it is a superfluid [31, 64] and the dimensionality of the system [65]. In our experiment, the condensate is in a pancake shape as the vertical frequency of our trap is much larger than its radial frequency ($\omega_z \gg \omega_r$). The condensate can exist in both 2D and 3D depending upon the chemical potential $\mu$. In the following section, we will discuss the different modes of excitations in both 3D and 2D cases.

### 1.4.1 In-plane collective modes in the 3D regime

Let's first consider the 3D case where the condensate is trapped under the condition $\mu > \hbar\omega_z \gg \hbar\omega_r$ and is at rest. We can describe this system using time-dependent GPE (1.29) and also using the hydrodynamic formulations (1.39) and (1.43). To determine the in-plane collective modes, we can linearize the hydrodynamic equations and compute the effect of small fluctuations of the atomic density around the steady-state solution described by the Thomas-Fermi profile. This will lead to the following dispersion relation for the collective modes in $x - y$ plane [66]:

$$\omega^2 = \omega_r^2 \left( \frac{4}{3}n^2 + \frac{4}{3}mn + 2n + m \right). \tag{1.63}$$

Here $n$ and $m$ are the two quantum numbers, $n$ corresponds to the number of radial nodes of the collective mode and $m$ corresponds to the $z$ axis projection of the angular momentum. In equation (1.63), the case $n = 0$ and $m = 1$ corresponds to the dipole excitation with a frequency equal to the radial trapping frequency:

$$\omega = \omega_r. \tag{1.64}$$

This dipole mode has no radial node and corresponds to the oscillation of the center of mass. For $n = 0$ and $m = 2$, we get surface mode known as quadrupole mode and the frequency of this mode is given by:

$$\omega = \sqrt{2}\omega_r. \tag{1.65}$$

For a non-rotating superfluid, this mode corresponds to the out-of-phase oscillation of the cloud radii. This mode does not exist in a classical gas so we can excite the quadrupole mode in the system in order to distinguish the superfluid from a classical gas.
For $n = 1$ and $m = 0$, we observe another mode of excitation which is not a surface mode as it has a radial node. This mode corresponds to the oscillation of the condensate radius and is known by the name of monopole mode (also breathing mode). The frequency of this mode is given by:

$$\omega = \sqrt{\frac{10}{3}}\omega_r. \tag{1.66}$$

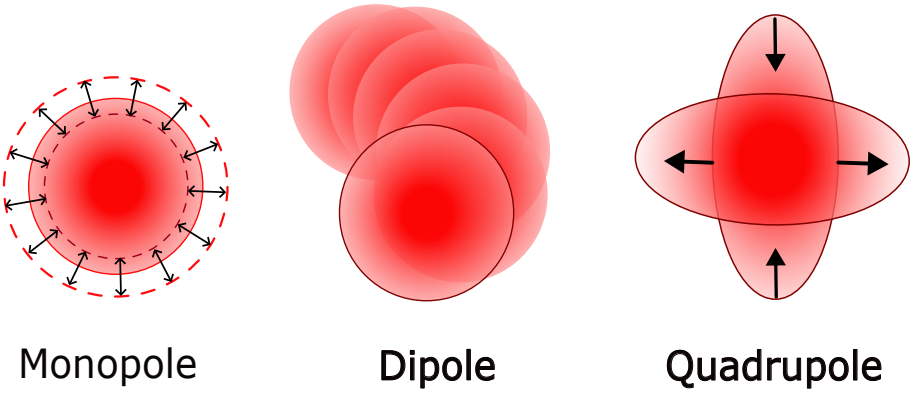



**Figure 1.4** — Image showing the different collective modes in a trapped condensate. Left to right: monopole mode, dipole mode and quadrupole mode.

### 1.4.2 Collective modes in the quasi-2D gas

Let's now consider the case of quasi-2D condensate which is trapped under the condition $\hbar\omega_z \gg \mu - 1/2\hbar\omega_z \gg \hbar\omega_r$. In the quasi-2D regime, the dispersion relation is different as the Thomas-Fermi approximation is not valid in the vertical direction. In this case, we can still observe similar modes as in the 3D case but some of the modes have different frequencies [65, 66]. The dispersion relation is given by:

$$\omega^2 = \omega_r^2(2n^2 + 2mn + 2n + m). \tag{1.67}$$

The frequency of dipole mode in quasi-2D regime is the same as in 3D regime, i.e., $\omega = \omega_r$. The quadrupole mode in the quasi-2D regime also has the same frequency as in the 3D regime, i.e.,

$$\omega = \sqrt{2}\omega_r. \tag{1.68}$$

The monopole mode in the quasi-2D regime has the frequency given by:

$$\omega = 2\omega_r. \tag{1.69}$$

The frequency is different here as compared to the 3D regime. This means that exciting monopole mode and measuring its frequency can be used to distinguish between the quasi-2D regime and the 3D regime [65]. This is because this mode, which affects the central density, is sensitive to the equation of state of the gas, which is different in 2D and in 3D.

Chapter 2

# Radio-frequency Dressed Trapping Potential

In our group, we are interested in studying quantum gases in 2D. To enable this study the radio-frequency (rf) dressed adiabatic potential is an effective tool. Rf dressed potentials allow us to trap a quantum gas with a reasonably good lifetime and low heating rate. Rf-dressed traps provide interesting trapping geometries as they are tunable and they provide as well a smooth potential for the atoms as compared to an optical dipole trap. This chapter provides a theoretical description for understanding the rf-dressed potentials and is closely based on previously published work of Hélène Perrin and Barry Garraway [47]. In this chapter, I will use the same notations as in the referred review.

O. Zobay and B.M. Garraway proposed for the first time in 2001 the realisation of rf-dressed potentials using an rf field and a static magnetic field [67]. The idea behind this was to couple the different Zeeman sublevels in an inhomogeneous static magnetic field in order to create avoided crossings and to trap atoms on isomagnetic surfaces. The first realisation of an rf-dressed trap was achieved in 2003 at LPL [68,69], where the group could confine a thermal gas in an rf-dressed potential. Later on, the group explored the 2D character of a BEC in an rf-dressed trap in 2013 [70] and studied the collective modes of 2D superfluid [64, 65, 71]. Rf dressing has also been used to generate a double well potential [72], ring potentials by combining this method with optical potentials [73–75], lattice potentials [76], time-averaged potentials [77–80] and multiple-radiofrequency dressed adiabatic potentials [81]. A supersonic rotating superfluid was achieved in the rf-dressed trap during the thesis of Yanliang Guo [82, 83]. The compensation of gravity in the rf-dressed trap has also been performed in our group [84], where the force exerted by gravity on the trapped atoms was compensated by varying the magnetic field gradient and the rf coupling amplitude, resulting in a curved quantum gas filling the lower hemisphere of an ellipsoid.

In this chapter, I will give a mathematical description of the rf-dressed potential. I will first start by describing the interaction of an atom with a static magnetic field and then I will discuss the coupling of an atom with the rf field and how it leads to the dressing of states. I will then discuss the adiabatic potentials and how we use a quadrupole magnetic field and an rf field to create a bubble trap in our experiment. I will also describe the geometry of the bubble trap and its behaviour depending on the polarisation of the rf field.

## 2.1 Rf-dressed atoms in adiabatic potentials

### 2.1.1 Trapping of atoms in an inhomogeneous magnetic field

The realisation of rf-dressed potential relies on the fact that the spin of an atom can couple to a static magnetic field as well as to an oscillating magnetic field. In this section, I will first provide a description of the interaction of the atomic spin with the static magnetic field.
Let us consider an atom with total angular momentum $F$ evolving in a static and uniform magnetic field $\mathbf{B}_0 = B_0\mathbf{e}_z$ with $z$ being the quantisation axis. The total angular momentum $F$ is the sum of the nuclear spin $I$, the electronic spin $S$, and the orbital angular momentum $L$. The total angular momentum operator is noted $\hat{\mathbf{F}}$ and its projection along $\mathbf{e}_z$ is noted $\hat{F}_z$. We can find a basis in which both $\hat{\mathbf{F}}^2$ and $\hat{F}_z$ are diagonal. The spin eigenstates are noted as $|F,m\rangle_z$ in this basis with the following eigenvalues:

$$\hat{\mathbf{F}}^2|F,m\rangle_z = F(F+1)\hbar^2|F,m\rangle_z, \tag{2.1}$$
$$\hat{F}_z|F,m\rangle_z = m\hbar|F,m\rangle_z, \tag{2.2}$$

where $m\hbar$ is the projection of the spin on $z$ axis and $m$ can take any value in the range $\{-F,-F+1,...,F-1,F\}$. The Hamiltonian of the magnetic dipolar interaction between the atomic spin and the field is written as follows:

$$\hat{H}_0 = \frac{g_F\mu_B}{\hbar}\mathbf{B}_0\cdot\hat{\mathbf{F}} = \frac{g_F\mu_B}{\hbar}B_0\hat{F}_z = s\omega_0\hat{F}_z, \tag{2.3}$$

where $g_F$ is the Landé factor of the atomic hyperfine state, $\mu_B$ is the Bohr magneton, $\omega_0 = |g_F|\mu_B B_0/\hbar$ is the Larmor frequency and we have introduced the sign $s = g_F/|g_F|$ of the Landé factor [47]. The energies of the eigenstates (also called Zeeman sub-levels) of the corresponding Hamiltonian are given by:

$$E_{m_F} = sm\hbar\omega_0. \tag{2.4}$$

In the above equation, the energy $E_m$ can have different signs because $m$ and $g_F$ can both be positive or negative. In the case where $s=-1$, as is the case in the $F=1$ ground state of rubidium, the $|m\rangle_z$ state with $m<0$ makes the eigenenergy positive resulting in an atom attracted towards the region where the field is weak. In this case, the $|m\rangle_z$ state is a "low-field seeking state". In the opposite situation where $m>0$, the atoms are attracted towards the region where the field is high and the $|m\rangle_z$ state in this case is a "high-field seeking state". In the case where the magnetic field is not uniform $\mathbf{B}_0(\mathbf{r})$, for equation (2.4) to be a trapping potential, the atoms need to follow the local eigenstate at each position in space. If this is the case, the atoms experience a potential resulting from their position-dependent eigenenergy $sm\hbar\omega_0(\mathbf{r})$. This holds if the field $\mathbf{B}_0(\mathbf{r})$ does not vary too fast, otherwise the adiabaticity condition is broken which leads to Majorana losses [46].

We now understand the basic principle of trapping an atom in a static magnetic field. We saw that the trapping of atoms in the region of maximum or minimum magnetic field depends upon the sign of $mg_F$. However, Wing's theorem [85] tells us that the norm of the static magnetic field can not have a maximum in a free space. Thus it is necessary to trap atoms in a low-field seeking state.

Now we will examine the situation where we add an rf field to the static magnetic field.

### 2.1.2 Description of rf field

Before describing the interaction between atoms and the rf field, I will first provide a description of the rf field. For this, we will first consider the simple case of an atom placed in a static uniform magnetic field $\mathbf{B}_0 = B_0\mathbf{e}_z$ and a uniform oscillating rf magnetic field of frequency $\omega$. We can define an arbitrary magnetic field oscillating at rf frequency $\omega$ as:

$$\mathbf{B}_1(t) = B_x\cos(\omega t + \phi_x)\mathbf{e}_x + B_y\cos(\omega t + \phi_y)\mathbf{e}_y + B_z\cos(\omega t + \phi_z)\mathbf{e}_z. \tag{2.5}$$

We can simplify the above equation using complex notation:

$$\mathbf{B}_1(t) = \boldsymbol{\mathcal{B}}_1 e^{-i\omega t} + c.c. \tag{2.6}$$

where $\boldsymbol{\mathcal{B}}_\mathbf{1}$ is the complex amplitude and is written as:

$$\boldsymbol{\mathcal{B}}_1 = \frac{B_x}{2}e^{-i\phi_x}\mathbf{e}_x + \frac{B_y}{2}e^{-i\phi_y}\mathbf{e}_y + \frac{B_z}{2}e^{-i\phi_z}\mathbf{e}_z. \tag{2.7}$$

$\boldsymbol{\mathcal{B}}_1$ can also be described with complex polarisation of the field $\boldsymbol{\epsilon}$ whose norm is 1 as:

$$\boldsymbol{\mathcal{B}}_1 = \mathcal{B}_1\boldsymbol{\epsilon}. \tag{2.8}$$

We can also decompose the rf polarisation in the spherical basis $(\mathbf{e}_+, \mathbf{e}_-, \mathbf{e}_0)$ instead of orthogonal basis $(\mathbf{e}_x, \mathbf{e}_y, \mathbf{e}_z)$. The changes between these two bases are as follows:

$$\mathbf{e}_+ = -\frac{1}{\sqrt{2}}(\mathbf{e}_x + i\mathbf{e}_y), \mathbf{e}_- = \frac{1}{\sqrt{2}}(\mathbf{e}_x - i\mathbf{e}_y), \mathbf{e}_0 = \mathbf{e}_z. \tag{2.9}$$

As the component $B_z$ of the rf field along the $z$-axis is aligned with the static magnetic field, we can neglect the effect of this component provided that $B_z \ll B_0$ [86, 87]. Therefore, we only take into account the orthogonal components and write the rf field amplitude as:

$$\boldsymbol{\mathcal{B}}_1 = B_+\mathbf{e}_+ + B_-\mathbf{e}_-, \tag{2.10}$$

where $B_+$ and $B_-$ are the complex amplitudes given by:

$$B_\pm = \mathbf{e}_\pm^*\cdot\boldsymbol{\mathcal{B}}_1 = \frac{1}{2\sqrt{2}}(\mp B_x e^{-i\phi_x} + iB_y e^{-i\phi_y}). \tag{2.11}$$

We can also write the projection of the spin operator in the spherical basis as:

$$\hat{\mathbf{F}}\cdot\mathbf{e}_\pm = \mp\frac{1}{\sqrt{2}}\hat{F}_\pm, \tag{2.12}$$

where $\hat{F}_+$ and $\hat{F}_-$ are the raising and the lowering operators and defined as $\hat{F}_\pm = \hat{F}_x \pm i\hat{F}_y$.

#### Coupling between the atoms and the rf field

Now we will consider the interaction between an atom and the rf field introduced in the previous section. The coupling between the atomic spin and the rf field can be described as [47]:

$$\hat{V}_1 = \mathbf{B}_1(t)\cdot\hat{\mathbf{F}} = \frac{g_F\mu_B}{\hbar}\boldsymbol{\mathcal{B}}_1\cdot\hat{\mathbf{F}}e^{-i\omega t} + h.c. \tag{2.13}$$

$$= \frac{g_F\mu_B}{\hbar}\left[-\frac{1}{\sqrt{2}}B_+\hat{F}_+ + \frac{1}{\sqrt{2}}B_-\hat{F}_-\right]e^{-i\omega t} + h.c. \tag{2.14}$$

We can also write the above expression as follows [47]:

$$\hat{V}_1 = s\left[\frac{\Omega_+}{2}\hat{F}_+ + \frac{\Omega_-}{2}\hat{F}_-\right]e^{-i\omega t} + h.c. \tag{2.15}$$

where $\Omega_\pm$ is the coupling amplitude and is defined as:

$$\Omega_\pm = \mp\sqrt{2}\frac{|g_F|\mu_B}{\hbar}B_\pm. \tag{2.16}$$

Once we have the term defining the interaction of an atom with the rf field, we can write the total Hamiltonian describing the atomic state as:

$$\hat{H} = \hat{H}_0 + \hat{V}_1. \tag{2.17}$$

Replacing $\hat{H}_0$ and $V_1$ in the above equation by their respective expressions, we get:

$$\hat{H} = s\omega_0\hat{F}_z + s\left[\frac{\Omega_+}{2}\hat{F}_+e^{-i\omega t} + \frac{\Omega_+^*}{2}\hat{F}_-e^{i\omega t} + \frac{\Omega_-}{2}\hat{F}_-e^{-i\omega t} + \frac{\Omega_-^*}{2}\hat{F}_+e^{i\omega t}\right]. \tag{2.18}$$

The first term in the equation (2.18) corresponds to the precession of spin around the $z$-axis at the frequency $\omega_0$ and the rest of the terms correspond to the transition between different $|m\rangle_z$ states and these transitions will be resonant at $\omega = \omega_0$.

Now we will see what happens in the basis rotating at frequency $s\omega$ around $z$. We define the rotated states as:

$$|\psi_{\text{rot}}\rangle = \exp\left(\frac{-is\omega t}{\hbar}\hat{F}_z\right)|\psi\rangle. \tag{2.19}$$

In this rotated basis we can define the detuning $\delta = \omega - \omega_0$ and write the Hamiltonian in this basis as [47]:

$$\hat{H}_{\text{rot}} = -s\delta\hat{F}_z + s\left[\frac{\Omega_+}{2}\hat{F}_+e^{i(s-1)\omega t} + \frac{\Omega_+^*}{2}\hat{F}_-e^{-i(s-1)\omega t}\right] \tag{2.20}$$

$$+ s\left[\frac{\Omega_-}{2}\hat{F}_-e^{-i(s+1)\omega t} + \frac{\Omega_-^*}{2}\hat{F}_+e^{i(s+1)\omega t}\right]. \tag{2.21}$$

Depending on the sign of $s$, either the first two terms or the last two terms in the brackets become static and the other two terms will evolve at the high frequency $\pm 2\omega$. Assuming that the detuning $\delta$ and the rf coupling $\Omega_\pm$ are much smaller than the frequency $\omega$, we can apply the Rotating Wave Approximation (RWA). Under this approximation, the two time-dependent terms evolving much faster than the rest of the system will average to 0. Again the choice of the two terms terms going to 0 depends on the sign of $s$. We can denote the coupling amplitude of the two remaining terms as $\Omega_1$, where $\Omega_1 = -\sqrt{2}g_F\mu_B B_s/\hbar$. The effective Hamiltonian under the RWA approximation then becomes:

$$\hat{H}_{\text{eff}} = -s\delta\hat{F}_z + s\frac{|\Omega_1|}{2}\left[\hat{F}_+ + \hat{F}_-\right] \tag{2.22}$$

$$= s\left(-\delta\hat{F}_z + |\Omega_1|\hat{F}_x\right), \tag{2.23}$$

which then can be rewritten in terms of spin Hamiltonian as:

$$\hat{H}_{\text{eff}} = \Omega\hat{F}_\theta, \tag{2.24}$$

where $\Omega$ is the generalised Rabi frequency and is defined as:

$$\Omega = \sqrt{\delta^2 + |\Omega_1|^2}, \tag{2.25}$$

and $\hat{F}_\theta$ is the spin projection defined as:

$$\hat{F}_\theta = \cos(\theta)\hat{F}_z + \sin(\theta)\hat{F}_x, \tag{2.26}$$

with,

$$\theta = \cos^{-1}\left(\frac{-\delta}{\Omega}\right) + \frac{s-1}{2}\pi. \tag{2.27}$$

$\hat{H}_{\text{eff}}$ is the effective Hamiltonian of an atomic spin interacting with a static effective magnetic field $\mathbf{B}_{\text{eff}}$, pointing in the $\mathbf{e}_\theta$ direction and is defined as:

$$\mathbf{B}_{\text{eff}} = \frac{\hbar\Omega}{|g_F|\mu_B}\mathbf{e}_\theta. \tag{2.28}$$

We can define the eigenstates of $\hat{H}_{\text{eff}}$ in the basis set by the quantization axis $s\mathbf{e}_\theta$ as:

$$|m\rangle_\theta = e^{-i\theta\hat{F}_y/\hbar}|m\rangle_z \tag{2.29}$$

and the eigenenergies of the corresponding states are given by:

$$E_m = m\hbar\Omega. \tag{2.30}$$

The interaction between an atom and the rf field creates an avoided crossing at the resonance ($\delta = 0$) where the states are split by $\hbar|\Omega_1|$. With the convention of the orientation of the quantisation axis, $\mathbf{e}_\theta$ with respect to the effective magnetic field, the low field-seeking states, with higher energies, always correspond to $m > 0$.

### 2.1.3 Rf dressed adiabatic potential

In the previous section, I have introduced the concept of dressed states in a uniform static magnetic and rf field. The Larmor frequency $\omega_0$ does not depend on position in this particular case. However, to trap the atoms the magnetic field should be inhomogeneous resulting in a position-dependent detuning $\delta(\mathbf{r})$ and Rabi coupling $\Omega_1(\mathbf{r})$. Assuming that the eigenstates vary slowly as the atom moves in the position-dependent coupling, the atom will adiabatically follow the eigenstates of the Hamiltonian and will feel an effective potential given by:

$$V_{\text{m}}(\mathbf{r}) = m\hbar\Omega(\mathbf{r}) = m\hbar\sqrt{\delta^2(\mathbf{r}) + \Omega_1(\mathbf{r})^2}, \tag{2.31}$$

where $\delta(\mathbf{r})$ is the position-dependent detuning defined as:

$$\delta(\mathbf{r}) = \omega - \omega_0(\mathbf{r}), \tag{2.32}$$

and the local Lamor frequency $\omega_0(\mathbf{r}) = |g_F|\mu_B B_0(\mathbf{r})/\hbar$ now depends on position. We have assumed for simplicity that $\Omega_1$ is real.

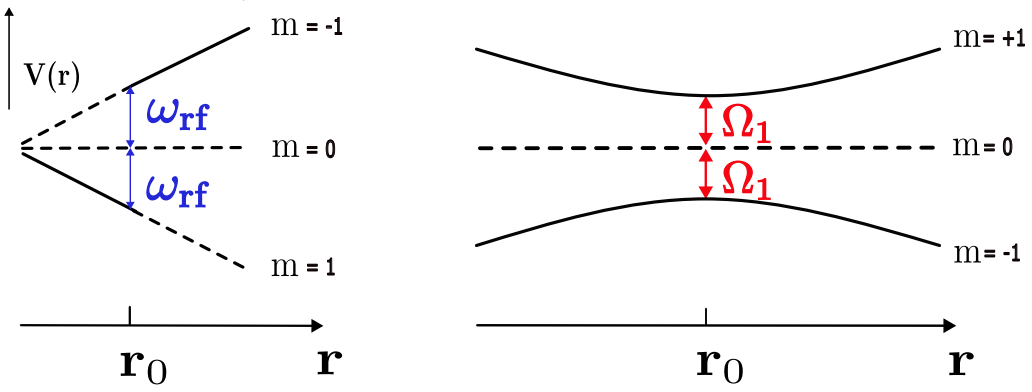



**Figure 2.1** — On the left we have the magnetic potential of the uncoupled states with a total spin $F = 1$ in a linear magnetic trap. The resonance occurs at $r_0$. On the right, we have an adiabatic potential, corresponding to the three dressed states with a position-independent Rabi coupling $\Omega_1$. At the resonance position where $\delta(r_0) = 0$, the frequency splitting is $\Omega_1$.

Let us first discuss the effect of the position-dependent detuning with a uniform coupling $\Omega_1$. The position dependency of $\delta$ in equation (2.31) tells that the atoms will be trapped in the potential where $\delta(\mathbf{r})$ is zero, in other words, the position where the rf frequency is resonant with the Larmor frequency $\omega_0$. For a given rf frequency this corresponds to an isomagnetic surface. The local magnetic field gradient and the Rabi coupling determine the strength of the confinement. Fig. 2.1 depicts an adiabatic potential for the case $F = 1$. The field increases linearly with the coordinate $\mathbf{r}$ such that $\omega_0(\mathbf{r}) = |\nabla\omega_0|r \approx \alpha r$, where $\alpha \approx |\nabla\omega_0|$ is the local magnetic gradient given in units of frequency and $r_0$ is the place where resonance occurs. At the resonance position, the adiabatic potential provides an avoided crossing, with a frequency splitting equal to the Rabi coupling (right picture in Fig. 2.1).

The gradient of the Larmor frequency $\nabla\omega_0$ is in the direction normal to the surface, so we can find the trapping frequency along this transverse direction as [47]:

$$\omega_{\text{transverse}} = \alpha\sqrt{\frac{F\hbar}{M\Omega_1}} \tag{2.33}$$

where $M$ is the atomic mass. Now, if the coupling is position dependent, the states $|m\rangle$ with $m > 0$ have the potential minimum at the resonant position providing a way to trap the atoms in the dressed state when the detuning varies with the position. Assuming that the atoms are moving at a constant velocity ($\mathbf{v}$) in the trap, the adiabaticity criterion can be written as [47]:

$$|\mathbf{v}\cdot[\Omega_1(\mathbf{r})\nabla\delta - \delta(\mathbf{r})\nabla\Omega_1]| \ll [\delta^2(r) + \Omega_1^2(r)]^{3/2}. \tag{2.34}$$

Close to the resonance surface, we get $|\mathbf{v}\cdot\nabla\delta| \ll \Omega_1^2$ or $\alpha v_{\text{transverse}} \ll \Omega_1^2$. If the above condition is satisfied, the spin will adiabatically follow the orientation of the effective local magnetic field. For a given gradient of the magnetic field, we can write this adiabatic condition under the form:

$$\omega_{\text{transverse}} \ll \Omega_1^2. \tag{2.35}$$

### 2.1.4 Local Rabi coupling

To find the value of the potential given by equation (2.31), we need to know the expression of the local Rabi coupling $\Omega_1(\mathbf{r})$. To this aim, we will first start by writing the static magnetic field and the rf field in a classical way as we did before:

$$\mathbf{B}_0(\mathbf{r}) = B_0(\mathbf{r})\mathbf{u}(\mathbf{r}), \tag{2.36}$$

$$\mathbf{B}_1(\mathbf{r},t) = \mathcal{B}_1(\mathbf{r})\boldsymbol{\epsilon}(\mathbf{r})e^{-i\omega t} + c.c. \tag{2.37}$$

Here $\mathbf{u}(\mathbf{r})$ is the unitary vector indicating the local orientation of the static magnetic field and $\boldsymbol{\epsilon}(\mathbf{r})$ is the complex polarisation of the rf field with $|\boldsymbol{\epsilon}(\mathbf{r})| = 1$. We have seen that in the RWA, the expression of $\Omega_1$ depends on the local component of $\mathbf{B}_1(\mathbf{r},t)$ along the polarisation $\sigma^s$. We can describe this component in the local spherical basis $(\mathbf{e}_+(\mathbf{r}), \mathbf{e}_-(\mathbf{r}), \mathbf{u}(\mathbf{r}))$ as $\mathcal{B}_1(\mathbf{r})\mathbf{e}_s^*\cdot\boldsymbol{\epsilon}(\mathbf{r})$. In the same basis, the local Rabi coupling can thus be defined as [47]:

$$\Omega_1(\mathbf{r}) = -\sqrt{2}\frac{g_F\mu_B}{\hbar}\mathcal{B}_1(\mathbf{r})\mathbf{e}_s^*\cdot\boldsymbol{\epsilon}(\mathbf{r}) \tag{2.38}$$

$$= -s\Omega_{\max}(\mathbf{r})\mathbf{e}_s^*\cdot\boldsymbol{\epsilon}(\mathbf{r}) \tag{2.39}$$

where $\Omega_{\max}(\mathbf{r}) = \sqrt{2}|g_F\mu_B B_1(\mathbf{r})|/\hbar$ is the maximum coupling one can achieve. By using the properties of the spherical basis, $\Omega_1(\mathbf{r})$ can also be written as follows [47]:

$$|\Omega_1(\mathbf{r})| = \frac{\Omega_{\max}}{2}|\boldsymbol{\epsilon}\times\mathbf{u} + is\mathbf{u}\times(\boldsymbol{\epsilon}\times\mathbf{u})| \tag{2.40}$$

$$= \frac{\Omega_{\max}}{2}\sqrt{1-|\boldsymbol{\epsilon}\cdot\mathbf{u}|^2+|\boldsymbol{\epsilon}\times\mathbf{u}|^2+2is\mathbf{u}\cdot(\boldsymbol{\epsilon}\times\boldsymbol{\epsilon}^*)}. \tag{2.41}$$

Here we have the general expression of the local Rabi coupling. In the case where the polarisation of the rf field is circular $\sigma^s$ with respect to the $z$-axis, the expression for local Rabi coupling can be simplified as:

$$|\Omega_1(\mathbf{r})| = \frac{\Omega_{\max}(\mathbf{r})}{2}[1+u_z(\mathbf{r})] \tag{2.42}$$

with $u_z(\mathbf{r}) = \mathbf{u}\cdot\mathbf{e}_z$. In another case where the polarisation of the rf field is linear with respect to the $z$-axis, the local Rabi coupling becomes:

$$|\Omega_1(\mathbf{r})| = \Omega_{\max}(\mathbf{r})\sqrt{\frac{1-u_z(\mathbf{r})^2}{2}}. \tag{2.43}$$

With all these expressions for the local Rabi coupling, we can now describe any trapping configuration depending upon the polarization of the rf field.

## 2.2 Dressed quadrupole trap

We have discussed the properties of the adiabatic potentials and Rabi coupling in the previous section. In this particular section, we will discuss the trap we use in our experiment, i.e., the dressed quadrupole trap. The minimum of the potential of this trap lies on an ellipsoid and that's why we also call it a bubble trap.
We can easily obtain a quadrupole magnetic field using a pair of coils in an anti-Helmholtz configuration. The field we obtain is linear and is described as follows:

$$\mathbf{B}_0(\mathbf{r}) = b'(x\mathbf{e}_x + y\mathbf{e}_y - 2z\mathbf{e}_z). \tag{2.44}$$

We can note from the above expression that the field increases from the center of the trap along any of the $x$, $y$ and $z$ directions. We can also write the magnitude of the field as:

$$B_0(\mathbf{r}) = b'\sqrt{x^2 + y^2 + 4z^2}. \tag{2.45}$$

The corresponding local Larmor frequency is:

$$\omega_0(\mathbf{r}) = \alpha\sqrt{x^2 + y^2 + 4z^2} = \alpha\ell \tag{2.46}$$

where $\ell = \sqrt{x^2 + y^2 + 4z^2}$ and $\alpha$ is the magnetic gradient in the horizontal $(x - y)$ plane in the units of frequency and is defined as:

$$\alpha = \frac{|g_F|\mu_b b'}{\hbar}. \tag{2.47}$$

For a given rf frequency $\omega$, the atoms are confined on the isomagnetic surface $\omega_0(\mathbf{r}) = \omega$, which corresponds to an ellipsoid with its horizontal radius twice the vertical radius. The expression is as follows:

$$x^2 + y^2 + 4z^2 = r_{\mathrm{b}}^2 \tag{2.48}$$

with $r_{\mathrm{b}}$ being the radius of the semi-major axis and is given by:

$$r_{\mathrm{b}} = \frac{\omega}{\alpha}. \tag{2.49}$$

As gravity is always aligned with the vertical axis of the trap, the atoms are attracted towards the bottom of the trap resulting in a pancake-shaped cloud.
On the resonant surface $\ell = r_{\mathrm{b}}$, we can also write the orientation of the local magnetic field which is necessary to compute the local coupling as [47]:

$$\mathbf{u} = \frac{x\mathbf{e}_x + y\mathbf{e}_y - 2z\mathbf{e}_z}{\sqrt{x^2 + y^2 + 4z^2}} = \frac{x\mathbf{e}_x + y\mathbf{e}_y - 2z\mathbf{e}_z}{r_{\mathrm{b}}}. \tag{2.50}$$

We will now discuss the potential depending on the different polarisations of the rf field.

### 2.2.1 Circular Polarisation

In our experiment, we work with $^{87}$Rb atoms and for these atoms evolving in a magnetic field, their ground state is the lowest hyperfine state $F = 1$ with $g_F = -1/2$. Therefore, for further discussion, we will assume $s$ to be $-1$.
We can make a rotationally symmetrical trap using a circularly polarised rf field with respect to the $z$ axis. In theory, it can simply be produced using a pair of antennas placed orthogonally along the $x$ and $y$ axis generating two rf fields of the same amplitude with a phase difference of $\pi/2$. Atoms at the bottom of the bubble trap feel the magnetic field aligned along the $+z$ axis such that an rf field with $\sigma^-$ polarization will maximize the coupling $\Omega_1$ at this point. The polarization of the rf field $\sigma^-$ can be written as:

$$\boldsymbol{\epsilon} = \frac{1}{\sqrt{2}}(\mathbf{e}_x - i\mathbf{e}_y). \tag{2.51}$$

As we have already determined the local Rabi coupling for a circularly polarised rf field equation (2.42), we can simplify the term $u_z(\mathbf{r})$ in the following equation as:

$$u_z = \mathbf{u}\cdot\mathbf{e}_z = \frac{x\mathbf{e}_x + y\mathbf{e}_y - 2z\mathbf{e}_z}{r_\mathrm{b}}\cdot\mathbf{e}_z = -\frac{2z}{r_\mathrm{b}}. \tag{2.52}$$

Therefore, the local Rabi coupling on the resonant surface can be written as:

$$|\Omega_1(\mathbf{r})| = \frac{\Omega_\mathrm{max}}{2}(1+u_z) = \frac{\Omega_\mathrm{max}}{2}\left(1-\frac{2z}{r_\mathrm{b}}\right) \tag{2.53}$$

where $\Omega_0$ is the maximum Rabi coupling obtained at the bottom of the bubble trap ($z = -r_\mathrm{b}/2$). We can also note from the equation (2.53) that the Rabi coupling vanishes at the top of the bubble trap ($z = r_\mathrm{b}/2$).
The potential of the bubble trap consists of the dressed adiabatic potential $V_\mathrm{m}(\mathbf{r})$ and the gravitational potential $Mgz$:

$$V_\mathrm{bubble}(\mathbf{r}) = \hbar\sqrt{\delta^2(\mathbf{r}) + \Omega_1(\mathbf{r})^2} + Mgz, \tag{2.54}$$

$$V_\mathrm{bubble}(\mathbf{r}) = \hbar\sqrt{(\omega-\alpha\ell)^2 + \frac{\Omega_0^2}{4}\left(1-\frac{2z}{r_\mathrm{b}}\right)^2} + Mgz. \tag{2.55}$$

Now, taking $\delta(\mathbf{r}) = (\omega - \alpha\ell) = 0$, we can write the potential of the bubble trap restricted to the resonant surface $\ell = r_\mathrm{b}$ as follows:

$$V_\mathrm{bubble}(z) = \hbar|\Omega_1(\mathbf{r})| + Mgz \tag{2.56}$$

$$= \hbar\frac{\Omega_0}{2}\left(1-\frac{2z}{r_\mathrm{b}}\right) + Mgz \tag{2.57}$$

$$= \frac{\hbar\Omega_0}{2} + \left(Mg - \frac{\hbar\Omega_0}{r_\mathrm{b}}\right)z. \tag{2.58}$$

If $\hbar\Omega_0 > Mgr_\mathrm{b}$, the potential will have its minimum at the top of the bubble trap and in this case, the atoms are pushed towards this minimum. But as the Rabi coupling is zero at this point, the atoms can not follow the dressed state there and will get their spin flipped resulting in Landau-Zener losses. In simple words, this point of minimum potential acts as a hole for the atoms. Therefore, for the atoms to remain confined at the bottom of the bubble trap, the following conditions must be satisfied:
First:

$$\hbar\Omega_0 < Mgr_\mathrm{b}. \tag{2.59}$$

In this way, gravity is dominant and the minimum of the potential is at the position where the Rabi coupling is maximum, i.e., at the bottom of the trap.
Second:

$$\frac{Mg}{2\hbar\alpha} = \varepsilon < 1. \tag{2.60}$$

This is to make sure that the effect of gravity is not greater than the magnetic gradient so that the atoms remain trapped at the bottom of the bubble trap and do not fall down. These two conditions together imply that we must have $\Omega_0 < 2\omega$.

The minimum of the potential is slightly shifted below the resonant surface due to gravity. It is located at $(x = 0, y = 0, z = z_\mathrm{eq})$, where $z_\mathrm{eq}$ is given by [70]:

$$z_{\rm eq} = -\frac{r_{\rm b}}{2}\left(1 + \frac{\varepsilon}{\sqrt{1-\varepsilon^2}}\frac{\Omega_0}{\omega}\right). \tag{2.61}$$

By doing the second-order expansion around the potential minimum, we can find the oscillation frequencies at the bottom of the trap [70]:

$$\omega_r = \sqrt{\frac{g}{4|z_{\rm eq}|}}\left[1 - \frac{\hbar\Omega_0}{2Mg|z_{\rm eq}|}\sqrt{1-\varepsilon^2}\right]^{1/2}, \tag{2.62}$$

$$\omega_z = 2\alpha\sqrt{\frac{\hbar}{M\Omega_0}}(1-\varepsilon^2)^{3/4}. \tag{2.63}$$

$\omega_r$ is a pendulum frequency associated to an effective radius of curvature of $\sim 4|z_{\rm eq}|$.

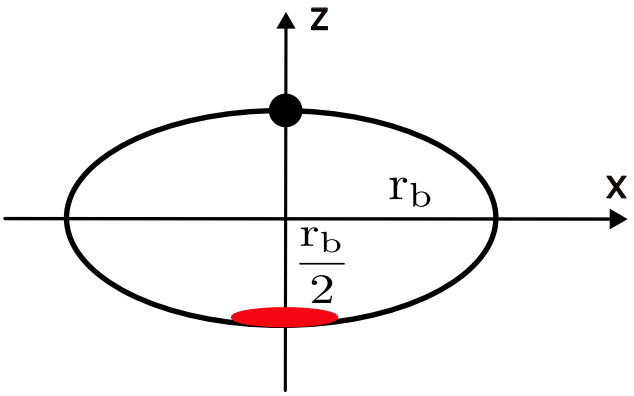



**Figure 2.2** — Bubble trap with circularly polarised rf field along the $z$ axis. Atoms are located at the bottom of the trap due to gravity. The semi-major axis and semi-minor axis are $r_b$ and $r_b/2$. The black circle on the top of the trap corresponds to the hole. The trap is rotationally invariant.

### 2.2.2 Elliptical Polarisation

In our experiment, we need an elliptically polarized rf field to break the rotational invariance and rotate a superfluid in a bubble trap. Chapter 4 presents the experiment where we intentionally change the polarisation of rf field from circular to elliptic (details are present in the chapter) to rotate the trap to eventually study the dynamics of the vortices that emerged in a rotating superfluid. The case of elliptical polarization in the $x-y$ plane has been described in the PhD thesis of Mathieu de Goër de Herve [42]. The polarization can be written as:

$$\epsilon = \cos(\Theta)e_x + e^{i\Phi}\sin(\Theta)e_y, \tag{2.64}$$

here $\Theta$ and $\Phi$ parametrize the amplitude difference and the phase difference between the rf fields produced by the pair of orthogonal antennas. Elliptical polarisation results in the appearance of two holes on the surface of the bubble trap (see Fig.2.3), coordinates of which

are given by:

$$\begin{aligned} x &= r_{\mathrm{b}} \sin\theta \cos\phi, \\ y &= r_{\mathrm{b}} \cos\theta \sin\phi, \\ z &= \frac{r_{\mathrm{b}}}{2} \cos\theta \end{aligned} \tag{2.65}$$

The polar coordinates $(\theta, \phi)$ locate the position of the holes and as their position is controlled by the polarisation of rf field, we can relate these coordinates to the amplitude and the phase difference of the antennas as follows:

$$\cos\theta = \frac{\sin(2\Theta)\sin(\Phi)}{1+\sqrt{1-\sin^2(2\Theta)\sin^2\Phi}}, \tag{2.66}$$

$$\tan(2\phi) = \tan(2\Theta)\cos\Phi. \tag{2.67}$$

Equation (2.67) gives the two solutions $\phi$ and $\phi+\pi$, which corresponds to the orientation of the semi-major axis of the elliptic polarisation with respect to the $x$-axis, meaning that the two holes are symmetric with respect to the $z$-axis. Equation (2.66) gives the information about the vertical position of the holes. For circular polarisation, we have $\cos(\theta) = \pm 1$ meaning that the holes are either at the top or at the bottom of the bubble. For a linear polarisation, $\cos(\theta) = 0$ means that the holes are the equator of the bubble.

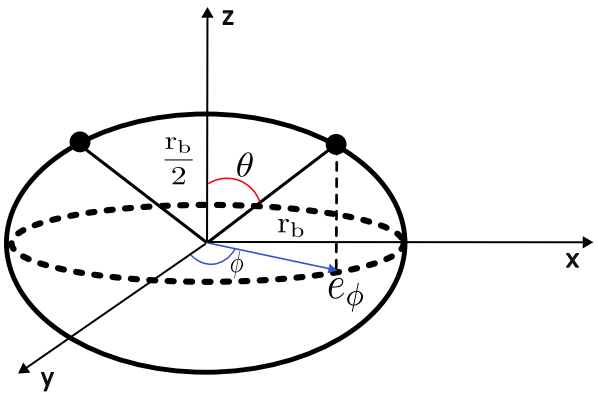



**Figure 2.3** — Figure shows the position of the holes (black dots) in scaled spherical coordinates.

The oscillation frequencies along the 3 direction at the bottom of the trap are:

$$\omega_x = \sqrt{\frac{g}{4|z_{\mathrm{eq}}|}}\left[1-\frac{\hbar\Omega_0}{2Mg|z_{\mathrm{eq}}|}\sqrt{1-\varepsilon^2}\left(1-\sqrt{\frac{1}{\eta_{\mathrm{xy}}}-1}\right)\right]^{1/2}, \tag{2.68}$$

$$\omega_y = \sqrt{\frac{g}{4|z_{\mathrm{eq}}|}}\left[1-\frac{\hbar\Omega_0}{2Mg|z_{\mathrm{eq}}|}\sqrt{1-\varepsilon^2}\left(1+\sqrt{\frac{1}{\eta_{\mathrm{xy}}}-1}\right)\right]^{1/2}, \tag{2.69}$$

$$\omega_z = 2\alpha\sqrt{\frac{\hbar}{M\Omega_0}}(1-\varepsilon^2)^{3/4}, \tag{2.70}$$

where $\eta_{\rm xy}$ defines the anisotropy of the coupling in the $x-y$ plane and takes values between 0 and 1:

$$\eta_{\rm xy} = \frac{1+\sin(2\Theta\sin\Phi)}{2}. \tag{2.71}$$

We can also define the anisotropy of the bubble trap $\epsilon_{\rm aniso}$ when we put a condensate into rotation as:

$$\epsilon_{\rm aniso} = \frac{\omega_x^2-\omega_y^2}{\omega_x^2+\omega_y^2} = \frac{\sqrt{1-\eta_{\rm xy}}}{\frac{2MgR}{\hbar\Omega_0\sqrt{1-\varepsilon^2}}-\sqrt{\eta_{\rm xy}}}. \tag{2.72}$$

We will be recalling this expression in Chapter 4 while discussing the experimental sequence for rotating a condensate in a bubble trap.

### 2.2.3 Determination of local Rabi coupling in the experiment

In the experiment, we can perform an rf spectroscopy measurement to determine the local Rabi coupling which corresponds to the energy splitting between successive dressed states. To do so we use a dedicated antenna which generates a weak rf field that couples the two dressed states $|F=1,m=1\rangle$ and $|F=1,m=0\rangle$ but only $|F=1,m=1\rangle$ is trapped. As the rf frequency produced by the spectroscopy antenna becomes resonant with the Rabi coupling, the atoms are transferred to the untrapped state $|F=1,m=0\rangle$ resulting in atom losses. Scanning the spectroscopy rf frequency and plotting the number of atoms left in the trapping state gives the spectrum shown in Fig 2.4. By fitting with a Lorentzian we get the resonant position and deduce the Rabi coupling at the position of atoms in the following way. We have the equilibrium position $z_{\rm eq}$ of the atomic cloud at the bottom of the bubble trap from equation (2.61). The Larmor frequency at this position is given by:

$$\begin{aligned}
\omega_0 &= |2\alpha z_{\rm eq}|, && (2.73)\\
&= 2r_{\rm b}\left(1+\frac{\varepsilon}{\sqrt{1-\varepsilon^2}}\frac{\Omega_0}{\omega}\right), && (2.74)\\
&= \left(\omega+\frac{\varepsilon}{\sqrt{1-\varepsilon^2}}\Omega_0\right). && (2.75)
\end{aligned}$$

We can now write the detuning as:

$$|\delta| = |\omega-\omega_0| = \frac{\varepsilon}{\sqrt{1-\varepsilon^2}}\Omega_0. \tag{2.76}$$

As we have the expression for detuning, we can define the gap between the dressed states measured by the rf spectroscopy:

$$\begin{aligned}
\Omega_{\rm res} &= \Omega(z_{\rm eq}), && (2.77)\\
&= \sqrt{\delta^2+\Omega_0^2}, && (2.78)\\
&= \frac{\Omega_0}{\sqrt{1-\varepsilon^2}}, && (2.79)
\end{aligned}$$

where $\Omega_{\rm res}$ is the frequency deduced from the fit. The Rabi coupling can then be calculated as follows:

$$\Omega_0 = \sqrt{1-\varepsilon^2}\Omega_{\rm res}. \tag{2.80}$$

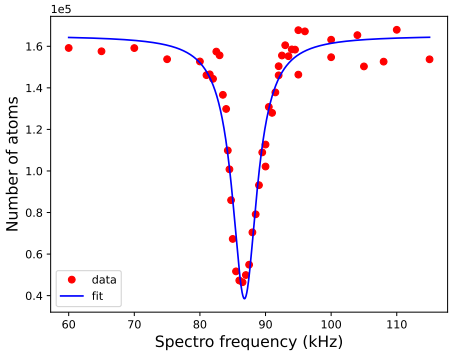



**Figure 2.4** — Spectroscopy measurement performed in the bubble trap in red circles and the Lorentzian fit in the blue line. We find a Rabi coupling $(\Omega_0/2\pi) = 83.8(3)\,\mathrm{kHz}$.

## 2.3 Conclusion

In this chapter, I have provided the important theoretical information required to understand the final trap we use in our experiment, i.e., the bubble trap, to study the dynamics of a superfluid. The procedure of transferring the atoms to this trap will be detailed in the next chapter. The rf field for the dressing of atoms in our experiment is generated using three antennas: two antennas placed orthogonally with horizontal axes and one with a vertical axis around the science cell. These antennas are controlled by the DDS (Direct Digital Synthesizer), discussed in the next chapter as well. The dressed quadrupole trap has several advantages: it incorporates a very convenient knob to compensate gravity on the resonant bubble surface [84] and its potential is slightly anharmonic thus allowing us to achieve a high rotation rate to study superfluid dynamics [83] and provides a good lifetime and low heating rate.

# Part II

# Thermal melting of a vortex lattice

# Chapter 3

# Experimental setup: first version

In this chapter, I will describe our experimental setup along with the laser chain configuration that we had at the beginning of my PhD thesis with which we did the study of fast rotating superfluid presented in Chapter 4. The improved version of the experiment is described in Chapter 6.

The experiment that I will present in this chapter was built during the PhD theses of Thomas Liennard [88] and Karina Merloti [89] to cool down the sample of rubidium 87 atoms. The motivation to use rubidium 87 atoms emerged due to the following factors :

- it has a simple electronic structure and has a cyclic transition in $D_2$ line (see Fig. 3.1) in near-infrared and is easily accessible using cheap lasers. We have access to this transition using a frequency-doubled telecom fiber laser or laser diodes;
- it has collisional properties favourable for performing evaporative cooling thus leading to the realisation of the first BEC in 1995 [22];

The production of a BEC involves the simultaneous operation of various components. Certain requirements must be fulfilled in order to produce a condensate. One important requirement is the presence of a high-quality vacuum, as this helps minimize atom loss caused by collisions with residual gas. One also needs lasers stabilized on the relevant transitions of rubidium as well as a magnetic field for trapping atoms. Finally, we need to be able to communicate with different devices present in the experiment and have time precision of the order of one microsecond as our imaging pulses have a duration of around 17 µs. We use a National Instrument PXIe 1073 rack system to host two PXIe-6535 cards for the numerical outputs and one PXIe-6738 card for the analog outputs, to control the instruments and generate pulses. This system provides 64 digital outputs and 32 16-bit analog outputs. The Labscript software suite controls the system, it is an open-source software developed in the quantum fluids group at Monash University [90] and is written in Python. This software uses a programming model that stores only the changes in values of parameters and uses a synchronization signal to update the outputs at any given time. To generate the synchronization signal, we use a microcontroller board. This control system was implemented during the PhD thesis of David Rey [91] and simplified the way of handling different parameters to control the experiment as compared to the old control system, for detailed discussion refer to the thesis of David Rey.

Fig.3.1 represents the energy level diagram of $^{87}$Rb with all the necessary laser beams required in the experiment.

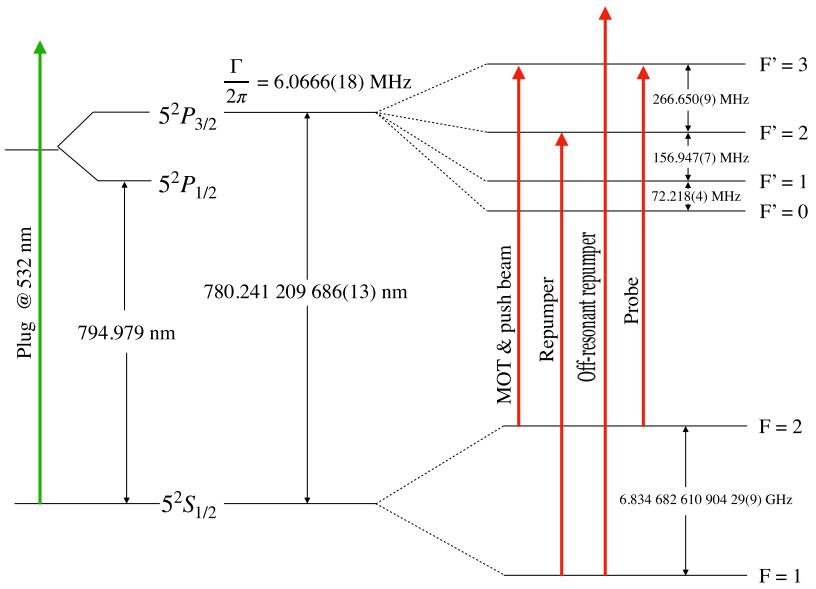



**Figure 3.1** — Energy level of the rubidium 87 atom and the different lasers used on our experiment. Figure adapted from [92].

## 3.1 Overview of the experimental apparatus

In our experiment we have a vacuum chamber made up of three parts: a 2D magneto-optical trap (2D-MOT), a 3D magneto-optical trap (3D-MOT) in an octogonal chamber and a cuboidal glass cell also called the science cell (Fig.3.2).

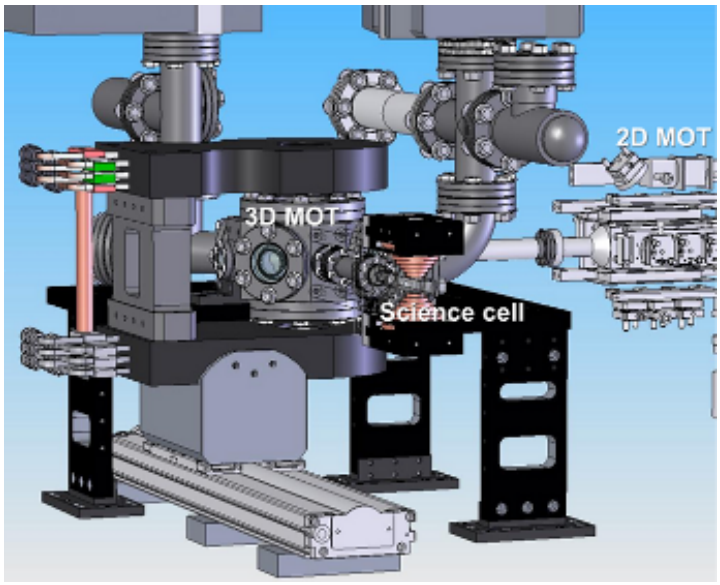



**Figure 3.2** — Representation of the 2D-MOT, 3D-MOT and the science cell. The magnetic coils of the 3D-MOT are mounted on a movable support. Figure taken from [89].

### 3.1.1 2D-MOT

We bought our 2D-MOT from LNE-SYRTE, and its operation is discussed in detail in the PhD thesis of Patrick Cheinet [93]. The 2D-MOT is composed of three pairs of counter-propagating cooling laser beams in horizontal and vertical directions respectively.

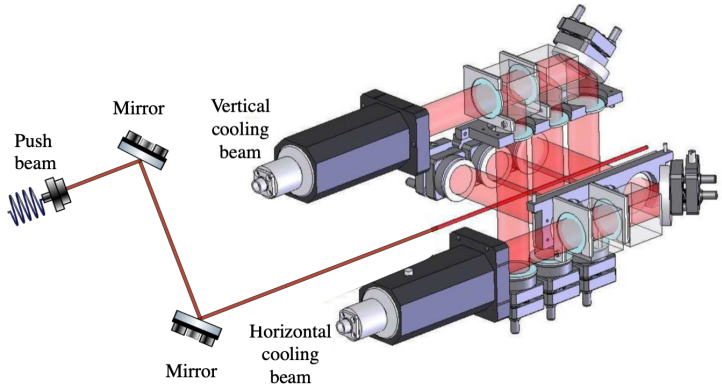



**Figure 3.3** — Design of optics of the 2D-MOT. The 2D-MOT chamber and the magnetic coils are not represented here. Figure taken from [89] and adapted to the present situation.

These beams are circularly polarised and red detuned from the transition $|5S_{1/2}, F = 2\rangle \rightarrow |5P_{3/2}, F = 3\rangle$ of $D_2$ line of $^{87}$Rb (Fig.3.1). The cooling laser beams are mixed with the repumper beams locked on the transition $|5S_{1/2}, F = 1\rangle \rightarrow |5P_{3/2}, F = 2\rangle$ in order to bring back to the cyclic transition the atoms de-excited towards the hyperfine level $|5S_{1/2}, F = 1\rangle$. The 2D-MOT is connected via a CF-16 valve to the reservoir of rubidium atoms, which itself is encircled with a heating wire connected to a continuous current supply and with a thermocouple to get information about the temperature of the reservoir. The temperature of the reservoir can be controlled by varying the current value. The reservoir is heated at about 75°C, producing the rubidium vapour which is then cooled down in the transversal direction by the cooling laser beams in the presence of a transverse magnetic field gradient created using two pairs of coils in an anti-Helmholtz configuration. The 2D-MOT chamber is pumped by an ion pump ($2\text{L.s}^{-1}$).

As we can see in Fig. 3.3, on one end of the 2D-MOT we have 2 collimators providing a horizontal cooling beam and a vertical cooling beam. A push beam reaches the 2D-MOT chamber via two mirrors. Once the atoms are laser-cooled in the 2D-MOT, we obtain a line of trapped atoms at a low temperature in the transverse direction. We transfer these atoms to the 3D-MOT using the push beam aligned along the line of atoms. This beam has the same frequency as the cooling beams and pushes the atoms continuously towards the 3D-MOT through an exit hole of 2D-MOT of diameter 1.5 mm, which is connected to the differential pumping tube of diameter 16 mm and length of 18 cm, linking it to the 3D-MOT.

Although the 2D-MOT worked perfectly under high vacuum for more than 10 years, at the start of the 2nd year of my PhD, we encountered a vacuum problem due to the leakage on one indium seal on the 2D-MOT chamber. To detect the leakage we used the turbomolecular pumping bench to pump the chamber and we put ethanol on each porthole of the 2D-MOT chamber. We observed the drop in pressure of the ionic pump and that of the turbo as the ethanol on the leaking porthole froze and blocked the leakage temporarily (Fig. 3.4).

To solve the leakage problem, we proceeded as follows. We first fixed a homemade flange on the leaking porthole to apply a constrain and lower the pressure. We then heated the 2D-MOT chamber up to 100 °C using the heating cables to get rid of any impurity present in the chamber. After a few days we came back to ambient temperature. By doing this we could retrieve the same vacuum quality as before.

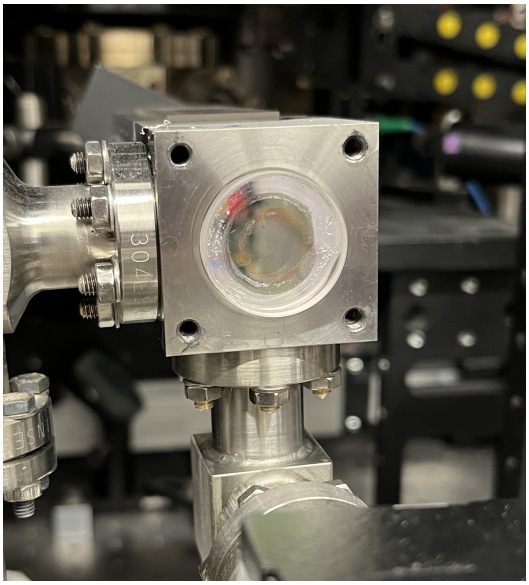


**Figure 3.4** — View of the leaking porthole of the 2D-MOT chamber. We can clearly see the solidification of the ethanol around the porthole.

### 3.1.2 3D-MOT and magnetic transport

The 3D-MOT is created inside the octagonal metallic chamber with four CF-40, two CF-16 and two CF-63 viewports. All viewports are coated with an anti-reflective coating optimized for wavelength 532 nm and 650-1100nm. The 3D-MOT is pumped by an ion pump 25 $\mathrm{Ls}^{-1}$ and is connected to the 2D-MOT as explained in section 3.1.1 and to the science cell through differential pumping tube as well. In the 3D-MOT the atoms are trapped at the center and cooled down by the radiation pressure force of the cooling laser beams in the presence of magnetic field gradient. In the 3D-MOT we have 3 pairs of independent contrapropagating cooling laser beams in 3 directions respectively. These cooling beams are also circularly polarised and are detuned by $-2.25\,\Gamma$ from the transition $|5S_{1/2}, F = 2\rangle \rightarrow |5P_{3/2}, F = 3\rangle$. Each cooling beam is mixed with the repumper beam locked on the transition $|5S_{1/2}, F = 1\rangle \rightarrow |5P_{3/2}, F = 2\rangle$, for the same purpose as explained in section 3.1.1. The six beams come from the six collimators with integrated quarter-wave plates (fabricated at LNE-SYRTE by David Holeville) providing the circularly polarised beams of 2.4 cm in diameter. These collimators are connected to a commercial polarisation-controlled fiber cluster 2×6 system from Schäfter+Kirchhoff. At the two entries of this system, we send two beams (the cooling laser and the repumper laser) and these beams are then mixed and divided into 6 beams using polarising cubes and half waveplates. The half waveplates allow us to control the power of each beam independently.

The magnetic quadrupole field for this trap is created using the coils situated at the

exterior of the 3D-MOT chamber as shown in Fig. 3.2 and are mounted on a movable support that we can translate over a distance of 28cm to transport the atoms from the MOT chamber to the glass cell. To be able to keep atoms confined in the quadrupole trap during transport, a large gradient is needed resulting in the heating of coils. To prevent this, an efficient cooling of coils is required. That's why the coils are made of hollow copper wire to let circulate cold water. To supply the current in these coils, we use two separate power supplies with some small imbalance in the current values in order to align the atomic cloud's position with the differential pumping tube separating the 3D-MOT chamber and the science cell.

These magnetic transport coils were fabricated during the thesis of Karina Merlotti and more details can be found there [89]. The transport coils are operated on the experiment with currents in the range of 22 A to 400 A and produce a horizontal gradient of $0.25\,\mathrm{Gcm^{-1}A^{-1}}$. We adopted this method to move the zero of the quadrupole magnetic field and transport atoms from the 3D-MOT chamber to the science chamber rather than multiple pairs of coils with a modulated current as in Ref. [94]. This is beacause the former way gives us more optical access around the science cell as the magnetic transport coils go back to their initial position once the atoms are transferred. This magnetic transport system has been working really well since its installation, it does a round trip at each run of the experiment, resulting in 200 round trips on average every day.

### 3.1.3 Science Cell

We produce the BEC of $^{87}$Rb in a science cell. The cell is made up of quartz and it has an anti-reflected coating on the exterior surface for wavelengths 532 nm and $650 - 1100$nm. It is pumped by an ionic pump $25\,\mathrm{Ls^{-1}}$ and a titanium sublimation pump is attached to it and can be activated if needed. Two coils in an anti-Helmholtz configuration are placed above and below the science cell to create a magnetic quadrupole field (Fig. 3.5). These coils were built and assembled during the PhD thesis of Thomas Liennard [88, 95, 96]. These coils are operated on the experiment with currents in the range of 28 A to 110 A and produce a horizontal gradient of $1.98\,\mathrm{Gcm^{-1}A^{-1}}$.

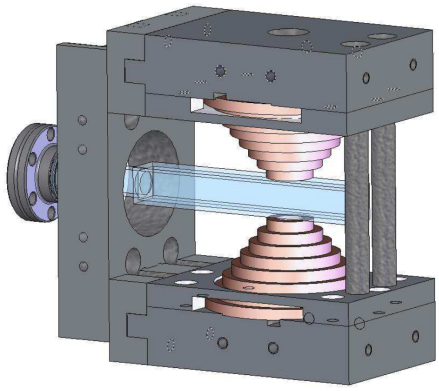


**Figure 3.5** — Image of the science cell with the magnetic coils in anti-Helmholtz configuration used to produce the quadrupole magnetic field. Figure taken from [89].

Below (Fig. 3.6) is the upside view of the main part of our experiment. We can identify

the 2D-MOT attached to the rubidium atom source, a 3D-MOT, the magnetic transport coils, the science cell and the plug beam focalised around the center of the magnetic quadrupole trap in the science cell and that will be introduced in Sec.3.3.5.

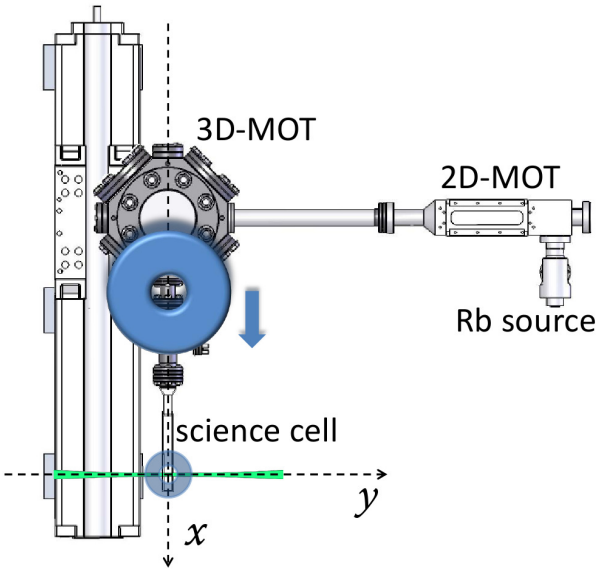



**Figure 3.6** — Upside view of the experimental system. The moving coil in the image is that of magnetic transport.

## 3.2 Compensation coils

In our experiment, we have three pairs of meter-scale square coils surrounding the whole vacuum chamber to compensate for the Earth's magnetic field at the position of the 3D-MOT. Once we have transported the atoms to the science cell, we switch off the current in these coils and a set of two pairs of rectangular coils of dimensions 10 cm by 5 cm are then used to create a homogeneous magnetic field component in the longitudinal and vertical directions near the center of the science cell. These coils are used to compensate for any unwanted magnetic fields at the final quadrupole trap position so that the position of the trap is independent of the magnetic gradient. These coils are also used to produce homogeneous magnetic fields during the imaging sequence.

## 3.3 Initial laser configuration

The initial laser system was comprised of four lasers of wavelength 780 nm which included the master laser (also used for probing the atoms), two repumper lasers, a laser for 2D and 3D-MOT and one laser of wavelength 532 nm (Verdi laser) for a plugged quadrupole trap.

### 3.3.1 Master laser

The master laser is an extended cavity diode laser (Narrowdiode from Radiant Dyes) locked on the crossover between the transitions $|5S_{1/2}, F = 2\rangle \rightarrow |5P_{3/2}, F = 2\rangle$ and $|5S_{1/2}, F =$

$2\rangle \rightarrow |5P_{3/2}, F = 3\rangle$ by saturated absorption technique. This laser served as a reference to lock the cooling laser with a beat note on a photodiode. It was also injected in two separate optical fibers to resonantly probe the atomic cloud (in horizontal and vertical directions) at the end of the experimental sequence (see Fig. 3.1). The probe pulses were created with the help of a double-pass acousto-optic modulator (AOM).

### 3.3.2 Cooling laser

This laser provides the cooling beams for the 2D-MOT and 3D-MOT respectively and also the push beam which is used to transfer the atoms from 2D-MOT to 3D-MOT. It is a telecom fiber laser at wavelength 1560 nm amplified to 10 W and frequency doubled in a single pass PPLN crystal, giving about 1 W of power at 780 nm. Its power is controlled by an AOM and is divided into four paths: 2 for 2D-MOT cooling beams (horizontal and vertical), 1 for 3D-MOT and 1 for push beam. More details about its development can be found in [88].

### 3.3.3 Repumper laser

In the initial experimental setup, the repumper laser was a Sanyo 780 nm diode laser locked on a saturated absorption in a rubidium vapour cell. This diode laser was later replaced during my PhD thesis by another extended cavity diode laser (Narrowdiode from Radiant Dyes) (details in Chapter 6). We use repumper laser in our experiment at a frequency resonant with the transition $|5S_{1/2}, F = 1\rangle \rightarrow |5P_{3/2}, F = 2\rangle$ of the $D_2$ line of $^{87}$Rb. Apart from being used for 2D and 3D-MOT, it is also injected in a separated fiber to repump the atoms during the imaging sequence along the horizontal direction (Fig.3.7). It is centered a few millimeters below the final trap and has a waist of around 4 mm. It is used to image the atomic cloud after 15 to 27 ms of time of flight (TOF) expansion. A part of the repumper laser (Sanyo diode) was also used to lock an off-resonant repumper laser with a beatnote on a fast photodiode.

### 3.3.4 Off resonant repumper laser

This repumper laser was implemented in our experiment during the PhD thesis of Camilla de Rossi [97] to image the high-density atomic cloud in situ, i.e., without time-of-flight (TOF) expansion, along the vertical direction. This repumper beam (Fig.3.7) propagates along the $x$-axis and is centered at the final trap position with a waist of 0.7 mm. Initially, it was another Sanyo 780 nm laser diode which was also replaced by the same Narrowdiode laser as for Repumper (see Chapter 6). As the frequency of this laser was controlled through a beatnote with the resonant repumper beam, we used to detune its frequency by +600 MHz from the transition $|5S_{1/2}, F = 1\rangle \rightarrow |5P_{3/2}, F = 2\rangle$ (as shown in the figure 3.1) to reduce the optical depth which helps in repumping uniformly the high-density atomic cloud.

### 3.3.5 Blue detuned (532 nm) high power laser for a plugged quadrupole trap

It is impossible to reach the BEC phase in a pure quadrupole magnetic trap by cooling atoms using the rf evaporation method. It is because when we cool down the atoms, the density at the center of the trap increases and as the field vanishes at the center of the quadrupole trap, the atoms flip from trapping to an anti-trapping state leading to Majorana losses. These losses can be limited by adding a far detuned dipole trap either blue detuned (plug) [23, 98]

or a red detuned (dimple) [99]. In the early days of my PhD, we worked with a blue detuned dipole trap using a plug beam produced by a 10 W @ 532 nm Verdi laser. The working principle of blue detuned optical dipole trap can be found in detail in the PhD thesis of Karina Merlotti [89] and in the article [45], even though the laser used was not the same at that time (10 W @ 532nm Millenia laser) but the principle is the same. The main idea is to focus the plug beam near the center of the quadrupole trap (creating a repulsive force for the atoms) in order to prevent the atoms from approaching the center of the quadrupole trap during evaporation. The waist of the plug beam used was 46(3) µm with a power of 5.8 W near the position of the atoms.

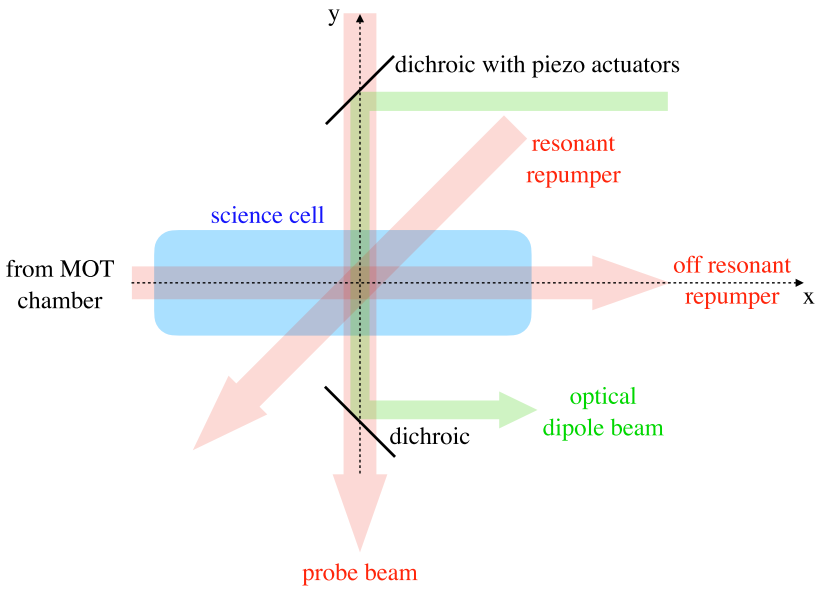



**Figure 3.7** — Visualisation of different lasers passing through the science cell in the horizontal plane.

Fig. 3.7 shows the top view of various lasers passing through the science cell. We can see that the plug beam was aligned with the probe beam in a horizontal direction with the help of two dichroic mirrors which reflect the beam at 532 nm and let the beam at 780 nm go through.

## 3.4 Experimental sequence

In this section, I will discuss the experimental sequence (Fig.3.8) we used to produce a BEC in a plugged quadrupole trap and its transfer to the bubble trap.

### From 3D-MOT to the magnetic quadrupole trap in the cell

We start the experimental sequence by loading the atoms in the 3D-MOT. Once the atoms are in 3D-MOT we perform the phase of compression which lasts for 9 ms, during which we push the horizontal magnetic gradient from 5.75 to 22.5 $\mathrm{Gcm^{-1}}$ and the detuning of the cooling laser passes from $-3\Gamma$ to $-4\Gamma$. This allows us to compress the cloud for a better

matching with the magnetic trap. Once the atoms are compressed, we increase again the detuning of the cooling laser from $-4\Gamma$ to $-19\Gamma$ to further cool down the atoms in a molasses phase.
After the molasses phase, we switch off the repumper 2.5 ms before switching off the cooling laser and we ramp the horizontal gradient up to 87.5 $\mathrm{Gcm}^{-1}$ in 100 ms. As we switch off the repumper, the atoms go into the state $F = 1$. Then these atoms get transferred into the quadrupole magnetic trap produced by the coils of the transport where only the atoms in $|F = 1, m_F = -1\rangle$ remain trapped, the others being lost. We then transport the atoms towards the science cell in 1050 ms and transfer them into the quadrupole magnetic trap of the science cell. To transfer the atoms, we ramp down the gradient in the transport coils to zero and increase the horizontal gradient in the coils of the quadrupole trap in the cell from 0 to 98.4 $\mathrm{Gcm}^{-1}$ simultaneously in 400 ms. Once the atoms are transferred, the transport goes back to its initial position 25 ms after the current in its coils reaches zero. At the end of this phase, we have around $10^8$ atoms at a temperature of around 150 µK trapped in a magnetic quadrupole trap.

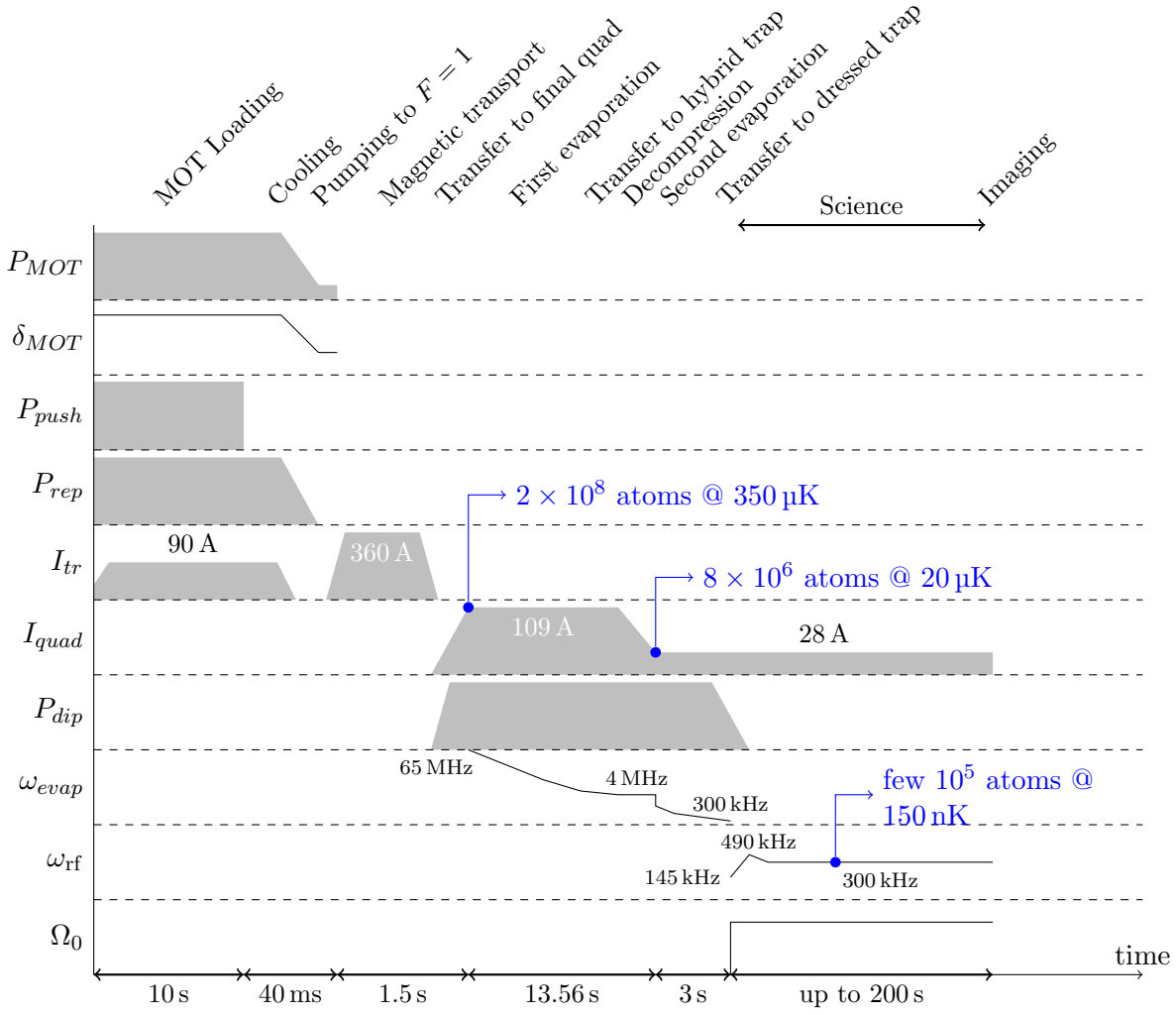



**Figure 3.8** — Flowchart of the experimental sequence.

### Evaporation in a plugged quadrupole trap

To reach the BEC transition it is necessary to perform the evaporation cooling on the trapped atoms in a quadrupole trap. One of the efficient ways of performing evaporative cooling is to use an rf field. When we apply rf field at a given frequency on the atoms, it couples different Zeeman sublevels leading to the spin-flip of the atoms from trapping to the anti-trapping state, as the rf field reaches resonance with the atoms. This results in the elimination of the atoms with high energy leading to a decrease in temperature of the atomic cloud and an increase in density at the center of the trap. However, it is impossible to cool down atoms in a pure magnetic quadrupole trap using rf evaporation to reach the BEC phase (explained in the Sec.3.3.5). To perform evaporative cooling in a quadrupole trap we turn on the plug beam and to increase the efficiency of the evaporation we increase the horizontal gradient of the magnetic field to its maximum value 225.5 $\mathrm{Gcm}^{-1}$ in 300 ms leading to the high temperature of 350 µK. We then perform the first part of the evaporation using the rf field. We turn on the rf field at 65 MHz and ramp it down to 4 MHz in 13.63 s. The rf ramp is divided into 4 linear ramps [89] and was optimised (Fig. 3.9).

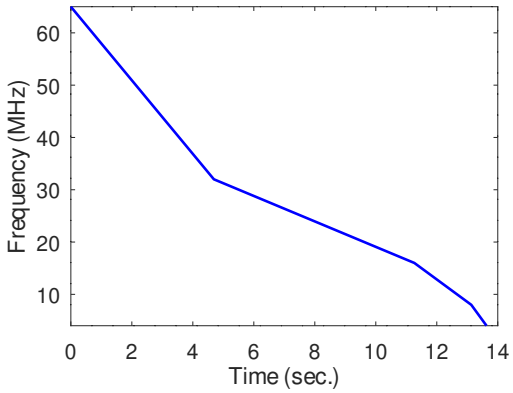



**Figure 3.9** — The blue line represents the rf field frequency as a function of time. The whole curve represents the first part of rf evaporation performed at maximum gradient as discussed above. Figure adapted from [89].

At the end of this phase we have $8 \times 10^6$ atoms at a temperature of 20 µK and the phase-space density (PSD) scaling as $N^{-3.1}$ [45]. At this point, the Majorana losses become important and the use of the plug beam is not sufficient to prevent the losses [89]. In this case, the best option is to go through a decompression phase. We perform this decompression by linearly ramping down the horizontal gradient of the magnetic field to 56 $\mathrm{Gcm}^{-1}$ in 50 ms. We then perform the second part of the evaporation ramp from 2 MHz to 300 kHz in 3 s. After this phase, we have obtained a sample of $4 \times 10^5$ atoms at a temperature of 200 nK out of which around $2 \times 10^5$ atoms are condensed and the sample is ready to get transferred into the final trap, i.e., the bubble trap.

### Loading of bubble trap

Once we have a cool enough sample of atoms, we would like to transfer them to the bubble trap. To make the transfer we proceed as follows: First, we turn on the circularly polarized dressing rf field at a frequency lower than the resonance frequency of atoms in the plugged

quadrupole trap. Then, we ramp up the dressing field frequency to a certain value and ramp down the power of the plug beam to zero. Also, the loading procedure is independent of the polarization of the rf dressing field.

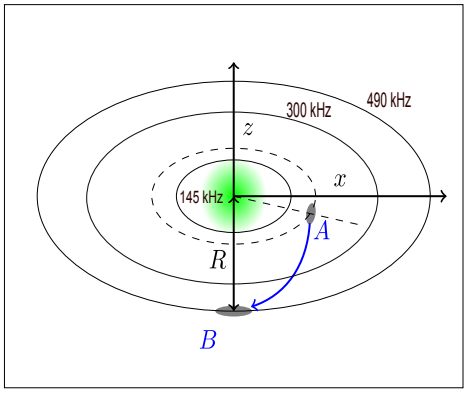



**Figure 3.10** — Bubble trap loading procedure in the plug beam configuration. A: initial position of the atomic cloud in plugged quadrupole trap. B: final position of the atomic cloud in the bubble trap.

Fig.3.10 illustrates the transfer process from the plugged quadrupole to the bubble trap. In a plugged quadrupole trap atoms are off-centered (point A in Fig.3.10) and the frequency of the resonant surface at this position is found by performing a spectroscopy measurement: 250 kHz. We start the transfer process by switching on the rf field at 145 kHz (inner solid black ellipsoid in Fig.3.10) and ramp up its amplitude from 0 to $\Omega_1 = 2\pi \times 50\,\text{kHz}$ in 5 ms. We then ramp the frequency of the dressing field at a constant amplitude from its initial value to 490 kHz in 120 ms (outer solid black ellipsoid) and simultaneously we ramp down the power of the plug beam to zero in 150 ms. The change in the dressing frequency from 145 kHz to 490 kHz changes the radius $R$ of the bubble from 37.7 µm to 127.4 µm. During the ramping of the frequency, the rf field crosses the resonant surface of the atoms in the plugged quadrupole trap and catches them. As we turn off the plug beam during the transfer process while inflating the bubble simultaneously, atoms do not feel the influence of the plug beam anymore and fall at the bottom of the bubble trap due to gravity (from point $A$ to point $B$ as shown in Fig.3.10). This movement of atoms from the point $A$ to the point $B$ can easily excite the center-of-mass (COM) oscillations along the $x$ axis. The transfer process is optimised to minimise these excitations. Finally, we ramp down the frequency of rf dressing field to its final value 300 kHz in 175 ms (middle solid black ellipsoid). At this point, the radius $R$ of the bubble trap is 75 µm. At the end of the transfer process, we obtain a sample of around $3 \times 10^5$ atoms at a temperature of 150 nK. We also have an rf knife polarized linearly along the $z$ axis during the process at a frequency 100 kHz above the trap bottom and its frequency is linearly ramped down to 20 kHz above the trap bottom during the first ramp of the rf dressing field. This is done to limit the trap depth and prevent heating. We can change its value to change the atomic cloud's temperature and the condensate fraction from 0 to 1.

## 3.5 Radiofrequency sources

We have multiple rf sources in our experiment: rf for the evaporation to produce a BEC in a plugged quadrupole trap, rf for the dressing of atoms, rf for spectroscopy measurement and rf for the evaporation in the bubble trap. First I will discuss the rf source and antennas used for the dressing of atoms and then describe the other rf sources.

### 3.5.1 Antennas for dressing

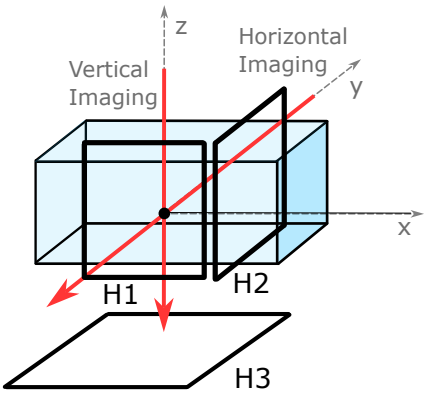



**Figure 3.11** — Visualisation of the configuration of rf dressing antennas around the science cell. The horizontal antennas are square in shape with 16 mm sides and are made of 10 loops of copper wire. The antenna H1 is placed 16.5 mm away from the atoms and the antenna H2 is placed 12.5 mm away from the atoms. The antenna H3 is made of 4 loops of copper wire with dimensions $11 \times 6.5$ mm placed 57 mm below the position of atoms. Figure taken from [82].

In our experiment, the final trap is a bubble trap which is made up of dressing the atoms in the quadrupole magnetic trap using the rf field of circular polarisation. We use three antennas placed orthogonally (as shown in Fig. 3.11) to produce the rf field of arbitrary polarization. In our experiment, to create a rotationally invariant bubble trap, we need an rf field of circular polarisation with respect to the $z$ axis.

In theory, we can produce a circularly polarised rf field with respect to $z$-axis using a pair of antennas placed orthogonally in the $x-y$ plane with the same amplitude and a dephasing of $\pi/2$. However, experimentally it was not possible to achieve a perfect circular polarisation using only antennas H1 and H2 [42]. This is a consequence of the fact that if one of the antennas of the horizontal axis is slightly tilted, the polarization of the rf field will no longer be circular in the $x-y$ plane but elliptical (details can be found in the PhD thesis of Mathieu de Goër de Herve [42]). To ensure the circular polarisation in the $x-y$ plane an additional antenna was added in the $z$ direction.

The antennas are controlled with a DDS (Direct Digital Synthesizer), which was developed in the electronic workshop at LPL [42]. It is an eight-output fully programmable DDS. It is made of a pair of two DDS devices of four outputs each (AD9959) receiving a 10MHz clock signal and controlled by a micro-controller unit (TM4C123). The outputs of the DDS are amplified by wide-band instrumentation amplifiers up to a maximum power of 20 dBm and

are controlled by a fast rf switch. It converts the 10MHz clock signal into 8 analog periodic signals of the form $A\cos(\omega t+\phi)$, where the amplitude $A$ has 10-bit resolution, the frequency $\omega$ has 32-bit resolution and the phase $\phi$ has 14-bit resolution. We use 3 of the outputs of the DDS to produce a fully controllable rf field at the center of the quadrupole trap and we have the possibility to tune the rf field to any arbitrary polarization.

### 3.5.2 Other rf antennas

Apart from the antennas for dressing, we also have an antenna to perform the spectroscopy measurement in the plugged quadrupole trap and the bubble trap at a fixed frequency, fed by Stanford synthesizer DS345. We have an antenna to perform the first part of rf evaporation in the plugged quadrupole trap. The rf signal for this part of evaporation is generated by using one of the outputs of the DDS amplified by a 10 W rf amplifier. We have an antenna to perform rf evaporation in the bubble trap and for the second part of the rf evaporation in the plugged quadrupole trap. The rf signal for the rf evaporation in the bubble trap is generated using one of the outputs of the DDS and the signal for the final part of the evaporation in the plugged quadrupole trap is generated using another Stanford synthesizer DS345. Both signals are sent in one antenna through the combiner (ZSC-2-2). All these antennas provide an rf field linearly polarised along the $y$ direction.

In our experiment, we can also perform the rf evaporation in the bubble trap using a weak rf field polarized along the $z$ axis. This is done by adding the rf signal from one of the outputs of the DDS on the same antenna as H3 (Fig.3.11) using an operational amplifier.

## 3.6 Imaging system

In this section, I will present the imaging setup that we use to study the dynamics of the BEC. From Fig.3.11, we can note that we have two imaging axes in our experiment: Horizontal (along $y$ axis) and vertical (along $z$ axis). Through the horizontal axis, we image the cloud after TOF expansion while through the vertical axis, we can image the cloud both in situ or after TOF expansion. In situ imaging allows us to record the in-trap density distribution while imaging after TOF expansion gives access to the momentum distribution thus allowing us to measure the temperature and the atom numbers more accurately. It also expands the profile which enables us to see for example the vortices when putting a superfluid into rotation.
Both (in situ measurement and TOF measurement) provide complementary diagnostic tools. We will see in the next section that the in situ imaging of the cloud requires the use of a high-intensity probe.

### 3.6.1 Absorption imaging

#### Principle

The working principle of absorption imaging relies on the use of a probing beam which is at resonance with the atoms. In our case, we use the probing beam locked on the transition $|5S_{1/2}, F=2\rangle \rightarrow |5P_{3/2}, F=3\rangle$ of $D_2$ line of $^{87}$Rb. We can extract information about our atomic sample by comparing the profile of the probe beam with and without the interaction with the atoms. The absorption of the photons of the probe beam is related to the atomic cloud's shape (see first picture of the figure 3.12). As the probe beam used to image atoms is

resonant, atoms exchange a lot of photons during the process and this leads to the destruction of the atomic cloud. The cloud has thus to be prepared for each experimental measurement we want to make.

Supposing that the probe beam is propagating along the $z$ axis and has a detuning of $\delta$ with respect to the resonant frequency of the atomic transition, we can write the optical density $D_z(x,y)$ along the $z$ direction from the Beer-Lambert law under the form:

$$D_z(x,y) = -\ln \frac{I_f(x,y) - I_d(x,y)}{I_i(x,y) - I_d(x,y)}, \tag{3.1}$$

where $I_f(x,y)$ (Fig.3.12 picture a) and $I_i(x,y)$ (Fig.3.12 picture b) are the intensities of the probe beam after and before going across the atomic cloud and $I_d(x,y)$ is the background profile (without probe and atoms, Fig.3.12 picture c). Assuming that the intensity of the incident beam is much weaker than the saturation intensity ($I_i \ll I_{\text{sat}}$), we can write the relation between the optical density $D_z(x,y)$ and the atomic density $n_0(x,y,z)$ as:

$$D_z(x,y) = \sigma \int n_0(x,y,z)dz = \sigma n_z \tag{3.2}$$

where $\sigma$ is the effective absorption cross-section and $n_z = \int n_0(x,y,z)dz$ is the density integrated along the probe axis. This cross-section is independent of the intensity of the incident beam when it is lower than the saturation intensity and is written as:

$$\sigma = \frac{\sigma_0}{1 + \frac{4\delta^2}{\Gamma^2}}. \tag{3.3}$$

$\sigma_0 = 3\lambda^2/(2\pi)$ is the resonant optical cross-section, where $\lambda$ is the wavelength of the probe beam. By knowing the initial and final intensities and the effective cross-section, we can deduce the atomic distribution integrated along the $z$ direction as follows:

$$n(x,y) = -\frac{1}{\sigma} \ln \frac{I_f(x,y) - I_d(x,y)}{I_i(x,y) - I_d(x,y)}. \tag{3.4}$$

This is represented in Fig.3.12 d). But when we try to image the in situ, high-density atomic cloud, we can not work with a low-intensity probe beam because this would lead to the complete absorption of the photons by the atoms resulting in an infinite density according to the equation (3.4). Therefore, we need to use the probe beam with intensity $I$ higher than the saturation intensity $I_{\text{sat}}$ in order to saturate the atomic transitions [42, 97, 100]. In this particular case the effective cross-section depends on the intensity of the probe beam and is expressed under the form:

$$\sigma = \frac{\sigma_0}{c^* + \frac{I}{I_{\text{sat}}}}, \tag{3.5}$$

where $c^*$ is a dimensionless parameter and can be measured experimentally [100, 101]. $c^*$ is a parameter that takes into account the deviation of the circular polarisation of the probe beam. We can write the optical density as:

$$\sigma_0 n(x,y) = -c^* \ln \left[ \frac{I_f(x,y) - I_d(x,y)}{I_i(x,y) - I_d(x,y)} \right] + \frac{I_f(x,y) - I_i(x,y)}{I_{\text{sat}}}. \tag{3.6}$$

The first term corresponds to the usual Beer-Lambert law and the second term gives the high-intensity corrections and depends on the intensity of the probe beam with and without atoms.

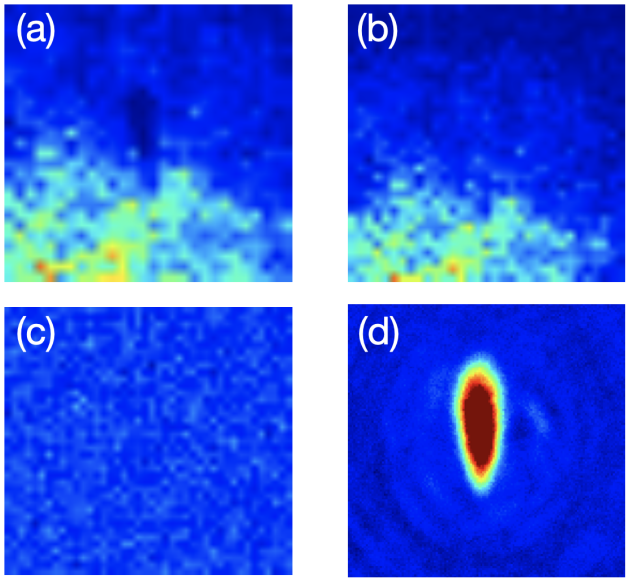



**Figure 3.12** – a) Probe beam profile after interaction with the atoms, b) Probe beam profile without atoms, c) Background image without probe and without atoms, d) Atomic density profile after the TOF expansion experiment deduced using the first three images.

Special care must be taken to image a highly dense atomic cloud. To this aim, we can either repump only a fraction of the atoms or increase the intensity of the probe beam. However, our standard technique to repump the atoms to the $F = 2$ hyperfine state is not appropriate to image very dense clouds, as is often the case for in situ imaging. Repumping the high-density atomic cloud with a resonant repumper can lead to errors in the measured density as the atoms interacting first with the beam will absorb more photons than the atoms in the back of the cloud. We can note from the equation (3.4) that the repumper beam's transmission increases as the effective cross-section decreases. The solution to ensure a homogeneous effect of the repumper is to decrease the effective cross-section by increasing the detuning of the repumper beam according to the equation (3.3). Therefore, we use a far detuned repumper (by +600 MHz from the transition $|5S_{1/2}, F = 1\rangle \rightarrow |5P_{3/2}, F = 2\rangle$) in order to uniformly repump the atoms while imaging the cloud in situ [97].

### 3.6.2 Horizontal imaging setup

The horizontal imaging setup is meant to image the density distribution after the TOF expansion to determine the temperature, number of atoms and BEC fraction of the atomic cloud. To do this, we use a laser beam tuned on the transition $|5S_{1/2}, F = 2\rangle \rightarrow |5P_{3/2}, F = 3\rangle$ and of waist 2.7mm propagating along $y$ axis. The cloud is imaged onto the camera (Andor-iXon) using a pair of lenses (Fig. 3.13) providing a magnification of 2.17. The camera we use has a 1004×1002 pixel matrix with a pixel size of $8 \times 8\mu m^2$. This probe beam is aligned below the trap ($\approx 2.5$ mm), which allows us to image the cloud after 10 to 30 ms of time-of-flight

expansion. We also use a small homogeneous magnetic field of magnitude 1.9 G along the $y$ axis to define the quantisation axis of the atoms. As the polarization of the probe beam is elliptical, we calibrate the factor $c^*$ of Eq.(3.6) directly with the atomic signal (see the PhD thesis of Mathieu de Goër de Herve [42]). To perform the imaging of the atomic cloud we first repump the atoms in the ground state $F = 2$ manifold 100 µs before the end of TOF expansion using a resonant repumper pulse of duration 100 µs then we shine the probe pulse of duration 17 µs on the atoms.

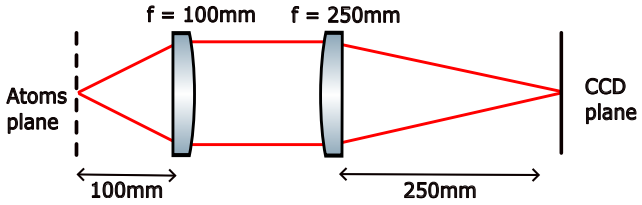



**Figure 3.13** — Lens configuration of the horizontal imaging system providing the magnification of 2.17. The dashed vertical line corresponds to the plane of the atoms while the solid vertical line corresponds to the CCD camera place.

### 3.6.3 Vertical imaging setup

The vertical imaging setup is meant to image the in situ profile of the atomic cloud and also after TOF expansion to observe for example the vortex lattice. To do this, we use a circularly polarized beam propagating along the $z$ direction with a waist of 0.7mm and locked on the transition $|5S_{1/2}, F = 2\rangle \rightarrow |5P_{3/2}, F = 3\rangle$. The probe pulse lasts for about 20 µs. In this imaging configuration, the probe beam is imaged with four lenses (figure 3.14) onto the camera (Andor - Luca) providing a magnification of 7.8. For in situ imaging, we use the second repumper beam to repump uniformly a fraction of the atoms without changing the density profile of the atomic cloud before probing it. Whereas for imaging after TOF expansion we use the resonant repumper. In order to perform both in situ and TOF measurements, the whole imaging setup (camera and lenses) is mounted on a 3-axes micrometric translation which allows us to position the object plane at the desired position. As we have the moving transport coils in our experiment (as shown in Fig. 3.6), the first lens of the imaging setup is always 10 cm below the position of atoms in the trap, which results in the low numerical aperture (of around 0.1). This limits the optical resolution to 4 µm and provides the depth of field of around 78 µm. The camera used here also has a 1004×1002 pixel matrix with each pixel size of $8 \times 8\mu m^2$.

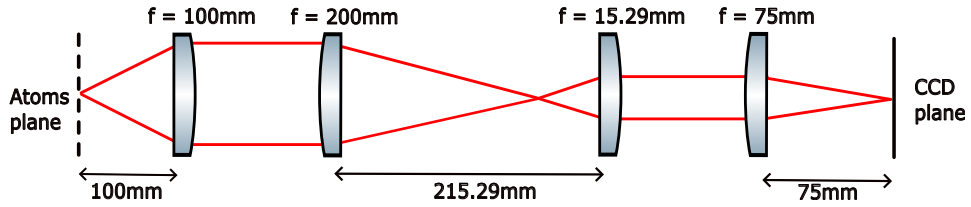



**Figure 3.14** — Lens configuration of the vertical imaging system providing the magnification of 7.8. The dashed vertical line corresponds to the plane of the atoms while the solid vertical line corresponds to the CCD camera place.

## 3.7 Conclusion

In this chapter, I described the experimental setup we use to study weakly interacting Bose gases in a quasi-2D regime (Chapter 4). I first discussed the vacuum chambers (2D-MOT, 3D-MOT and the science cell) and then the initial laser configuration. The experimental sequence described in this chapter allows us to produce an ultracold sample of a few $10^5$ atoms at a temperature below 200 nK. The fluctuation in the atom number is of the order of 10%. The experimental sequence to produce a BEC takes about 30 s and the lifetime of the atoms in a bubble trap is of the order of 120 s.

The performance of this experimental setup is satisfactory however it exhibits some limitations. For example, the transfer of atoms from the plugged quadrupole trap to the bubble trap is complicated as the initial and final trap positions are not the same, leading to the excitation of the COM motion. This limitation was overcome in our experiment by replacing the plug trap with a red detuned dipole trap (1064 nm) and the characterisation of the trap is briefly explained in Chapter 5 of this PhD thesis.

Another limitation is related to the imaging system. In the absorption imaging process, we work with a probe beam which is resonant with the atoms leading to the complete absorption of the photons of the probe as it interacts with the atoms. This allows us to make only a single measurement at a time. This can be very time-consuming to see the dynamics of a rotating superfluid in a bubble trap as in this regime the energy scale becomes small resulting in slow dynamics and we will have to repeat the whole experimental sequence each time to make the measurements at different timestamps. To overcome this limitation we have implemented a non-destructive imaging scheme to make in situ measurements of the density profile of our cold atom sample (see Chapter 7). The basic idea is to use a probe beam which is vary far detuned from the resonance frequency of the imaging transition such that the atomic sample behaves like a phase object resulting in a phase shift in the probe beam. The interaction of the probe with atoms produces a diffraction pattern and the information of the atomic sample's density is encoded in this diffraction pattern. The density profile can be recovered by measuring the diffraction pattern after a short propagation distance and using a reconstruction algorithm to deduce the shape of the diffracting phase object [102]. As the probe beam is vary far detuned, the absorption remains low and this process can be repeated to take multiple in-trap images of the density profile. The implementation of this imaging scheme can be extremely useful to study the dynamics of a superfluid, as we can record a movie of the in situ dynamics before releasing the atoms and taking a last image after TOF expansion to calibrate the atom number and temperature.

To have laser detunings for the different beams, and to perform non-destruction imaging, we upgraded our 780 nm laser chain by locking all the lasers to a master laser using beatnotes (see Chapter 6).

# Chapter 4

# Thermal melting of a vortex lattice in a quasi 2D Bose gas

This chapter reports the first observation of the thermal melting of a vortex lattice in a quasi-2D rotating superfluid. The most considered theory for explaining the melting scenario of a 2D crystal has been developed by Kosterlitz, Thouless, Halperin, Nelson and Young (KTHNY theory) [37, 43, 44]. This theory has been developed considering the fact that true long-range order (LRO) does not exist in 2D crystals at any finite temperature because of their thermal instability as per the Mermin-Wagner-Hohenberg theorem [103, 104]. Still, a crystal is expected to have a quasi-long-range order at sufficiently low temperature. According to the KHTNY theory, melting in 2D crystals occurs through two consecutive phase transitions: from solid to hexatic and from hexatic to liquid and these two transitions are characterised by the thermal activation and unbinding of lattice defects. The validity of this theory has been tested both numerically [105–109] and experimentally. However, most of the experimental studies have been performed using classical objects like colloidal solutions [110–117], or air-fluidized dust or spheres [118, 119]. KTHNY melting scenario has also been observed experimentally in quantum vortex lattices in thin superconductors [120–123]. Rapidly rotating BECs also exhibit quantized vortices that arrange in a triangular lattice [34, 124, 125] thus providing the possibility to observe the KTHNY melting scenario in these systems.

In this chapter, I will start by explaining, in Sec.4.1, the KHTNY theory which will be helpful in understanding the phase transitions during the melting scenario. I will discuss the prediction for melting temperature $T_m$ made by Gifford and Baym [126] in Sec.4.1.2 and will also introduce the correlation functions in Sec.4.1.3, which will be needed to characterize the translational and the orientational order of the vortex lattice. The rotation of a trapped condensate in a bubble trap will then be explained in Sec.4.2. In this section of the chapter I will describe the potential of the trap in a rotating frame, experimental protocol to put atoms in rotation, spin-up evaporation process and the measurement of the rotation rate. Sec.4.3 is dedicated to the methods applied to detect the vortices and to determine their respective arrangement in the experimental density profile of a rotating quasi-2D superfluid. I will then present in Sec.4.4, the analysis of the experimental dataset performed to characterize the translational and the orientational order of the vortex lattice through their respective correlation functions. Finally, I conclude this chapter by presenting the Fourier analysis of the experimental dataset in Sec.4.5, which is another simpler way to discuss the melting

scenario. The algorithm to detect the vortices in our experimental dataset and the model to characterize the orders of the vortex lattice have been implemented and adapted by Romain Dubessy.

## 4.1 KTHNY theory

### 4.1.1 Two-step melting of 2D crystals

In the KTHNY theory, two critical temperatures, $T_1$ and $T_2$ ($T_1 < T_2$), play key roles in the phase transitions of a 2D vortex lattice. Below $T_1$, the vortex lattice maintains quasi-long-range translation and orientational order but may contain defects in the form of bound pairs of dislocations (fig.4.1). These dislocations are formed by adjacent lattice sites with 5 and 7 nearest neighbours. The melting temperature $T_m$, as estimated by Gifford and Baym [126], provides an upper bound for $T_1$. As the temperature rises above $T_1$, thermal fluctuations cause the dislocation pairs to unbind, leading to the proliferation of free dislocations Fig.4.2. This disrupts the quasi-long-range translational order but does not completely destroy the quasi-long-range orientational order. As shown in Fig.4.2 the lattice remains exactly the same away from the dislocation pair. At this point the vortex lattice is in a hexatic phase [127], characterized by an algebraic decay of the orientational correlation function.

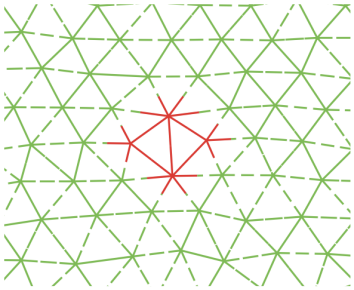


**Figure 4.1** — Example of a triangular vortex lattice with local defects. We can notice two sites with five neighbours and two sites with seven neighbours bound to each other. Figure taken from [107, 128].

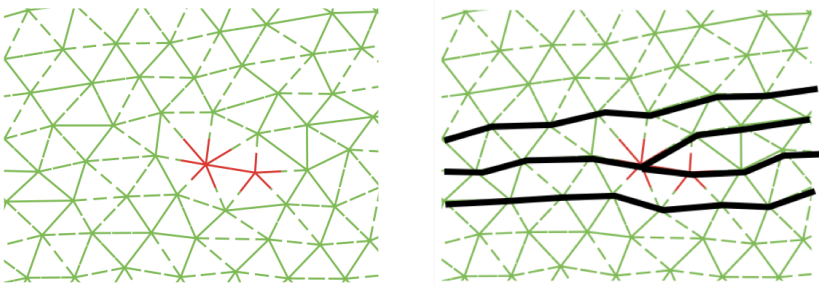


**Figure 4.2** — Isolated dislocation consisting of one site with five neighbours bound to another site with seven neighbours. Figure from [107, 128].

Lastly, when the temperature exceeds the second threshold, $T_2$, the dislocations become free 5-fold and 7-fold defects (Fig.4.3) and these defects change the orientation of the lattice. This is called disclination. This destroys the orientational order, and the system transitions into the liquid phase. The orientational correlation function decays exponentially in this regime.

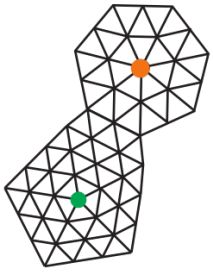


**Figure 4.3** — Disclination corresponding to the free one 5-fold and one 7-fold defect. The proliferation of these kind of defects in the lattice destroys completely the orientational order. Figure from [129].

### 4.1.2 Prediction of Gifford and Baym

In the context of rotating quantum gases, Gifford and Baym [126] provide an evaluation of an upper bound $T_m$ of the first transition temperature $T_1$, based on the KTHNY scenario at a fixed rotation frequency $\Omega$ for a condensate rotating in a rotationally invariant trap. The estimation of the melting temperature depends on the anisotropy of the trap $\omega_r/\omega_z$, where $\omega_r$ is the radial trapping frequency and $\omega_z$ is the trapping frequency along the rotation axis. For cigar-shaped traps ($\omega_r > \omega_z$), the melting temperature is close to the condensation temperature thus making it difficult to observe the melting transition in the superfluid phase [130]. For oblate gases as in our case ($\omega_z > \omega_r$), the melting transition is expected to occur at a temperature significantly lower than the superfluid critical temperature thus giving the possibility to observe this melting transition of a vortex lattice in the superfluid phase. The melting temperature $T_m$ for a rotating quasi-2D superfluid is shown to be bounded, obeying the condition:

$$T_m \leq \frac{2\pi\hbar^2\rho_0}{Mk_B\mathcal{D}_s(T_m)}, \tag{4.1}$$

where $\mathcal{D}_s(T_m)$ is the phase-space density of a superfluid at the melting temperature. Here, $\rho_0$ is the density at the center of the trap given by:

$$\rho_0 = \mu \times \frac{M}{\hbar^2\tilde{g}}, \tag{4.2}$$

where $\mu$ is the chemical potential, $M$ is the atomic mass and $\tilde{g} = \sqrt{8\pi}a_s/a_z$ is the 2D interaction constant defined in Chapter 1.

### 4.1.3 Correlation functions

To characterize the translational and orientational order of the vortex lattice during the melting transition, it is necessary to define the correlation functions for both orders.

#### 4.1.3.1 Pair correlation function

We will be using the pair correlation function $g(r)$ to characterize the translational order of the vortex lattice. This correlation function is defined as the ratio of the number of pairs of vortices $P_v^{\exp}(r)$ split by distance $r$ in the experimental profile of a vortex lattice and the number of pairs of vortices $\overline{P_v}(r)$ split by distance $r$ for a uniform vortex density $n_v$ computed in a disc of radius $R$.

$$g(r) = \frac{P_v^{\exp}(r)}{\overline{P_v}(r)}. \tag{4.3}$$

The pair correlation function presents oscillation in the crystal phase, which are exponentially damped in the hexatic phase. We will use it to characterize the first transition at $T = T_1$.

#### 4.1.3.2 Orientational correlation function

The orientational order is characterised by the orientational correlation function $G_6(r)$ [43]. It is defined using the orientation order parameter which can be given for each vortex $k$ at a position $\mathbf{r}_k$ by:

$$\Psi_k^{(6)} = \frac{1}{N_k} \sum_{j=1}^{N_k} e^{6i\theta_{kj}}, \tag{4.4}$$

where the sum runs over the $N_k$ first neighbours and $\theta_{kj}$ is the angle between a fixed axis and the bond linking the sites $k$ and $j$ (Fig.4.4).

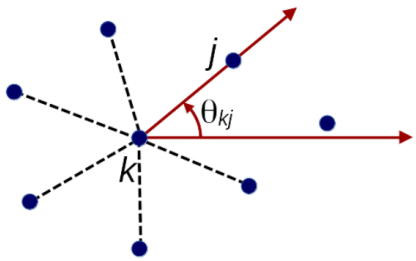



**Figure 4.4** — Representation of the angle $\theta_{kj}$ to compute the orientational order parameter, Eq.(4.4).

We can then write the orientational correlation function as:

$$G_6(r) = \langle \Psi_k^{(6)} * \Psi_p^{(6)} \rangle_{|\mathbf{r}_k - \mathbf{r}_p| \sim r} \tag{4.5}$$

where the average is taken over all pairs of vortices split by a distance $r$. The orientational correlation function also presents oscillations. Its envelope is constant in the crystalline phase, decays algebraically in the hexatic phase and exponentially in the liquid phase. We will use it to characterize the second transition between the hexatic and liquid phases at $T = T_2$.

## 4.2 Rotating superfluid in a bubble trap

We will study the KTHNY scenario with our quantum gas. We would like to achieve a fast rotation rate in order to observe the thermal melting of the vortex lattice. For this purpose, we can not simply use a trap with harmonic confinement because the centrifugal force will overcome the confinement potential as the rotation frequency $\Omega$ reaches or exceeds the radial trapping frequency $\omega_r$ of the harmonic trap [131], as discussed below in Sec.4.2.1. Therefore, in order to achieve a high rotation rate comparable to the radial trapping frequency, a high order of confinement is necessary. We can have this kind of confinement in a harmonic plus quartic trap [125, 132, 133] as in this case, the confining potential rises as $r^4$ when $\Omega = \omega_r$. In our experiment, the bubble trap introduced in Chapter 2 has quartic confinement and it allows us to achieve high rotation rates. This property of the trap has previously been explored in the group [83]. Before providing the details of the experimental sequence implemented to put atoms into rotation, I will first describe the potential of the bubble trap in the rotating frame.

### 4.2.1 Potential in the rotating frame

We can rewrite the potential of the bubble trap described in Chapter 2 in the frame rotating at an effective frequency $\Omega$ as:

$$V_{\mathrm{rot}}(r,z) = \hbar\sqrt{(\alpha\ell-\omega)^2+\Omega_0(r,z)^2} + Mgz - \frac{1}{2}M\Omega^2 r^2. \tag{4.6}$$

We recall that in the absence of rotation ($\Omega = 0$), the trap minimum is located at $r = 0$ and $z = z_{\mathrm{eq}}$ with

$$z_{\mathrm{eq}} = -\frac{\omega}{2\alpha}\left(1 + \frac{\varepsilon}{\sqrt{1-\varepsilon^2}}\frac{\Omega_0}{\omega}\right). \tag{4.7}$$

The harmonic approximation is valid for $|z - z_{\mathrm{eq}}|, r \ll \omega/\alpha$. Up to the fourth order, the radial confinement of the bubble trap can be modelled as a harmonic oscillator with a quartic correction and the potential can be written as [83]:

$$V_{\mathrm{trap}}(r,z) = \frac{1}{2}M\omega_r^2\left(r^2 + \lambda_{\mathrm{quar}}\frac{r^4}{a_r^2}\right) + \frac{M\omega_z^2 z^2}{2}, \tag{4.8}$$

where $\lambda_{\mathrm{quar}}$ is the dimensionless coefficient of the quartic term and $a_r = \sqrt{\hbar/(M\omega_r)}$ is the radial length of the harmonic oscillator. The quartic correction term at the bottom of the bubble trap can be written as [42]:

$$\lambda_{\mathrm{quar}} = \frac{a_r^2}{4r_{\mathrm{b}}^2}. \tag{4.9}$$

In our experiment, the radial trapping frequency is $\omega_r = 2\pi \times 34\,\mathrm{Hz}$, and the horizontal radius of the ellipsoid is $r_{\mathrm{b}} = 75\,\mu\mathrm{m}$. Therefore, the value of the coefficient of the quadratic term in Eq.(4.8) is $\lambda_{\mathrm{quar}} \simeq 1.5 \times 10^{-4}$ which describes the weak anharmonicity of the trap. We can apply the Thomas-Fermi approximation in order to estimate the Thomas-Fermi radius in the horizontal plane [133]:

$$R_{\pm}^2 = \frac{a_r^2}{2k}\left[\frac{\Omega^2}{\omega_r^2} - 1 \pm \sqrt{\left(\frac{\Omega^2}{\omega_r^2} - 1\right)^2 + \frac{8k\mu}{\hbar\omega_r}}\right]. \tag{4.10}$$

For this chapter, we will only consider the case $\Omega \leq \omega_r$ such that $R_-^2 < 0$ while $R_+^2 > 0$ always holds. In this way, we will have Thomas-Fermi density going to zero only at the edges of the superfluid for $r = R_+$ while if $R_-^2 > 0$, this would result in a Thomas-Fermi density going to zero also at the center of the rotating condensate resulting in a dynamical ring configuration which has been already explored in the group [83].

### 4.2.2 Experimental details and protocol for rotation

In principle, to observe the thermal melting transition for a vortex lattice, one should vary the temperature across $T_1$ and $T_2$ at a fixed rotation frequency $\Omega$. However, the transition can also result from a change of $\Omega$ at fixed $T$, as all the relevant energies decrease as $\Omega$ increases due to the centrifugal force. As it is more convenient for us to change $\Omega$ at fixed $T$ which is 18 nK in our case, we proceed in this way and analyse the data as a function of the reduced temperature $\tau = T/T_{\mathrm{BKT}}(N, \Omega)$. Here, $T_{\mathrm{BKT}}(N, \Omega)$ is a critical temperature for superfluid transition for a quasi-2D superfluid estimated with a semi-classical approach [134]. $N$ refers to the number of atoms. Comparing to $T_{\mathrm{BKT}}$ is relevant because this is the leading mechanism for superfluidity in our quasi-two-dimensional samples [39]. The dependence of the temperature $\tau$ with the rotation rate $\Omega/\omega_r$ is represented in Fig.4.5. The estimation of $T_c^0$ and $T_{BKT}$ as a function of $\Omega$ and atom number $N$ has been explained in Sec.A.2 of Appendix A.

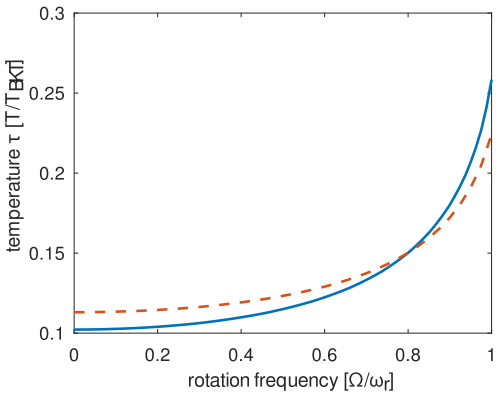



**Figure 4.5** — Temperature $\tau = T/T_{\mathrm{BKT}}$ as a function of the reduced rotation frequency $\Omega/\omega_r$ (solid blue curve). The dashed red curve indicates for reference the ratio of the temperature to the ideal BEC critical temperature $T/T_c^0$, computed using a three-dimensional semi-classical formula, for a harmonic plus quartic potential. Both curves are computed for the temperature measured in the experiment $T = 18\,\mathrm{nK}$.

We start by preparing a degenerate Bose gas of $^{87}$Rb in a dressed quadrupole trap (bubble trap) with a quadrupole horizontal magnetic gradient of $\alpha = 2\pi \times 3.97\,\mathrm{kHz/\mu m}$, rf dressing frequency of $\omega = 2\pi \times 300\,\mathrm{kHz}$ and the rf coupling $\Omega_1 = 2\pi \times 49\,\mathrm{kHz}$. The oscillation

frequencies at the bottom of the bubble trap in radial and vertical directions in the harmonic limit are: $\omega_r = 2\pi \times 34\,\text{kHz}$ and $\omega_z = 2\pi \times 360\,\text{kHz}$ which makes the cloud at the bottom of the bubble trap highly oblate in shape ($\omega_r/\omega_z = 10.5$). As explained in Chapter 3, the rf field is generated using 3 antennas with orthogonal axes controlled using the 3 outputs of the DDS source and the polarization is optimised to be circular with respect to the $z$ axis to ensure that the trap is rotationally invariant. Another output of the DDS source is used to generate an rf field to perform evaporation in the bubble trap to control the temperature and the atom number by limiting the trap depth. The initial frequency of this rf-knife is: $\omega_{\text{kn}} = 2\pi \times 80\,\text{kHz}$.

To set the atomic cloud into rotation we follow the approach of [61, 83]. We simply induce the anisotropy on a fast time scale and rotate the trap axis at a constant frequency. The transfer of angular momentum from a rotating anisotropic trap to an atomic cloud has already been investigated for dilute condensates [135, 136]. This method results in dynamic instability [137] resulting in a large deformation of a condensate which relaxes to a rotationally symmetric state containing a large vortex lattice [138, 139].

In our experiment, we first change the polarization of the rf dressing field from circular to elliptical. We do this by increasing the rf amplitude of one horizontal antenna and decreasing the amplitude of the second horizontal antenna by varying the term $\Theta$ in Eq.(2.64) and then rotate the $\Theta$ and $\Phi$ at the same time while keeping the anisotropy constant. After rotating for the desired number of turns we come back to our rotationally invariant trapping configuration by changing the polarization to circular. This way allows us to obtain a rotating superfluid at the bottom of the bubble trap. The effective rotation frequency $\Omega$ is not the same as the applied rotation frequency $\Omega_{\text{rot}}$ as in addition to its dependency on the applied rotation frequency it also depends on the duration of the rotation, the trap anisotropy and the spin-up evaporation due to rf-knife [83]. It is thus measured from a modelling and a comparison to a numerical simulation of the expansion for each experimental data [48]. We recall the expression of the trap anisotropy (see Eq.(2.72) of Chapter 2): $\epsilon_{\text{aniso}} = \frac{\sqrt{1-\eta_{\text{xy}}}}{\frac{2MgR}{\hbar\Omega_0\sqrt{1-\varepsilon^2}} - \sqrt{\eta_{\text{xy}}}}$.

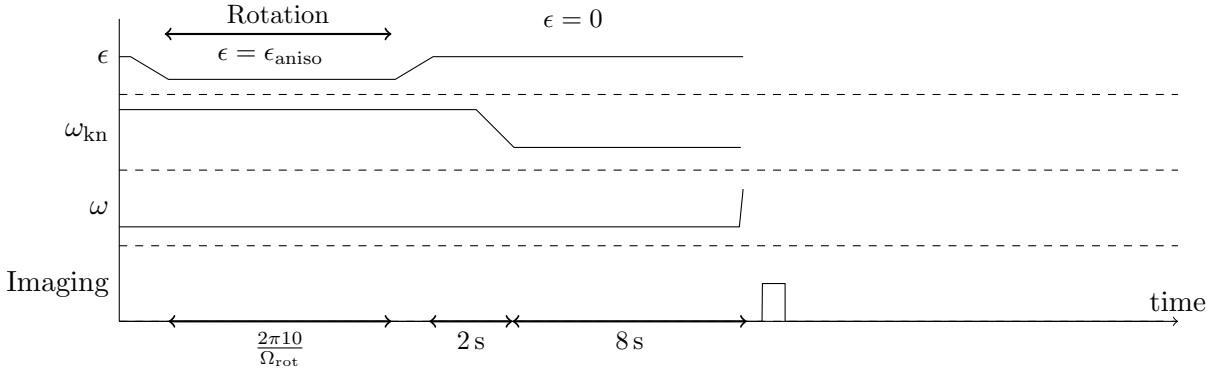



**Figure 4.6** — Experimental sequence for setting a condensate into rotation.

During the rotation procedure, see Fig.4.6, we vary $\epsilon_{\text{aniso}}$ from 0.04 to 0.2 and rotate the trap axis for 10 full turns at a frequency in the range $\Omega_{\text{rot}} \in (0.59, 0.88) \times \omega_r$. Then, we wait for 1 s, lower the rf knife frequency to $\omega_{\text{kn}} = 2\pi \times 60\,\text{kHz}$ in 1 s and wait for 8 more seconds in the trap before imaging the rotating superfluid after 27 ms of TOF expansion, following

an abrupt switch-off of the rf field and the current in the quadrupole coils. Before switching off the rf dressing field, its frequency is ramped to $\omega = 2\pi \times 340\,\text{kHz}$ in 300 µs in order to transfer the atomic cloud from the dressed state $|m = 1\rangle_\theta$ to the bare spin state $|m = -1\rangle_z$ to avoid spin separation during the TOF expansion which would result in the blurring of the vortex lattice.

After the whole procedure, we obtain $N = 10^5$ atoms with fluctuation of 10%. The final temperature is found to be almost constant ($T = 18\,\text{nK}$) for different effective rotation frequencies and is set by the final frequency of the rf-knife. The temperature is of the order of $\hbar\omega_z/k_BT$, therefore we can say that all the rotating atomic clouds are in the quasi 2D regime. We image the cloud along the vertical direction using the absorption imaging scheme (explained in Chapter 3) with a magnification of 7.8 and resolution of 4 µm. As the optical resolution is not high enough to see the vortices in situ, the TOF expansion is necessary to magnify the vortex core size to make it visible.

### 4.2.3 Spin-up evaporation

During the procedure, we note that the horizontal size of the rotating superfluid increases as the rf-knife frequency $\omega_{\text{kn}}$ decreases and this can only be explained if the evaporation induces an increase in rotation rate [83]. In order to examine the increase in rotation rate as a function of rf-knife frequency, we implement an rf evaporation ramp after the stirring process and deduce the effective rotation frequency from the size of the cloud and the number of atoms in it. To perform evaporation we add a weak rf signal on the antenna $H_3$ (see Fig. 3.11) in order to truncate the trap depth without breaking the rotational invariance such that the angular momentum is conserved. Spin-up evaporation mechanism has already been observed [130] and it is a direct consequence of the conservation of angular momentum. During the evaporation process, the rf-knife selectively evaporates the atoms with low angular momentum because the local Rabi coupling on the resonant surface is inhomogeneous, such that the trap depth is reduced for the atoms that are closer to the axis of rotation. The trap depth can be estimated from the difference between the rf-knife frequency $\omega_{\text{kn}}$ and the local Rabi coupling $\Omega_1(\mathbf{r})$:

$$\hbar\omega_{\text{trap}} = \hbar(\omega_{\text{kn}} - \Omega_1(\mathbf{r})). \tag{4.11}$$

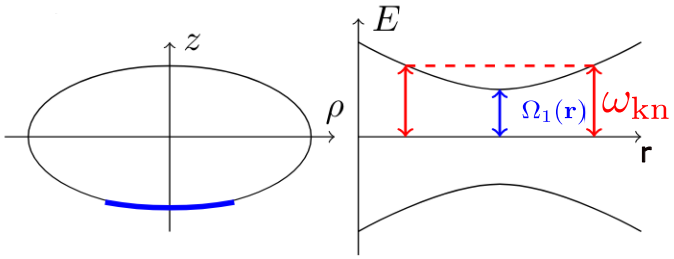



**Figure 4.7** — Left: trapped atomic cloud (in blue) at the bottom of the bubble trap undergoing an inhomogeneous Rabi coupling $\Omega(\mathbf{r})$. Right: sketch of the trap depth in the transverse direction determined by the rf-knife frequency $\omega_{\text{kn}}$ and the local Rabi coupling $\Omega_1$. The dressed state is open on both sides of the resonance due to the presence of the rf knife. Figure from [92].

Fig.4.7 shows the sketch of the adiabatic potential trap depth in the presence of the rf-knife. As the atoms with lower angular momentum are removed during the process, this results in the increase of average angular momentum per particle thus leading to the increase in rotation rate. Fig.4.8 shows that the rotation rate increases as the frequency of rf-knife decreases.

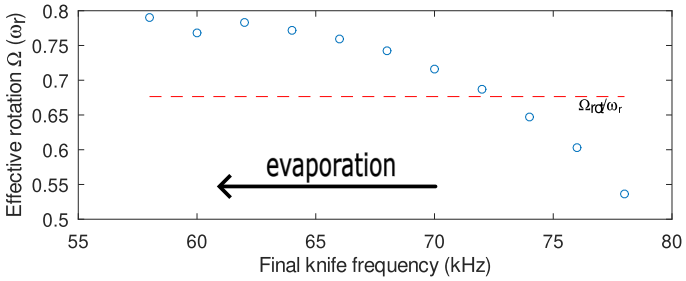



**Figure 4.8** — The plot shows the increase of the rotation rate $\Omega/\omega_r$ as the final knife frequency $\omega_{\rm kn}$ is decreased during the evaporation stage, and the dashed red line indicates the stirring frequency ($\Omega_{\rm rot}/\omega_r$) for reference.

### 4.2.4 Measurement of the effective rotation frequency $\Omega$

This section is closely based on Ref. [48] and its supplemental material. As mentioned earlier, the effective rotation frequency is not the same as the applied rotation frequency, as other factors like trap anisotropy, duration of rotation, and post-evaporation play an important role. Therefore, to calibrate the effective rotation frequency, Romain Dubessy has performed numerical simulation to compare the measured Thomas-Fermi radius after the TOF expansion with the numerically simulated in situ Thomas-Fermi radius (see supplemental material of [48]).

To simulate the in situ Thoms-Fermi radius of a quasi-2D superfluid, we use a simple growth stochastic projected Gross-Pitaevskii equation (SPGPE) [140]:

$$i\hbar\frac{\partial\psi_{\mathcal{C}}}{\partial t} = \mathcal{P}_{\mathcal{C}}\left[(1-i\gamma)\left(H_0 + g|\psi_{\mathcal{C}}|^2 - \mu - \Omega L_z\right)\psi_{\mathcal{C}} + \eta\right], \tag{4.12}$$

where $\mathcal{P}_{\mathcal{C}}$ is the projector to the relevant subspace, $\psi_{\mathcal{C}}$ is the projected wavefunction, $H_0 = -\hbar^2/(2M) \times \boldsymbol{\nabla}^2 + V_{\rm trap}(r,z)$ is the single particle Hamiltonian with $V_{\rm trap}(r,z)$ given at Eq.(4.8), $\gamma$ is a damping rate and the fluctuating field $\eta$ is characterized by its second order correlations: $\langle\eta(\boldsymbol{r},t)^*\eta(\boldsymbol{r}',t')\rangle = 2\hbar k_B T\gamma\delta(\boldsymbol{r}-\boldsymbol{r}')\delta(t-t')$. The approximate potential is separable, this allows an efficient implementation of the projector $\mathcal{P}_{\mathcal{C}}$ using a mixed Laguerre-Gauss/Gauss-Hermite basis along $r$ and $z$ respectively and an exact evaluation of the non-linear term with the appropriate quadrature [140].

We then evaluate the equilibrium state on a regular three-dimensional grid in real space and use a split-step Fourier based numerical scheme to solve the Gross-Pitaevskii equation (GPE) describing the free expansion, using scaled coordinates: $\tilde{\boldsymbol{r}} \equiv (x/\lambda_r(t), y/\lambda_r(t), z/\lambda_z(t))$, where $\lambda_r(t) = \sqrt{1+(\Omega t)^2}$ takes into account a ballistic scaling due to the rotation and $\lambda_z(t) = \sqrt{1+(\omega_z t)^2}$ reflects the fast vertical expansion. This allows us to track the full dynamics on a fixed grid of size $512 \times 512 \times 16$, despite the large magnification of all scales during the expansion. For the simulation we take $N = 10^5$ atoms, quartic correction coefficient $\lambda_{\rm quar} = 1.5 \times 10^{-4}$, rotation rate $\Omega/\omega_r = 0.9$ and temperature $T = 18\,\text{nK}$.

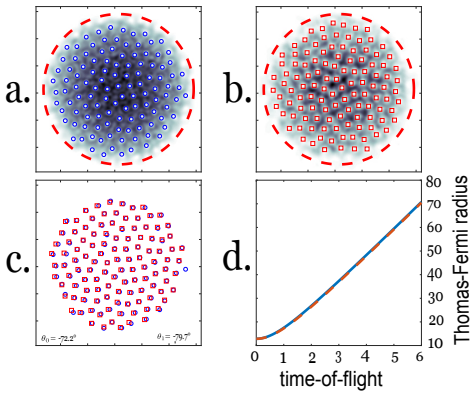



**Figure 4.9** — a) Density computed using a SPGPE simulation of the equilibrium state b) Density profile computed after a 28 ms TOF expansion. The dashed red circles identify the Thomas-Fermi radius $R_+$. In both pictures the positions of the vortices are identified with the blue circles and red squares, respectively. c) Comparison between the two vortex lattices, after scaling and rotating by an optimal angle $\theta_1$. These three images are of size $512 \times 512$. d) Evolution of the Thomas-Fermi radius during the TOF expansion simulated using the full GPE simulation (in blue line) and its comparison with the ballistic scaling (in red dashed line). Figures are in the units of µm.

Fig.4.9a) represents the in situ density profile of a quasi-2D rotating superfluid computed using the SPGPE simulation. Fig.4.9b) shows the computed density profile of a rotating quasi-2D superfluid after 28 ms of TOF expansion. The lengths are scaled by $\sqrt{1+(\Omega t_{\rm TOF})^2}$. Fig.4.9c) represents the comparison between the two vortex lattices, after scaling by $R_+^{\rm TOF}/R_+^{\rm in\,situ}$ and rotating by an optimal angle $\theta_1$ slightly smaller (in magnitude) than the naive expectation: $\theta_0 = -\arctan\left(\sqrt{1+(\Omega t_{\rm TOF})^2} \times R_+^{\rm TOF}/R_+^{\rm in\,situ}\right)$. Fig.4.9d) represents the evolution of the Thomas-Fermi radius during the TOF expansion simulated using the full GPE simulation (in blue line) and its comparison with the ballistic scaling $\sqrt{1+(\Omega t_{\rm TOF})^2}$ (in red dashed line). This simulation shows that the scaling factor is a good parameter to recover the rotation frequency, see Fig.4.9, and that the analysis of vortex positions done after time-of-flight is relevant to describe the properties of the vortex lattice before time-of-flight, once the scaling is taken into account.

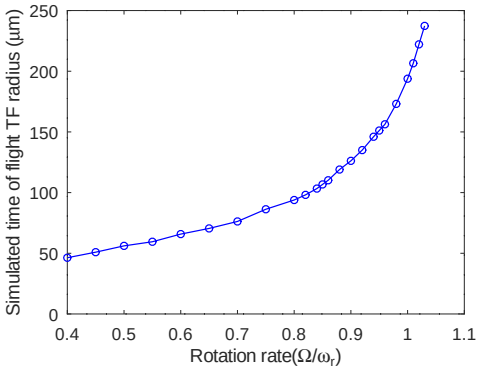



**Figure 4.10** — Simulated Thomas-Fermi radius during TOF expansion as a function of rotation rate $\Omega/\Omega_r$.

## 4.3 Detection of vortices and Delaunay triangulation

The detection of vortices and their arrangement in the density profile of a rotating superfluid is important for observing the melting scenario. Fig.4.11 represent raw density profiles as a function of rotation frequency imaged after 27 ms of TOF expansion using the vertical absorption imaging setup. We can note that as the rotation frequency increases the vortex number increases, as well as the cloud size.

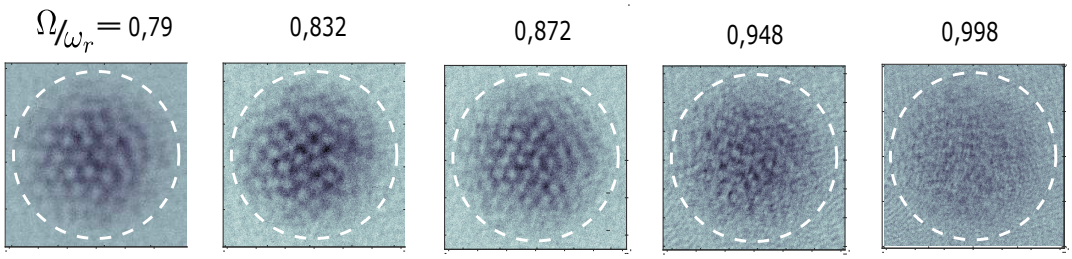



**Figure 4.11** — Density profiles of a rotating superfluid as a function of rotation frequency taken after 27 ms of TOF expansion for different values of $\Omega/\omega_r$. The white dashed circle in all the images indicates the Thomas-Fermi radius.

Once we have a density profile of a rotating superfluid, we apply the Laplacian-of-Gaussian blob detection algorithm [141, 142] on the profile in order to locate vortices. We start by filtering the experimental density data to remove imaging noise by convolving it with a Gaussian filter. The width of the Gaussian function depends on the size of the object to be detected, which is vortex cores in our case. We set it to $\sigma = 6\,\mu$m. After that, taking the Laplacian of the density profile produces a positive signal at the places where the density is minimum, which corresponds to the vortices (first column of Fig.4.12). The vortices are then detected by determining the positions of positive signals with a threshold algorithm (second column of Fig.4.12).

Now that we have detected the vortices, we would like to understand their arrangement to observe the defects mentioned in KTHNY theory, i.e., vortex sites with 5 and 7 neighbours. By looking at the arrangement of the vortices, we can discuss qualitatively the melting scenario. For this purpose, we perform a Delaunay triangulation to define the elementary cells of the lattice to label each vortex by its number of neighbours in the lattice to identify defects (last column of Fig.4.12). Delaunay triangulation is a procedure which forms triangles by mapping the connections between points such that no point lies within the circumcircle of any triangle. This procedure is effective in mapping the connection with the nearest neighbours. From this analysis, we obtain the distribution of the number of nearest neighbours to each vortex and it is done by counting the number of triangles connected to a vortex. The last column of Fig.4.12 shows the vortex sites with different numbers of nearest neighbours determined using Delaunay triangulation. The vortex sites represented in blue circles have 6 neighbours, in pink circles have 5 neighbours and those in red squares have 7 neighbours. We can note that as the rotation frequency increases, the 5 and 7-fold defects also increase thus indicating the presence of a melting scenario according to the KTHNY theory.

To discuss the melting scenario quantitatively, I will present the analysis of the characterization of the translational and the orientational order using the correlation functions defined in Sec.4.1.3.

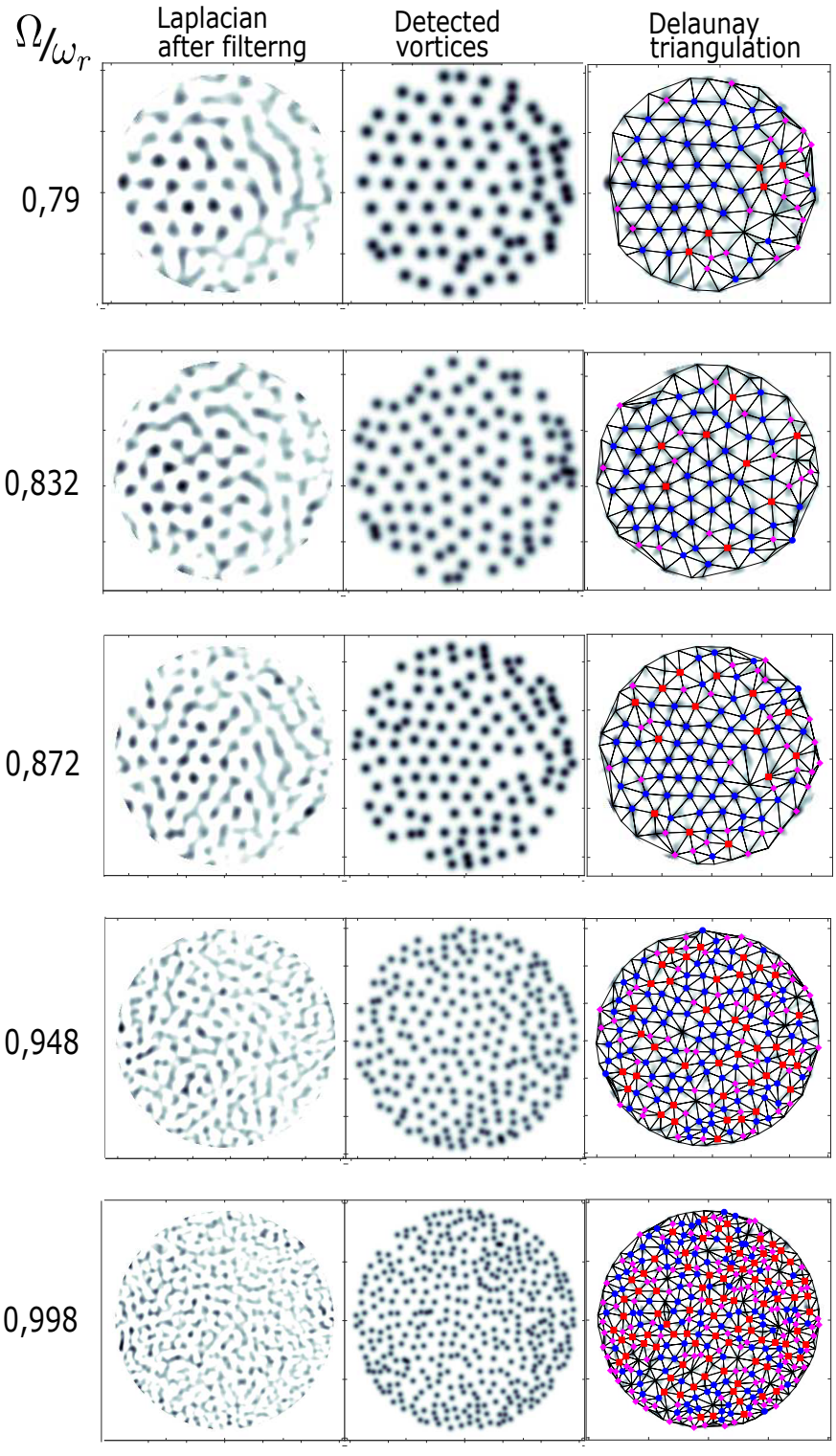



**Figure 4.12** — Automatic detection of the vortices for different rotation rates $\Omega/\omega_r$. The first column represents the Laplacian of the filtered density profiles of a rotating superfluid as a function of the rotation frequency. The second column represents the vortices detected by the algorithm for different density profiles. The third column represents the arrangement of the vortices determined using Delaunay triangulation. The blue circle vortex sites have 6 nearest neighbours, 5 nearest neighbours in pink and 7 nearest neighbours in red square.

## 4.4 Analysis of results by correlation functions

### 4.4.1 Characterization of translational order

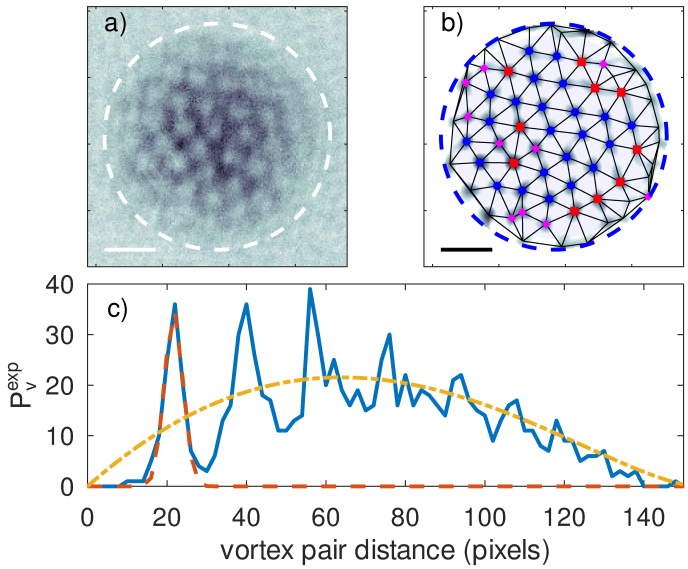



**Figure 4.13** — a) Density profile of a quasi-two-dimensional rotating superfluid imaged after 27 ms of TOF expansion, b) Delaunay triangulation performed once the vortices are detected, c) Distribution of the vortex pair distance $P_v^{\exp}(r)$ computed experimentally (blue line), Gaussian fit to the first peak (orange dashed line) and prediction of $\overline{P_v}(r)$ for a uniform vortex density $n_v$ (dashed yellow line). In a) and b) the dashed circle corresponds to the Thomas-Fermi radius and the horizontal line is a 40-pixel reference scale. Figure from [48].

To characterise the translation order of the vortex lattice using the pair correlation function defined in Sec.4.1.3.1, we compute the number of vortex pairs $P_v^{\exp}(r)$ in the experimental data separated by a distance between $r - \delta r/2$ and $r + \delta r/2$ where $\delta r = 2$ pixels. The effective size of one pixel in our vertical imaging setup is $1.03\,\mu\text{m} \times 1.03\,\mu\text{m}$. The computed $P_v^{\exp}$ presents peaks as a function of vortex pair distance which corresponds to a LRO present in the vortex lattice (blue line in Fig.4.13c). Gaussian fitting of the position of the first peak gives the mean next-neighbour distance $a$. We can compute the mean vortex density as a function of $a$ [124]:

$$n_v = \frac{2}{\sqrt{3}a^2}. \tag{4.13}$$

Now we need the number of vortex pairs $\overline{P_v}(r)$ for a uniform vortex density $n_v$, to compute the pair correlation function $g(r)$ given at Eq.(4.3). The dashed yellow line represented in Fig. 4.13c) corresponds to the number of vortex pairs $\overline{P_v}(r)$ split by distance $r \pm \delta r/2$ computed in a disk of radius $R_{\text{eff}}$ equivalent to 90% of the Thomas-Fermi radius $R_+$ of the experimental

density profile for a uniform continuous vortex density $n_v$:

$$\overline{P_v}(r) = 2\pi n_v^2 R_{\rm eff}^2 r\delta r \left[\arccos\left(\frac{r}{2R_{\rm eff}}\right) - \frac{r}{2R_{\rm eff}}\sqrt{1-\frac{r^2}{4R_{\rm eff}^2}}\right]. \tag{4.14}$$

For the detailed calculation of $\overline{P_v}(r)$ see Sec.A.1 of Appendix A.

Fig.4.14 shows the evolution of the pair correlation function $g(r)$ for increasing rotation rate. The curve represents the data averaged over at least three experimental runs, corresponding to the same rotation frequency within $\pm 1.25\%$. Also, we have to adjust the vortex density $n_v$ slightly by 24% for the large values of $\Omega$, in order to reach $g(r) \sim 1$ at large distances. The plots for the pair correlation function in Fig.4.14 for different rotation rates have been labelled as a function of corresponding values of temperature $\tau$. The data for $g(r)$ represented in Fig.4.14 have oscillation characteristics of long-range order in the sample at a small effective temperature $\tau$.

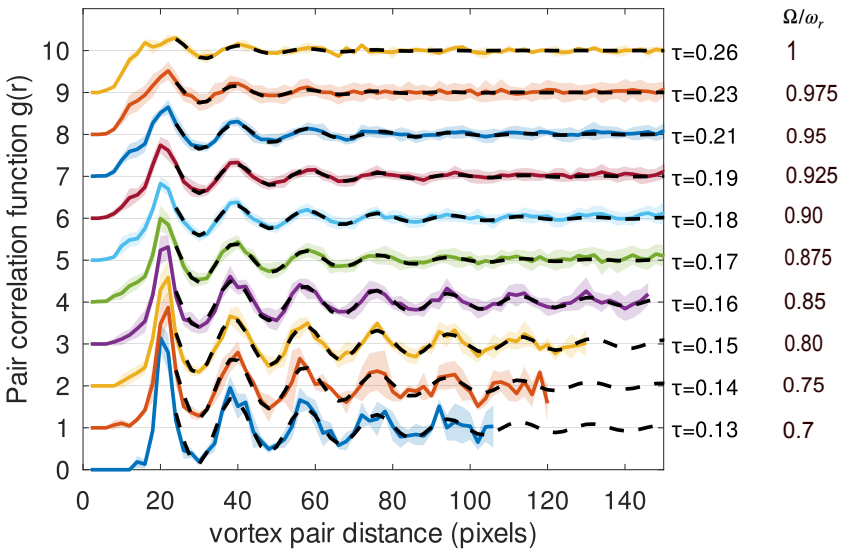



**Figure 4.14** — Pair correlation function $g(r)$ showing a loss of order for increasing rotation rate $\Omega/\omega_r = [0.70, 0.75, 0.80, 0.85, 0.875, 0.90, 0.925, 0.95, 0.975, 1.0]$, from bottom to top. The black dashed curves are the fits to the decaying oscillations. Each curve is shifted vertically by 1 for clarity, with the temperature $\tau$ indicated on the right-hand side corresponding to the respective rotation rate. The shaded areas indicate the one-sigma statistical uncertainty arising from 3 experimental realizations. Figure from [48].

The amplitude of the first peak of the oscillation decreases as the effective temperature increases and eventually disappears, probably giving the signature of a solid to liquid transition. We fit the decay of the oscillations with the following function:

$$f_g(r) = 1 + A_g \cos[kr + \delta] e^{-r/\ell_g}, \tag{4.15}$$

in order to extract the correlation length $\ell_g$ [107]. The correlation length $\ell_g$ is reduced as $\tau$ increases. We will see later if this correlation length along with the orientational correlation

length will help in determining the threshold value for the melting transition. For this purpose, I will next present the result regarding the orientational order of the vortex lattices as a function of increasing rotation rate.

### 4.4.2 Characterization of orientational order

For characterizing the orientational order of a vortex lattice, we need to compute the orientational correlation function $G_6$ defined in Sec.4.1.3.2, for the vortex pairs split by a distance $r \pm \delta r/2$. Fig. 4.15 shows the orientational correlation function computed for increasing rotation rate as a function of the vortex pair distance.

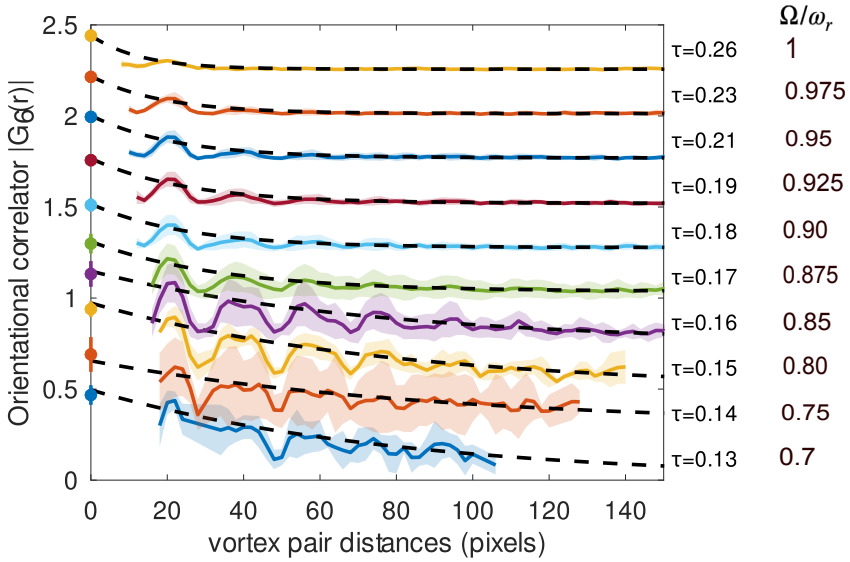



**Figure 4.15** — a) Decay of the orientational correlations $|G_6(r)|$ with the increasing rotation rate. The values for rotation rate are the same as in Fig. 4.14. Each curve is shifted vertically by 0.25 for clarity, along with the reduced temperature $\tau$ indicated on the right-hand side. The black dashed curves are fits to the envelopes by decaying exponential model (Eq.(4.16)). The shaded areas indicate the one-sigma statistical uncertainty arising from 3 experimental realizations. Figure from [48].

To deduce the nearest neighbours we used Delaunay triangulation as explained before. It is evident from Fig. 4.15 that the decay of the orientational correlation function occurs on a shorter length scale as $\Omega$ increases. We extract the correlation length $\ell_{G_6}$ by fitting the decaying envelope with the exponential function:

$$f_e(r) = A_G e^{-r/\ell_{G_6}} + B. \tag{4.16}$$

Fig. 4.16 shows the comparison between the two correlation lengths, $\ell_g$ in blue open circles and $\ell_{G_6}$ in red open squares, as a function of rotation frequency $\Omega$. We can note from Fig.4.16 that $\ell_g$ is always smaller than the typical size of the system given by the Thomas-Fermi radius and thus there is no long-range translational order in our experimental samples. On the other hand, $\ell_{G_6}$ is of the order of the Thomas-Fermi radius at a low rotation rate

($\Omega \leq 0.8 \times \omega_r$) and drops significantly for $\Omega > 0.875 \times \omega_r$. This means that at low rotation frequency, the orientational order extends over the size of the system while the translational order has already vanished. This indicates that the vortex lattice is in the hexatic phase and transitions to the liquid phase at a higher rotation rate. From the measurements, the reduced melting temperature is found to be $\tau_m = 0.16 \pm 0.1$ which corresponds to $\Omega_m/\omega_r = 0.84 \pm 0.04$ which is significantly lower than the value that we find using the prediction by Gifford and Baym, i.e., $\tau \simeq 0.5$ [126].

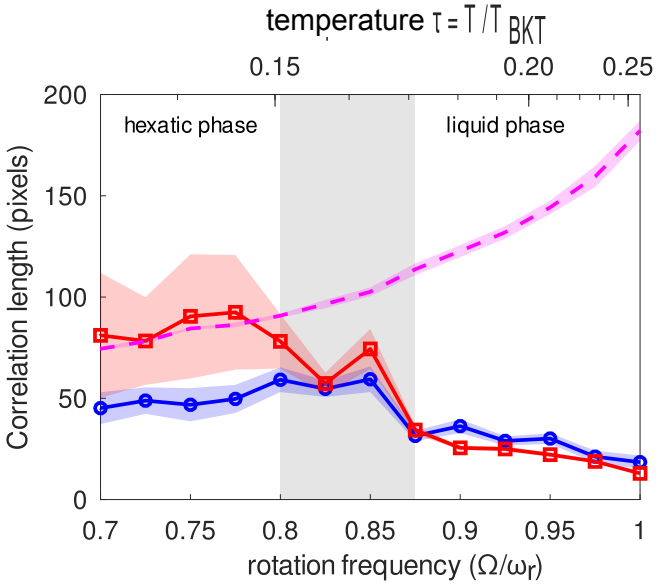



**Figure 4.16** — Correlation lengths $\ell_{G_6}$ and $\ell_g$ extracted from the fitted exponential decaying envelope of $|G_6(r)|$ (red open squares) and $g(r)$ (blue open circles), respectively, as a function of the rotation rate $\Omega/\omega_r$ (bottom axis) or temperature $\tau$ (top axis, notice the nonlinear scale). The solid lines connecting the points are guides to the eye. The light blue and red shaded area indicate the uncertainty on the values extracted from the fit. The dashed magenta line shows the Thomas-Fermi radius for each reduced rotation rate, which gives the system size. The shaded grey region indicates the crossover between the hexatic and liquid phases. Figure from [48].

Fig.4.17 represents the same data as in Fig. 4.15 using a log-log scale and compares with a fit by an algebraically decaying function. The small number of vortices also impacts the dynamical range of the signal, which saturates at long distances. We fit the data with the following model:

$$f_a(r) = C/r^{\eta_6} + D. \tag{4.17}$$

The exponent $\eta_6$ is close to 0.5 for rotation frequency $\Omega \leq 0.85 \times \omega_r$ which is significantly larger than the expected value of 0.25 at the hexatic to liquid transition. Our measurements do not clearly show a transition from an algebraic to an exponential decay and this limitation of the system comes from finite size effects and the circular boundary of the condensate itself induces defects in the lattice.

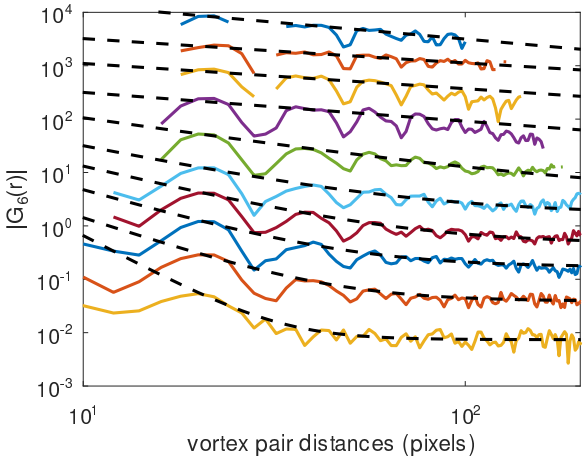



**Figure 4.17** — Decay of the orientational correlation function $|G_6(r)|$ with increasing reduced rotation frequency. The data is same as that of Fig.4.15. The dashed lines show a fit by an algebraically decaying function (Eq.4.17). The curves are shifted vertically for clarity. Figure from [48].

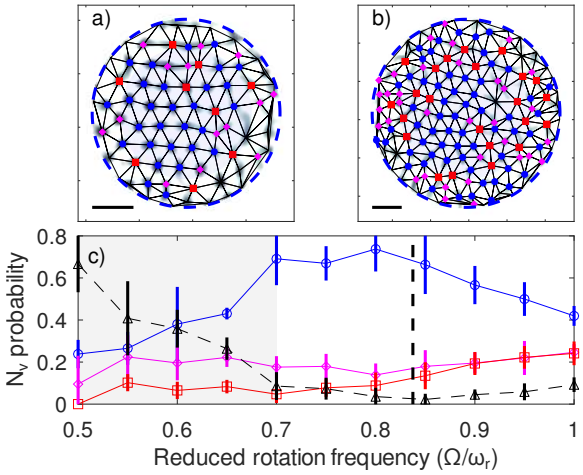



**Figure 4.18** — a) Vortex lattice for $\Omega/\omega_r = 0.76$, b) vortex lattice for $\Omega/\omega_r = 0.9$. Blue disks, magenta diamonds and red squares indicate lattice sites with 6, 5 and 7 neighbours, respectively. Horizontal black line is 40 pixels long. c) Probability of finding a vortex with $N_v$ neighbours, as a function of $\Omega/\omega_r$: blue circles $N_v = 6$, magenta diamonds $N_v = 5$, red squares $N_v = 7$ and black triangles all other values. The thick dashed vertical black line indicates $\Omega_m \simeq 0.84 \times \omega_r$. The error bars correspond to the one-sigma statistical uncertainty. Finite size effects are dominant in the light grey shaded area. Figure from [48].

To quantify the impact of finite size effects, we have examined the distribution of defects in the vortex lattice within a radius of $R_{\text{eff}} = 0.7 \times R_+$ thus avoiding the low-density region at the edge of the cloud. Fig. 4.18a) and b) represent two vortex lattices below and above

the hexatic to liquid phase transition and Fig. 4.18c) represents the probability for a site to have a given number of neighbours as a function of rotation frequency. We can note from Fig. 4.18c) that for $\Omega > 0.7 \times \omega_r$, a significant fraction of sites have either less than 5 or more than 7 neighbours. We also observe that the probability of finding sites with 5 neighbors is higher than that for sites with 7 neighbors when $\Omega/\omega_r < 0.9$. This can be attributed to vortex detection errors, where the algorithm mistakenly counts a single vortex twice if its positions are close, which leads to an over representation of 5-neighbor sites. However, the continuous increase in the probability of finding 7-neighbor sites is linked to the formation of 5-7 dislocations, whether bound or unbound, and a notable decrease in the number of sites with 6 neighbors when $\Omega > \Omega_m$. This behavior further supports a melting scenario consistent with the KTHNY theory.

## 4.5 Evidence of thermal melting through Fourier analysis

In this section, I will discuss the melting of vortex lattice through the Fourier analysis.

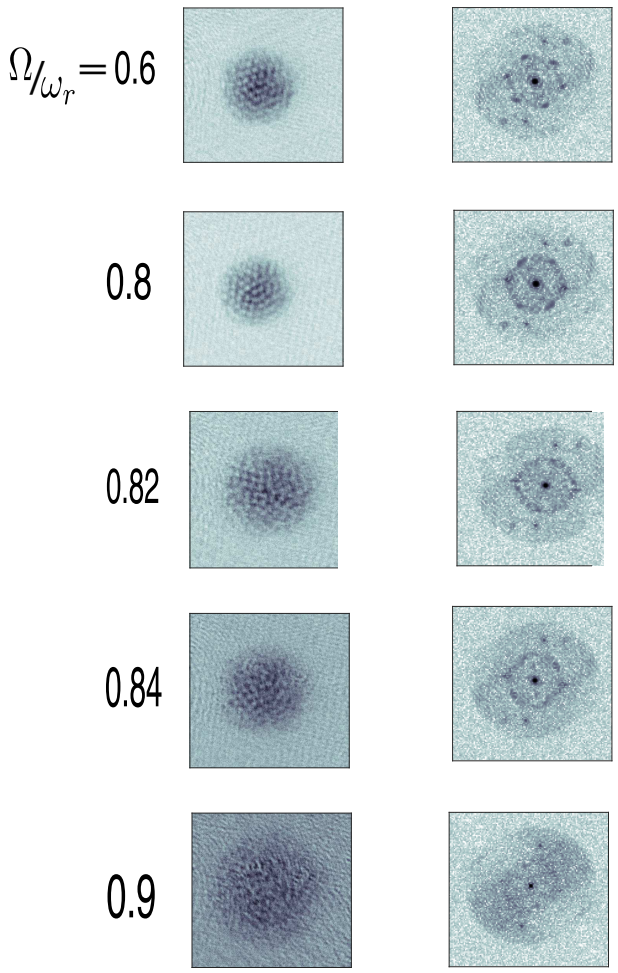



**Figure 4.19** — Images on the left column represent the density profiles of the rotating superfluid after 27 ms of TOF expansion for different values of $\Omega/\omega_r$. Images on the right column represent the 2D Fourier transform of the corresponding density profiles.

We will quantify the loss of the hexatic phase in a vortex lattice by computing the 2D Fourier transform of the experimental density profiles:

$$\tilde{n}_k(k_x, k_y) = \int dxdy \exp(-ik_x x) \exp(-ik_y y)\tilde{n}(x, y), \tag{4.18}$$

where $\tilde{n}$ is the vertically integrated density profile of the rotating condensate. Fig. 4.19 represents the density profiles of rotating superfluid images after TOF expansion along their corresponding 2D Fourier transforms for different rotation rates $\Omega/\omega_r$. We can note from the computed 2D Fourier transforms (Fig.4.19) that for low rotation frequency six individual peaks are visible which corresponds to the hexatic phase and as the rotation frequency increases, the peaks get blurred along the azimuthal direction and eventually turn into a ring resulting in the loss of both positional and angular ordering. At an even higher rotation rate as shown in Fig.4.19 for $\Omega/\omega_r = 0.9$, this ring disappears.

We can compute an average of the 2D Fourier transform over a region in $k$:

$$S(\theta) = \int_{k_1}^{k_2} dk\, \tilde{n}_k(k, \theta) \tag{4.19}$$

where $k = \sqrt{k_x^2 + k_y^2}$, $\theta = \arctan(k_y/k_x)$ and the limits of the integral are shown in Fig.4.20.

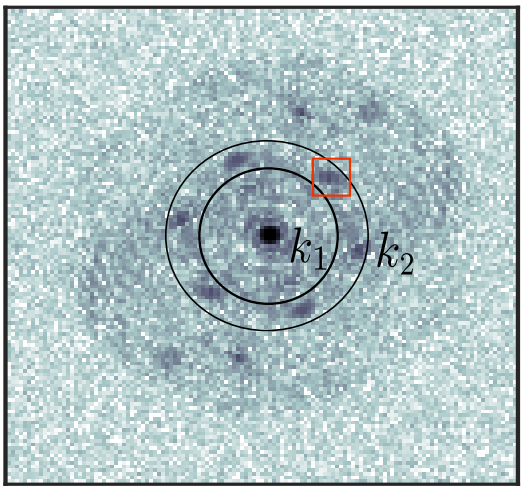



**Figure 4.20** – Figure of the 2D Fourier transform of the experimental density profile for $\Omega/\omega_r = 0.6$. The black circles indicate the limit we have used to compute the angular average and the red square indicates one of the six peaks.

By fitting the shape of one of the observed peaks in the 2D Fourier transform of the density profile (red square in Fig. 4.20) for different rotation frequencies by a square-root Lorentzian (SRL) model [113]:

$$S(\theta) = A([\theta - \theta_0]^2 + \Delta\theta^2)^{-1/2} \tag{4.20}$$

with $A$ being the amplitude, $\theta$ being the in-plane angle that varies from 0 to $2\pi$, $\theta_0$ being the position of the first peak and $\Delta\theta$ being the SRL angular width, we can show that the amplitude of the peak decreases as a function of rotation frequency.

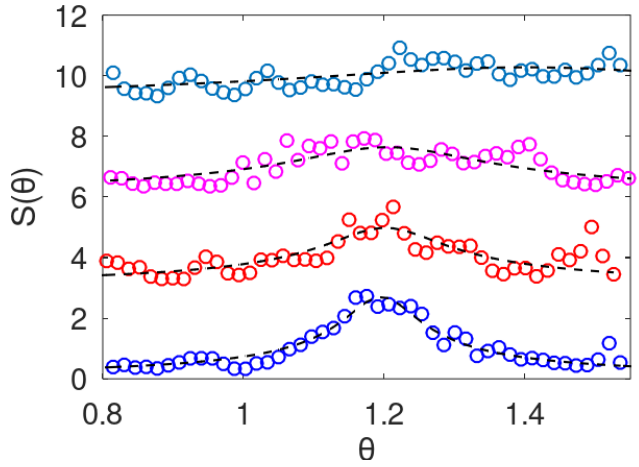



**Figure 4.21** — Angular dependence of the first peak of the 2D Fourier transform. Coloured circles correspond to the experimental data for $\Omega/\omega_r = 0.6, 0.76, 0.80, 0.90$ from bottom to top and the black dashed lines are the SRL fits. The curves are shifted on the vertical scale for clarity.

Fig. 4.21 shows the plot of the first peaks as function of $\theta$ for $\Omega/\omega_r = 0.6, 0.76, 0.80, 0.90$ from bottom to top. We can note that the peak gets blurred as the rotation frequency increases resulting in a transition from the hexatic to the liquid phase.

## 4.6 Conclusion

In this Chapter, I have presented the first observation of the thermal melting of a vortex lattice in quasi-2D rotating Bose gas. I have shown that both correlation functions (pair and orientational) evolve as the rotation frequency increases resulting in a transition from the hexatic to the liquid phase. I have also shown that the loss of orientational order and the probability of finding lattice defects display a threshold with $\Omega$ which is consistent with the KTHNY scenario. The melting in our experiment is observed at a temperature lower than the theoretical prediction [126]. There are several factors which may explain this discrepancy: firstly, our system is not exactly 2D and therefore the models should include quasi-2D corrections which account for particles in the first few vertical excited states; another factor is that the density is inhomogeneous such that we rely on local density approximation to compare to the KTHNY theory; also the vortex lattices have a finite extension and therefore the melting scenario can be affected by the boundaries and lastly the vortex lattice order may be altered by the TOF expansion. The first two factors are usually well controlled in dilute atomic superfluid and should not change the theoretical predictions. In order to study the finite size effects it would be better to repeat the experiment with large lattices or at a fixed rotation rate and varying the temperature, which is challenging in our experiment.

# Part III

# Improved experimental setup

Chapter 5

# Bose-Einstein condensation in a hybrid dimple trap

I discussed in Chapter 3 the case of the plugged quadrupole trap and I explained that the plugged quadrupole configuration was likely to cause excitation of the center-of-mass motion while transferring atoms to the bubble trap. The amplitude of the oscillations of the center-of-mass motion of the atoms in the bubble trap was around 6 µm after optimisation, as described briefly in [89]. To overcome this limitation of the plugged quadrupole trap, we decided to change the trapping configuration to the hybrid dimple trap [143] (quadrupole and red-detuned dipole trap). This trapping configuration is realised by focusing the dimple beam at a position a few tens of micrometres below the center of the quadrupole trap providing harmonic confinement for atoms along the beam direction. To create the hybrid dimple trapping configuration in our experiment, we use a CW fiber laser amplified via CW fiber amplifier from *Keopsys* delivering 5 W at 1064 nm. The laser is red-detuned with respect to the $D_1$ and $D_2$ lines of $^{87}$Rb and creates an attractive potential for the atoms. Another advantage of using a red-detuned laser rather than a blue-detuned laser is that we can work with less power and the laser is less expensive. In the hybrid dimple trap, we can perform evaporation in either of the two different ways: optical or rf evaporation. In the former case, as the intensity of the dimple beam is proportional to its power, once the atoms from the quadrupole magnetic trap are transferred to the dipole trap one can remove atoms with higher energies by lowering the potential depth of the trap by decreasing the power of the dimple beam, resulting in atoms entering the BEC phase. In the latter case, we can perform the evaporation using the rf field in the same way as described in the case of the plugged quadrupole trap.

This chapter is dedicated to the detailed description of the production of a Bose-Einstein condensate (BEC) in the hybrid dimple trap. I will provide the details of the geometry of the trap (in Sec.5.1) and its characterisation (in Sec.5.2). I will then discuss the procedure to obtain a BEC using two different evaporation methods in the hybrid dimple trap (in Sec.5.3). Sec.5.4 describes the transfer process of atoms from the hybrid dimple trap to the bubble trap depending on the type of evaporation we perform. Finally, I will present the characteristics of the atomic cloud in the bubble trap such as the lifetime of atoms in the trap and the heating rate (in Sec.5.4.3), as well as the minimization of the center-of-mass motion of the atoms in this trap (in Sec.5.4.4).

## 5.1 Hybrid dimple trap

### 5.1.1 Optical setup

In this section I will describe the experiment configuration for the hybrid dimple trap. Fig.5.1 shows the optical setup installed in order to align the dimple beam inside the science cell to create a hybrid trapping configuration for atoms. We can also note that the horizontal probe beam is aligned in the same direction as the dimple beam, i.e., along $y$ axis. We use a pockels cell from *Thorlabs* in the optical setup for the dimple beam. It provides fast and precise control of the output light's polarization direction as a function of applied voltage. We also use shutters to block the dimple beam at a given time during the experimental sequence. The two mirrors after the shutter are in two different planes and the laser beam is at the angle of 45° on both mirrors. A lens of focal length 200 mm is used to focus the dimple beam in the science cell. As the horizontal probe beam is in the same direction as the dimple beam, we use the dicroic mirrors which reflect the light at 1064 nm and let the light at 780 nm go through. The first dichroic mirror in Fig.5.1 is piezo-actuated such that we can control the position of the focus of the dimple beam in the science cell (more details in Sec.5.2.3).

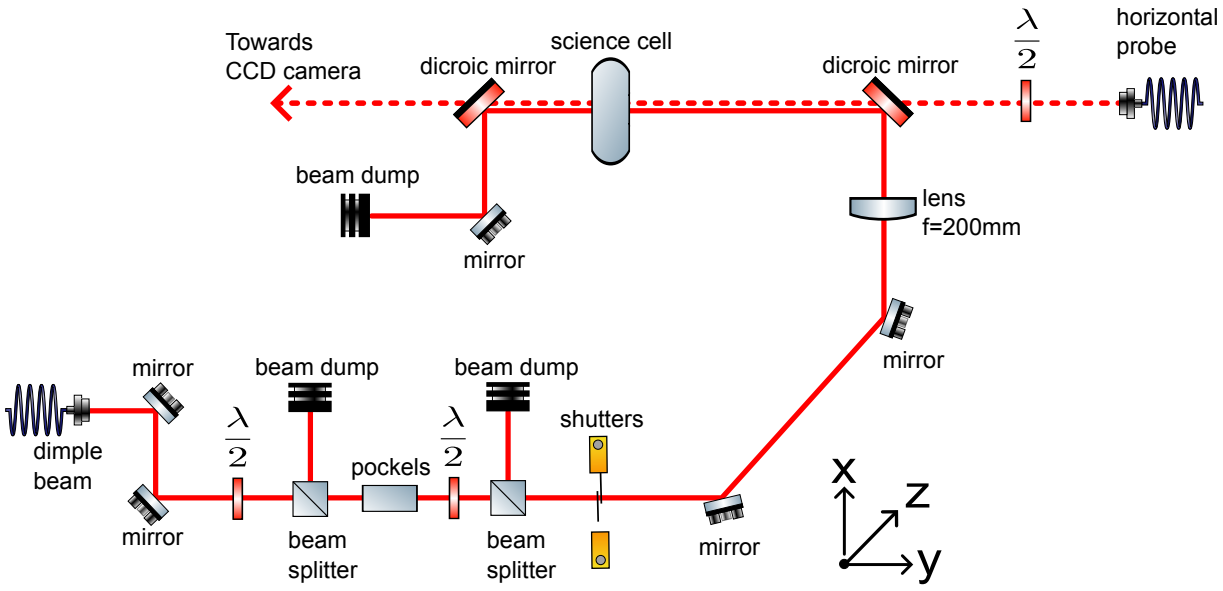



**Figure 5.1** — Design of the optical setup for dimple beam to create hybrid trapping configuration in the science cell.

The dimple beam is propagating along $y$ axis and is focused in a science cell with a waist of $\sim 70\,\mu$m. Thus the Rayleigh length is approximately 14 mm, and it is large enough such that its effect can be neglected on the trapping potential. We can therefore write the trapping potential for atoms in the hybrid dimple trap as:

$$U(r) = \hbar\alpha\sqrt{x^2+y^2+4z^2} + U_0 \exp\left[-2\frac{x^2}{w_x^2} - 2\frac{(z-z_c)^2}{w_z^2}\right] + Mgz. \tag{5.1}$$

In this expression, the first term corresponds to the magnetic quadrupole trap, the second term to the optical dipole potential, and the last one to the gravity. $\alpha$ is the magnetic

gradient in units of frequency for atoms in the electronic ground state $F = 1$, $w_x$ and $w_z$ are beam waists in the direction $x$ and $z$, $M$ is the atomic mass of $^{87}$Rb, $U_0 < 0$ is the dipole trap depth directly proportional to the power of dipole laser and inversely proportional to the product of waists in the $x$ and $z$ directions respectively ($U_0 \propto \frac{P}{w_x w_z}$), $z_c$ is the position of the focus of dimple beam below the quadrupole trap center (0,0,0) and $g$ is the acceleration due to earth's gravity.

### 5.1.2 Thermodynamic properties

Before discussing the production of BEC in the hybrid dimple trap, I will first provide a brief description of the thermodynamics of atoms in this trap. This will also help us to understand the cooling process in the trap. Given the potential for atoms in equation (5.1), we can express the effective trap volume [143] as a function of temperature using the equation:

$$V_0(T) = \int \exp\left[-\frac{U(r) - U_{\text{eq}}}{k_B T}\right] d^3r \tag{5.2}$$

where $U_{\text{eq}} = U(0, 0, z_{\text{eq}})$ is the minimum of the trap potential at the position $z_{\text{eq}}$. We will later use this position $z_{\text{eq}}$ as an intermediate point to characterise the other parameters of the dimple beam.

For a pure magnetic quadrupole trap, we have seen that we can approximate the potential $U(\mathbf{r})$ as:

$$U(\mathbf{r}) = \hbar\alpha\sqrt{x^2 + y^2 + 4z^2} + Mgz. \tag{5.3}$$

By inserting equation (5.3) in equation (5.2), we can calculate the effective volume as follows:

$$V_0(T) = \int \exp\left[-\frac{\hbar\alpha\sqrt{x^2 + y^2 + 4z^2} + Mgz}{k_B T}\right] d^3r. \tag{5.4}$$

By transforming the cartesian coordinates to spherical coordinates we get the following integral :

$$V_0(T) = \frac{1}{2}\int_0^\infty \int_0^\pi \int_0^{2\pi} \exp\left[-\frac{\hbar\alpha r + Mgr\cos\theta/2}{k_B T}\right] r^2 \sin\theta dr d\theta d\phi.$$

By first integrating on $\phi$ and $\theta$ we get the following expression:

$$V_0(T) = \frac{2\pi k_B T}{Mg}\int_0^\infty r^2 \exp\left[-\frac{\hbar\alpha r}{k_B T}\right]\left[\exp\left[\frac{Mgr}{2k_B T}\right] - \exp\left[-\frac{Mgr}{2k_B T}\right]\right] dr.$$

After computing the integral on $r$, we finally get the expression for the effective trap volume in the pure quadrupole case:

$$V_0(T) = \frac{4\pi}{(1-\varepsilon^2)^2}\left[\frac{k_B T}{\hbar\alpha}\right]^3 \tag{5.5}$$

where $\varepsilon$ is the gravitational sag parameter defined by Eq.(2.60) in Chapter 2. This formula for the effective volume provides a good approximation at high temperature $T \gg |U_0|/k_B$ for a quadrupole trap, when the quantum gas explores a large fraction of the potential.

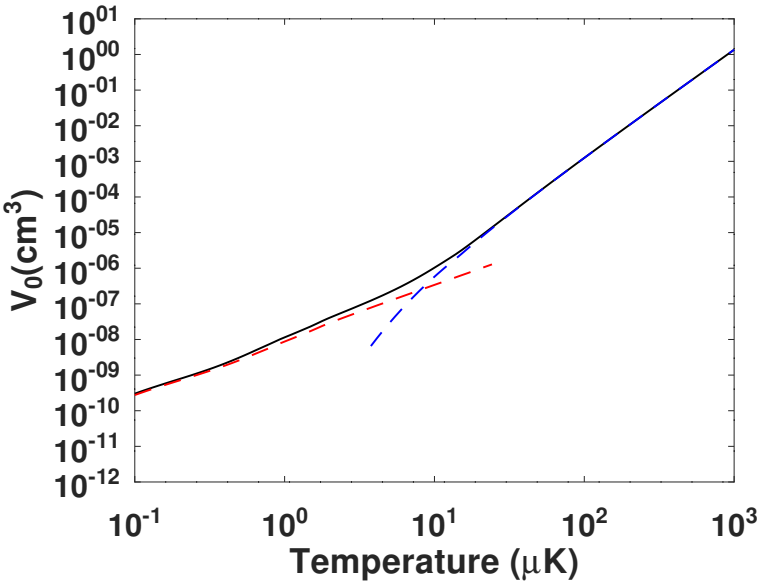



**Figure 5.2** — Numerically simulated volume of the hybrid dimple trap as a function of temperature. The black line plot corresponds to the total volume of the hybrid dimple trap. The blue dashed line plot corresponds to the volume using the quadrupole approximation. The red dashed line corresponds to the volume under pure harmonic approximation. For the numerical calculation, I used : $\alpha = 2\pi \times 4.14\,\mathrm{kHz\mu m^{-1}}$, $U_0/k_B = 20\,\mu\mathrm{K}$ and the beam waist along $x$ direction is 72.2 µm and along $z$ direction is 61.3 µm.

We can also compute analytically the effective volume for a pure harmonic trap:

$$U(\mathbf{r}) = \frac{1}{2}[M\omega_x^2 x^2 + M\omega_y^2 y^2 + M\omega_z^2 (z - z_{\mathrm{eq}})^2]. \tag{5.6}$$

We get:

$$V_0(T) = \int \exp\left[-\frac{(M\omega_x^2 x^2 + M\omega_y^2 y^2 + M\omega_z^2 (z - z_{eq})^2)}{2k_B T}\right] d^3 r.$$

Solving this integral results in the following expression:

$$V_0(T) = \left(\frac{2\pi k_B T}{M\overline{\omega}^2}\right)^{3/2}, \tag{5.7}$$

where $\overline{\omega} = (\omega_x \omega_y \omega_z)^{1/3}$. This formula of the effective volume provides a good approximation for the hybrid trap at low temperature when the gas is confined close to the minimum.

Fig.5.2 shows the effective trap volume as a function of the temperature and we can note that the volume at high temperature is in agreement with the total volume down to temperatures of order $U_0/k_B$.

From the volume we can determine the thermodynamic properties of our trapped gas. To do so we will first compute the partition function as :

$$\zeta(T) = \frac{V_0(T)}{\lambda_{\mathrm{T}}^3} \tag{5.8}$$

where $V_0(T)$ is the effective volume and $\lambda_T = \sqrt{2\pi\hbar^2/Mk_BT}$ is the thermal de-Broglie wavelength. By using $\zeta$, we can calculate the free energy:

$$F = -Nk_BT \ln \zeta, \tag{5.9}$$

and the peak phase-space density (PSD):

$$D = N/\zeta. \tag{5.10}$$

From the effective volume $V_0(T)$, we also get the density distribution:

$$n(r) = n_0 \exp\left[-\frac{U(r)}{k_BT}\right] = \frac{N}{V_0(T)} \exp\left[-\frac{U(r)}{k_BT}\right]. \tag{5.11}$$

We can also express entropy as:

$$S = -\partial F/\partial T. \tag{5.12}$$

Inserting equation (5.9) in equation (5.12) and solving it will lead to the following expression:

$$\frac{S}{Nk_B} = \ln \zeta + \frac{3}{2} + \frac{\overline{U}}{k_BT} \tag{5.13}$$

where $\overline{U} = \int d\mathbf{r}(U(\mathbf{r}) - U_{\text{eq}}) \exp(-(U(\mathbf{r}) - U_{\text{eq}})/k_BT)/V_0(T)$ is the average potential energy.

In the expression of free energy, peak phase-space density and the density distribution "$N$" refers to the total atom number. We can also compute the mean elastic collision rate as:

$$\Gamma_{\text{el}} = \frac{4}{\sqrt{\pi}} \overline{n} \sigma_{\text{el}} v_0 \tag{5.14}$$

where $\sigma_{\text{el}}$ is the effective elastic cross-section, $v_0 = \sqrt{k_BT/M}$ and $\overline{n} = \int \frac{n(r)^2}{N} d^3r$ is the average density which can be written as:

$$\overline{n} = \frac{N}{V_0(T)^2} \int \exp\left[-2\frac{U(r) - U_{\text{eq}}}{k_BT}\right] d^3r. \tag{5.15}$$

Considering Eq.(5.2) we can replace the integral part in Eq.(5.15) as:

$$\int \exp\left[-2\frac{U(r) - U_{\text{eq}}}{k_BT}\right] d^3r = V_0(T/2). \tag{5.16}$$

The final expression for average density $\overline{n}$ is thus:

$$\overline{n} = \frac{N}{V_0(T)^2} V_0(T/2). \tag{5.17}$$

Inserting this expression of $\overline{n}$ in Eq.(5.14) and replacing $\frac{4}{\sqrt{\pi}} v_0$ by $\overline{v}$, we get:

$$\Gamma_{\text{el}} = \sigma_{\text{el}} \overline{v} \frac{N}{V_0(T)^2} V_0(T/2). \tag{5.18}$$

This rate helps us to understand better the evaporation as if $\Gamma_{\text{el}}$ is very small as compared to the background gas collisions then the atoms will not thermalise. The typical collision rate for evaporative cooling in ultracold atom experiments is of the order of $100\,\text{s}^{-1}$. Now as I have introduced some important thermodynamic formulations necessary to understand the trap mechanism, I will now discuss the characterisation of the hybrid dimple trap.

## 5.2 Characterisation of the hybrid dimple trap

To fully characterise the hybrid dimple trap, we need to deduce the following quantities: the waists in the transverse plane of the dimple beam $w_x$ and $w_z$ assuming the beam is not perfectly isotropic at the position of the atoms, the position $z_c$ of focus with respect to the center of the qaudrupole trap $(x_c = 0, y_c = 0, z_c)$[1], the oscillation frequencies of the trap and the position of the minimum of the potential of the trap $z_H$. The quantities like the position of the minimum of the potential $z_H$ and the oscillation frequencies $(\omega_x, \omega_y, \omega_z)$ of the trap can be deduced from four independent measurements (Sec.5.2.4 and 5.2.5). The waists and the position of focus of the dimple can be calculated once we have deduced the oscillation frequencies and the position of the minimum of the trapping potential.

The main objective of the experiment is to produce the BEC in a hybrid dimple trap and then transfer it from the hybrid dimple trap to the bubble trap (Fig.5.3). Therefore, the dimple beam has to be focused below the quadrupole magnetic trap at a position very close to the bottom of the bubble trap in order to limit the excitations of the center of mass motion of the atoms during the transfer process.

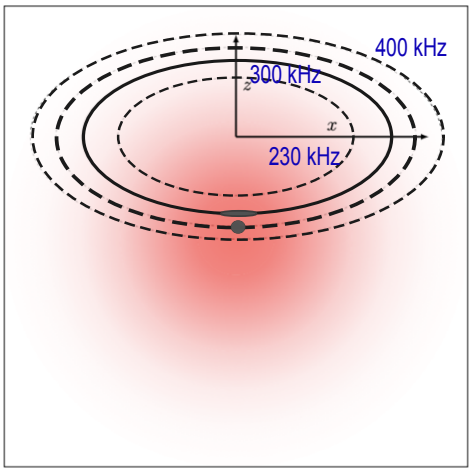



**Figure 5.3** — Transfer of the quantum gas from the hybrid trap (cloud represented with a lower grey dot) to the bubble trap (represented with a grey ellipse). The $x$ and $z$ axes are centered to the zero of the magnetic quadrupole trap. The dimple laser is represented as well at the isomagnetic surfaces corresponding, from outermost to innermost, to the end of the rf evaporation at 400 kHz, the center of the hybrid trap, the final shell (represented with a full black line) at 300 kHz and the initial rf frequency of the loading ramp at 230 kHz. Figure from [49].

### 5.2.1 Position of the focal point $z_c$

In the experiment, we only know approximately the position of the focus while we can measure the position of the trapped gas $(z_H)$. We will thus use the position of the minimum of the trap $z_H$ as an intermediate value in order to find the exact position of the focus $z_c$ of the

1. The magnetic trap ensures the position of the center of the trap along the $y$-axis ($y_c = 0$) as the force exerted by the dimple beam along this direction is negligible and we can also assume a perfect alignment of the dimple beam below the center of the quadrupole which ensures $x_c = 0$ (Sec.5.2.3).

dimple beam. To find the position of the focus $z_c$, we start by expressing, for a well-centered dimple beam, the potential along the $z$-axis as:

$$U(0,0,z) = 2\hbar\alpha|z| + Mgz - |U_0| \exp\left[-2\frac{(z-z_c)^2}{w_z^2}\right]. \tag{5.19}$$

We know that the minimum of the potential lies in the region $z < 0$, such that we can write $2\hbar\alpha|z| = -2\hbar\alpha z$. Assuming that $|U_0| > 2\hbar\alpha|z_c|$, the position $z_H$ can be determined by writing $\frac{dU(z_H)}{dz} = 0$:

$$-2\hbar\alpha + Mg + 4\frac{z_H - z_c}{w_z^2}|U_0| \exp\left[-2\frac{(z_H-z_c)^2}{w_z^2}\right] = 0, \tag{5.20}$$

$$2\hbar\alpha(1-\varepsilon)\frac{w_z^2}{z_H - z_c} = 4|U_0| \exp\left[-2\frac{(z_H-z_c)^2}{w_z^2}\right]. \tag{5.21}$$

Assuming $|z_H - z_c| \ll w_z$, we get:

$$z_c \simeq z_H - w_z^2 \frac{\hbar\alpha}{2|U_0|}(1-\varepsilon). \tag{5.22}$$

### 5.2.2 Oscillation frequencies

We can also relate the oscillation frequencies to the trap parameters by doing a second-order expansion of Eq.(5.1) as:

$$M\omega_y^2 = \frac{\partial^2 U}{\partial y^2}(0,0,z_H) = \frac{\hbar\alpha}{2|z_H|}, \tag{5.23}$$

$$M\omega_x^2 = \frac{\partial^2 U}{\partial x^2}(0,0,z_H) = \frac{\hbar\alpha}{2|z_H|} + \frac{4|U_0|}{w_x^2}, \tag{5.24}$$

$$M\omega_z^2 = \frac{\partial^2 U}{\partial z^2}(0,0,z_H) = \frac{4|U_0|}{w_z^2}\left[1 - \frac{\hbar^2\alpha^2 w_z^2(1-\varepsilon)^2}{|U_0|^2}\right]. \tag{5.25}$$

As we can directly measure the oscillation frequencies of the trap, these frequency-dependent equations will help determine the waists of the dimple beam.

All the formulas defined in Sec.5.2 assume that the dimple beam is well centered on the vertical axis, i.e., $x_c = 0$. Therefore in the next section, I will present the procedure followed to perfectly align the dimple beam with respect to the center of the quadrupole trap.

### 5.2.3 Alignment of the dimple beam

To perfectly align the dimple beam below the center of the quadrupole trap in order to ensure $x_c = 0$, we followed a two-step alignment procedure. Firstly, as the position of the dimple beam in the $(x, z)$ plane is controlled by a piezo-actuated mirror with a sensitivity of about $0.8\,\mu\mathrm{mV}^{-1}$ and as the dimple beam is colinear with our absorption imaging beam, we used a weak leak of the dimple beam through a dichroic filter to directly image its in situ position and perform a first rough alignment, limited by the optical resolution and aberrations. In a second fine alignment step, we use directly the atoms. We apply an rf-field at frequency

$\omega/(2\pi) = 400\,\text{kHz}$, strong enough to dress the atoms with Rabi coupling of $\Omega_0/2\pi = 50\,\text{kHz}$, and we record the atom losses induced by a full spin flip to the state $F = 1$, $m_F = 1$, in which atoms are expelled away from $y = 0$. This occurs when the Zeeman splitting between the sub-levels of the $F = 1$ manifold at the position of the atoms is resonant with the rf field. By moving around the dimple beam we were able to locate precisely the resonant ellipsoid $\alpha\sqrt{x^2 + y^2 + 4z^2} = \omega$ and position the beam center with respect to the magnetic field. Fig.5.4 represents two diagrams depicting the position of the dimple away from and close to the isomagnetic surface corresponding to the rf frequency of 400 kHz. This figure illustrate that as the dimple is focused outside the resonance surface we do not observe any atom loss but as the dimple beam approaches the resonant surface we start to observe atom losses.

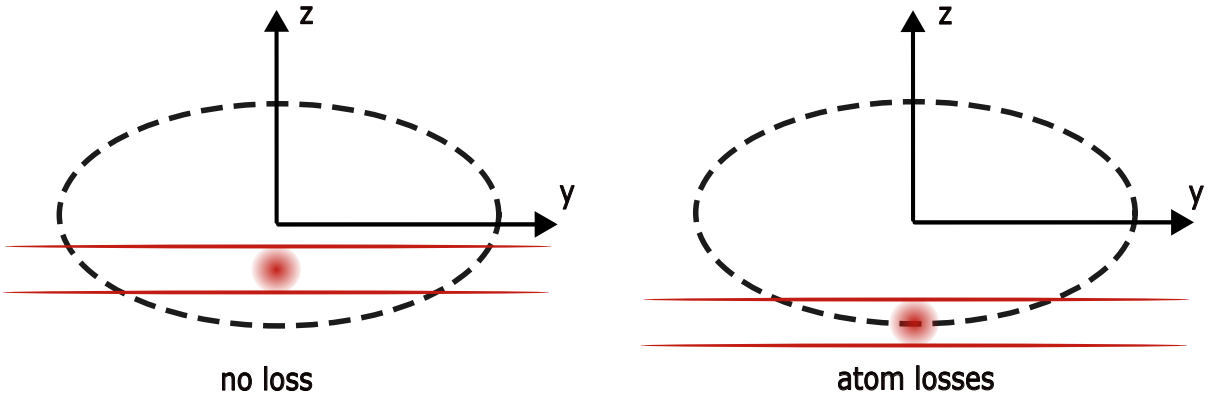



**Figure 5.4** — Isomagnetic surface corresponding to an rf frequency of 400 kHz along with the dimple beam propagating along the $y$-axis. When the beam is focused outside the resonance surface we observe no loss but as the position of the atoms becomes resonant with the rf field we observe atom losses.

### 5.2.4 Experimental determination of $z_H$

By doing the direct measurement of the oscillation frequency along the longitudinal direction ($\omega_y$), we can determine the position $z_H$ using the equation (5.23). However, taking into account only the linear Zeeman splitting as the local magnetic field is weak ($\sim 0.5\,\text{G}$) and differential light shifts from the dimple beam are completely negligible (of the order of a few Hz), it is more accurate to deduce $z_H$ from an rf spectroscopy measurement of the value of the linear Zeeman splitting in the quadrupole at equilibrium :

$$\omega_0 = 2\alpha|z_H|. \tag{5.26}$$

The value of $\omega_0$ is deduced from an rf-spectroscopy measurement. We shine a weak rf probe field during 500 ms onto the atoms inside the hybrid trap and scan the rf-frequency. The weak rf field only couples the trapped $m_F = -1$ state to the trapped $m_F = 0$ state contrary to the procedure implemented to align the dimple beam using a strong field (explained in Sec.5.2.3). Therefore, we do not observe strong atom losses but a heating, when reaching the resonance. This mechanism can be understood as an anti-evaporation mechanism, i.e., at resonance, the rf-field removes the coldest atoms from $m_F = -1$ and the remaining atoms are thermalised to a higher temperature. The atoms transferred to $m_F = 0$ remain trapped

but they can explore a much larger volume in the $y$ direction where the weak confinement is only due to the focusing of the dimple beam.

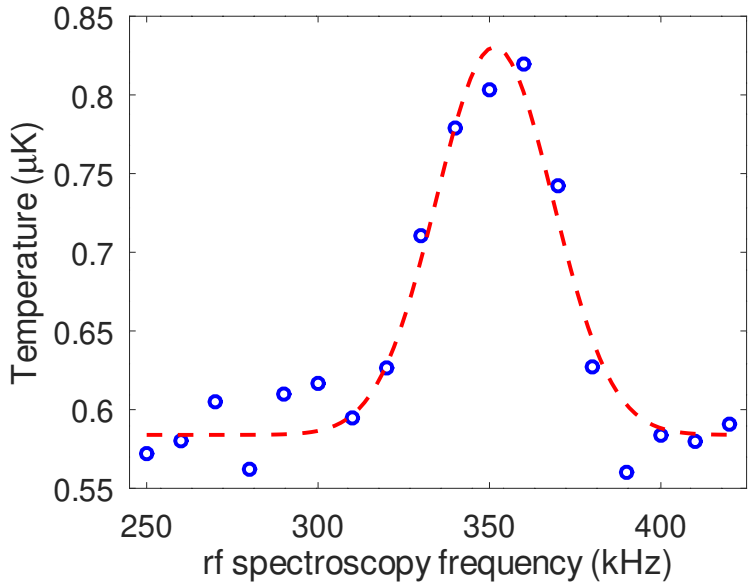



**Figure 5.5** — Temperature of the atomic cloud in the hybrid dimple trap as a function of the frequency of the weak rf probe. The dashed red line is a fit with a Gaussian model of the resonant behaviour.

Figure 5.5 shows such a measurement where we can clearly observe the resonance in temperature while the atom number remains constant at $N = 2.1(2) \times 10^5$. By fitting the resonance with a Gaussian fit, we obtain $\omega_0/(2\pi) = 351.5(12)\,\mathrm{kHz}$. The value of $\alpha/(2\pi)$ is $4.14\,\mathrm{kHz\mu m^{-1}}$. This gives the position of the trap minimum $z_H = -42.5(8)\,\mu\mathrm{m}$ (using equation 5.26).

### 5.2.5 Measurements of the oscillation frequencies

Now as we know the value of $z_{\mathrm{eq}}$, we can deduce directly the oscillation frequency in the $y$ direction using the equation (5.23) as, $\omega_y = \sqrt{\frac{\hbar\alpha}{2M|z_H|}} = \alpha\sqrt{\frac{\hbar}{M\omega_0}} = 2\pi \times 75.4\,\mathrm{Hz}$. This is in agreement with the experimental measurement of the oscillation frequency in the $y$ direction as shown in Fig.5.6.

To perform this measurement of the oscillation frequency in the $y$ direction, we modulate the current $I$ of the compensation coil along the $y$-axis with some modulation frequency $F_{\mathrm{mod}}$. This current modulation induces a position modulation of the trap minimum along the $y$-axis, resulting in the excitation of the atomic cloud in this direction. We impose the following modulation : $I(t) = I_0(1 + A_{\mathrm{mod}}\sin(2\pi F_{\mathrm{mod}}t))$ for 200 ms. Here, $I_0$ is the average current, $A_{\mathrm{mod}} = 0.05\%$, is the amplitude of the modulation. After 100ms of holding time, during which the atoms thermalise and the excitation is converted into heating, we release the trap and observe the temperature of the atom cloud as a function of the excitation frequency. We obtain the data shown in open blue circles in the figure 5.6. After fitting this data with a Gaussian function, we obtain a frequency of oscillation $\omega_y = 2\pi \times 75(1)\,\mathrm{Hz}$.

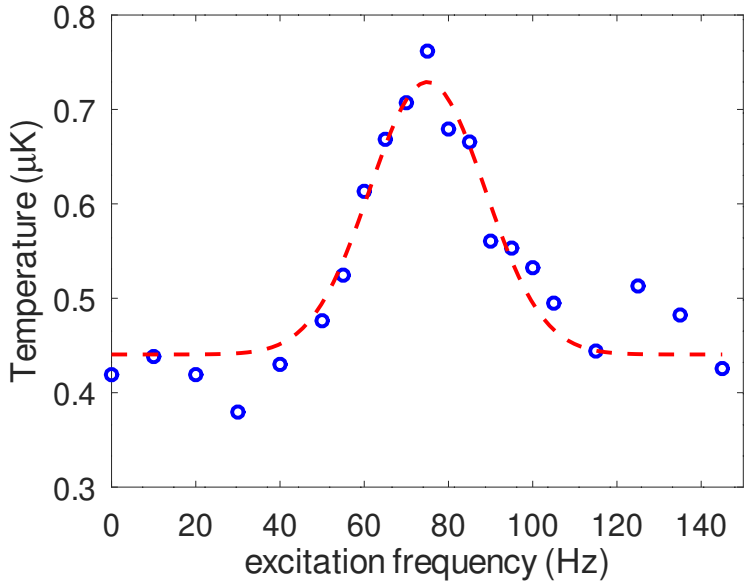



**Figure 5.6** — Temperature of the atomic cloud as a function of the excitation frequency in open blue circles. The experimental data is recorded after 23 ms of time-of-flight expansion and the dashed red line is a Gaussian fit to the data yielding $\omega_y = 2\pi \times 75(1)$ Hz.

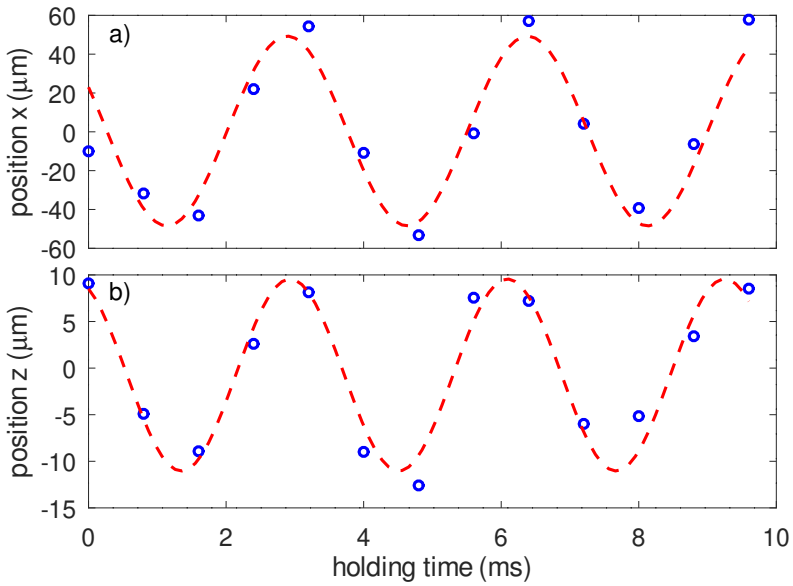



**Figure 5.7** — Open blue circles: dipolar oscillations of the center-of-mass of the atoms in the hybrid dimple trap a) along the $x$-axis and b) along the $z$-axis after excitation. The data is recorded after a 23 ms time-of-flight expansion. For both a) and b) the dashed red line is a sinusoidal fit to the experimental data. We find $\omega_x/(2\pi) = 286.1(69)$ Hz and $\omega_z/(2\pi) = 316.5(51)$ Hz.

The excitation performed on the atoms in the trap to determine the oscillation frequencies in the $x$ and $z$ directions was done in a different way. To excite the atoms along the $x$ direction,

we first increased the current of the compensation coil along the $x$-axis to 120% of its initial value in 50 ms, which displaces the trap center along $x$, and came back to the initial value of the current of the same compensation coil 1000 times faster, i.e., 0.05 ms. This sudden change in the trap minimum position in the $x$ direction excites the atoms and we record the position of the cloud center-of-mass as a function of holding time. The same technique was applied on the compensation coil in the $z$-axis to excite the system along the $z$ direction and we record again the position of the cloud center-of-mass as a function of holding time (see figure 5.7).

Figure 5.7a) and b) shows the measurement of the dipolar oscillations along the $x$ and $z$-axis, respectively. The sinusoidal fit to the data gives us the two oscillation frequencies $\omega_x/(2\pi) = 286.1(69)$ Hz and $\omega_z/(2\pi) = 316.5(51)$ Hz.

As we have deduced the oscillation frequencies of the trap and the position of the minimum of the trapping potential, we can now compute the position of the focus of the dimple beam along the $z$ axis ($z_c$) and the waist of the dimple beam.

### 5.2.6 Position of the focus of the dimple beam ($z_c$) and its waist

In order to deduced the waists along $x$ and $z$ direction we first replace $U_0$ in Eq (5.24) and (5.25) by the following expression:

$$U_0 = \frac{\chi P}{w_x w_z} \tag{5.27}$$

where $P$ is the power of the dimple beam incident on the atoms and $w_x$ and $w_z$ are the two waists and $\chi = \frac{3\pi c^2}{\omega_0^3}\frac{\Gamma}{\Delta_{\text{eff}}}$, where c is the speed of light, $\omega_0$ is the frequency of the $D_2$ line of $^{87}$Rb, $\Gamma$ is the linewidth and $\Delta_{\text{eff}} = \left(\frac{1}{3}\left(\frac{1}{\Delta_1} + \frac{2}{\Delta_2}\right)\right)^{-1}$ is the effective detuning of dimple laser from the $D_1$ and $D_2$ lines of the $^{87}$Rb. Finally, we apply the least square fitting procedure on Eqs.(5.24) and (5.25). The two waists are found to be $w_x = 72.7(17)$ µm and $w_z = 61.3(11)$ µm. For the experiment, we used $P = 1.92$ W for the dimple beam. We can thus finally deduce the trap depth $|U_0| = k_B \times 41.8$ µK using the equation (5.27). We finally get the value of $z_c = -49.3(11)$ µm using the Eq.(5.22).

## 5.3 Production of the condensate in a hybrid dimple trap

The experimental sequence used to produce the BEC in a hybrid dimple trap is the same as that of the plugged trap up to the decompression phase after the first part of rf evaporation (explained in Sec.3.4 in Chapter3). In this section, I will describe the experimental sequence after the first part of the rf evaporation.

### 5.3.1 Transfer to the hybrid trap and final evaporative cooling

Here, I will focus on describing the transfer of atoms from the quadrupole to the hybrid dimple trap and the two possible methods to perform the final evaporative cooling (rf and optical) on the trapped atoms in order to reach the condensation. I will first start with the rf evaporation, it is less complex than optical evaporation in terms of transferring the atoms in the final bubble trap. However, the latter turns out to be a more effective method in terms of having more condensed atoms in the trap.

To perform the final evaporation cooling we turn on the dimple beam 3.4 s after the initiation of the first rf evaporation and we ramp its power from zero to maximum (2.73 W) in 500 ms. The beam is sent through the science cell and is focused at around $\simeq 50\,\mu$m below the center of the quadrupole trap creating a hybrid trapping configuration for the atoms.

### Rf evaporation

To perform rf evaporation we first ramp down the power of the dimple beam from maximum (2.73 W) to 1.92 W to limit the scattering of spontaneous photons:

$$\Gamma_{\rm sc} = \frac{\Gamma^2}{\Delta_{\rm eff}^2}\frac{3c^2}{\hbar\omega_{\rm eff}^3}\frac{P}{w_x w_z} \tag{5.28}$$

with $\omega_{\rm eff} = (\omega_1 + 2\omega_2)/3$ and $\omega_{1,2}$ are the frequencies of the $D_{1,2}$ lines of $^{87}$Rb. $\Gamma_{\rm sc} = 0.15\,{\rm s}^{-1}$ for a power of 1.92 W and the waists given in Sec.5.2.6. A cut of the potential $V(0,0,z)$ along the $z$-axis with these parameters is represented in Fig.5.8.

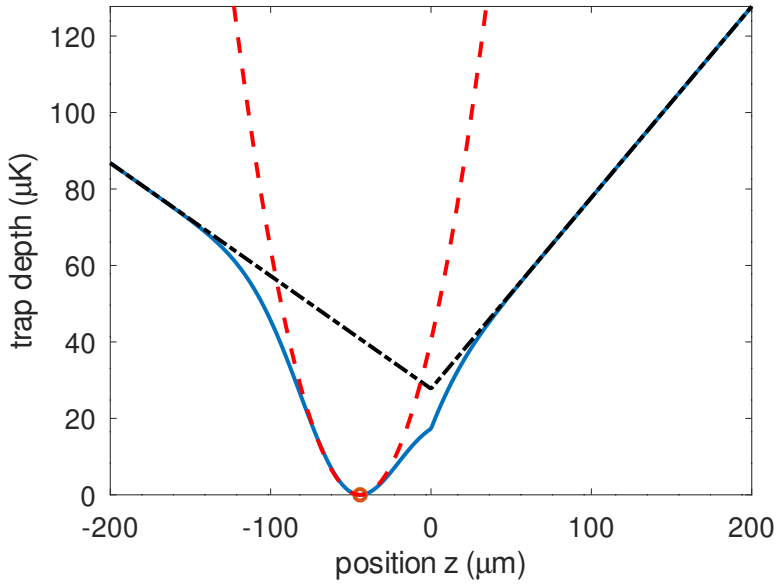



**Figure 5.8** — Blue line: cut in the total potential $V(0,0,z)$ along the $z$-axis given in units of μK, in blue line. Trap parameters are $\alpha = \alpha_h = 2\pi \times 4.14\,{\rm kHz\mu m}^{-1}$, $P = P_{\rm max} = 1.92\,{\rm W}$. The Red dashed line corresponds to the harmonic approximation near the trap bottom. The black dot-dashed line corresponds to the potential resulting from the quadrupole trap and gravity alone.

I now describe the last step of evaporation that leads to the formation of a BEC in the hybrid dimple trap. Immediately after the decompression phase explained in section 3.4, we proceed with final rf evaporation and ramp the rf frequency $\omega'$ from 1 MHz to 750 kHz in 1 second and then to 400 kHz in 2 s. This rf ramp is implemented using one of the outputs of the DDS introduced in Chapter 3. The rf field is strong enough such that the atoms initially in the trapped $m_F = -1$ state get transferred into the anti-trapped $m_F = 1$ state adiabatically as they reach the evaporation surface. It therefore effectively truncates the trap at a finite

energy allowing for efficient rf evaporation. With the parameters that we have, the trap saddle point is on the $y$-axis during evaporation and the trapping potential is purely magnetic along this axis, therefore ensuring that the trap depth is simply set by $\hbar(\omega^{'} - 2\alpha|z_{eq}|)$, i.e., the excess of magnetic energy with respect to the trap minimum. To observe the efficiency of the process we record the total number of atoms $N$ and the temperature $T$ during the rf ramp (see Fig. 5.9).

The temperature dependence on atom number is well reproduced by a power law with an exponent of 1.1 in Fig. 5.9 a). The power law is typically observed during the evaporation procedure [144, 145]. The peak PSD's progression during the evaporation is depicted in Fig. 5.9b). A bimodal condensate emerges in the time-of-flight distribution when the PSD crosses the condensation threshold for $N < 4 \times 10^5$ atoms. A power-law scaling with a slope of $-3.5$ is seen at large atom numbers. The collision rate, as depicted in Fig.5.9c), rises during the initial phase of the final evaporation, indicating the run-away regime. It then stabilises when the atom number falls below $N = 10^6$. The reason for this behaviour change is probably that when the cloud's total energy decreases, the preferential evaporation along the $y$-axis intensifies and the evaporation process transitions from a three-dimensional to a one-dimensional regime.

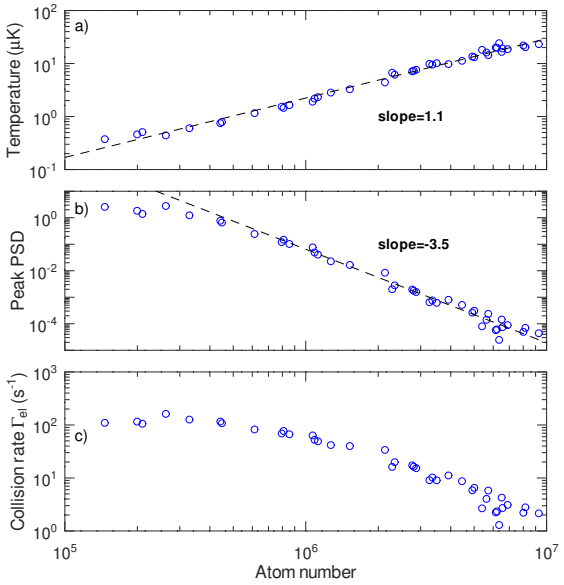



**Figure 5.9** — a) Temperature, b) peak phase space density and c) peak collision rate as a function of the atom number during the evaporation ramp in open blue circles in log-log scale. In a) and b) the dashed black line is a power law fit to the data.

Fig.5.10a) shows that as we go further in evaporation we observe a temperature scaling as $k_B T \propto \hbar(\omega' - 2\alpha|z_{\mathrm{eq}}|)$ as is expected if $T$ is set by the trap depth. Fig. 5.10b) represents the atoms in the hybrid dimple trap after final rf evaporation down to 400 kHz. In the end, the atom cloud has $2 \times 10^5$ atoms in total out of which $7{\times}10^4$ atoms are condensed. The atomic cloud has a temperature of 310 nK. The oscillation frequencies in the trap are (285.4 Hz, 73.8 Hz, 316.6 Hz) along the $x$, $y$ and $z$ directions respectively and the critical temperature to enter the BEC phase is 358 nK.

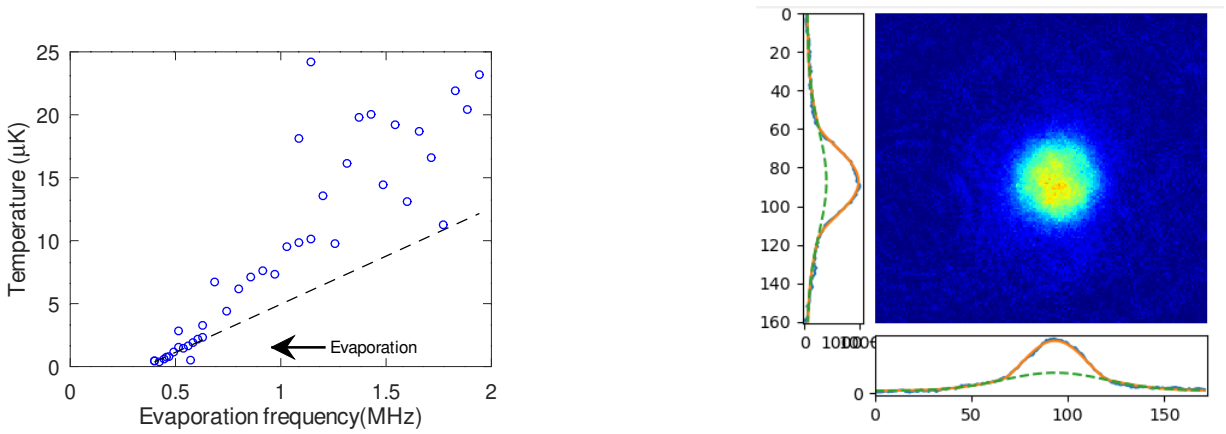



**Figure 5.10** — a) Blue circles: Temperature as a function of the frequency of the evaporation ramp. $y$-axis is in log scale. The dashed black line corresponds to $\hbar(\omega' - 2\alpha|z_{\rm eq}|)/k_B$, b) Absorption picture of the atoms from the hybrid dimple trap after the final rf evaporation taken after 23 ms of time-of-flight expansion. The cloud has $2 \times 10^5$ total atom number out of which $7 \times 10^4$ are condensed and the temperature of the atomic cloud is 310 nK.

### Optical evaporation

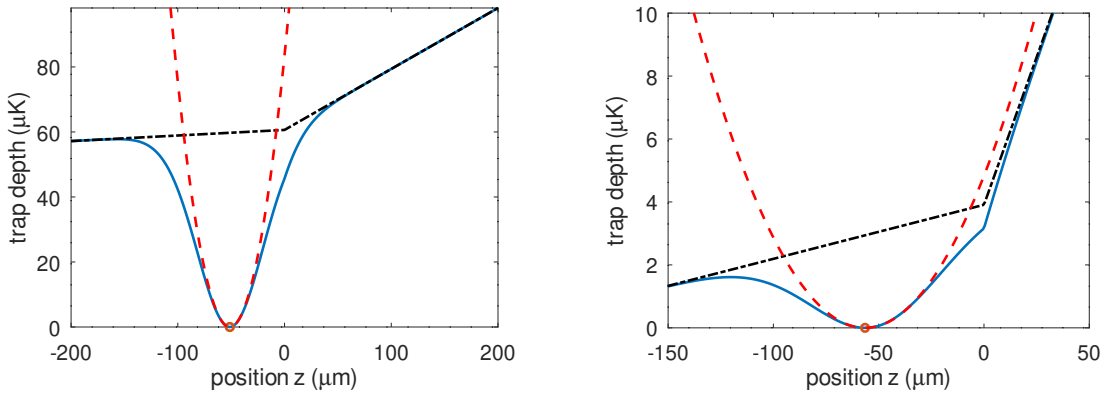



**Figure 5.11** — a) Cut in the total potential $V(0,0,z)$ along the $z$-axis given in units of μK, in blue line. Trap parameters are $\alpha = \alpha_h = 2\pi \times 0.88\,\mathrm{kHz\mu m^{-1}}$, $P = P_{\rm max} = 2.73\,\mathrm{W}$. The red dashed line corresponds to the harmonic approximation near the trap bottom. The black dot-dashed line corresponds to the potential resulting from the quadrupole trap and gravity alone.
b) Cut in the total potential $V(0,0,z)$ along the $z$-axis with the following trap parameters: $\alpha = \alpha_h = 2\pi \times 0.88\,\mathrm{kHz\mu m^{-1}}$, $P = 0.137\,\mathrm{W}$.

In this section, I will describe the procedure of optical evaporation, which is much more optimal in order to reach the BEC phase with more atoms. To perform this evaporation

once we are in the hybrid trap, we reduce the gradient of the quadrupole magnetic trap from $57.4\,\mathrm{Gcm}^{-1}$ to $12.3\,\mathrm{Gcm}^{-1}$ in 100 ms resulting in transfer of the atoms from the hybrid trap to the dimple solely. This is due to the low magnetic gradient which can not hold the atoms against gravity but as the gradient is not exactly zero it still provides the confinement along the $y$-axis. A cut of the potential $V(0,0,z)$ along the $z$-axis with these parameters is represented in Fig. 5.11a).

Now, as the magnetic gradient is very weak and all the atoms are in the dimple trap we perform the evaporation by reducing the power of the dimple beam to 5% (this decreases the trap depth) in 10 s, resulting in the expulsion of hot atoms from the trap. The ramp implemented for dimple power is exponential as a function of time. Fig.5.11b) represents the cut of the potential of the trap along the $z$-axis after the evaporation ramp. The ramp was optimised by maximising the number of atoms after the experimental sequence. Again, to observe the efficiency of the process we record the total number of atoms $N$ and the temperature $T$ during the ramp of the dimple beam power (see Fig. 5.12).

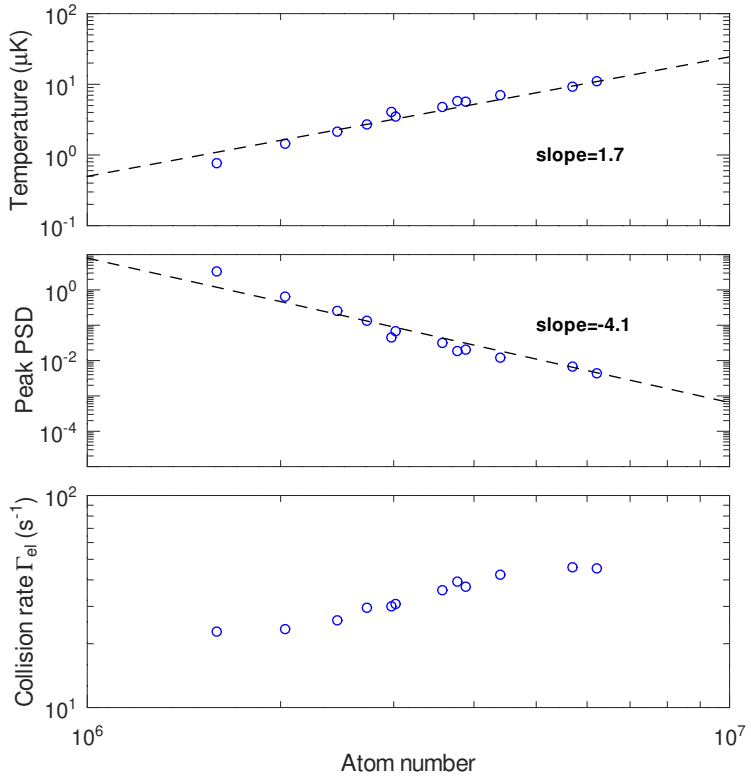



**Figure 5.12** – Figure shows the a) Temperature, b) peak phase space density and c) peak collision rate as a function of the atom number during the optical evaporation, in log-log scale. In a) and b) the dashed black line is a power law fit to the data.

Fig. 5.12a) represents the temperature dependence on the atom number with a power law with an exponent here of 1.7. Fig. 5.12 b) shows the evolution of the peak PSD during the optical evaporation. For $N < 2\times10^6$ atoms, the PSD reaches the condensation threshold and a condensate appears in the time-of-flight distribution that becomes bimodal. We observe a power law scaling, with a slope of $-4.1$. The collision rate, shown in Fig. 5.12 c), decreases

slightly during the evaporation. This is due to the fact that as we do evaporation by decreasing the power of the dimple trap, this opens more and more the trap for the atoms and prevents run-away evaporation [146]. We can note that the slope are larger than in Fig.5.9 therefore the efficiency of the optical evaporation is higher.

Fig. 5.13 represents the atoms in the dimple trap after the optical evaporation, which lasted 10s. Here, we have a total of $1 \times 10^6$ atoms out of which $2.5 \times 10^5$ atoms are condensed and the temperature of the atomic cloud is 244 nK. This atom number is 3 times larger than the atom number in the BEC obtained by final rf evaporation. It can also be noted from Fig. 5.12 b) that the atoms reach the condensation phase when $N$ is $10^6$ while in the case of rf evaporation, the atoms reach the condensation phase for $N < 4 \times 10^5$. The oscillation frequencies in this trap are (79.9 Hz, 30.2 Hz, 85.7 Hz) along the $x$, $y$ and $z$ directions respectively. The critical temperature to enter the BEC phase is around 270 nK.

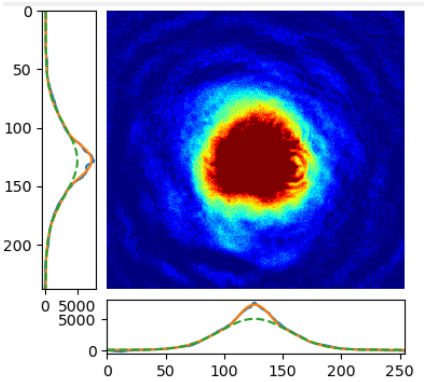



**Figure 5.13** — Absorption picture of the atoms from the dimple trap after the optical evaporation taken after 23 ms of time-of-flight expansion. The atomic cloud has a total of $1 \times 10^6$ atoms out of which around $2.5 \times 10^5$ atoms are condensed and the temperature of the atomic cloud is 244 nK.

## 5.4 Transfer to the bubble trap

The potential with both dimple and atom dressing can be written as:

$$V(\mathbf{r}) = \hbar\sqrt{(\alpha\ell(\mathbf{r}) - \omega)^2 + \Omega(r)^2} + U_0 \exp\left[-2\frac{x^2}{w_x^2} - 2\frac{(z - z_L)^2}{w_z^2}\right] + Mgz. \tag{5.29}$$

Once we have a cold atom sample in a hybrid dimple trap or in a dimple trap, the final goal is to transfer these atoms into the final bubble trap. The transfer process can be different depending on whether the prior trap is a hybrid dimple trap or a dimple trap.

The transfer of the atoms in the bubble trap from the hybrid dimple trap after the rf evaporation is a bit simpler than from the dimple trap after optical evaporation. I will first describe the transfer from the hybrid dimple trap.

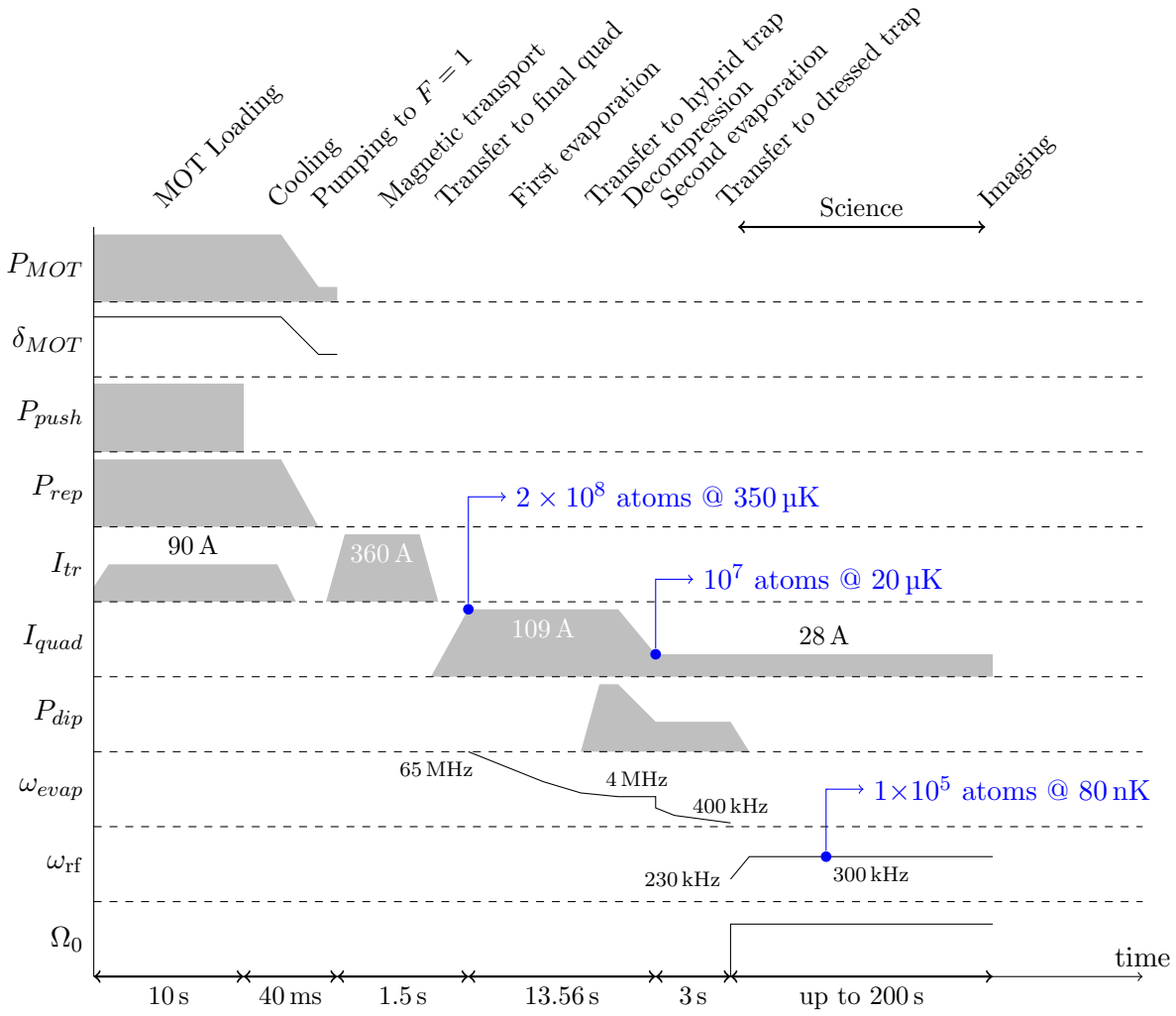



**Figure 5.14** — Flowchart of the experimental sequence in the case of final rf evaporation.

### 5.4.1 Transfer from hybrid dimple trap

We perform the dressing of the atoms after the BEC formation in the hybrid dimple trap. During the transfer, the vertical magnetic gradient remains the same, i.e. $57.4\,\mathrm{Gcm}^{-1}$. Fig.5.14 represents the experimental sequence from the beginning (3D MOT phase) to the transfer of BEC into the bubble trap in case of rf evaporation. The dressing phase comprises the following steps. We first switch on the dressing rf field at some initial frequency smaller than the resonance frequency of the atoms in the hybrid dimple trap (measured using the rf spectroscopy and described briefly in section 5.2.4). Once the dressing rf field is on, we ramp up its frequency to some final value, while decreasing the power of the dimple trap to zero resulting in the transfer of atoms from the hybrid dimple trap to the final rf dressed trap (details are provided below in this section).

After switching off the rf field used for evaporation, we turn on the rf dressing field of circular polarization along the $z$ direction produced by three orthogonal antennas [70]. The dressing field has a coupling amplitude of $\Omega_0/(2\pi) = 50\,\mathrm{kHz}$. The initial frequency of the rf dressing field is $\omega_i/(2\pi) = 230\,\mathrm{kHz}$, which corresponds to the inner dashed ellipse shown

in figure 5.3, below the resonant frequency at the location of the atoms. Then, we increase linearly the rf frequency of the dressing field up to a value of $\omega_f/(2\pi) = 300$ kHz in 150 ms while simultaneously ramping down the dimple trap power to zero in 150 ms as well. In this way we transfer the atomic cloud from the hybrid dimple trap into the bubble trap. The atoms sit at the bottom of the ellipsoidal of the bubble trap, as shown in Fig. 5.3. During the transfer, the atoms undergo a smooth expansion from the hybrid dimple trap of frequencies $(287\,\text{Hz}, 75\,\text{Hz}, 317\,\text{Hz})$ to a pancake-shape in the bubble trap of frequencies $(34\,\text{Hz}, 34\,\text{Hz}, 378\,\text{Hz})$ (Fig. 5.15). The average frequency $\omega_{\text{avg}} = (\omega_x\omega_y\omega_z)^{1/3}$ decreases during the transfer, resulting in an adiabatic decrease of the atomic cloud's temperature. To further reduce the final temperature of the atomic cloud and to control the condensate fraction we have an additional rf knife to evaporate more atoms in the atomic cloud by limiting the depth of the bubble trap.

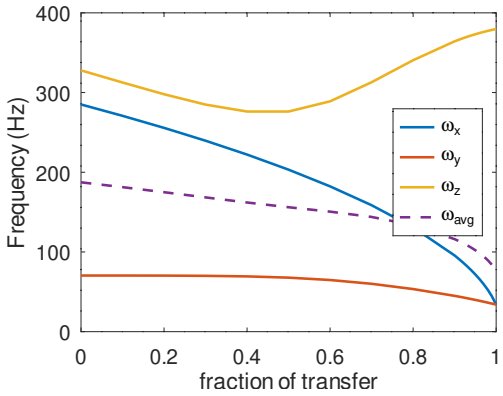



**Figure 5.15** — Evolution of the trapping frequencies during transfer from the hybrid dimple trap to the bubble trap, in the case of rf evaporation.

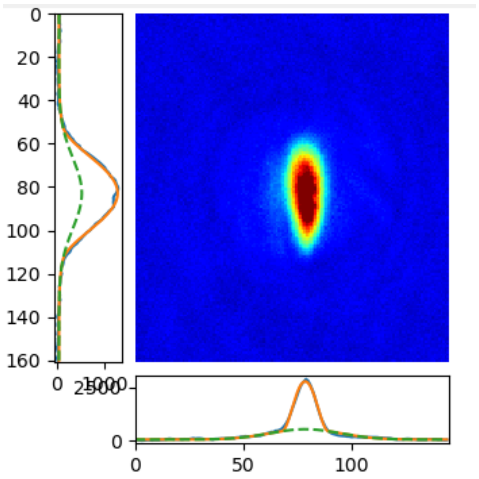



**Figure 5.16** — Absorption image of the atomic cloud released from the bubble trap after 23 ms of time-of-flight expansion. The atomic cloud has a total of $1.8 \times 10^5$ atoms out of which $1 \times 10^5$ are condensed and the temperature of the cloud is 75 nK.

Once the transfer is over, we hold the atoms for 100 ms in the trap and then observe the atomic cloud after 23 ms of time-of-flight as shown in Fig. 5.16. We can note from Fig. 5.16 that the atomic cloud is highly anisotropic. This is due to the fact that the frequency of the trap in the $z$ direction is 10 times higher than the frequency in the radial direction, thus the atoms are more confined in the vertical direction. When we do a time-of-flight experiment, the atomic cloud gets more elongated in the $z$ direction. In the end, the atomic cloud has total of $1.8 \times 10^5$ atom number out of which $1 \times 10^5$ are condensed and the temperature of the atomic cloud is 75 nK.

### 5.4.2 Transfer from the dimple trap

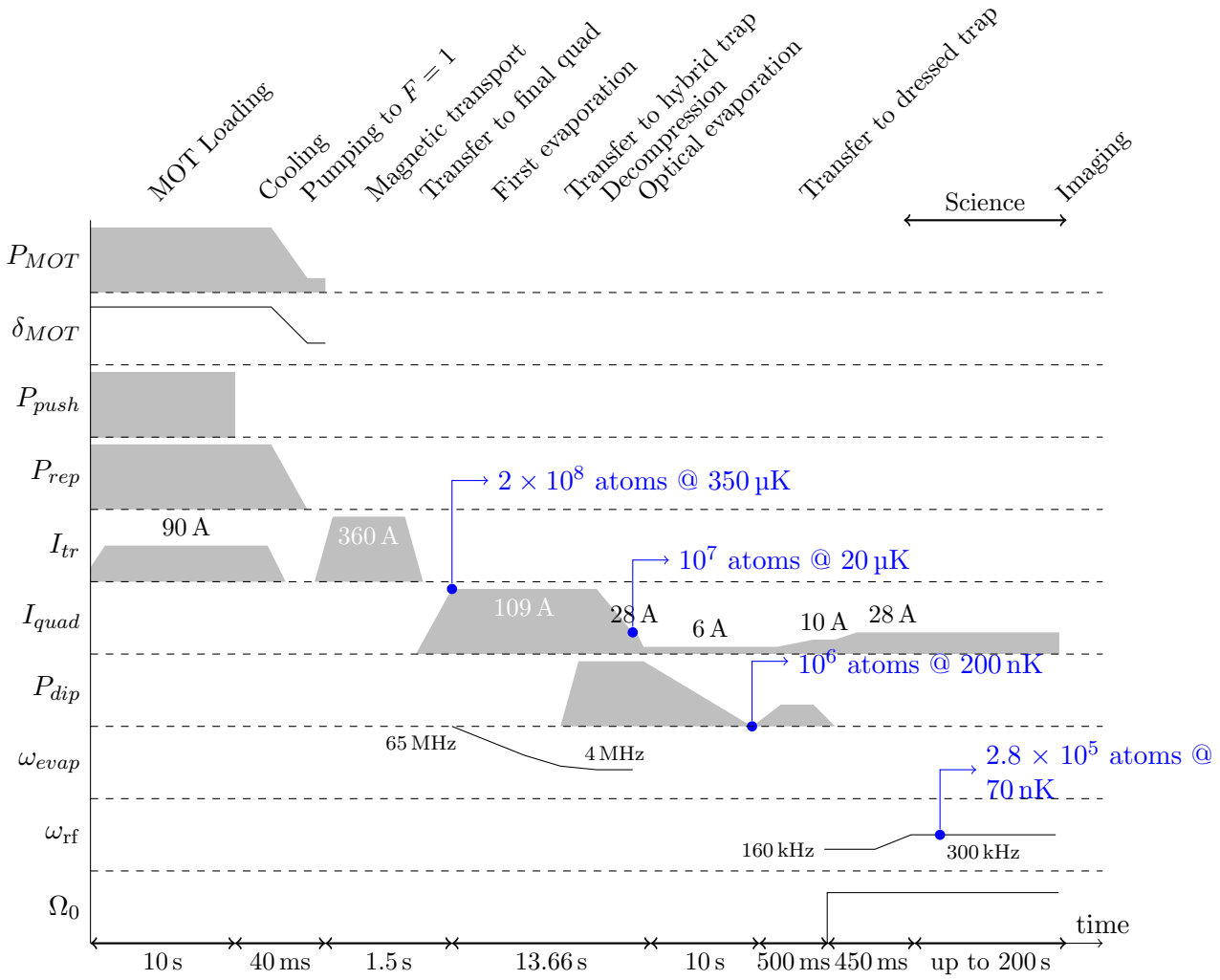



**Figure 5.17** — Flowchart of the experimental sequence in the case of optical evaporation.

Fig.5.17 represents the experimental sequence from the beginning (3D MOT phase) to the transfer of BEC in the bubble trap in case of optical evaporation. We decrease a lot the magnetic gradient in order to transfer the atoms to the dimple trap from the hybrid dimple

trap to perform the optical evaporation. This low magnetic gradient is not appropriate for the final loading into the bubble trap. We have to bring back the gradient to its initial value ($57.4\,\mathrm{Gcm^{-1}}$) to perform the transfer of atoms into the bubble trap. To do so, we first start with the phase of re-compression just after the optical evaporation, where we increase the power of the dimple beam from 5% (as it was at the end of the evaporation) to 16% in 100 ms. Then we ramp the magnetic gradient from $12.3\,\mathrm{Gcm^{-1}}$ to $20.5\,\mathrm{Gcm^{-1}}$. We start the first phase of dressing, 10 ms after the recompression phase, using the rf dressing field with circular polarisation along the $z$ direction and with the same coupling amplitude as described in 5.4.1. The initial frequency of the rf dressing field is $\omega_i/(2\pi) = 160\,\mathrm{kHz}$. At the beginning of the dressing ramp, we ramp down the power of the dimple trap to zero in 150 ms. Now the atoms are in the bubble trap of magnetic gradient $20.5\,\mathrm{Gcm^{-1}}$ and with the dressing frequency of $\omega_i/(2\pi) = 160\,\mathrm{kHz}$. Once the dimple trap is turned off, we increase the gradient of the magnetic field to $57.4\,\mathrm{Gcm^{-1}}$ in 150 ms. As the gradient reaches $57.4\,\mathrm{Gcm^{-1}}$, we ramp up the dressing frequency to its final value, i.e., $\omega_i/(2\pi) = 300\,\mathrm{kHz}$ in 150 ms, thus ending up having all the atoms in the final bubble trap. Even if this process is more complex than the one described in 5.4.1, we have more atoms in the final trap making it easier to study the dynamics of the BEC and other modes of excitation. If we have more atoms in the trap, even if during the excitation the system becomes dilute we can still have a reasonable signal to observe.

Below is an image of the BEC that we observe again after 23 ms of the time-of-flight expansion. In the end, the atomic cloud has a total of $3.4 \times 10^5$ atom number out of which $2.85 \times 10^5$ are condensed and the temperature of the atomic cloud is 65 nK. Fig.5.19 shows the evolution of the trap frequencies during the passage from the dimple to the bubble trap. Here the average frequency $\omega_{\mathrm{avg}}$ also decreases during the transfer resulting in a temperature decrease for an adiabatic transfer.

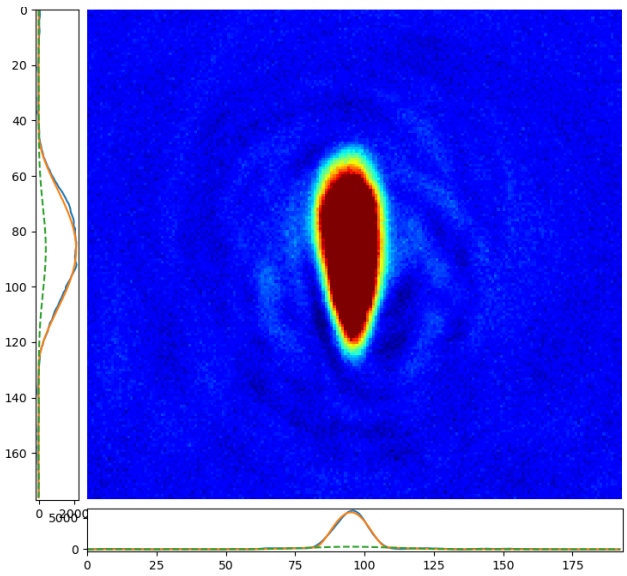



**Figure 5.18** — Absorption picture of the atomic cloud released from the bubble trap after 23 ms of time-of-flight expansion. The atomic cloud has a total of $3.4 \times 10^5$ atoms out of which $2.85 \times 10^5$ are condensed and the temperature of the could is 65 nK.

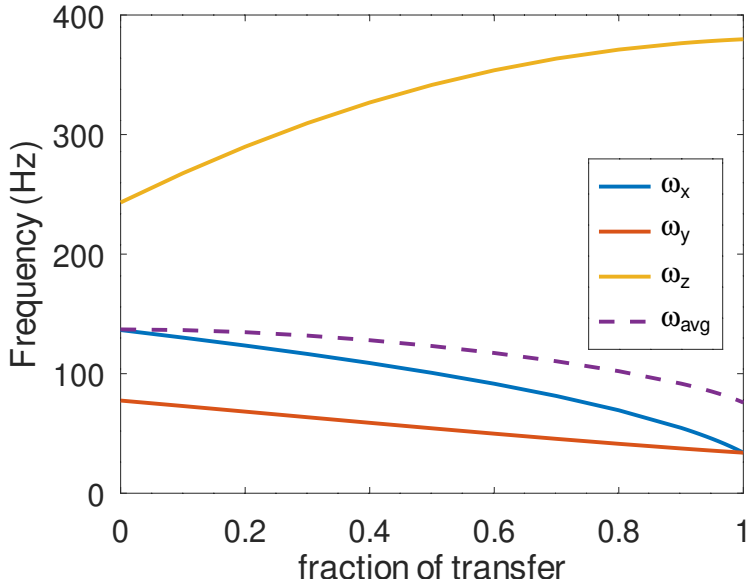



**Figure 5.19** — Evolution of the trapping frequencies during the transfer from the dimple trap to the bubble trap in the case of optical evaporation.

### 5.4.3 Lifetime of atoms and heating rate in the bubble trap

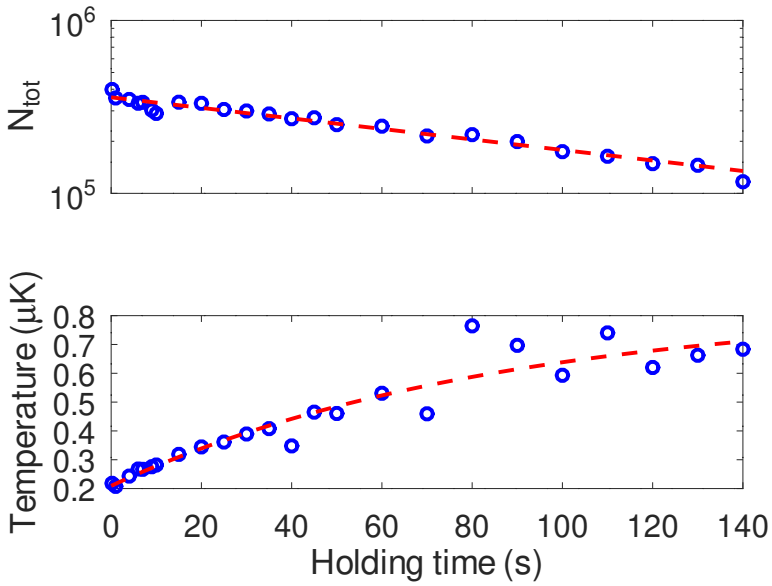



**Figure 5.20** — a) Blue circles: experimentally recorded atom numbers as a function of holding time, red dashed line: exponential fit to the data. b) Blue circles: experimentally recorded temperature of the atomic cloud as a function of holding time, red dashed line: exponential fit to the data.

Now we would like to know about the lifetime of the atomic cloud in the bubble trap and the heating rate as it is interesting to know how long we can keep the ultracold sample in a trap

to be able to perform different types of excitations to study the dynamics, for example the study of collective modes of a trapped gas. We measure the lifetime of the atoms and the heating rate in the final bubble trap. To measure the lifetime and heating rate, we observe the atomic cloud as a function of holding time in the trap and we record the atom number and the temperature. Figure 5.20 a) shows the atom number as a function of holding time and we fit the decreasing atom number with an exponential function and find the lifetime of 142(8) s limited by collisions with the background gas. Figure 5.20 b) shows the temperature of atomic cloud as a function of holding time and again by fitting the data with an exponential we find the heating rate $\gamma = 7(4)\,\mathrm{nKs}^{-1}$.

### 5.4.4 Optimisation of the excitation of the center-of-mass motion

When the atomic cloud is transferred into the bubble trap, the horizontal position of the dimple beam becomes important. We observe that without any additional optimization, the residual amplitude of the center-of-mass motion in the bubble trap is already below ±5 µm. We can minimise this excitation by optimising the position of the dimple beam. To do this, we simply check the atomic cloud properties after the transfer: atom number, temperature and center-of-mass position as a function of the position of the dimple beam which we can control using a piezo-actuated mirror (described in Sec.5.2.3). Importantly, these quantities related to the atomic cloud can be obtained with a single run of the experiment which allows for a reasonable optimization time. Figure 5.21 represents the final residual oscillation after the optimisation of the horizontal dimple position. The oscillation amplitude of ±8 µm after expansion corresponds to ±1.6 µm of in-trap amplitude, which is much less than the extension of the quantum gas whose Thomas-Fermi radius is 16 µm.

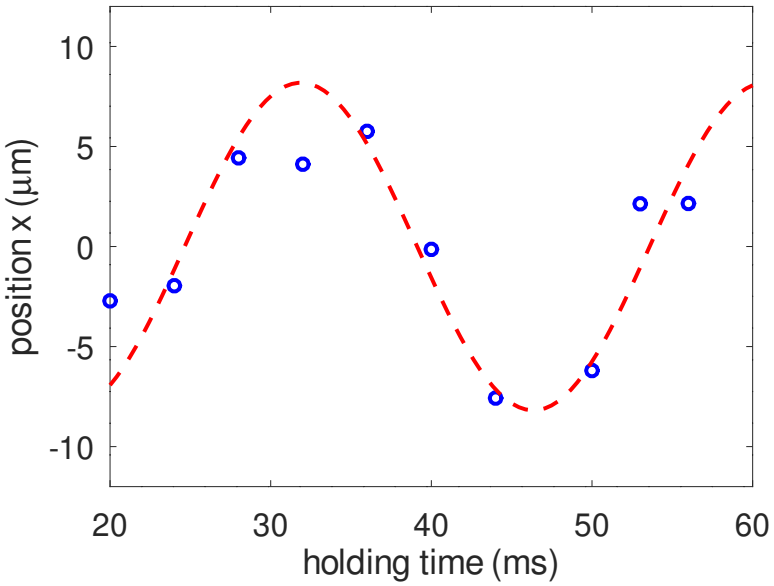



**Figure 5.21** — Blue circles: Residual oscillations of the center-of-mass motion along the $x$-axis in the bubble trap measured after a 23 ms of TOF expansion. As the oscillation frequency along the $x$-axis in the bubble trap is 34 Hz, the oscillation amplitude of ±8 µm after TOF expansion corresponds to in-trap oscillations of amplitude ±1.6 µm.

## 5.5 Conclusion

In this chapter, I have discussed the installation of the dimple beam and the working principle of the hybrid dimple trap. I have described the characterization of the dimple and the two different experimental sequences (rf evaporation and optical evaporation) implemented to obtain the ultracold sample of the atoms in the hybrid dimple trap and the optical evaporation technique turned out to be more efficient than the rf evaporation. Then, I explained the transfer process to the bubble trap depending on the evaporation technique used prior to this step. In both cases, the average trapping frequency decreases during the transfer which results in a decrease in the temperature of the atomic cloud for an adiabatic transfer. The lifetime of the atoms in the final bubble trap is found to be 142 s and the amplitude of the residual oscillation of the center-of-mass motion of the atoms is found to be $\pm 1.6\,\mu$m. This represents a significant improvement with respect to the residual excitations observed when the condensate is prepared initially in a plugged quadrupole trap, where they were of the order of 5 µm.

# Chapter 6

# New laser system

## 6.1 Need of a new laser system

The laser chain configuration presented in Chapter 3 had some drawbacks regarding the experiment we would like to perform, for example the in-trap non-destructive imaging of the ultracold atoms. This imaging scheme requires an additional probe beam which is highly detuned from the resonant frequency of the imaging transition and was not present in the initial experimental setup. Also, the two repumper lasers (resonant and off-resonant) mentioned in Chapter 3 were Sanyo diode lasers which are no longer produced so this also motivated us to modify the earlier laser system. To overcome these problems we upgraded our 780 nm laser chain by replacing Sanyo diode lasers with extended cavity narrowdiode lasers from Radiant Dyes and we locked all the lasers to the master laser using beatnotes in order to achieve desirable detuning of different beams used in the experiment.

## 6.2 Upgraded laser chain

The new laser chain is organised as follows:

- Master laser: We have the same master laser as presented in Chapter 3 but this time it is locked by saturated absorption to the crossover line $F = 3 \longrightarrow F^{'} = 3\&4$ of the $D_2$ line of $^{85}$Rb. This laser serves as an optical frequency reference for the experiment and is used at a fixed frequency.

- First narrowdiode laser from Radiant Dyes: This laser provides the probe beam for absorption imaging in the horizontal and the vertical directions respectively. It is locked by beatnote to the master laser. For the rest of this chapter, we will call this laser by the name $F = 2$. The reason for naming this laser $F = 2$ is that this laser is locked close to the transition $F = 2 \longrightarrow F^{'} = 3$ of the $D_2$ line of $^{87}$Rb.

- Another narrowdiode laser from Radiant Dyes: This laser provides two repumping beams (resonant and off-resonant) and also a probe beam for non-destructive imaging. This laser is also locked by beatnote with the master laser. It has a large tunability of up to 1.2 GHz, as it is used both as a resonant repumper beam and as a non-destructive probe beam. For the rest of this chapter, we will call this laser $F = 1$ for simplicity

and the reason here is that this laser is locked close to the transition $F = 1 \longrightarrow F' = 2$ of the $D_2$ line of $^{87}$Rb.

- Cooling laser: This is the same laser as mentioned in Chapter 3 and is used for 2D and 3D MOT as previously. This laser is now locked by beatnote to the $F = 2$ laser unlike the previous version where it was locked with the master laser.

Fig. 6.1a) shows the beams required for the experimental sequence.

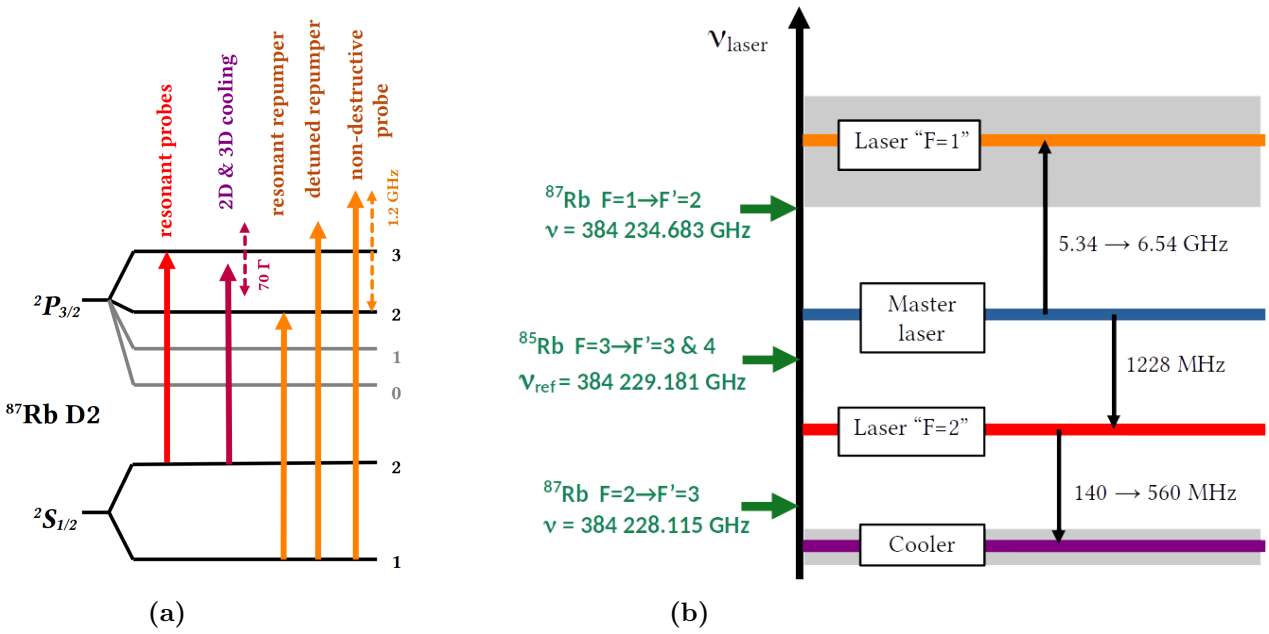



**Figure 6.1** – a) Energy level diagram of the $D_2$ line of $^{87}$Rb with different beams. Red arrow: $F = 2$ laser, dark red arrow: cooling laser and orange arrows: $F = 1$ laser. b) Frequency stabilization diagram. A black arrow indicates that the laser at the tip of the arrow is phase-locked to the laser at its base.

## 6.3 Master laser

The master laser is locked to a hyperfine component of the $D_2$ line of $^{85}$Rb using the saturated absorption technique in the cell with modulation transfer. The hyperfine component chosen is the crossing line $F = 3 \longrightarrow F' = 3\&4$ of $^{85}$Rb, a more abundant isotope ($\simeq 72\%$) than $^{87}$Rb. Its frequency is equal to [147]:

$$f_{3\longrightarrow 3\&4} = f_{\text{ref}} = 384\,229\,181.4\,\text{MHz}. \tag{6.1}$$

### 6.3.1 Optical setup and locking scheme

To lock the master laser, its frequency is modulated using an Acousto-optic modulator (AOM) (as in Chapter 3, see also Fig.6.2) at the frequency $f_{\text{AOM}} = -103.6\,\text{MHz}$, where $|f_{\text{AOM}}|$ is the operating frequency of the AOM, which modulates the frequency of the diffracted beam to $-1$ order. Once the laser is locked, its frequency is:

$$f_{\text{master}} = f_{\text{ref}} + f_{\text{AOM}}/2 = 384\,229\,233.2\,\text{MHz}, \tag{6.2}$$

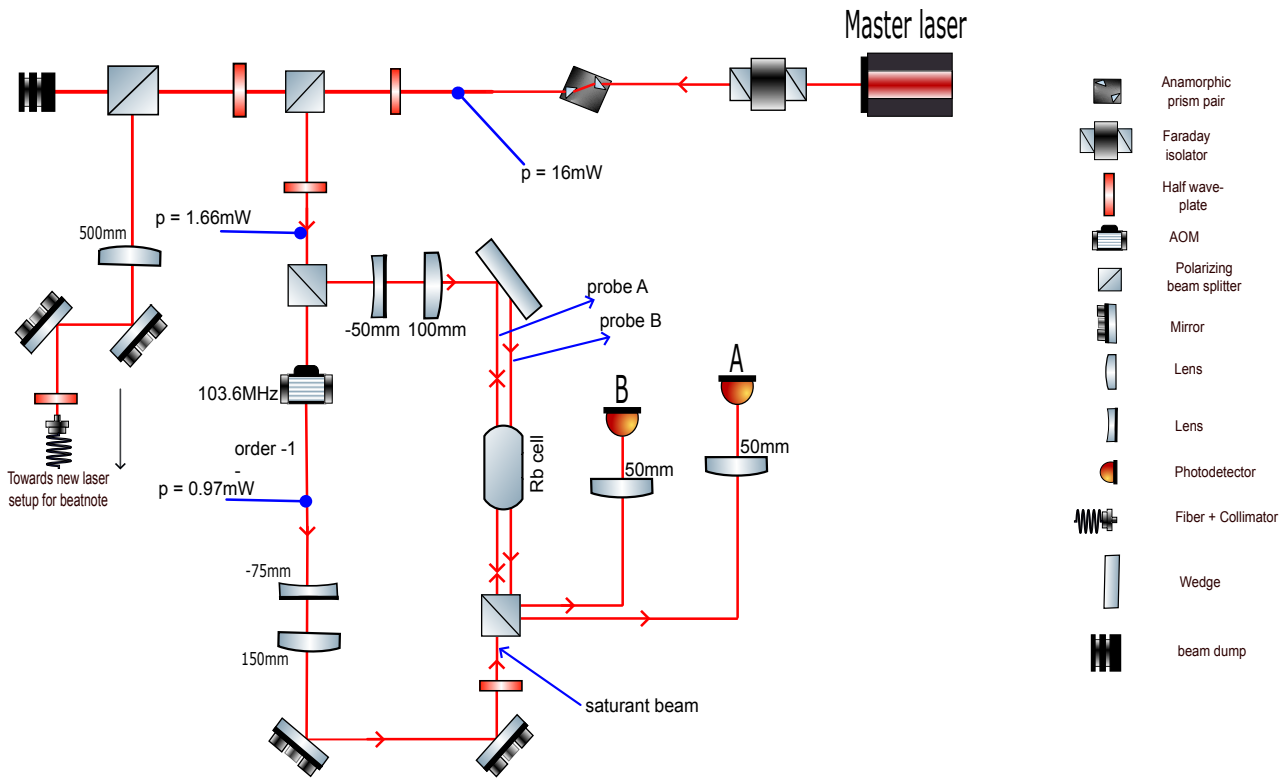



**Figure 6.2** — Optical setup of master laser

Fig.6.2 Experimental setup of the saturated absorption. Two probe beams are used, one of them is superimposed on the saturating beam. The difference between the two transmission signals A-B is demodulated. This scheme aims to suppress the Gaussian envelope in the lock-in amplifier module's input signal in order to limit the risk of saturation of the input stage and to minimise the offset of the demodulated signal.

### Some useful values

The operating point of the master laser is 78.2 mA with 10.30 kΩ being the value of the thermistor setting the temperature of the laser box and 12.440 kΩ for the temperature of the laser diode. The Faraday optical isolator used in the optical setup has a transmission of 66%. The waist of the laser beam after the optical isolator is $w_x = 1.96\,\text{mm}$ and $w_y = 0.93\,\text{mm}$ along the $x$ and $y$ axis. After the anamorphic prism pair, the beam spot is quasi-circular with waist of $w = 510\,\mu\text{m}$.

The AOM of the saturated absorption setup is powered by a 2 W rf signal, with a frequency set by a voltage-controlled oscillator (VCO). The output of the ramp generation module labelled $V_{\text{mod}}$, see Fig.6.3, sets the VCO frequency. Two variable resistors (Fig.6.3) are used to adjust its DC component $V_{\text{mod}}^{\text{DC}}$ and AC component $V_{\text{mod}}^{\text{AC}}$ independently. For $V_{\text{mod}}^{\text{DC}} = 2.75\,\text{V}$, the measured central frequency of the AOM is $f_{\text{AOM}} = 103.6(2)\,\text{MHz}$. The AC component oscillates at 156 kHz. A subtractor circuit is used to make the difference between the signals of probe A and probe B delivered by the photodetectors. As the two probe beams do not have the same power even before passing through the Rb cell, it is important to balance the amplitude of the signals using a potentiometer at the input of the circuit. The electronics

for the lock used here are those of the previous laser system. The digital lock-in module is based on the Field-Programmable Gate Arrays (FPGA) component that performs the first harmonic demodulation of the input signal at around 150 kHz. The module also generates the correction signals via analogue stages and has 3 gain settings (Fig.6.3). Fig. 6.4 shows the saturated absorption signal obtained with the saturated absorption technique.

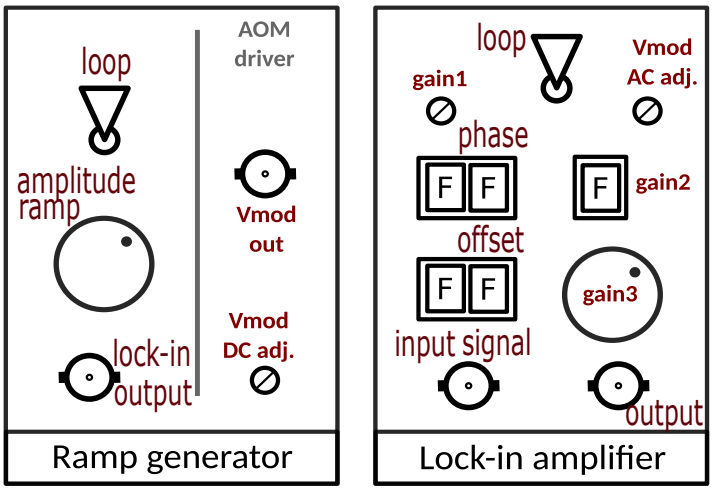
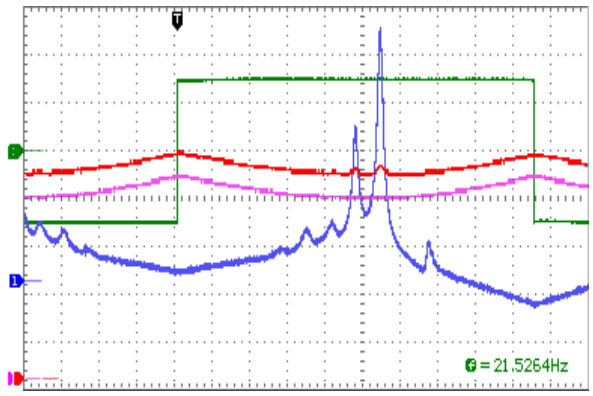
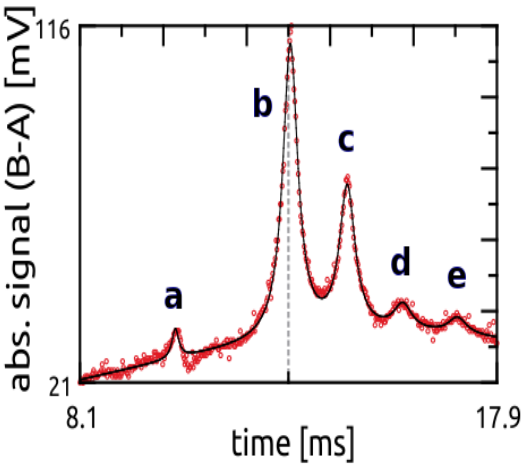



**Figure 6.3** — Design of the controller of AOM and a lock-in amplifier module used in the optical setup for master laser.




**(a)** In green: synchronization signal. In red: saturated probe A signal (404 mV/div). In pink: unsaturated probe B signal (404 mV/div). In blue: A-B (20 mV/div). The "zeros" of signals A and B are overlapped.




**(b)** Hyperfine components: a: $3 \rightarrow 4$, b: $3 \rightarrow 3\&4$, c: $3 \rightarrow 2\&4$, d: $3 \rightarrow 3$, e: $3 \rightarrow 2\&3$. Red circles: differential absorption signal. Black line: fit by a sum of Lorentzians and a Gaussian pedestal.

**Figure 6.4** — Spectrum of the $F = 3 \rightarrow F'$ transitions of $^{85}$Rb. In b) the transition $F = 3 \rightarrow F' = 2$ is out of frame. These figures are produced by Thomas Badr, an engineer in our group.

We finally sought to improve the signal-to-noise ratio of the demodulated signal without making it too large, by adjusting the gains of the lock-in amplifier module and the parameters of the saturating beam. The parameters adopted for the saturating beam are: $P_{\text{sat}} = 30\,\mu\text{W}$ and $V_{\text{mod}}^{\text{AC}} = 336\,\text{mV}$ (Fig.6.5). To find the optimal values of the saturating beam power and the modulation amplitude, we observe the demodulated signal for different values of $P_{\text{sat}}$ and $V_{\text{mod}}^{\text{AC}}$. The demodulated signals were then adjusted by the sum Lorentzian derivatives (black solid lines in Fig.6.5):

$$g(\omega) = K \cdot \frac{df}{d\omega}, \tag{6.3}$$

with

$$f(\omega) = A \cdot \left(1 + \left(\frac{\omega - \omega_0}{\Gamma'/2}\right)^2\right)^{-1}, \tag{6.4}$$

where $\omega_0$ is the frequency of the component, $\Gamma'$ is the full width at half-maximum, $A$ is the amplitude of the profile and $K$ (in $\text{s}^{-1}$) is a function of the gain settings of the lock-in amplifier module. We then choose the value of the modulation amplitude and the minimum power of the saturant beam for which the width $\Gamma'$ is minimum and the amplitude of the demodulated signal is high enough such that we have a good signal-to-noise ratio.

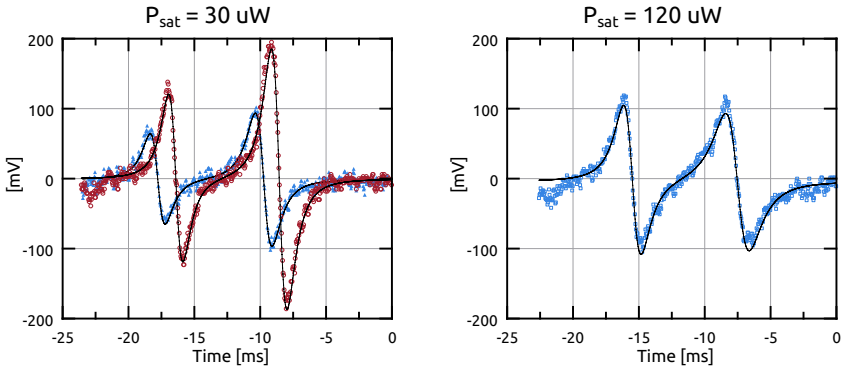



**Figure 6.5** — Demodulated signal and the fit with the sum of Lorentzian derivatives in the vicinity of the components $F = 3 \rightarrow F' = 2\&3$ and $F = 3 \rightarrow F' = 3\&4$. Left: $P_{\text{sat}} = 30\,\mu\text{W}$, $V_{\text{mod}}^{\text{AC}} = 336\,\text{mV}$ (in red) and $V_{\text{mod}}^{\text{AC}} = 212\,\text{mV}$ (in blue). Right: $P_{\text{sat}} = 120\,\mu\text{W}$, $V_{\text{mod}}^{\text{AC}} = 212\,\text{mV}$.

## 6.4 New NarrowDiode lasers from Radiant Dyes

The two newly installed lasers are of the same type as the master laser (as mentioned above), i.e., NarrowDiode linear extended cavity laser diodes from Radiant Dyes. The system's tunability range is claimed to be 20 nm. However, the tunability of the laser diode itself is only 5 nm. Coarse spectral tuning with frequency jumps of 25 GHz is obtained by manually tilting the intracavity interference filter. We can achieve finer tuning by adjusting the temperature of the diode and then the length of the cavity as the coupler is mounted on the ceramic piezoelectric. Fig.6.6 represents the internal design of the NarrowDiode laser. The natural

position of the interference filter is not the normal incidence with respect to the intracavity beam. The maximum transmission of the filter is expected for an incidence of 6°.

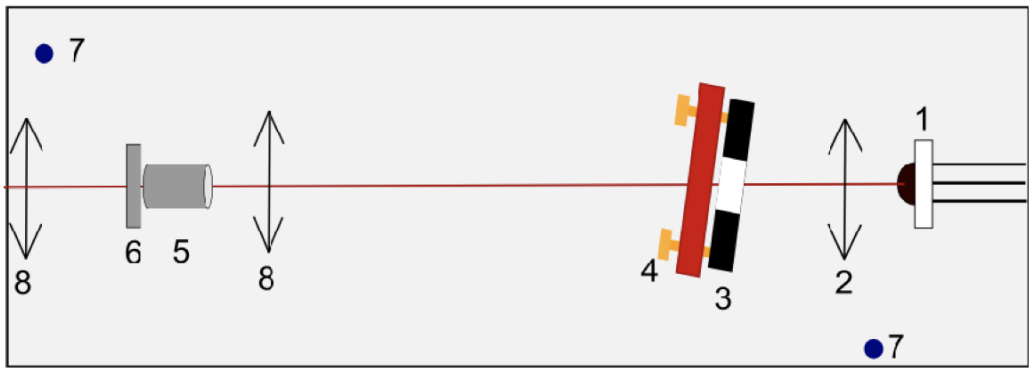



**Figure 6.6** — Internal design of the NarrowDiode laser. Components marked with numbers are: 1 - Laser Diode, 2 - Collimation Lens, 3 - Interference Filter, 4 - Screws for wavelength adjustment, 5 - Piezoelectric Actuator, 6 - Output Coupler, 7 Thermistors, 8 - Collimation Lenses. This figure is taken from the laser manual.

### 6.4.1 Controllers for lasers

The master laser and the cooling laser use the current and temperature controllers developed in the electronic workshop in our lab LPL. However, the new lasers $F = 1$ and $F = 2$ are controlled by the commercial controllers purchased with the lasers. The commercial controllers have the following three control modules:

- Current control module: The power supply module can deliver the current in the range of 0 to 150 mA. However, the current is factory-limited depending on the laser diode installed in the laser head: typically 130 mA maximum in the case of the two new sources. We measure the sensitivity of the change in frequency as a function of current: $-70\,\mathrm{MHz/mA}$.

- Temperature control module: It is used to adjust the temperature setpoint of the laser head housing and to display the associated error signal. The measured housing temperature is not displayed. It is also used to adjust the temperature setpoint, display the temperature of the laser diode and visualise the error signal.

- PZT driver module: The piezoelectric ceramic supporting the coupler is polarised between 0 and 800 V. The sensitivity of the emitted frequency as a function of the applied voltage was roughly measured: $+10\,\mathrm{MHz}/V_{\mathrm{pzt}}$.

The frequency tunability with PZT alone is around 1.5 GHz and with "feed-forward" (modulation of the current as a function of the voltage applied to the ceramic), it is theoretically possible to achieve 4 GHz tunability without mode hopping.

The maximum power delivered by the lasers $F = 1$ and $F = 2$ is $\sim 50\,\mathrm{mW}$ with a waist of $\sim 500\,\mu\mathrm{m}$ at the exit of last collimation lens and the mode of the lasers is $\mathrm{TEM}_{00}$.

## 6.5 Optical setup with new lasers

Fig.6.7 represents the updated optical setup with the new lasers which provide us with all the necessary beams required for the experiments. We have improved the flexibility on the detuning of their respective frequencies which is achieved by implementing the beatnote locking scheme between the lasers. I use different colours for each laser in Fig.6.7 to make it easier for the visualization. One particularity of this setup is that we inject the vertical resonant probe beam and the non-destructive probe beam in the same fiber in order to be able to perform both types of imaging along the vertical direction. This could be possible with the help of shutters which block or let the probe beams pass through the fiber depending on the imaging technique chosen in the experimental sequence.

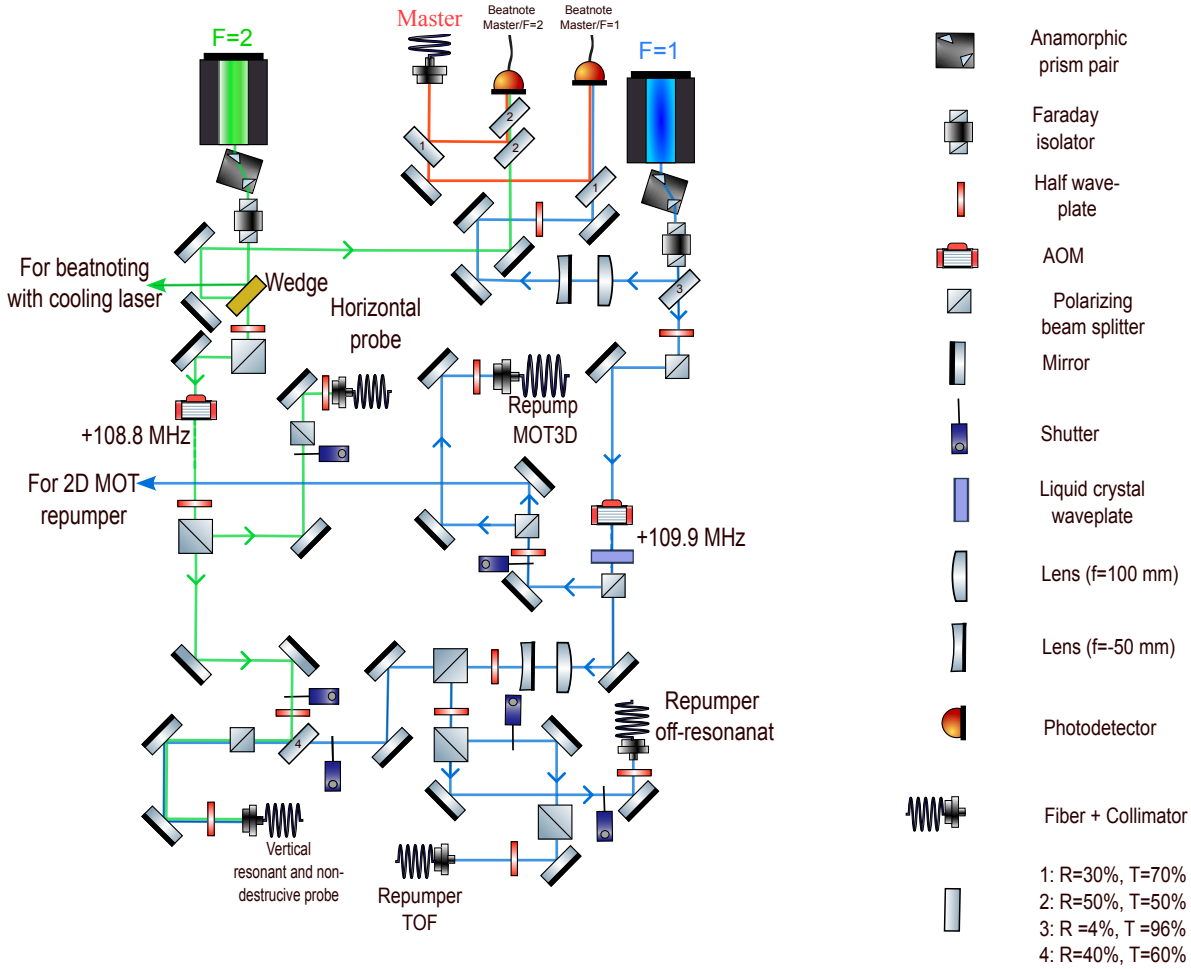



**Figure 6.7** — Updated optical setup. R and T refers to the reflection and the transmission coefficient.

In the optical chain of the $F = 2$ laser, the AOM used has a frequency of 108.8 MHz and in that of $F = 1$ laser, the AOM used has a frequency of 109.9 MHz. After this AOM in the optical path of $F = 1$ laser, we used a liquid crystal waveplate in order to transfer the maximum power towards the 3D MOT repumper at the beginning of the sequence and then

redirect the whole power towards the other repumpers and the non-destructive imaging fibers during the imaging part in the sequence. The advantage of using this waveplate over a standard half-waveplate is that we can control the orientation of its polarisation axis during the sequence as this liquid crystal waveplate is controlled using a square wave signal generated by a function generator and therefore we can vary the orientation of this waveplate by modulating the amplitude of the signal during the experimental sequence. This modulation during the experimental sequence is performed by triggering the input of the function generator with one of the analog outputs of the PXIe 1073 rack system in our experiment. In order to calibrate this waveplate I measured the power at the transmission of the cube after the liquid crystal waveplate as a function of the input command value for the amplitude. By fitting the voltage as a function of transmission (as shown in Fig.6.8), I could create a function which allows to control the transmission through the cube as a function of transmission needed in the experiment.

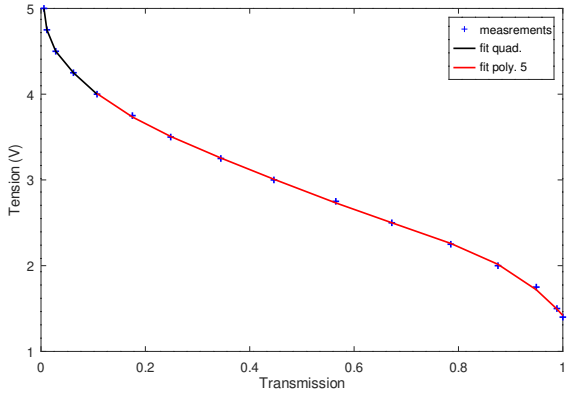



**Figure 6.8** — Input voltage as a function of transmission. The first few points of the input voltage as a function of the transmission are fitted with a quadratic function and the rest with the fifth-degree polynomial function. The idea of fitting with two polynomial functions was adopted as the fit with only either of the two polynomial functions was not accurate.

When the transmission is 0, this means that the maximum laser power is going towards the 3D MOT repumper fiber and when the transmission is maximum this means that the maximum laser power is going towards the other repumpers and non-destructive imaging fibers. The only limitation that I found of this waveplate is that its response time is slow. Therefore, during the experimental sequence, if we need to change the orientation of this waveplate at some instance, the command for this change should be anticipated by a few seconds before that instance (2 s in our case).

I will now describe the different beatnote signals available on the updated experimental setup and the approach used to obtain these signals.

### 6.5.1 Frequency beatnote between the $F = 1$ laser and the master laser

To achieve this beatnote signal, the master laser beam and the $F = 1$ laser beam are injected into an SMF-28 type optical fibre. We then optimised the coupling of the $F = 1$ beam and the Master beam with the coupling efficiencies in the fibre of $\eta_{F=1} = 84\%$ and $\eta_{\text{master}} = 70\%$.

The beatnote is in the range $5.35 - 6.35$ GHz. We chose to divide the beatnote frequency by 64 in order to use standard and affordable components for the electronics.

The beatnote signal through the fiber is sent to the rack-mounted box (Fig.6.9) which has the following configuration:

- DX12CF photodetector: This a fibered optic photodetector (type SMF-28 single-mode fibre with FC/PC connector) with the following characteristics: sensitivity 700-870 nm, bandwidth DC-10 GHz, maximum optical power 10 dBm, i.e., 10 mW.

- ZX85-12G-S+ polarisation tee: It has a bandwidth of DC-12 GHz and is placed after the photodetector and before the amplification stage, it separates the DC and AC parts of the signal. The DC part is used to estimate the level of optical power received by the photodetector. A level above 25 mV is found to be good for the beatnote locking.

- ZJL-7G+ amplifiers: These amplifiers are polarised at 12 V and have a bandwidth DC-7 GHz and gain in the range of 7.5 to 10 dB. These amplifiers are stable but limited to low output power (10 dBm).

- Prescaler HMC434: It has a high bandwidth in the range of 0.2 to 8 GHz. It provides the division of the frequency by 8 and we use a pair of this prescaler to get the division by 64. These prescalers are demanding in terms of input level therefore four ZJL-7G+ amplifiers were required, as well as an amplifier (10 dB) placed between the two prescalers. If the input power is insufficient, there is no division, i.e., the fundamental frequency of the output signal is the same as that of the input frequency. A coupler ZHDC-16-63-S+ is used between two prescalers to have the possibility to monitor the beatnote frequency signal.

- A voltage-controlled oscillator (VCO) used in this configuration has a working range of 75 MHz to 150 MHz.

As this laser has to be locked on the transition $|5S_{1/2}, F = 1\rangle \rightarrow |5P_{3/2}, F = 2\rangle$ of $^{87}$Rb at the frequency 384 234 383.2 MHz and the AOM used is working at a frequency of 108.8 MHz (order +1), the laser has to be at a frequency of 384 234 274.4 MHz for the resonant repumper. Therefore the beatnote frequency between the laser $F = 1$ and the master laser in this particular case is 5.341 GHz. As this frequency is later divided by 64, the reference frequency for VCO is 83.45 MHz. After the division, the beatnote signal should be locked at this frequency. In the case of off-resonant repumper which is detuned by +600 MHz from the transition $|5S_{1/2}, F = 1\rangle \rightarrow |5P_{3/2}, F = 2\rangle$ of $^{87}$Rb, the beatnote frequency before the division will be 5.941 GHz and after the division step this frequency becomes 92.83 MHz. In the case of non-destructive imaging where the probe can be detuned up to 1.2 GHz, the beatnote frequency before the division step is 6.541 GHz and after the division step the beatnote frequency is 102.2 MHz. In Fig.6.10, plot on the top shows the relation between the beatnote frequency observed on the spectrum analyser as a function of the frequency set at the VCO and the plot on the bottom shows the diference between the beatnote frequencies observed and set at VCO. The VCO provides accurate beatnote frequency within the range $83\,\text{MHz} - 102\,\text{MHz}$. The reason for which the VCO is not providing the accurate beatnote frequency at $f_{\text{VCO}} < 83$ MHz is that we are close the lower limiting value of the VCO, i.e., 75 MHz. As we approach this value, the amplitude of the signal provided by VCO gradually decreases resulting in an inaccurate operation.

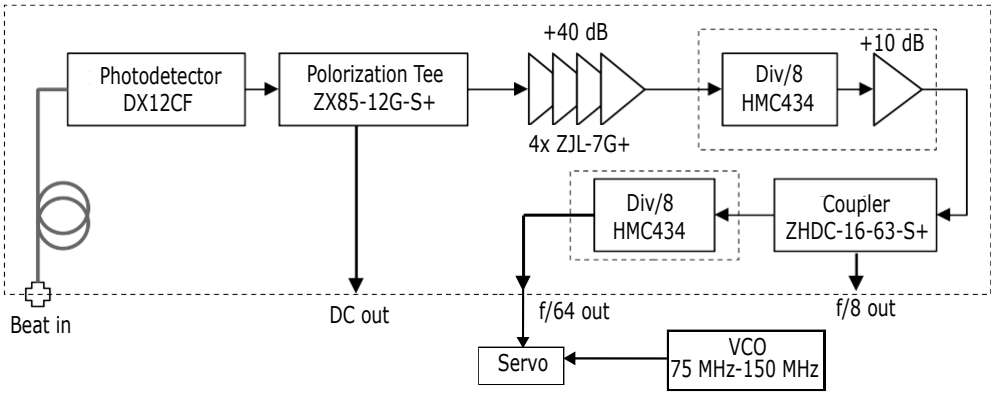



**Figure 6.9** — Sketch of the electronic system for the production of the locking signal. Detection of the beatnote signal between the $F = 1$ laser and the master laser, followed by frequency division.

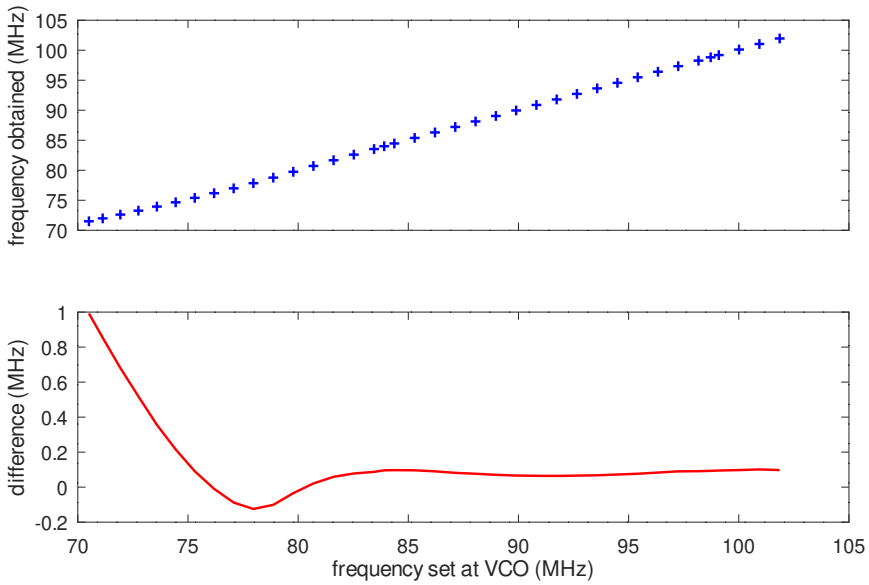



**Figure 6.10** — Beatnote frequency observed on the spectrum analyser as a function of the frequency of the VCO. The second figure shows the difference between the frequency obtained on the spectrum analyser and the frequency set at VCO.

### 6.5.2 Frequency beatnote between the $F = 2$ laser and the master laser

The $F = 2$ laser is controlled by its beatnote at a frequency of approximately at 1228 MHz below the frequency of the master laser. The photodiode used to detect beatnote signal is a model Hamamatsu S5973-01. It has a bandwidth of $\sim 1.5$ GHz and is followed by an amplifier stage with a gain of 40 dB and a bandwidth in the range of 10 kHz to 2 GHz. Fig.6.11 shows the response of the photodiode as a function of frequency.

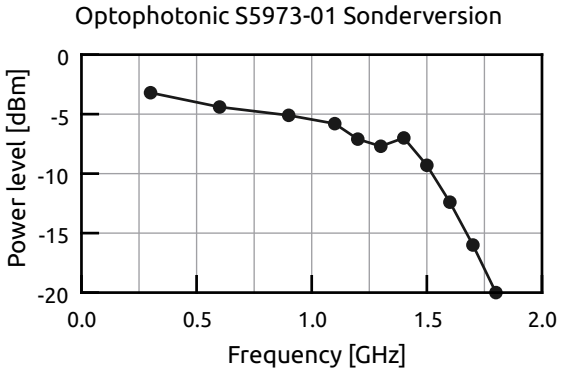



**Figure 6.11** — Frequency response of the photodiode with 200 µW of incident power of each beam.

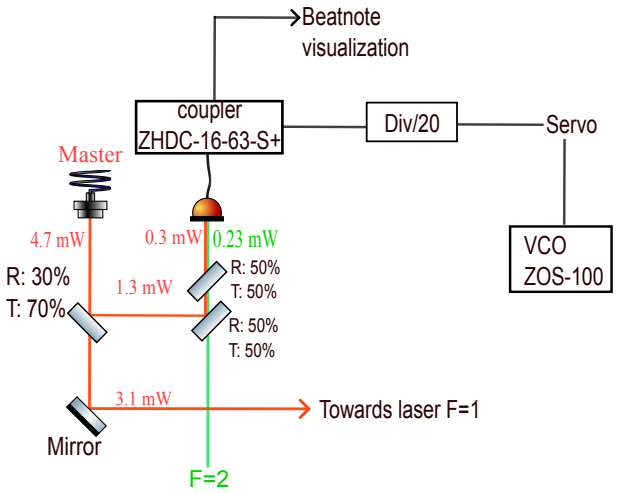



**Figure 6.12** — Setup for obtaining the beatnote frequency of 1228 MHz. In the figure, R refers to the reflection and T to the transmission.

Fig.6.12 shows the different components used to obtain the beatnote frequency signal between the master laser and the $F = 2$ laser.

- We use a ZHDC-16-63-S+ coupler from Mini-Circuits. It has a bandwidth in the range of 50 MHz to 6 GHz. It is used to outcouple a small part of the signal (−16 dB) in order to visualise the beatnote signal before the division step.

- Divider by 20: This divider has been manufactured in the electronic workshop of LPL and is based on a Prescaler MC12080. The division factor, adjustable between 10 and 80, is set here to 20 by logic levels at the component inputs. Although the operating range of the MC12080 is specified as 100 MHz to 1.1 GHz with input levels of −15 dBm to 4 dBm, our box operates up to 1.5 GHz and at lower input powers. For example, we observed correct division at 1.2 GHz with an input level of −23 dBm.

- The voltage-controlled oscillator (VCO) used is ZOS-100 from Mini-Circuits. It works in a frequency range of 50 MHz to 100 MHz and provides a signal with an output power of +9 dBm.

As this laser is locked to the transition $|5S_{1/2}, F = 2\rangle \rightarrow |5P_{3/2}, F = 3\rangle$ of $^{87}$Rb which has a frequency 384 228 115.2 MHz and the AOM used in the optical chain of the laser $F = 2$ is working at a frequency of 109.9 MHz (order +1), the laser has to be at frequency 384 228 005.3 MHz. Therefore the frequency of the beatnote between the master laser and the laser $F = 2$ is 1.228 GHz and after the division by 20 this frequency becomes 61.4 MHz. Fig.6.13 shows the beatnote frequency observed on the spectrum analyser as a function of the frequency set for the VCO. We can note from the following figure that the beatnote frequency obtained is accurate in the range of 50 MHz to 70 MHz, corresponding to a tuning range of 400 MHz for the $F = 2$ laser. The deviation from the lower values of the beatnote frequencies set at VCO for $f_{\mathrm{VCO}} < 50$ MHz is due to the same reason as that of VCO for laser $F = 1$. The deviation for $f_{\mathrm{VCO}} > 70$ MHz is due to the fact that the photodetector's power level drops significantly for the beatnote signal of frequency greater than 1.4 GHz (Fig.6.11), i.e., greater than 70 MHz after the division by 20.

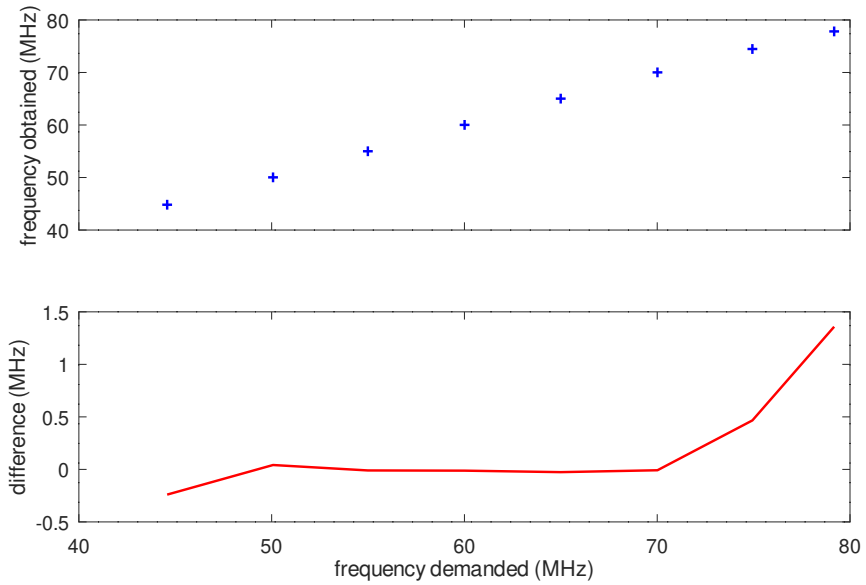



**Figure 6.13** — Beatnote frequency observed on the spectrum analyser as a function of the frequency of the VCO. The second figure shows the difference between the frequency obtained on the spectrum analyser and the frequency set at the VCO.

### 6.5.3 Frequency beatnote between the $F = 2$ laser and the cooling laser

The locking approach for cooling laser is exactly the same as in the previous setup. The only difference is that now the cooling laser is locked through beatnote with the $F = 2$ laser rather than directly with the master laser. Fig.6.14 shows the optical setup for the cooling laser which is exactly the same as before [88]. The beatnote part of the setup is more elaborated in Fig.6.15.

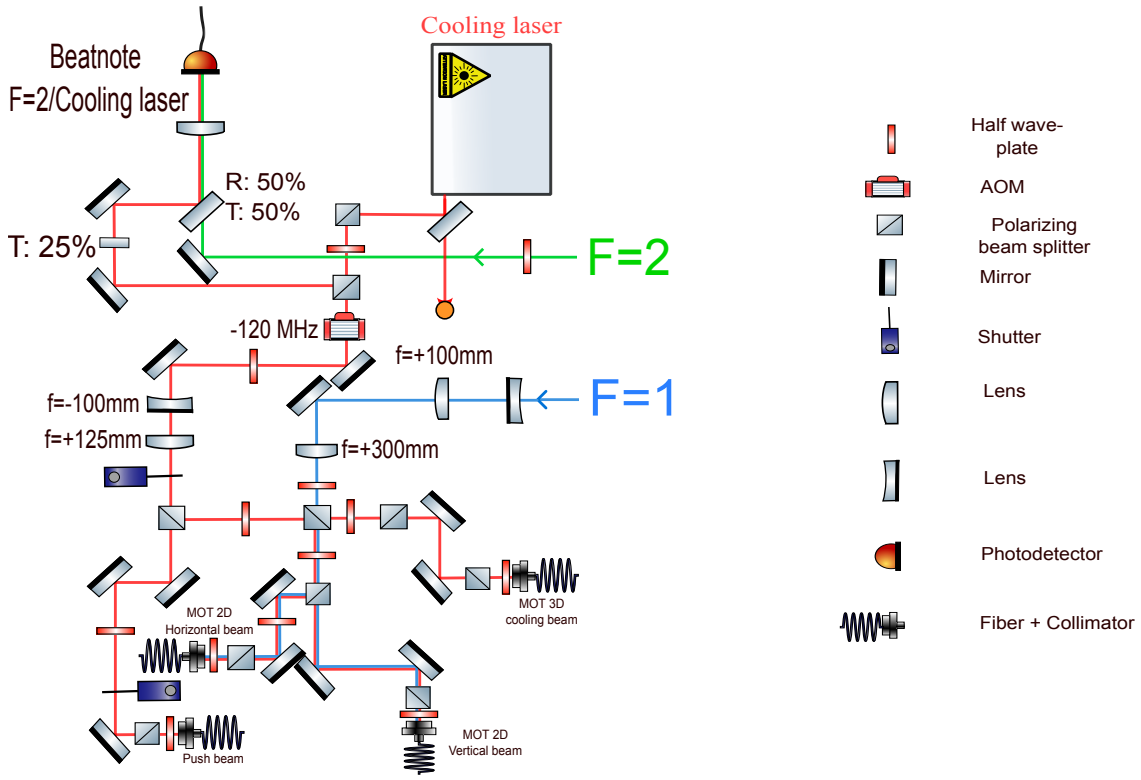



**Figure 6.14** – Optical setup for cooling laser. This setup has not been modified. The only changes as compared to the previous setup [88] are the two laser beams coming from the $F = 2$ and $F = 1$ lasers rather than the master laser and the Sanyo diode laser.

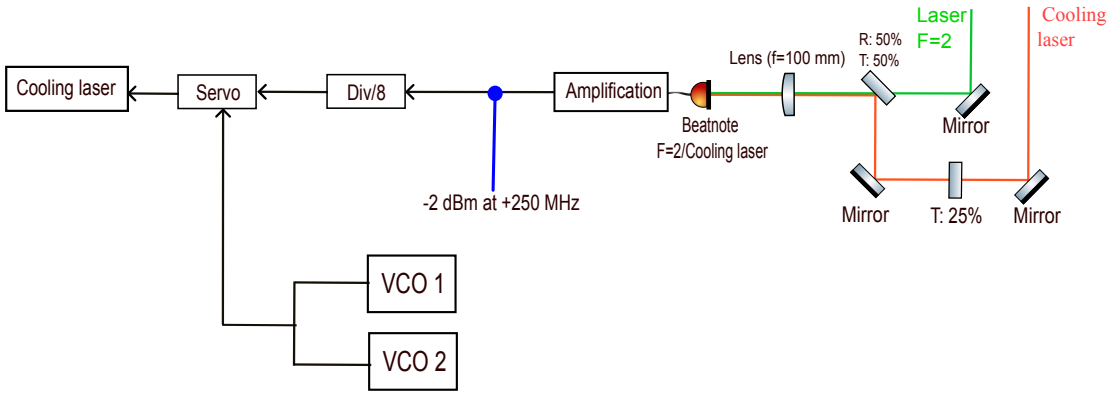



**Figure 6.15** – Sketch of the setup used for obtaining the beatnote signal between the cooling laser and the $F = 2$ laser.

The AOM used in this optical setup is operating at the frequency of 120 MHz (order $-1$) and as the cooling beams for the 2D and 3D MOT are detuned by $-2.25\,\Gamma$ from the transition $|5S_{1/2}, F = 2\rangle \rightarrow |5P_{3/2}, F = 3\rangle$ of $^{87}$Rb, the laser frequency should be $f_{\text{cooling}} = 384\,228\,221.7$ MHz. The frequency of the $F = 2$ laser is $f_{F=2} = 384\,228\,005.3$ MHz therefore

the frequency of the beatnote is $f = 216.6\,\text{MHz}$ and as this beatnote frequency is divided by 8, the final beatnote frequency is 27 MHz. This frequency is quite small to be generated by a single VCO therefore we use two VCOs in the working range of 75 MHz to 150 MHz and take the difference of the frequencies of their respective signal to generate a resultant frequency of 27 MHz.

## 6.6 Problems encountered on the updated setup

I encountered a few problems with the newly installed NarrowDiode lasers after the installation of the optical setup. In the case of the laser $F = 1$, I noticed over time a progressive decrease in the coupling efficiency of all the fibers (3D-MOT repumper, resonant repumper, off-resonant repumper and the non-destructive beam) associated with this laser. This was due to the fact that the laser beam itself was deviating from its initial position (chosen during the alignment). The deviation was larger along the horizontal direction than the vertical. The reason behind this deviation was that the last collimation lens (labeled as 8 in Fig.6.6) was not well-fixed. In fact the diameter of the mount was slightly bigger than the diameter of the support of the lens thus making it difficult to stay stable. To overcome this problem, we decided to glue it, applying the following procedure: I first encircled a layer of thread seal tape over the support of the lens. In this way I could fix the lens in the mount tight enough to fix it with a small amount of glue at the top between the mount and the support of the lens. In the case of the $F = 2$ laser, the problem was more complicated. A rise in the threshold value of the current was observed over time, resulting in a reduced power delivered by the laser as compared to its initial performances for a given value of the current (Fig.6.16).

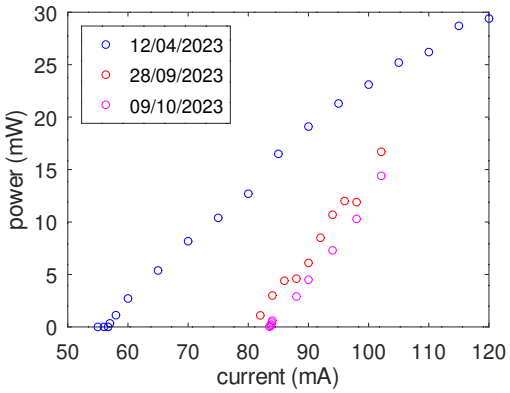
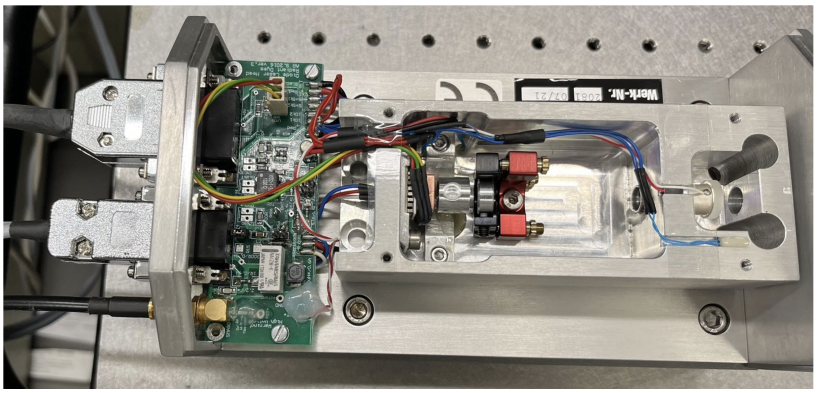


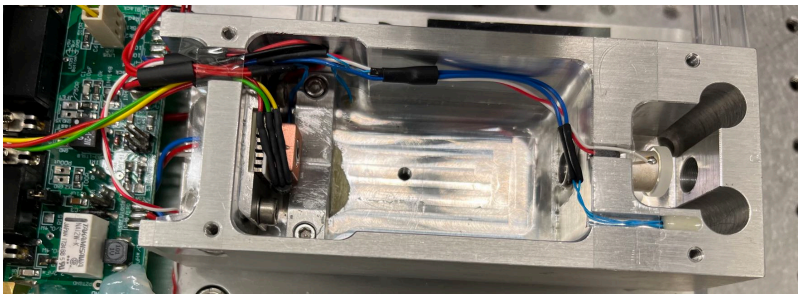

**Figure 6.16** — Power delivered by the laser $F = 2$ as a function of current for three different dates.

The solution to this problem needed the realignment of the cavity of the laser. For the realignment procedure, I followed the steps mentioned in the document sent by the Radiant Dyes company to our request. I started by removing the first collimation lens and the interferential filter (Fig.6.17). I then prepared the homemade positioning setup to place and adjust the collimation lens to its optimal position as shown in Fig.6.18. We can see in Fig.6.18 that the lens is attached with a point of glue at the tip of the stem. With this configuration, I made sure that the beam after the first lens is collimated and is centered on the first lens.

I then observed the signal of the laser beam on the photodiode while modulating the current to reduce the lasing threshold. After optimising the position of the lens in the $x$, $y$ and $z$ direction, I obtained the lasing operation.



**(a)** Before intervention



**(b)** After the removal of the interferential filter and the collimation lens.

**Figure 6.17** — Cavity of the $F = 2$ laser.

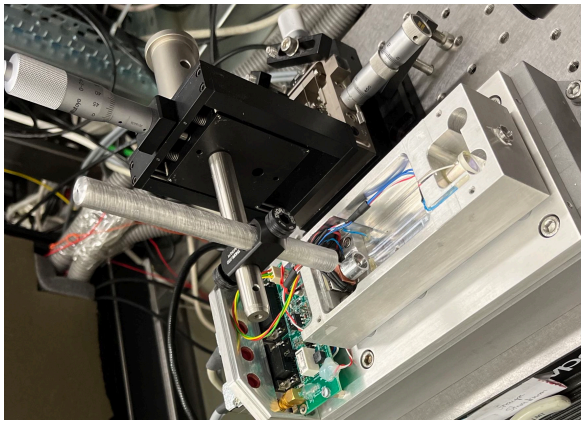


**Figure 6.18** — Homemade setup designed to place and adjust the collimation lens to its optimal position. This homemade positioning setup allows us to move the lens in the $x$, $y$ and $z$ directions.

Once the laser operation is established, I measured the power delivered by the laser as a function of current and the threshold from this measurement was found to be at 40 mA. Fig.6.19 shows the measurement performed after the optimisation of the position of the collimation lens.

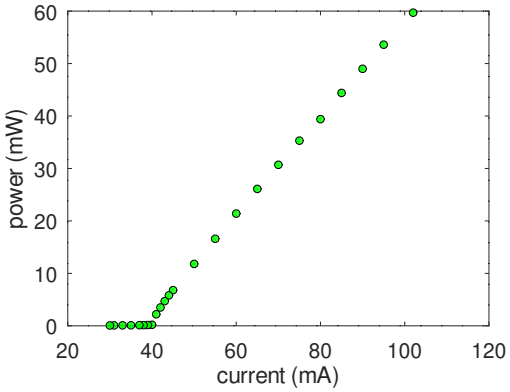



**Figure 6.19** — Measurement of the threshold for lasing: power delivered by the $F = 2$ laser as a function of current after the alignment of the collimation lens.

After this, I placed the interferential filter back, as shown in Fig.6.20. I adjusted its position by touching is vertical and horizontal alignment. The horizontal alignment was more critical. Finally, I achieved the working point for this laser ($f = 384\,228.1$ GHz) at the current value of $I = 102$ mA and the temperature of the laser diode at 20.1 °C and the voltage for the piezo element at 350 V.

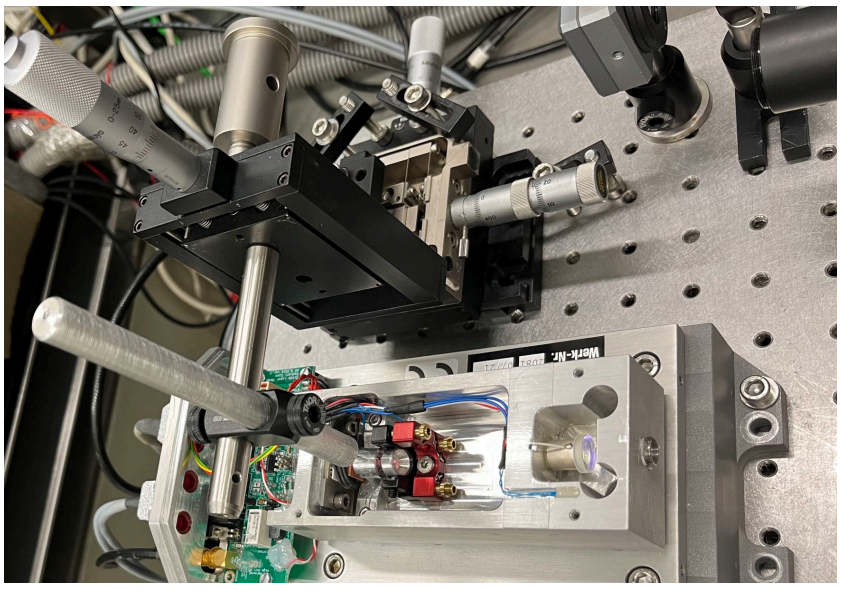


**Figure 6.20** — Cavity after the realignment procedure.

After the adjustment of the interferential filter, I measured the power delivered by the laser

as a function of the current to determine the threshold value after the complete realignment. The threshold was found at 45 mA (Fig.6.21).

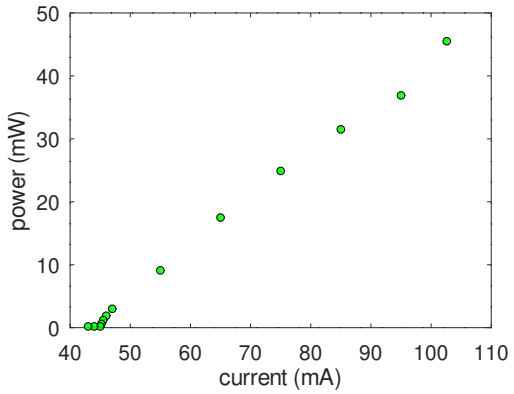



**Figure 6.21** — Measurement of the threshold for lasing after complete realignment.

As soon as the alignment procedure was completed I glued the collimation lens using "LOCTITE EA3423" to its holder at its basis exactly in the same way as it was before the alignment procedure. This glue gets harder very slowly thus allowing us to realign the lens during this time. I then monitored the power delivered by the laser at a given current (102 mA, every hour on the following day. Whenever I observed a drop in the delivered power, I touched the positioning of the collimation lens to optimise the delivered power. Once the lens was perfectly glued to its support I removed the stem attached to it by gently pulling it up using the alignment setting in the vertical direction (Fig.6.18).

## 6.7 Conclusion

In this chapter, I described the newly updated experimental setup, with the saturated absorption scheme implemented to lock the master laser on the crossing line of the transitions $F = 3 \longrightarrow F' = 3\&4$ of $^{85}$Rb, and the use of this laser's frequency as a reference for locking other lasers using beatnote. This optical setup provides all the beams necessary for the experiment with the required tunability of their frequencies. As soon as this update was done we could find the usual performance of the experiment, i.e., a few $10^5$ ultracold atoms sample at around 190 nK in the bubble trap with a lifetime of 120 s. We could also perform the in-trap non-destructive imaging of the atoms (details in chapter 7). This new optical setup is more robust and less complicated as compared to the setup explained in Chapter 3 as we have less lasers used in the experiment. To be specific, we only have one repumping laser, that can be tuned widely to serve both as resonant repumper and as a far-detuned repumper for imaging dense clouds. The same laser can also be used to implement a non-destructive imaging scheme, that will be described in the next chapter.

# Chapter 7

# Non-destructive imaging

In this chapter, I will discuss a non-destructive in-trap imaging of the ultracold atoms we have recently implemented in our experiment. The motivation behind implementing this method is to overcome the limitation of the absorption imaging method, i.e., one experimental measurement per sequence. This makes the acquisition of a dataset more time-consuming and in addition, the measurements performed using the absorption imaging method are more prone to experimental fluctuations. The non-destructive imaging method in an experiment allows us to take several in-trap images of the ultracold atoms without completely destroying the sample [102], which is mandatory to follow a time-dependent phenomenon that cannot be reproduced with the exact same initial conditions in successive experimental runs. The destruction of the atomic sample depends on the detuning of the probe beam from the imaging transition, the probe pulse duration and its intensity $I$. In this chapter, I will use the term saturation parameter $s_0 = I/I_{\text{sat}}$ with $I_{\text{sat}}$ being the saturation intensity of the imaging transition, to discuss destructiveness of signal for different intensities of the probe beam.

## 7.1 Theory of non-destructive imaging

To understand the physics behind this imaging method, I will start by writing the refractive index of the atomic ensemble [148]:

$$n(\mathbf{r}, z) = 1 + \frac{\sigma_0 \lambda \rho(\mathbf{r}, z)}{4\pi} \left( \frac{i}{1+\delta^2} - \frac{\delta}{1+\delta^2} \right) \tag{7.1}$$

where $\sigma_0$ is the resonant cross-section, $\lambda$ is the wavelength, $\rho$ is the atomic density, $\delta = \Delta/(\Gamma/2)$ is the probe detuning $\Delta$ in units of the line-width $\Gamma$, $z$ is the position along the imaging axis and $\mathbf{r}$ is the position in the plane transverse to the imaging axis. As the probe beam interacts with the atomic cloud, it gets attenuated and phase-shifted and the resultant field can be written as:

$$E(\mathbf{r}) = E_0 \exp\left( i \frac{2\pi}{\lambda} \int (n(\mathbf{r}, z) - 1) dz \right) = t(\mathbf{r}) E_0 e^{i\phi(\mathbf{r})} \tag{7.2}$$

where $t(\mathbf{r})$ and $\phi(\mathbf{r})$ are the transmission coefficient and the phase-shift:

$$t(\mathbf{r}) = \exp\left(-\frac{\tilde{n}(\mathbf{r})\sigma_0}{2}\frac{1}{1+\delta^2}\right), \tag{7.3}$$

$$\phi(\mathbf{r}) = -\frac{\tilde{n}(\mathbf{r})\sigma_0}{2}\frac{\delta}{1+\delta^2}. \tag{7.4}$$

$\tilde{n}(\mathbf{r}) = \int n(\mathbf{r}, z)dz$ is the column density. When the probe is at resonance with the imaging transition ($\delta = 0$), there is no phase-shift and only the imaginary part of the refractive index contributes to the resultant signal in the form of absorption. When the probe beam is very far detuned from the imaging transition and its intensity and pulse duration are optimised to limit resonant scattering, the transmission coefficient approaches 1 and the phase-shift becomes non-zero. Therefore the information of the atomic cloud is now encoded in this phase-shift of the probe beam. In order to deduce the density profile of the atomic cloud, we thus need to retrieve the phase-shift of the probe.

During the imaging process we image an atomic cloud for a certain duration of time $t$ therefore we need to consider the effect of the probe on the atomic cloud in order make the imaging procedure non-destructive. The scattering rate for a two-level system can be expressed as:

$$R_{\text{scatt}} = \frac{\Gamma}{2}\frac{s_0}{1+s_0+\delta^2}. \tag{7.5}$$

We can estimate the increase of cloud's temperature for a probe pulse of duration $t$ as [149]:

$$\Delta T = 2tT_{\text{rec}}R_{\text{scatt}}, \tag{7.6}$$

where $T_{\text{rec}}$ is the recoil temperature for $^{87}$Rb and is around 360 nK. Fig.7.1 represents the increase in atomic cloud's temperature per unit of time as a function of detuning for three different values of saturation parameter $s_0$ and the probe pulse duration of 20 µs.

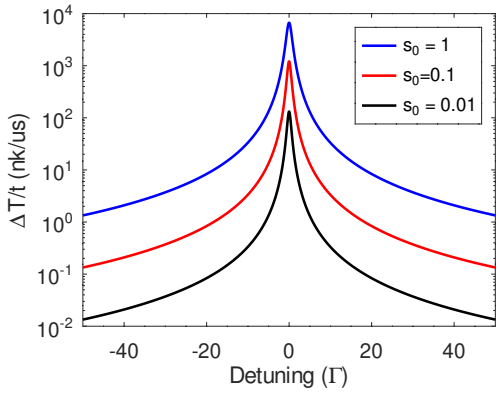



**Figure 7.1** — Theoretical prediction of increase in cloud's temperature per unit of time as a function of detuning for a two-level system for three different values of $s_0$. The atomic species considered here is rubidium and the probe pulse duration is 20 µs.

We will see later in this chapter (in Sec.7.4.1) that we can not simply choose to work with low intensities of the probe beam and high detunings in order to make the process more

non-destructive as these conditions will also result in low signal to noise ratio (SNR). We will recall this model in Sec.7.4.1 when commenting on the experimental results. In the next section, I will explain the different techniques that exist to perform non-destructive imaging on ultra-cold atoms and which one of them we have implemented in our experiment.

## 7.2 Different available techniques

One of the common methods for performing non-destructive imaging is the dark-field imaging [150–152]. This technique relies on separating the non-interacting part of the probe beam and leaving only the scattered light contribute to the signal recorded by the camera. Fig.7.2 represents the setup for the dark field imaging where the probe beam which is far-detuned from the resonance is shone on the atomic sample. The part of the light which interacts with the atoms experiences the dispersion which is collimated by the first lens and then focused on the camera by the second lens while the unperturbed part of the probe beam is focused by the first lens on the dark spot which absorbs the light.

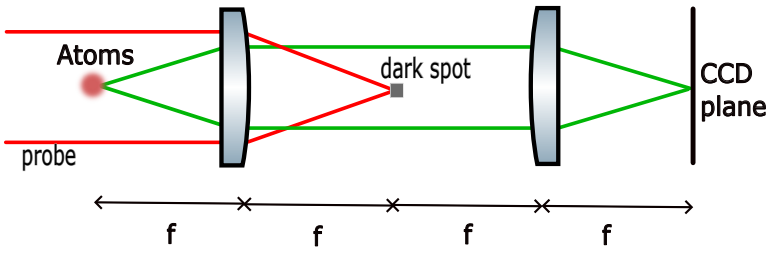



**Figure 7.2** — Diagram of the dark-field imaging setup.

The intensity signal detected by the camera can be written as:

$$I(\mathbf{r}) = \frac{1}{2} c\epsilon_0 |E(\mathbf{r})|^2, \tag{7.7}$$

where $c$ is the speed of light, $\epsilon_0$ is the vacuum permittivity and $E$ is the electric field after the interaction of the probe beam with the atomic sample and is given by:

$$E(\mathbf{r}) = E_{\text{probe}}(t(\mathbf{r})e^{i\phi(\mathbf{r})} - 1). \tag{7.8}$$

Here $-1$ is specific to the dark spot. The intensity equation can be rewritten as:

$$I(\mathbf{r}) = I_0(t(\mathbf{r})^2 - 2t(\mathbf{r})\cos\phi(\mathbf{r}) + 1), \tag{7.9}$$

where $I_0 = \frac{1}{2} c\epsilon_0 |E_{\text{probe}}|^2$. As the probe beam is vary far detuned, the absorption is very small and the transmission coefficient is of the order of 1. In this case, the above intensity equation can be simplified as:

$$I(\mathbf{r}) = 2I_0(1 - \cos\phi(\mathbf{r})). \tag{7.10}$$

We can further develop this expression of the intensity through a Taylor expansion in the limit where the phase-shift caused by the atomic sample is small:

$$I(\mathbf{r}) \approx I_0\phi(\mathbf{r})^2. \tag{7.11}$$

The limitation of this method is that the position of the dark-spot has to be precise to microns which makes the implementation of this imaging setup challenging. Another limitation is that in the dark-field imaging method, the noise of the camera itself become considerable. There exists an improved version of this imaging method called phase-contrast imaging where the dark-spot is replaced by an optical object called phase-plate in order to boost the signal-to-noise [153, 154].

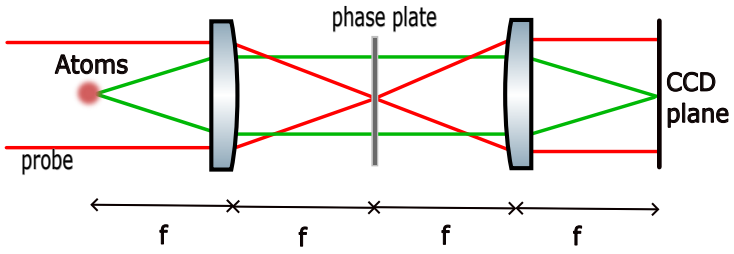



**Figure 7.3** — Diagram of the phase-contrast imaging setup.

Fig.7.3 represents the diagram of a phase-contrast imaging setup where the part of the probe which interacts with the atoms is re-imaged on the CCD camera in the same way as described in the dark-field imaging scheme. However, the non-interacted light is now focused by the first lens on the phase-plate which is an optically flat object with a small dip or bump in the center. When the non-interacted light is focused at the center of this phase-plate, it acquires a phase-shift and is then re-imaged on the CCD by the second lens. In this case, we observe an increase in the final signal on the camera as compared to the dark-field imaging as now we have the contribution from the non-interacted part of the probe beam. We can write the final electric field as:

$$E(\mathbf{r}) = E_{\text{probe}} e^{i\theta} + E_{\text{probe}}(t(\mathbf{r}) e^{i\phi(\mathbf{r})} - 1), \tag{7.12}$$

where $\theta$ is the phase-shift acquired by the non-interacted part of the probe beam from the phase-plate. The intensity of the signal incident on the camera is:

$$I(\mathbf{r}) = I_0(2 + t(\mathbf{r})^2 - 2t(\mathbf{r}) \cos\phi(\mathbf{r}) + 2t(\mathbf{r}) \cos(\phi(\mathbf{r}) - \theta) - 2\cos\theta). \tag{7.13}$$

In the case where $\theta = \frac{\pi}{2}$ and the phase-shift is small, the final intensity can be written as:

$$I(\mathbf{r}) = I_0(1 + 2\phi(\mathbf{r})). \tag{7.14}$$

The value of the phase-shift $\theta$ is constant and is fixed by the manufacturer which is the limitation of using this imaging method and also the alignment of the phase-plate needs to be precise.

Another well-known imaging method is called the polarization phase contrast imaging, where a magnetic field is used to polarize the spin of the atomic sample and rotate the polarization of the interacted part of light through birefringence in comparison with the non-interacted part of the probe beam [155–157].

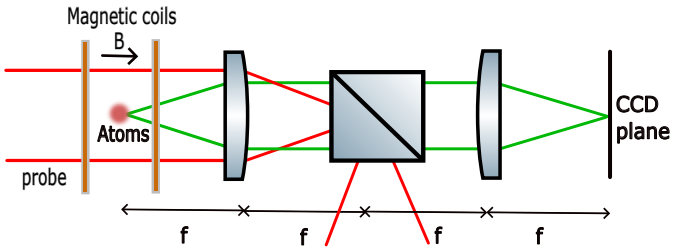



**Figure 7.4** — Diagram of the polarization phase-contrast imaging setup.

Through this method, we can either work in the dark-field regime or in the bright-field regime (phase-contrast imaging) by rotating the polarization of the probe beam thus making it possible to perform two different imaging methods without having a need of a dark-spot or a phase-plate. However, it requires an additional magnetic field to operate and a polarizer beam-splitter in the optical path. In our case, to perform non-destructive imaging we want to conserve the same optical setup as for absorption imaging in order to perform both measurements along the same axis without making any principal change in the optical setup.

In order to be able to perform both non-destructive and absorption imaging of the atoms the most convenient technique that I found is Shadowgraph Imaging which has already been implemented and tested on an ultra-cold atom experiment [102]. In the next section, I will explain this imaging technique.

## 7.3 Shadowgraph imaging

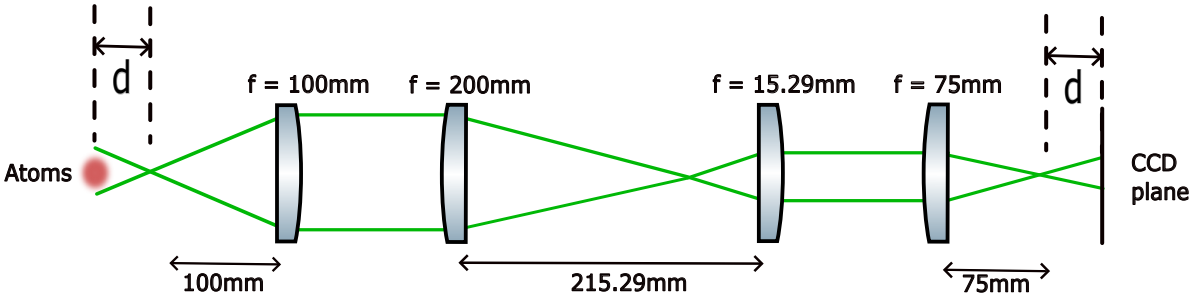



**Figure 7.5** — Diagram of a shadowgraph imaging setup.

Shadowgraph imaging, unlike dark-field imaging, phase-contrast imaging, or polarization phase-contrast imaging, does not require any additional optical elements other than those of a standard absorption imaging setup. The working principle of this method is however the same as other methods, i.e., we use a very far detuned probe beam which gets phase-shifted as it interacts with the atomic cloud. This imaging technique was first described by R. Hooke [158] and has been widely used in X-ray tomography [159].

Fig.7.5 represents the optical setup for implementing shadowgraph imaging along the vertical axis in our experiment and it is the same as the one described in Chapter 3. The only difference is that the imaging plane is off-focused by a distance $d$ from the atoms. As the

probe beam after the interaction with the atoms produces a diffraction pattern, the intensity of which is governed by the Fresnel propagator $P_d$ in the near-field regime:

$$P_d(\mathbf{r}) = \frac{1}{i\lambda d} \exp\left(i\frac{\pi}{\lambda d}|\mathbf{r}|^2\right), \tag{7.15}$$

we can define the intensity recorded in the CCD camera after a distance of propagation $d$ as the modulus square of the convolution of the electric field with the Fresnel propagator:

$$I_d(\mathbf{r}) = |E(\mathbf{r}) * P_d(\mathbf{r})|^2, \tag{7.16}$$

where $*$ denotes the convolution operator. The above equation becomes easier when transformed in the Fourier space. We can define the Fourier transform as:

$$\tilde{g}(\mathbf{f}) = \int g(\mathbf{r}) \exp\left(-i2\pi\mathbf{r}\cdot\mathbf{f}\right) d\mathbf{r}. \tag{7.17}$$

Under this convention, we can write the Fresnel propagator in the Fourier domain as:

$$\tilde{P}_d(\mathbf{f}) = \exp\left(-i\pi\lambda d|\mathbf{f}|^2\right). \tag{7.18}$$

The final intensity after the Fourier transformation can be expressed as:

$$\tilde{I}_d(\mathbf{f}) = \int E\left(\mathbf{r} - \frac{\lambda d}{2}\mathbf{f}\right) E^*\left(\mathbf{r} + \frac{\lambda d}{2}\mathbf{f}\right) \exp\left(-i2\pi\mathbf{r}\cdot\mathbf{f}\right) d\mathbf{r}. \tag{7.19}$$

For the small values of $d$ (Fresnel regime, $d \ll 2R_{\mathrm{TF}}^2/\lambda$), where $R_{\mathrm{TF}}$ is the Thomas-Fermi radius of the atomic cloud and $\lambda$ is the wavelength of the probe beam, we can approximate the electric field after the interaction using the Taylor expansion as:

$$E\left(\mathbf{r} \pm \frac{\lambda d}{2}\mathbf{f}\right) \approx E(\mathbf{r}) \pm \frac{\lambda d}{2}\mathbf{f}\cdot\nabla E(\mathbf{r}). \tag{7.20}$$

After substituting this expression of the electric field in Eq.(7.19) and taking the inverse Fourier transform, we get the following expression of the final intensity:

$$I_d(\mathbf{r}) = I_0(\mathbf{r}) - \frac{\lambda d}{2\pi}\nabla[I_0(\mathbf{r})\nabla\phi(\mathbf{r})]. \tag{7.21}$$

As we can notice, this method requires two intensity profiles at two different positions in order to solve the inverse problem. However, we can simplify this problem assuming that the absorption is negligible ($t(\mathbf{r}) \approx 1$) and as the extension of the atomic cloud ($R_{\mathrm{TF}} \approx 20\,\mu\mathrm{m}$) is very small compared to the waist of the probe beam ($w = 0.7\,\mathrm{mm}$), $I_0(\mathbf{r}) \approx I_0$ and can be taken outside the gradient operator. This approximation will allow us to take images at a single position along the direction of propagation:

$$I_d(\mathbf{r}) = I_0\left[1 - \frac{\lambda d}{2\pi}\nabla^2\phi(\mathbf{r})\right]. \tag{7.22}$$

This approximation is called the transport-of-intensity equation (TIE) [159]. We can now simply write the phase-shift as:

$$\phi(\mathbf{r}) = -\frac{2\pi}{\lambda d}\nabla^{-2}\left[\frac{I_d(\mathbf{r})}{I_0} - 1\right]. \tag{7.23}$$

The difficult part here is to compute the inverse of the Laplacian. In order to simplify the calculation we can transform the inverse of the Laplacian in the Fourier space as follows:

$$\nabla^{-2} = \frac{1}{4\pi^2}\mathcal{F}^{-1}\frac{1}{f_x^2 + f_y^2 + \alpha}\mathcal{F}, \tag{7.24}$$

where $\alpha = (\max(D_x, D_y))^{-1}$ is the regulation parameter used to fix the singularity which occurs at the origin of the Fourier domain ($f_x = f_y = 0$) [160] and $D_x$ and $D_y$ are the dimensions of the image. As the value of $\alpha$ depends on the dimension of the image, the method is more efficient when the dimension is chosen close around the shadowgraph signal.

### 7.3.1 Alignment of the camera

#### 7.3.1.1 Focal point

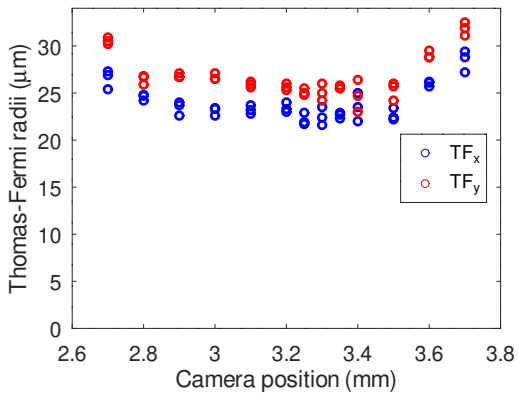



**Figure 7.6** — Thomas-Fermi radii of the BEC imaged in situ along the vertical direction using absorption imaging.

For the successful implementation of the shadowgraph imaging technique, the position of the imaging plane from the atomic cloud position is crucial in order to achieve the diffraction pattern of the intensity profile while still being in the near-field regime as TIE approximation works well for a small distance of propagation. For the imaging purpose, we are using the same camera (LUCA-R from ANDOR technology) as before. To calibrate the position of the CCD camera we first determined the position of the focus with respect to the atoms by performing absorption imaging. To perform this experiment we prepared the BEC in a bubble trap using the experimental sequence described in Chapter 5 and then we imaged the atomic cloud in situ using the resonant probe beam locked on the transition $F = 2 \longrightarrow F^{'} = 3$ of the $D_2$ line of $^{87}$Rb. In Fig. 7.6 I have plotted the Thomas-Fermi radii along the $x$ and $y$ axis of the atomic cloud imaged in situ along the vertical direction. For each position of the camera, three experimental runs were performed. The focal position corresponds to the minimum size of the imaged cloud. The position of the focus was found to be 3.3 mm. The cloud appears sharp with absorption imaging over a relatively wide range, typically $\pm 0.1$ mm. Given the lens numerical aperture (NA$\sim$ 0.1), this is not unreasonable, it is within the expected depth of field of $\pm 80\,\mu$m.

#### 7.3.1.2 Determination of the distance of propagation ($d$)

Once the focus point of the imaging plane with respect to the atoms has been determined, we need to find a suitable distance of propagation ($d$) from the focal point in our experiment in order to perform the shadowgraph imaging. For this purpose, we record the intensity profiles of the shadowgraph signal as a function of the position of the CCD camera for two values of the probe detuning, $\pm 85\,\Gamma$. As explained in Chapter 6 this probe is different from the resonant probe beam and is dedicated to perform non-destructive in situ measurements. As the atoms are in state $F = 1$ in the bubble trap, in order to perform in situ shadowgraph measurements as a function of the position of the camera, the non-destructive probe is detuned from the transition $F = 1 \longrightarrow F^{'} = 2$ of the $D_2$ line of $^{87}$Rb (Fig.7.7).

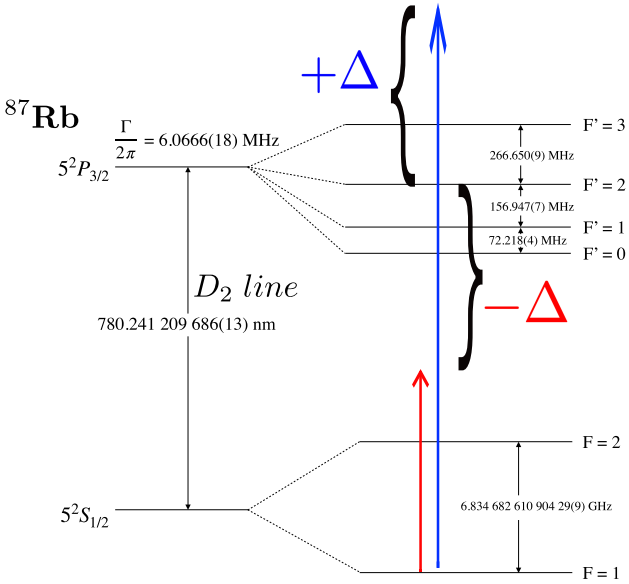
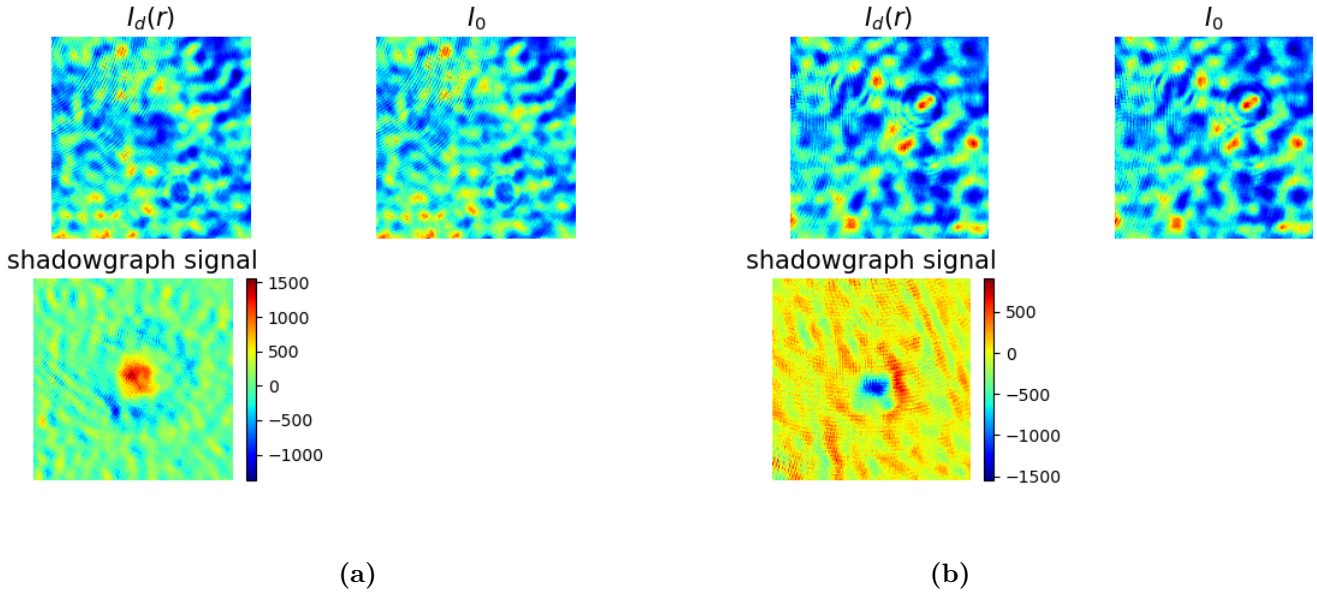



**Figure 7.7** — Energy level diagram of the $D_2$ line of $^{87}$Rb along with the non-destructive probe beam (green arrow) locked on the transition $F = 1 \longrightarrow F^{'} = 2$. The blue arrow represents the positive detuning of the probe beam ($+\delta$) and the red downward arrow represents the negative detuning of the probe beam ($-\delta$).

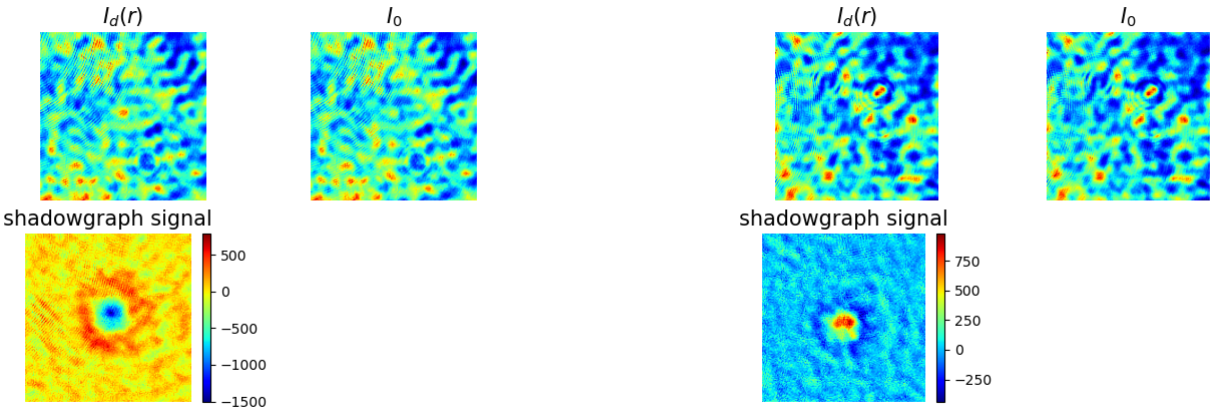
This probe beam is injected into the same vertical fiber as that of vertical resonant probe beam (as described in Chapter 6). This is done to be able to perform imaging by both absorption and non-destructive means. We use two shutters for the two probe beams before the entry of fiber and this helps us to block or let one of the probe pass through the fiber depending on the chosen method of imaging. In order to image the shadowgraph signal, while we prepare the BEC in a bubble trap, we change the polarization of the liquid crystal waveplate (details in Chapter 6) two seconds before the imaging sequence to direct the beam of $F = 1$ laser towards the vertical imaging fiber. We then ramp the detuning of the probe beam from 0 to $\pm 85\,\Gamma$, 1.1 s before the beginning of the imaging sequence. Once we have prepared the BEC, we hold it for 100 ms in the trap and we take the in situ image 10 ms before the end of the holding time followed by the image of the probe beam without atoms 30 ms after the first image. Fig.7.8a and 7.8b show the shadowgraph signal for the detuning of $-85\,\Gamma$ at the camera position 2.14 mm and 3.7 mm. The shadowgraph signal is simply

approximated as $(I_d(\mathbf{r}) - I_0)$, without computing the inverse Laplacian. Fig.7.9a and 7.9b show the shadowgraph signal for the detuning of $+85\,\Gamma$ at the camera position 2.14 mm and 3.7 mm.




**(a)** **(b)**

**Figure 7.8** — Shadowgraph signals along with the probe profile with and without atoms for two different vertical positions of the CCD camera, a) 2.14 mm and b) 3.7 mm at a detuning of $-85\,\Gamma$.




**(a)** **(b)**

**Figure 7.9** — Shadowgraph signals along with the probe profile with and without atoms for two different vertical positions of the CCD camera, a) 2.14 mm and b) 3.7 mm at a detuning of $+85\,\Gamma$.

In Fig.7.10, the shadowgraph signal value at the center of the intensity profiles normalized by the intensity profile taken at the focal point is plotted as a function of the camera position. The signal for both detunings is of different sign and it goes from negative to positive for $+85\,\Gamma$ and from positive to negative for $-85\,\Gamma$ while passing through the focal point as we scan the position of the camera along the vertical direction. The points between 3 mm and 3.4 mm are not plotted intentionally in Fig.7.10 as the signal at these point around the focus was not intense enough to be observed on the camera.

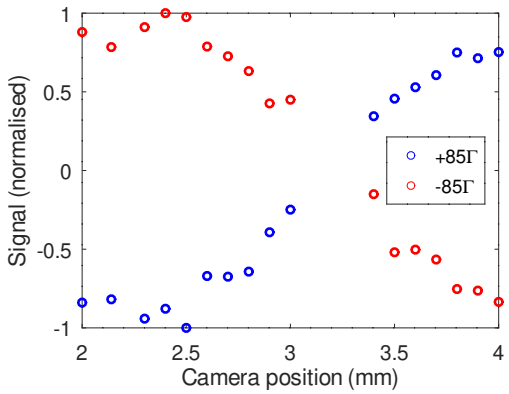



**Figure 7.10** — Scan of the vertical position of the CCD camera. The shadowgraph signal is recorded for a detuning of $\pm 85\,\Gamma$.

We chose 3.7 mm to be the vertical position of the camera to perform non-destructive imaging with positive detunings of the probe beam as this was the first point from the focus at which we observed a clear shadowgraph signal.

### 7.3.2 Measurement of Thomas-Fermi radius

The distance of propagation $d$ that we have chosen is already larger ($400\,\mu$m) than our assumption for TIE approximation. At this distance of propagation, using TIE approximation on the following theoretical density model:

$$n(\mathbf{r}) = \frac{4}{3}\frac{\mu R_z}{g_{\text{int}}}\left(1 - \frac{x^2}{R_x^2} - \frac{y^2}{R_y^2}\right)^{\frac{3}{2}}, \tag{7.25}$$

we observe around 6% increase in the values of Thomas-Fermi radii of the computed density profile as compared to that at $d = 1\,\mu$m. Fig.7.11 and Fig.7.12 represent the density profile of theoretical model and computed density profiles using TIE approximation for $d = 1\,\mu$m and $d = 400\,\mu$m. The trap parameters used for the model are identical as the ones of our experiment and we took $10^5$ atoms and $\Delta = 100\,\Gamma$. We can note from Fig.7.12 that for large distance of propagation we start to observe an additional diffraction ring and the main signal starts to broaden which leads to the increase in Thomas-Fermi radius.

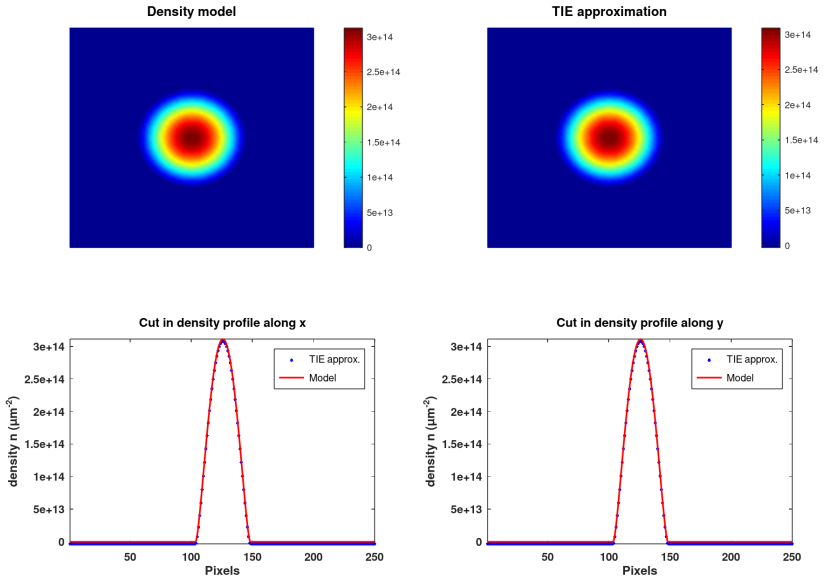



**Figure 7.11** — Top row: density profile of the theoretical model and density profile computed using the TIE approximation on the theoretical signal for $d = 1\,\mu\text{m}$ and $\Delta = 100\,\Gamma$. Bottom row: cut in both the density profiles along $x$ and $y$.

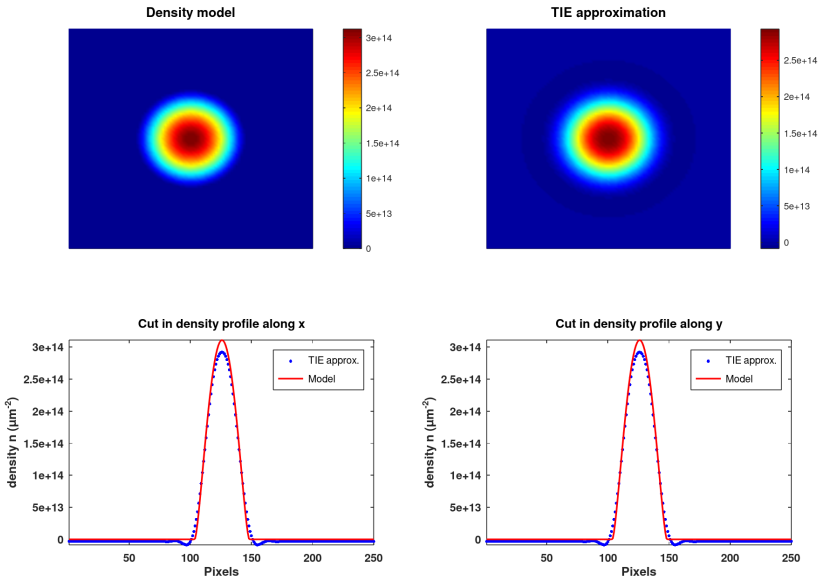



**Figure 7.12** — Top row: density profile of the theoretical model and the density profile computed using the TIE approximation on the theoretical signal for $d = 400\,\mu\text{m}$ and $\Delta = 100\,\Gamma$. Bottom row: cut in both the density profiles along $x$ and $y$.

Once we have acquired the intensity profiles with atoms after the propagation and the intensity profile without atoms in our experiment, we can retrieve the phase-shift using Eq.7.23. Fig.7.13 represents the shadowgraph signal taken at a camera position of 3.7 mm and the

phase-shift retrieved using this signal for a probe beam of detuning $+85\,\Gamma$, the pulse of duration $20\,\mu s$ and $s_0 = 20$.

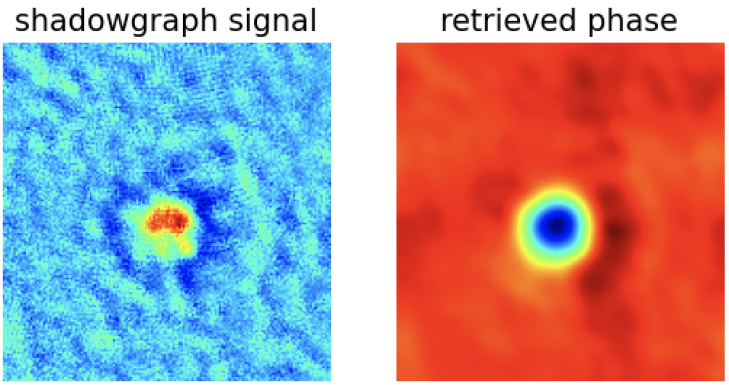



**Figure 7.13** — Shadowgraph signal (left) and the phase-shift signal (right) retrieved using Eq.(7.23). The detuning of the probe beam is $+85\,\Gamma$ and the pulse duration is $20\,\mu s$.

Now as we have the information of the phase, we can simply compute the optical density of the ultra-cold sample using Eq.(7.4). Fig.7.14 shows the computed atomic density of the sample with the Thomas-Fermi radius of $23\,\mu m$. The red square in Fig.7.14 is to define the region of interest in order to calculate the signal to noise ratio (SNR). In this particular measurement the SNR is found to be 45 which is significantly lower as compared to the absorption imaging (SNR $\sim 600$).

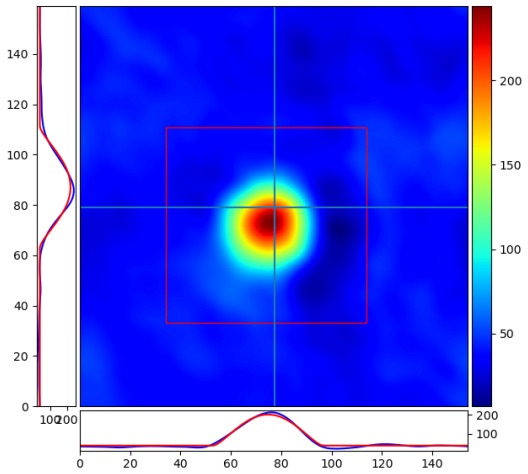



**Figure 7.14** — Atomic density of an ultracold sample in a bubble trap imaged in situ using the shadowgraph technique. The sample has a Thomas-Fermi radius of $23\,\mu m$.

The fitted Thomas-Fermi radius agrees with the in situ measurement measurement performed at focus using the absorption imaging (Fig.7.6). The density profile of the BEC imaged in situ at the focus using absorption imaging is shown in Fig.7.15.

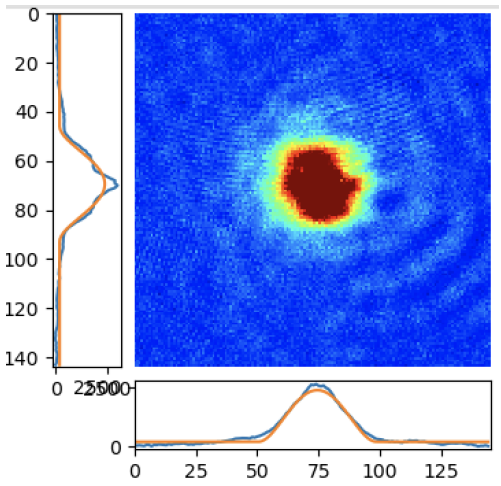
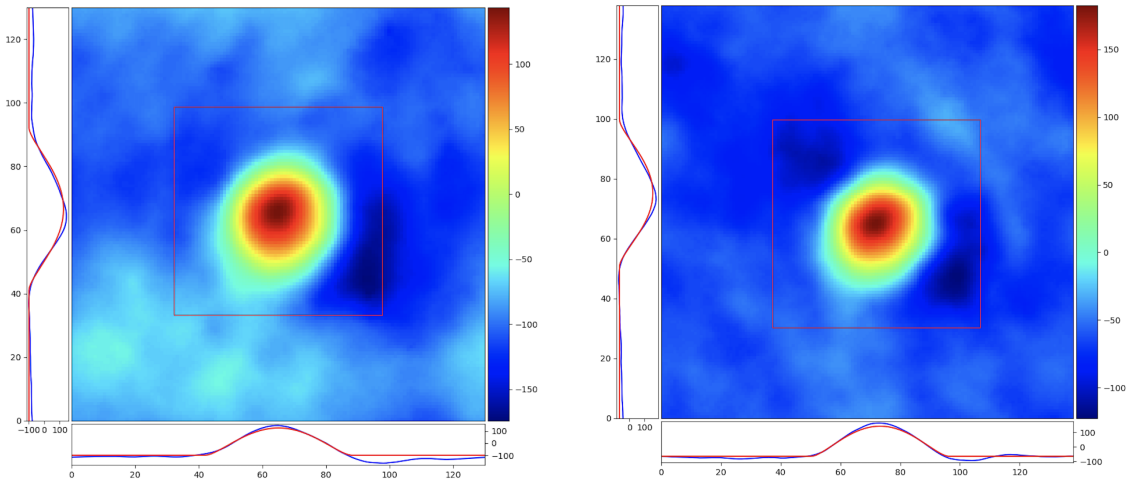



**Figure 7.15** — Atomic density of the sample imaged in situ using absorption imaging method. We find a Thomas-Fermi radius of 24 µm.

### 7.3.3 Effect of the EMCCD gain



**(a)** **(b)**

**Figure 7.16** — Density profile of an ultracold sample imaged using a) no EMCCD gain, b) EMCCD gain = 40.

Now the goal is to test shadowgraph imaging for different values of detuning and the saturation parameter in order to find a optimal values for which the destruction is minimum and we still have enough signal to be imaged by the camera. We will first look at the single

non-destructive measurement using a probe deutuned by $\Delta = +85\,\Gamma$ with pulse duration of 20 µs and $s_0 = 1.2$ which is relatively low (Fig.7.16a). The result turned out to have more noise as compared to Fig.7.14 leading to low SNR ($\sim 20$). This is due the fact that the low value of saturation parameter results in a very weak signal to be imaged by the CCD camera. However, there is one of the functionality of camera (LUCA-R) called EMCCD operation which helped us to improve the SNR while working with the low intensities of the probe beam. EMCCD stands for "Electron Multiplying Charged Coupled Device" and this operation allows to add gain to the camera in order to detect the weak signals. The EMCCD gain can take values up to 120. The linear gain at 40 turned out to be optimal as after this value detector's pixels become more sensitive leading to the increase in noise due to residual light which results in low SNR. At EMCCD gain of 40 the SNR was found to be $\sim 40$ (Fig.7.16b).

## 7.4 Acquisition of multiple images

Once we have aligned the imaging setup with respect to the atoms and found the vertical position of the camera to perform the shadowgraph imaging, we implemented the acquisition of multiple successive images by the camera during the experimental sequence. The time between the acquisition of each image is fixed at 80 ms and the maximum number of shadowgraph intensity profiles imaged by the camera is limited to 23. These two limitations are due to the use of the full frame of the camera, i.e., $1004 \times 1002$ pixel matrix. For now, the CCD camera can take 23 shadowgraph images, one image of the probe beam without atoms and one background image in total per experimental sequence.

### 7.4.1 Residual atomic losses

In this section, I will present the measurements performed to acquired multiple in situ images of the BEC in a bubble trap using the shadowgraph imaging system at different values of the detuning and the saturation parameter ($s_0$). We start the experimental sequence by preparing the BEC in a bubble trap and then hold the BEC in a trap for 1 s. During the holding time we activate the acquisition of the shadowgraph images. We take the first shadowgraph image 30 ms after the beginning of the holding time followed by nine more shadowgraph images with each image separated by 80 ms in time. Each imaging pulse has a duration of 20 µs and $s_0$ is 0.18. After holding time we switch off the trap and let the atoms fall for 23 ms before imaging them using absorption imaging. Once it is over, we take the image of the detuned probe beam without atoms ($I_0$) and an image of the background (without probe and atoms). Absorption imaging is performed to compute the number of atoms left and the temperature of the atomic cloud after the shadowgraph measurements.

Two experimental runs were performed for each detuning. Fig.7.17 represents the total atom number along with condensed atom number left (in red dots) and the temperature (in blue dots) of the atomic cloud after TOF expansion and SNR of a non-destructive signal as a function of the probe detuning. We can note that as we approach the resonance there is more absorption of the photons resulting in a reduced atom number in the end of the experiment and higher SNR and as the detuning increases the absorption decreases resulting in a larger atom number in the end and lower value of SNR. By fitting the experimental data with the model given by Eq.7.5 (black cross in Fig.7.17) we observe that the model is not in agreement with the experimental data as we seem to have more absorption than predicted by the two-level model. However, if we consider that the polarization of the probe beam

is not perfectly circular, in this case the two-level approximation will not hold as the other additional hyperfine substates will get populated. Therefore, in order to correct this kind of inperfections, we should define an effective saturation parameter $s_{\text{eff}} = s_0/\alpha_{\text{polar}}$, where $\alpha_{\text{polar}}$ is a dimensionless coefficient and will take into account the imperfections [100,161,162]. Now, we can rewrite Eq.(7.5) as:

$$R_{\text{scatt}}^{\alpha_{\text{polar}}} = \frac{\Gamma}{2} \frac{s_0/\alpha_{\text{polar}}}{1 + s_0/\alpha_{\text{polar}} + \delta^2}. \tag{7.26}$$

By fitting the experimental data with this modified model which takes into account the population of additional hyperfine substates we get the result represented in blue crosses in Fig.7.17. The model seems to satisfy the experimental data for $\alpha_{\text{polar}} = 0.2$. The variation in temperature of the atomic cloud in Fig.7.17 is not clear as a function of the detuning because there is an rf-knife present during the experiment which is keeping the cloud's temperature almost unchanged during the experimental sequence.

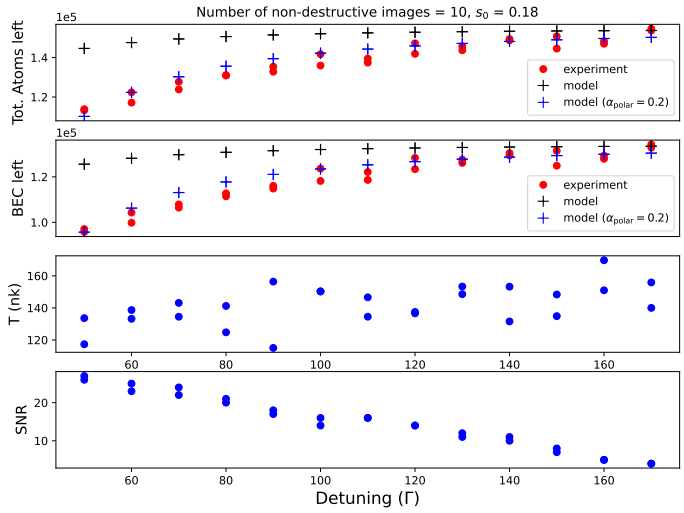



**Figure 7.17** — Measurements of the a) remaining atom number,b) condensed atom number, c) temperature of the BEC after 23 ms of TOF expansion after ten non-destructive measurements and d) SNR of the non-destructive measurement for $s_0 = 0.18$.

### 7.4.2 Choice of the optimal imaging parameters

We now consider which would be the best experimental parameters for the probe (detuning, saturation parameter) to perform a series of weakly destructive images. We will determine the best option for 10 consecutive images separated by 80 ms. Fig.7.18 shows the computed density profile using TIE approximation for three different detunings (50 Γ, 100 Γ and 160 Γ) and $s_0 = 0.18$. We can note from this figure that the SNR decreases as a function of the detuning (see also Fig.7.17). The total atom loss after 10 non-destructive measurements at 50 Γ was found to be 47%, at 100 Γ it was 20% and at 160 Γ the absorption was 11%.

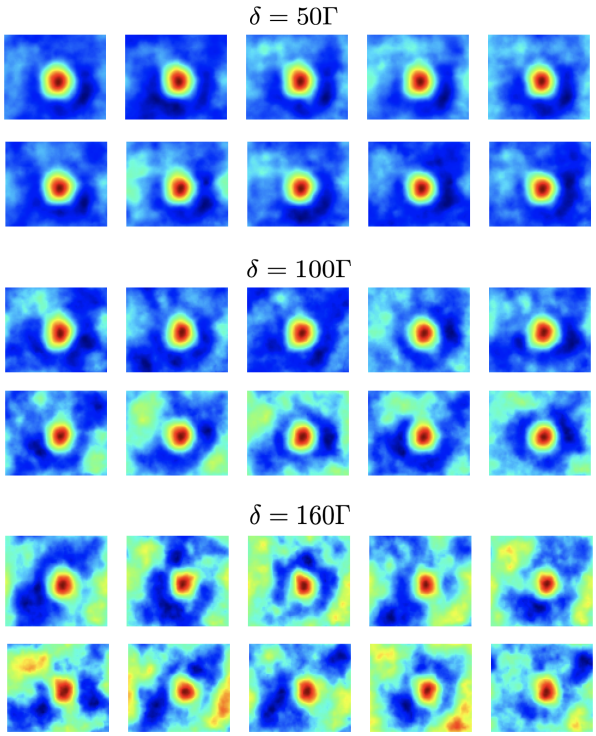



**Figure 7.18** — Computed density profile using the phase equation (7.23) after the TIE approximation for three different detunings ($50\,\Gamma$, $100\,\Gamma$ and $160\,\Gamma$). The saturation parameter is $s_0 = 0.18$.

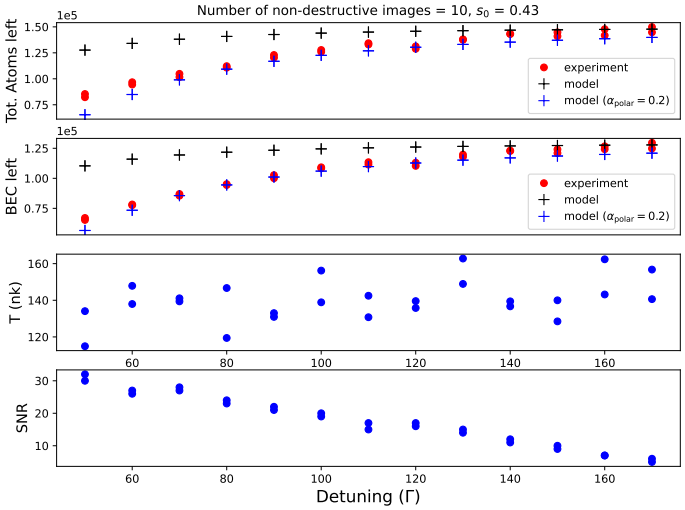



**Figure 7.19** — Measurements of the a) remaining atom number,b) condensed atom number, c) temperature of the BEC after 23 ms of TOF expansion after ten non-destructive measurements and d) SNR of the non-destructive measurement for $s_0 = 0.43$.

Fig.7.19a)to c) represents the experimental data for $s_0 = 0.43$ as a function of detuning taken after 23 ms of TOF expansion after 10 non-destructive measurements and Fig.7.19d) represents the SNR of non-destructive meansurements. The duration of the non-destructive imaging pulse is same as before, i.e., 20 µs. The experimental is fitted again with two models Eq.(7.5) and Eq.(7.26). Fig.7.20 represents the computed density profiles using TIE approximation for three different detunings (50 Γ, 100 Γ and 160 Γ) with $s_0$ being 0.43. At 50 Γ the total atom loss after the 10 non-destructive measurements was 47%, at 100 Γ it was 29% and at 160 Γ the absorption was found to be 17%.

The increase in absorption as compared to the measurement shown in Fig.7.17 is due to the higher value of $s_0$ but on the other hand the computed density profile has less noise as compared to the previous case at higher values of detuning.

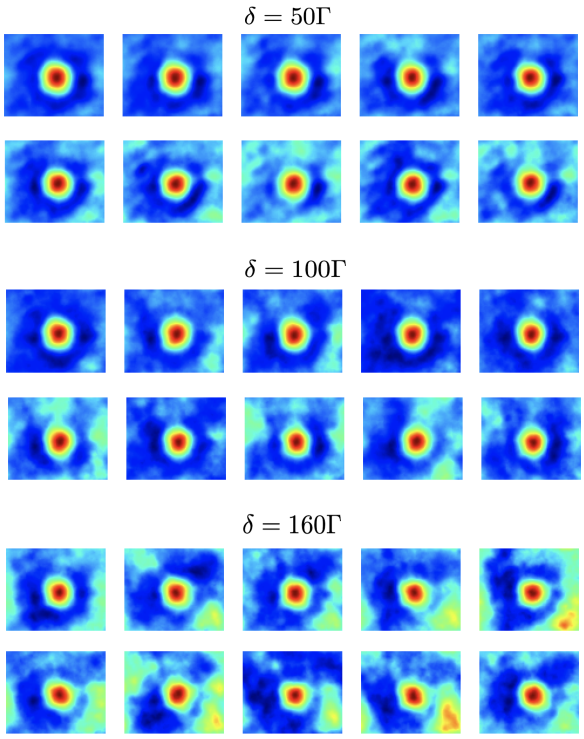



**Figure 7.20** – Computed density profile using the phase equation (7.23) after the TIE approximation for three different detunings (50 Γ, 100 Γ and 160 Γ). The saturation parameter is $s_0 = 0.43$.

Ideally, we can choose to work at this value of $s_0$, i.e., 0.43 and at detuning $\Delta \sim 100\,\Gamma$ with imaging pulse duration being 20 µs. This experimental choice of parameters will allow us to take at least 10 non-destructive measurements at a time with a total atom loss of $20-30\%$ and a SNR of 20.

## 7.5 Conclusion

In this chapter, I have described the newly implemented shadowgraph imaging method that we have implemented in our experiment and explained why it was the ideal imaging technique for our experiment out of other available techniques. I detailed the calibration process for the CCD camera to implement the shadowgraph technique and the behaviour of the TIE approximation method for a large distance of propagation. The computed optical density profile using shadowgraph imaging was found to give a correct estimate for the Thomas-Fermi radii, similar to that of absorption imaging method. EMCCD gain option in the CCD camera helped us to work with lower intensities of the non-destructive probe beam in order to make the process as non-destructive as possible. I also presented the experimental data recorded using the shadowgraph imaging as a function of different values of imaging parameters and we realised that a compromise has to be made between the destructiveness of the imaging process and the SNR. The chosen imaging parameter will allow us to make around 10 non-destructive measurements before the total absorption reaches 30%. The temporary limitation of this imaging method is the acquisition of only 23 images per sequence with the time gap of 80 ms between each image and this can be resolved by selecting a region of interest (ROI) around the signal on the CCD camera rather than using its full frame for the experimental images. The future goal now is to study the in situ dynamics of the condensate and create a movie of the dynamics while performing different kinds of excitations, for example the excitation of collective modes explained in Chapter 1, using the shadowgraph imaging setup that I implemented during my PhD thesis.

# Conclusion

In this PhD thesis, I have shown the very first observation of the melting of vortex lattice in a rapidly rotating quasi-2D superfluid at the bottom of the bubble trap, due to thermal fluctuations. The melting usually occurs through two consecutive phase transitions: from crystalline to hexatic and from hexatic to liquid phase. To observe the melting transitions in our experiment we looked at the arrangement of vortex lattice as a function of increasing rotation frequency ($\Omega$) and we observed only the hexatic to liquid phase transition. We did not observe any long-range translational order as the correlation length related to the pair correlation function was always smaller than the typical size of the system. The hexatic to liquid transition was observed with the slow decay of the orientional correlation function below the melting point and then the decay became fast as we crossed the melting point. This is due to the increased proliferation of dislocations of sites with 5 and 7 neighbours above the melting temperature. The temperature at which we observed the melting transition was not in agreement with the value estimated using the Gifford and Baym prediction. This discrepancy can be related to the finite size extension of a vortex lattice as the melting scenario can be affected by the boundaries. The future perspective towards this experiment would be to study the finite-size effects. In order to do so, we can perform the experiment with large vortex lattices or we can vary the temperature of the atomic ensemble while keeping the fixed rotation rate. Another way of studying the finite-size effects would be to perform the classical field simulations. One more interesting experiment we can perform is to study the effects of the curvature of the bubble trap on the rotating superfluid.

The BEC transfered in the bubble trap to carry out the observation of thermal melting of the quasi-2D superfluid once put in rotation, was produced in a plugged quadrupole configuration. A 10 W, 532 nm plug beam was focused around the center of the quadrupole trap to prevent the atoms from reaching the quadrupole center during the evaporation process. The position of this plug beam was critical as this could easily impart the excitation of the center of mass motion of the atoms during the transfer to the bubble trap and could cause the heating. During the first year of my PhD thesis, we decided to change the trapping configuration from plugged-quadrupole to hybrid dimple (quadrupole and red detuned dimple laser). In this new configuration, a 5 W, 1064 nm dimple beam was focused a few tens of micrometers below the center of the quadrupole trap. This was done to make the transfer process adiabatic as the position of the dimple beam is close to the bottom of the bubble trap. Therefore the atoms can get easily transferred without following any long trajectory unlike the plugged-quadrupole configuration, which can cause excitation of the center of mass

motion of the atoms. The residual amplitude of the oscillation of the center of mass motion was reduced as compared to the plugged quadrupole configuration.

Another major change made during my PhD thesis was the upgrade of 780 nm laser chain in our experimental setup. The motivation behind this change was to perform non-destructive in situ imaging of ultracold atoms using a highly-detuned probe beam from the imaging transition. The new setup has been detailed in Chapter 6. Another reason for the change was also related to the fact that two repumper lasers used initially in our experiment were Sanyo diode lasers which are no longer produced. Therefore, we replaced these two lasers with a Narrowdiode laser from Radiant Dyes which also serves as a non-destructive probe beam. Now, on our upgraded laser system we have one Narrowdiode laser from Radiant Dyes for absorption imaging along the horizontal and vertical directions, one for two repumpers (resonant and off-resonant) and non-destructive imaging, another one serves as a master laser and a 1560 nm telecom fiber laser for 2D and 3D-MOT. In order to achieve desirable detuning for different laser beams used during the experiment, we have locked all the lasers to the master laser using beatnotes.

The motivation behind implementing the non-destructive imaging method is to record the in situ dynamics of the trapped BEC in a bubble trap under different kinds of excitations, by taking multiple images in time during the single experimental sequence. This was not possible using the absorption imaging method as the probe beam being in resonance with the imaging transitions leads to absorption of photons by the atoms during the interaction, which results in atoms going out of the trap due to recoil or transfer to an untrapped state. Chapter 7 describes the working principle of non-destructive imaging and more precisely the imaging method that we decided to opt for our experiment, i.e., shadowgraph imaging. The reason behind choosing shadowgraph imaging was that this imaging method does not require any additional optical element other than that used in the absorption imaging setup. This allows us to perform both absorption imaging and non-destructive imaging along the same axis.

The implementation of the non-destructive imaging method on our experimental setup opens interesting perspectives. First, it gives access to the study of the in-trap dynamics of the BEC in real-time. We can perform the collective modes excitations (explained in Chapter 1) on the trapped BEC and take several pictures in time during the experimental sequence thus making the measurements taken in similar conditions and less affected by the experimental fluctuations. Another kind of excitation that can be interesting to perform is to rotate the superfluid after compensating the gravity to explore the dynamics of the rotating superfluid on a curved 2D surface. The compensation of the gravity experiment has already been performed during the PhD thesis of Yanliang Guo [82] and therefore the method is well known. Through this kind of experiment, we can study how the dynamics related to the rotation of a superfluid behave with respect to the effects of curvature. This study can help us make an analogy with atmospheric physics to study for example the Rossby waves [163].

Another perspective is to improve the vertical imaging setup to be able to observe the vortices in situ. To make this improvement, the plan is to improve the imaging resolution to sub-micrometers and to use the $5S-6P$ transition of $^{87}$Rb in order to benefit from the smaller wavelength. With the improved imaging setup, it would be great to explore two-dimensional turbulence in a curved superfluid as superfluid hydrodynamics offers a way to model turbulent behaviours in a more controlled environment [164]. Another interesting experiment would be to study the dynamics of vortices and anti-vortices in a curved superfluid [165].

# Appendices

# Appendix A

# Useful quantities for the thermal melting of a vortex lattice

## A.1 Vortex pair number $\overline{P_v}$ for continuous uniform vortex density $n_v$

We assume a uniform vortex density $n_v$. We need to compute the number of vortex pairs $\overline{P_v}(r)$ inside a disk of radius $R_{\text{eff}}$ in this situation. To compute $\overline{P_v}(r)$, we start by considering a point $M$ at a distance $r'$ from the center of the disc of radius $R_{\text{eff}}$, then the number of points inside the disk at a distance between $r-\delta r/2$ and $r+\delta r/2$ from $M$ is given by $n_v \times r\delta r \times 2\alpha$, where $\alpha$ is an angle defined in Fig. A.1.

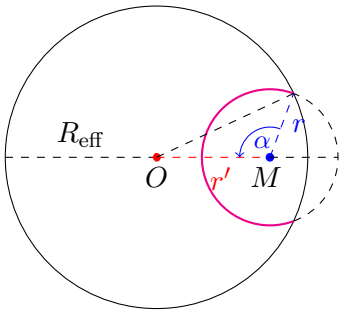



**Figure A.1** — Illustration of counting vortex pairs within a given distance of each other. It is equivalent to finding the length of the magenta arc if we assume a uniform vortex density over a disk.

The angle $\alpha$, between 0 and $\pi$ is uniquely defined by the following relations:

$$\cos\alpha = \frac{r^2 + r'^2 - R_{\text{eff}}^2}{2rr'} \text{ for } r' > |R_{\text{eff}} - r|, \tag{A.1}$$

$$\alpha = 0 \text{ for } r' < r - R_{\text{eff}} \text{ with } R_{\text{eff}} < r, \tag{A.2}$$

$$\alpha = \pi \text{ for } r' < R_{\text{eff}} - r \text{ with } R_{\text{eff}} > r. \tag{A.3}$$

Now, we can average over all the initial values for $r'$ inside the disk:

$$\overline{P_v}(r) = 2\pi n_v \int_0^{R_{\text{eff}}} r' dr' n_v r \delta r \times 2\alpha. \tag{A.4}$$

After solving the above equation, we get the following expression:

$$\overline{P_v}(r) = 2\pi n_v^2 R_{\text{eff}}^2 r \delta r \left[ \arccos\left(\frac{r}{2R_{\text{eff}}}\right) - \frac{r}{2R_{\text{eff}}} \sqrt{1 - \frac{r^2}{4R_{\text{eff}}^2}} \right]. \tag{A.5}$$

## A.2 Estimation of $T_c^0$ and $T_{\text{BKT}}$

To compute $T_c^0$ with the 3D semi-classical model:

$$\rho(\boldsymbol{r}) = \Lambda^{-3} g_{3/2} \left[ e^{-\beta V_\Omega(\boldsymbol{r})} \right]$$

with $V_\Omega(\boldsymbol{r})$ the 3D trap in the rotating frame and $g_{3/2}[x]$ the polylog function of order 3/2. We compute $N_c(T,\Omega) = \int d\boldsymbol{r}\, \rho(\boldsymbol{r})$ and solve $N_c(T,\Omega) = N_0$ for each value of $\Omega$ to get $T_c^0(\Omega)$, for $N_0 = 10^5$.

For the quasi-2D BKT model the approach is similar to compute the 2D density: $n(r) = \int dz\, \rho(\boldsymbol{r})$ (assuming rotational invariance to simplify)

$$n(r) = -\Lambda^{-2} \sum_{n_z=0}^{\infty} \ln\left[1 - e^{\beta(\mu_c - V_\Omega(\boldsymbol{r}) - 2\tilde{g}_T n(r)\hbar^2/M)}\right]$$

but we need extra input to find the transition. The critical phase space density is: $\mathcal{D}_c = \ln[380/\tilde{g}_T]$ (from Quantum Monte Carlo computation), where $\tilde{g}_T = \tilde{g}\sqrt{\tanh[\beta\hbar\omega_z/2]}$. Then we have to solve:

$$\mathcal{D}_c = -\sum_{n_z=0}^{\infty} \ln\left[1 - e^{\beta(x - n_z\hbar\omega_z)}\right]$$

and obtain the critical chemical potential: $\mu_c = x + \tilde{g}_T \mathcal{D}_c/\pi \times k_B T$. Then we solve the equation for the density and compute $N_{\text{BKT}}(T,\Omega)$, then solve $N_{\text{BKT}}(T,\Omega) = N_0$ to obtain $T_{\text{BKT}}(\Omega)$ for $N_0 = 10^5$.

# Bibliography


[1] A. Einstein, "Quantentheorie des einatomigen idealen Gases". *Sitzungsber. Kgl. Preuss. Akad. Wiss.*, 261–267 (1924).

[2] A. Einstein, "Quantentheorie des einatomigen idealen Gases. Zweite Abhandlung". *Sitzungsber. Kgl. Preuss. Akad. Wiss.*, 3–14 (1925).

[3] S.N. Bose, "Plancks Gesetz und Lichtquantenhypothese". *Z. Phys.* **26**, 178–181 (1924).

[4] P. Kapitza, "Viscosity of Liquid Helium below the $\lambda$-Point". *Nature* **141**, 74 (1938).

[5] J.F. Allen and A.D. Misener, "Flow of Liquid Helium II". *Nature* **141**, 75 (1938).

[6] F. London, "On the Bose-Einstein Condensation". *Phys. Rev.* **54**, 947–954 (Dec 1938).

[7] W. Ketterle, "When atoms behave as waves: Bose-Einstein condensation and the atom laser". *Rev. Mod. Phys.* **74**, 1131 (2002).

[8] E. A. Cornell and C. E. Wieman, "Nobel Lecture: Bose-Einstein condensation in a dilute gas, the first 70 years and some recent experiments". *Rev. Mod. Phys.* **74**, 875 (2002).

[9] C. Cohen-Tannoudji, "Nobel Lecture: Manipulating atoms with photons". *Rev. Mod. Phys.* **70**, 707 (1998).

[10] S. Chu, "Nobel Lecture: The manipulation of neutral particles". *Rev. Mod. Phys.* **70**, 685 (1998).

[11] W. D. Phillips, "Nobel Lecture: Laser cooling and trapping of neutral atoms". *Rev. Mod. Phys.* **70**, 721 (1998).

[12] M. Greiner, O. Mandel, T. Esslinger, T.W. Hänsch and I. Bloch, "Quantum Phase Transition from a Superfluid to a Mott Insulator in a Gas of Ultracold Atoms". *Nature* **415**, 39 (2002).

[13] W. S. Bakr, J. I. Gillen, A. Peng, S. Fölling and M. Greiner, "A quantum gas microscope for detecting single atoms in a Hubbard-regime optical lattice". *Nature* **462**, 74 (2009).

[14] J. F. Sherson, C. Weitenberg, M. Endres, M. Cheneau, I. Bloch and S. Kuhr, "Single-atom-resolved fluorescence imaging of an atomic Mott insulator". *Nature* **467**, 68 (2010).

[15] Manuel Endres, Hannes Bernien, Alexander Keesling, Harry Levine, Eric R. Anschuetz, Alexandre Krajenbrink, Crystal Senko, Vladan Vuletic, Markus Greiner and Mikhail D. Lukin, "Atom-by-atom assembly of defect-free one-dimensional cold atom arrays". *Science* **354** (6315), 1024–1027 (2016).

[16] S. Chu, L. Hollberg, J. E. Bjorkholm, A. Cable and A. Ashkin, "Three-dimensional viscous confinement and cooling of atoms by resonance radiation pressure". *Phys. Rev. Lett.* **55**, 48–51 (1985).

[17] E.L. Raab, M. Prentiss, A. Cable, S. Chu and D.E. Pritchard, "Trapping of neutral sodium atoms with radiation pressure". *Phys. Rev. Lett.* **59** (23), 2631–2634 (1987).

[18] S. Chu, J.E. Bjorkholm, A. Ashkin and A. Cable, "Experimental observation of optically trapped atoms". *Phys. Rev. Lett.* **57** (3), 314–317 (1986).

[19] Alan L. Migdall, John V. Prodan, William D. Phillips, Thomas H. Bergeman and Harold J. Metcalf, "First Observation of Magnetically Trapped Neutral Atoms". *Phys. Rev. Lett.* **54**, 2596–2599 (Jun 1985).

[20] H. F. Hess, "Evaporative cooling of magnetically trapped and compressed spinpolarized hydrogen". *Phys. Rev. B* **34**, 3476 (1986).

[21] N. Masuhara, J. M. Doyle, J. C. Sandberg, D. Kleppner, T. J. Greytak, H. F. Hess and G. P. Kochanski, "Evaporative cooling of spin-polarized atomic hydrogen". *Phys. Rev. Lett.* **61**, 935 (1988).

[22] M.H. Anderson, J.R. Ensher, M.R. Matthews, C.E. Wieman and E.A. Cornell, "Observation of Bose-Einstein condensation in a dilute atomic vapor". *Science* **269**, 198–201 (1995).

[23] K.B. Davis, M.-O. Mewes, M.R. Andrews, N.J. van Druten, D.S. Durfee, D.M. Kurn and W. Ketterle, "Bose-Einstein condensation in a gas of sodium atoms". *Phys. Rev. Lett.* **75** (22), 3969–3973 (1995).

[24] A. J. Leggett, "Superfluidity". *Rev. Mod. Phys.* **71**, S318 (1999).

[25] R.P. Feynman, "Chapter II Application of Quantum Mechanics to Liquid Helium". volume 1 of *Progress in Low Temperature Physics* pages 17 – 53, Elsevier (1955).

[26] V.F. Vinen, "The detection of single quanta of circulation in liquid helium II". *Proceedings of the Royal Society of London A: Mathematical, Physical and Engineering Sciences* **260** (1301), 218–236 (1961).

[27] G. B. Hess and W. M. Fairbank, "Measurements of Angular Momentum in Superfluid Helium". *Phys. Rev. Lett.* **19**, 216–218 (Jul 1967).

[28] E. J. Yarmchuk, M. J. V. Gordon and R. E. Packard, "Observation of Stationary Vortex Arrays in Rotating Superfluid Helium". *Phys. Rev. Lett.* **43**, 214–217 (Jul 1979).

[29] M.-O. Mewes, M.R. Andrews, N.J. van Druten, D.M. Kurn, D.S. Durfee, C.G. Townsend and W. Ketterle, "Collective excitations of a Bose-Einstein condensate in a magnetic trap". *Phys. Rev. Lett.* **77** (6), 988–991 (1996).

[30] D. S. Jin, J. R. Ensher, M. R. Matthews, C. E. Wieman and E. A. Cornell, "Collective Excitations of a Bose-Einstein Condensate in a Dilute Gas". *Phys. Rev. Lett.* **77**, 420–423 (Jul 1996).

[31] O. M. Maragò, S. A. Hopkins, J. Arlt, E. Hodby, G. Hechenblaikner and C. J. Foot, "Observation of the Scissors Mode and Evidence for Superfluidity of a Trapped Bose-Einstein Condensed Gas". *Phys. Rev. Lett.* **84**, 2056–2059 (Mar 2000).

[32] M. R. Matthews, B. P. Anderson, P. C. Haljan, D. S. Hall, C. E. Wieman and E. A. Cornell, "Vortices in a Bose–Einstein Condensate". *Phys. Rev. Lett.* **83** (13), 2498–2501 (Sep 1999).

[33] K. W. Madison, F. Chevy, W. Wohlleben and J. Dalibard, "Vortex formation in a stirred Bose-Einstein condensate". *Phys. Rev. Lett.* **84**, 806 (2000).

[34] J. R. Abo-Shaeer, C. Raman, J. M. Vogels and W. Ketterle, "Observation of Vortex Lattices in Bose-Einstein Condensates". *Science* **292**, 476 (2001).

[35] N. R. Cooper, N. K. Wilkin and J. M. F. Gunn, "Quantum Phases of Vortices in Rotating Bose–Einstein Condensates". *Phys. Rev. Lett.* **87** (12), 120 405 (Aug 2001).

[36] V. Berezinskii, "Destruction of long-range order in one-dimensional and 2-dimensional systems having a continuous symmetry group, 2 - quantum systems". *Sov. Phys. JETP-USSR* **34**, 610 (1972).

[37] J.M. Kosterlitz and D.J. Thouless, "Ordering, metastability and phase transitions in two-dimensional systems". *J. Phys. C : Solid State Phys.* **6**, 1181–1203 (1973).

[38] Z. Hadzibabic and J. Dalibard, "Two-dimensional Bose fluids: An atomic physics perspective". *Rivista del Nuovo Cimento* **34**, 389 (2011).

[39] Richard J. Fletcher, Martin Robert-de Saint-Vincent, Jay Man, Nir Navon, Robert P. Smith, Konrad G. H. Viebahn and Zoran Hadzibabic, "Connecting Berezinskii-Kosterlitz-Thouless and BEC Phase Transitions by Tuning Interactions in a Trapped Gas". *Phys. Rev. Lett.* **114**, 255 302 (Jun 2015).

[40] Tyler W. Neely, Guillaume Gauthier, Charles Glasspool, Matthew J. Davis and Matthew T. Reeves, "Melting of a vortex matter Wigner crystal". *Preprint arXiv:2402.09920* (2024).

[41] K. Merloti, R. Dubessy, L. Longchambon, A Perrin, P.-E. P-E Pottie, V. Lorent and H. Perrin, "A two-dimensional quantum gas in a magnetic trap". *New Journal of Physics* **15** (3), 033 007 (2013).

[42] Mathieu de Goër de Herve, *Superfluid dynamics of annular Bose gases.* PhD thesis, Université Paris 13 (2018).

[43] B. I. Halperin and David R. Nelson, "Theory of Two-Dimensional Melting". *Phys. Rev. Lett.* **41**, 121–124 (Jul 1978).

[44] A. P. Young, "Melting and the vector Coulomb gas in two dimensions". *Phys. Rev. B* **19**, 1855–1866 (1979).

[45] R. Dubessy, K. Merloti, L. Longchambon, P.-E. Pottie, T. Liennard, A. Perrin, V. Lorent and H. Perrin, "Rubidium-87 Bose-Einstein condensate in an optically plugged quadrupole trap". *Phys. Rev. A* **85**, 013 643 (Jan 2012).

[46] E. Majorana, "Atomi orientati in campo magnetico variabile". *Nuovo Cimento* **9**, 43–50 (1932).

[47] Hélène Perrin and Barry M. Garraway, "Chapter Four - Trapping Atoms With Radio Frequency Adiabatic Potentials". volume 66 of *Advances In Atomic, Molecular, and Optical Physics* pages 181 – 262, Academic Press (2017).

[48] Rishabh Sharma, David Rey, Laurent Longchambon, Aurélien Perrin, Hélène Perrin and Romain Dubessy, "Thermal Melting of a Vortex Lattice in a Quasi-Two-Dimensional Bose Gas". *Phys. Rev. Lett.* **133**, 143 401 (Sep 2024).

[49] David Rey, Simon Thomas, Rishabh Sharma, Thomas Badr, Laurent Longchambon, Romain Dubessy and Hélène Perrin, "Loading a quantum gas from a hybrid dimple trap to a shell trap". *Journal of Applied Physics* **132** (21), 214 401 (12 2022). https://pubs.aip.org/aip/jap/article-pdf/doi/10.1063/5.0123440/19910998/214401_1_5.0123440.pdf.

[50] F. Dalfovo, S. Giorgini, L.P. Pitaevskii and S. Stringari, "Theory of Bose-Einstein condensation in trapped gases". *Rev. Mod. Phys.* **71** (3), 463–512 (1999).

[51] Jean Dalibard, *Coherence and superfluidity in atomic gases*. Course "Atomes and radiation ", Collège de France, year 2015-2016.

[52] V. Bagnato and D. Kleppner, "Bose-Einstein condensation in low-dimensional traps". *Phys. Rev. A* **44** (11), 7439–7441 (1991).

[53] L. Pitaevskii and S. Stringari, *Bose-Einstein condensation*. Oxford University Press (2003).

[54] Oliver Penrose and Lars Onsager, "Bose-Einstein Condensation and Liquid Helium". *Phys. Rev.* **104**, 576–584 (Nov 1956).

[55] Claude Cohen-Tannoudji and David Guéry-Odelin, *Advances in Atomic Physics*. WORLD SCIENTIFIC (2011). https://www.worldscientific.com/doi/pdf/10.1142/6631, https://www.worldscientific.com/doi/abs/10.1142/6631 .

[56] J.T.M. Walraven, *Quantum Gases* (2017). Lecture notes, course given at the university of Amsterdam.

[57] S. Stringari, "Collective excitations of a trapped Bose-condensed gas". *Phys. Rev. Lett.* **77** (12), 2360–2363 (1996).

[58] L. Onsager, "Statistical hydrodynamics". *Il Nuovo Cimento Series 9* **6** (2), 279–287 (1949).

[59] Y. Shin, M. Saba, M. Vengalattore, T. A. Pasquini, C. Sanner, A. E. Leanhardt, M. Prentiss, D. E. Pritchard and W. Ketterle, "Dynamical Instability of a Doubly Quantized Vortex in a Bose-Einstein Condensate". *Phys. Rev. Lett.* **93**, 160 406 (Oct 2004).

[60] Y. Castin and R. Dum, "Bose-Einstein condensates with vortices in rotating traps". *The European Physical Journal D - Atomic, Molecular, Optical and Plasma Physics* **7** (3), 399–412 (Oct 1999).

[61] K. W. Madison, F. Chevy, W. Wohlleben and J. Dalibard, "Vortex Formation in a Stirred Bose-Einstein Condensate". *Phys. Rev. Lett.* **84**, 806–809 (Jan 2000).

[62] Z. Hadzibabic, P. Krüger, M. Cheneau, B. Battelier and J. Dalibard, "Berezinskii-Kosterlitz-Thouless crossover in a trapped atomic gas". *Nature* **441**, 1118 (2006).

[63] I. Bloch, J. Dalibard and W. Zwerger, "Many-body physics with ultracold gases". *Rev. Mod. Phys.* **80**, 885–964 (2008).

[64] Camilla De Rossi, Romain Dubessy, Karina Merloti, Mathieu de Goër de Herve, Thomas Badr, Aurélien Perrin, Laurent Longchambon and Hélène Perrin, "Probing superfluidity in a quasi two-dimensional Bose gas through its local dynamics". *New Journal of Physics* **18** (6), 062 001 (2016).

[65] Karina Merloti, Romain Dubessy, Laurent Longchambon, Maxim Olshanii and Hélène Perrin, "Breakdown of scale invariance in a quasi-two-dimensional Bose gas due to the presence of the third dimension". *Phys. Rev. A* **88**, 061 603 (Dec 2013).

[66] S. Stringari, "Dynamics of Bose-Einstein condensed gases in highly deformed traps". *Phys. Rev. A* **58**, 2385–2388 (Sep 1998).

[67] O. Zobay and B.M. Garraway, "Two-dimensional atom trapping in field-induced adiabatic potentials". *Phys. Rev. Lett.* **86** (7), 1195–1198 (2001).

[68] Y. Colombe, E. Knyazchyan, O. Morizot, B. Mercier, V. Lorent and H. Perrin, "Ultracold atoms confined in rf-induced two-dimensional trapping potentials". *Europhys. Lett.* **67** (4), 593–599 (2004).

[69] Y. Colombe, B. Mercier, H. Perrin and V. Lorent, "Loading a dressed Zeeman trap with cold atoms". In *Proceedings of the Euroschool on quantum gases in low dimensions, Les Houches 2003*, volume 116, edited by L. Pricoupenko, H. Perrin and M. Olshanii 247, J. Phys. IV (2004).

[70] K. Merloti, R. Dubessy, L. Longchambon, A. Perrin, P.-E. Pottie, V. Lorent and H. Perrin, "A two-dimensional quantum gas in a magnetic trap". *New Journal of Physics* **15** (3), 033 007 (2013).

[71] R. Dubessy, C. De Rossi, T. Badr, L. Longchambon and H. Perrin, "Imaging the collective excitations of an ultracold gas using statistical correlations". *New Journal of Physics* **16** (12), 122 001 (2014).

[72] T. Schumm, S. Hofferberth, L.M. Andersson, S. Wildermuth, S. Groth, I. Bar-Joseph, J. Schmiedmayer and P. Krüger, "Matter wave interferometry in a double well on an atom chip". *Nature Phys.* **1**, 57 (2005).

[73] O. Morizot, Y. Colombe, V. Lorent, H. Perrin and B.M. Garraway, "Ring trap for ultracold atoms". *Phys. Rev. A* **74**, 023 617 (2006).

[74] W. H. Heathcote, E. Nugent, B. T. Sheard and C. J. Foot, "A ring trap for ultracold atoms in an RF-dressed state". *New Journal of Physics* **10** (4), 043 012 (2008).

[75] Mathieu de Goër de Herve, Yanliang Guo, Camilla De Rossi, Avinash Kumar, Thomas Badr, Romain Dubessy, Laurent Longchambon and Hélène Perrin, "A versatile ring trap for quantum gases". *Journal of Physics B: Atomic, Molecular and Optical Physics* **54** (12), 125 302 (jun 2021).

[76] N. Lundblad, P. J. Lee, I. B. Spielman, B. L. Brown, W. D. Phillips and J. V. Porto, "Atoms in a Radio-Frequency-Dressed Optical Lattice". *Phys. Rev. Lett.* **100**, 150 401 (Apr 2008).

[77] Igor Lesanovsky and Wolf von Klitzing, "Time-Averaged Adiabatic Potentials: Versatile Matter-Wave Guides and Atom Traps". *Phys. Rev. Lett.* **99** (8), 083 001 (Aug 2007).

[78] B. E. Sherlock, M. Gildemeister, E. Owen, E. Nugent and C. J. Foot, "Time-averaged adiabatic ring potential for ultracold atoms". *Phys. Rev. A* **83**, 043 408 (Apr 2011).

[79] P Navez, S Pandey, H Mas, K Poulios, T Fernholz and W von Klitzing, "Matter-wave interferometers using TAAP rings". *New Journal of Physics* **18** (7), 075 014 (2016).

[80] S. Pandey, M. Hector, D. Giannis, T. Premjith, B. Vasiliki, V. Georgios, P Konstantinos and w. von Klitzing, "Hypersonic Bose–Einstein Condensates in Accelerator Rings". *Nature* **570**, 205–209 (Jun 2019).

[81] T. L. Harte, E. Bentine, K. Luksch, A. J. Barker, D. Trypogeorgos, B. Yuen and C. J. Foot, "Ultracold atoms in multiple radio-frequency dressed adiabatic potentials". *Phys. Rev. A* **97**, 013 616 (Jan 2018).

[82] Yanliang Guo, *Annular quantum gases in a bubble-shaped trap: from equilibrium to strong rotations*. PhD thesis, Université Paris 13 (2021).

[83] Y. Guo, R. Dubessy, M. De goër de Herve, A. Kumar, T. Badr, A. Perrin, L. Longchambon and H. Perrin, "Supersonic Rotation of a Superfluid: A Long-Lived Dynamical Ring". *Phys. Rev. Lett.* **124**, 025 301 (2020).

[84] Y. Guo, E. Mercado Gutierrez, D. Rey, T. Badr, A. Perrin, L. Longchambon, V. Bagnato, H. Perrin and R. Dubessy, "Expansion of a quantum gas in a shell trap". *New J. Phys.* **24**, 093 040 (2022).

[85] C. Cohen-Tannoudji, *Atomes ultra-froids – Piégeage non dissipatif et refroidissement évaporatif*. Cours de physique atomique et moléculaire, Collège de France, année 1996-1997.

[86] D.T. Pegg and G.W. Series, "Semi-classical theory of the Hanle effect with transverse static and oscillating magnetic fields". *Phys. Rev. Lett.* **54**, 2596–2599 (1985).

[87] D T Pegg, "Misalignment effects in magnetic resonance". *Journal of Physics B: Atomic and Molecular Physics* **6** (2), 241 (1973).

[88] Thomas Liennard, *Construction d'un montage de condensation de Bose–Einstein de rubidium et étude théorique d'un superfluide en rotation dans un anneau*. PhD thesis, Université Paris-Nord - Paris XIII (2011).

[89] Karina Merloti, *Condensat de Bose–Einstein dans un piège habillé: modes collectifs d'un superfluide en dimension deux*. PhD thesis, Université Paris 13 (2013).

[90] P. T. Starkey, C. J. Billington, S. P. Johnstone, M. Jasperse, K. Helmerson, L.D. Turner and R.P. Anderson, "A scripted control system for autonomous hardware-timed experiments". *Rev. Sci. Instrum.* **84** (8), 085 111 (2013).

[91] David Rey, *Control and Optimisation of Bose-Einstein condensate experiment*. PhD thesis, Université Paris 13 (2023).

[92] Romain Dubessy, *Contributions to the study of out-of-equilibrium superfluids in one and two dimensions, Habilitation à diriger des recherches (HDR)*. PhD thesis, Université Paris 13 (2023).

[93] P. Cheinet, *Condensat de Bose-Einstein, Conception et réalisation d'un gravimétre à atomes froids*. PhD thesis, Université Pierre et Marie Curie - Paris VI (2006).

[94] M. Greiner, I. Bloch, T.W. Hänsch and T. Esslinger, "Magnetic transport of trapped cold atoms over a large distance". *Phys. Rev. A* **63**, 031 401, 1–4 (2001).

[95] F. Orlhac, *Piégage d'atomes ultra-froids avec des champs magnétiques et des faisceaux lasers*. L3 internship report, Université de Cergy Pontoise (2010).

[96] F. Orlhac, *Piége magnéto-optique de rubidium et transport magnétique d'atomes froids*. Rapport de stage de recherche, École Polytechnique (2009).

[97] Camilla de Rossi, *Gaz de Bose en dimension deux : modes collectifs, superfluidité et piège annulaire*. PhD thesis, Université Paris 13 (2016).

[98] D. S. Naik and C. Raman, "Optically Plugged Quadrupole Trap for Bose-Einstein Condensates". *Phys. Rev. A* **71**, 033 617 (2005).

[99] Y.-J. Lin, A. R. Perry, R. L. Compton, I. B. Spielman and J. V. Porto, "Rapid production of $^{87}Rb$ Bose-Einstein condensates in a combined magnetic and optical potential". *Phys. Rev. A* **79** (6), 063 631 (Jun 2009).

[100] G. Reinaudi, T. Lahaye, Z. Wang and D. Guéry-Odelin, "Strong saturation absorption imaging of dense clouds of ultracold atoms". *Opt. Lett.* **32** (21), 3143–3145 (Nov 2007).

[101] Lauriane Chomaz, *Coherence and superfluidity of Bose gases in reduced dimensions: from harmonic traps to uniform fluids*. PhD thesis, Ecole Normale Supérieure (novembre 2014).

[102] P. B. Wigley, P. J. Everitt, K. S. Hardman, M. R. Hush, C. H. Wei, M. A. Sooriyabandara, P. Manju, J. D. Close, N. P. Robins and C. C. N. Kuhn, "Non-destructive shadowgraph imaging of ultra-cold atoms". *Opt. Lett.* **41** (20), 4795–4798 (Oct 2016).

[103] N. D. Mermin and H. Wagner, "Absence of Ferromagnetism or Antiferromagnetism in One- or Two-Dimensional Isotropic Heisenberg Models". *Phys. Rev. Lett.* **17**, 1133–1136 (1966).

[104] I. Bloch, "Quantum Gases". *Science* **319**, 1202 (2008).

[105] J. Iaconis, R. G. Melko and A. A. Burkov, "Continuous thermal melting of a two-dimensional Abrikosov vortex solid". *Phys. Rev. B* **82** (18), 180 504 (2010).

[106] Etienne P. Bernard and Werner Krauth, "Two-Step Melting in Two Dimensions: First-Order Liquid-Hexatic Transition". *Phys. Rev. Lett.* **107** (15), 155 704 (2011).

[107] Keola Wierschem and Efstratios Manousakis, "Simulation of melting of two-dimensional Lennard-Jones solids". *Phys. Rev. B* **83**, 214 108 (Jun 2011).

[108] Sebastian C. Kapfer and Werner Krauth, "Two-Dimensional Melting: From Liquid-Hexatic Coexistence to Continuous Transitions". *Phys. Rev. Lett.* **114** (3), 035 702 (2015).

[109] Yan-Wei Li and Massimo Pica Ciamarra, "Accurate determination of the translational correlation function of two-dimensional solids". *Phys. Rev. E* **100** (6), 062 606 (2019).

[110] C. A. Murray and D. H. Van Winkle, "Experimental observation of two-stage melting in a classical two-dimensional screened Coulomb system". *Phys. Rev. Lett.* **58** (12), 1200–1203 (1987).

[111] Yeke Tang, A. J. Armstrong, R. C. Mockler and W. J. O'Sullivan, "Free-expansion melting of a colloidal monolayer". *Phys. Rev. Lett.* **62** (20), 2401–2404 (1989).

[112] R. E. Kusner, J. A. Mann, J. Kerins and A. J. Dahm, "Two-Stage Melting of a Two-Dimensional Collodial Lattice with Dipole Interactions". *Phys. Rev. Lett.* **73** (23), 3113–3116 (1994).

[113] Andrew H. Marcus and Stuart A. Rice, "Observations of First-Order Liquid-to-Hexatic and Hexatic-to-Solid Phase Transitions in a Confined Colloid Suspension". *Phys. Rev. Lett.* **77** (12), 2577–2580 (1996).

[114] K. Zahn, R. Lenke and G. Maret, "Two-Stage Melting of Paramagnetic Colloidal Crystals in Two Dimensions". *Phys. Rev. Lett.* **82** (13), 2721–2724 (1999).

[115] Y. Han, N. Y. Ha, A. M. Alsayed and A. G. Yodh, "Melting of two-dimensional tunable-diameter colloidal crystals". *Phys. Rev. E* **77** (4), 041 406 (2008).

[116] Urs Gasser, Christoph Eisenmann, Georg Maret and Peter Keim, "Melting of Crystals in Two Dimensions". *ChemPhysChem* **11** (5), 963–970 (2010).

[117] Colm P. Kelleher, Rodrigo E. Guerra, Andrew D. Hollingsworth and Paul M. Chaikin, "Phase behavior of charged colloids at a fluid interface". *Phys. Rev. E* **95** (2), 022 602 (2017).

[118] O. F. Petrov, M. M. Vasiliev, O. S. Vaulina, K. B. Stacenko, E. V. Vasilieva, E. A. Lisin, Y. Tun and V. E. Fortov, "Solid-hexatic-liquid transition in a two-dimensional system of charged dust particles". *EPL* **111** (4), 45 002 (2015).

[119] Xiaoyan Sun, Yang Li, Yuqiang Ma and Zexin Zhang, "Direct observation of melting in a two-dimensional driven granular system". *Scientific Reports* **6** (1), 24 056 (2016).

[120] I. Guillamón, H. Suderow, A. Fernández-Pacheco, J. Sesé, R. Córdoba, J. M. De Teresa, M. R. Ibarra and S. Vieira, "Direct observation of melting in a two-dimensional superconducting vortex lattice". *Nature Physics* **5**, 651 (2009).

[121] I. Guillamón, R. Córdoba, J. Sesé, J. M. De Teresa, M. R. Ibarra, S. Vieira and H. Suderow, "Enhancement of long-range correlations in a 2D vortex lattice by an incommensurate 1D disorder potential". *Nature Physics* **10** (11), 851–856 (2014).

[122] M. Zehetmayer, "How the vortex lattice of a superconductor becomes disordered: a study by scanning tunneling spectroscopy". *Scientific Reports* **5** (1), 9244 (2015).

[123] Indranil Roy, Surajit Dutta, Aditya N. Roy Choudhury, Somak Basistha, Ilaria Maccari, Soumyajit Mandal, John Jesudasan, Vivas Bagwe, Claudio Castellani, Lara Benfatto and Pratap Raychaudhuri, "Melting of the Vortex Lattice through Intermediate Hexatic Fluid in an *a*–MoGe Thin Film". *Phys. Rev. Lett.* **122** (4), 047 001 (2019).

[124] I. Coddington, P. C. Haljan, P. Engels, V. Schweikhard, S. Tung and E. A. Cornell, "Experimental studies of equilibrium vortex properties in a Bose-condensed gas". *Phys. Rev. A* **70** (6), 063 607 (2004).

[125] V. Bretin, S. Stock, Y. Seurin and J. Dalibard, "Fast rotation of a Bose-Einstein condensate". *Phys. Rev. Lett.* **92** (5), 050 403, 1–4 (2004).

[126] S. Andrew Gifford and Gordon Baym, "Dislocation-mediated melting in superfluid vortex lattices". *Phys. Rev. A* **78**, 043 607 (Oct 2008).

[127] David R. Nelson and J. M. Kosterlitz, "Universal Jump in the Superfluid Density of Two-Dimensional Superfluids". *Phys. Rev. Lett.* **39** (19), 1201–1205 (1977).

[128] Jean Dalibard, *Fluides quantiques de basse dimension et transition de Kosterlitz-Thouless*. Course "Atomes et rayonnement ", Collège de France, year 2016-2017.

[129] "Figure taken from Wikipedia". `https://en.wikipedia.org/wiki/Hexatic_phase` .

[130] V. Schweikhard, I. Coddington, P. Engels, V.P. Mogendorff and E.A. Cornell, "Rapidly rotating Bose-Einstein condensates in and near the lowest Landau level". *Phys. Rev. Lett.* **92** (4), 040 404, 1–4 (2004).

[131] Alexander L. Fetter, "Rotating trapped Bose-Einstein condensates". *Rev. Mod. Phys.* **81** (2), 647–691 (May 2009).

[132] Alexander L. Fetter, B. Jackson and S. Stringari, "Rapid rotation of a Bose-Einstein condensate in a harmonic plus quartic trap". *Phys. Rev. A* **71**, 013 605 (Jan 2005).

[133] M. Cozzini, A. L. Fetter, B. Jackson and S. Stringari, "Oscillations of a Bose-Einstein Condensate Rotating in a Harmonic Plus Quartic Trap". *Phys. Rev. Lett.* **94**, 100 402 (Mar 2005).

[134] Markus Holzmann, Maguelonne Chevallier and Werner Krauth, "Semiclassical theory of the quasi–two-dimensional trapped Bose gas". *EPL* **82** (3), 30 001 (2008).

[135] F. Chevy, *Dynamique d'un condensat de Bose-Einstein*. PhD thesis, Université Pierre et Marie Curie – Paris VI (2001).

[136] K. W. Madison, F. Chevy, V. Bretin and J. Dalibard, "Stationary States of a Rotating Bose-Einstein Condensate: Routes to Vortex Nucleation". *Phys. Rev. Lett.* **86**, 4443–4446 (May 2001).

[137] S. Sinha and Y. Castin, "Dynamical instability of a rotating Bose–Einstein condensate". *Phys. Rev. Lett.* **87**, 190 402 (2001).

[138] Carlos Lobo, Alice Sinatra and Yvan Castin, "Vortex Lattice Formation in Bose-Einstein Condensates". *Phys. Rev. Lett.* **92**, 020 403 (Jan 2004).

[139] Richard J. Fletcher, Airlia Shaffer, Cedric C. Wilson, Parth B. Patel, Zhenjie Yan, Valentin Crépel, Biswaroop Mukherjee and Martin W. Zwierlein, "Geometric squeezing into the lowest Landau level". *Science* **372** (6548), 1318–1322 (2021). `https://www.science.org/doi/pdf/10.1126/science.aba7202`.

[140] A S Bradley, C W Gardiner and M J Davis, "Bose-Einstein condensation from a rotating thermal cloud: Vortex nucleation and lattice formation". *Phys. Rev. A* **77** (3), 033 616 (2008).

[141] A Rakonjac, A L Marchant, T P Billam, J L Helm, M. M. H. Yu, S A Gardiner and S L Cornish, "Measuring the disorder of vortex lattices in a Bose-Einstein condensate". *Phys. Rev. A* **93** (1), 013 607 (2016).

[142] T. Lindeberg, "Detecting salient blob-like image structures and their scales with a scale-space primal sketch: A method for focus-of-attention". *Int J Comput Vision* **11**, 283–318 (December 1993).

[143] Y.J. Lin, A. R. Perry, R. L. Compton, I. B. Spielman and J. V. Porto, "Rapid production of $^{87}$Rb Bose-Einstein condensates in a combined magnetic and optical potential". *Phys. Rev. A* **79**, 063 631 (Jun 2009).

[144] O.J. Luiten, M.W. Reynolds and J.T.M. Walraven, "Kinetic theory of the evaporative cooling of a trapped gas". *Phys. Rev. A* **53** (1), 381–389 (1996).

[145] W. Ketterle and N.J. van Druten, "Evaporative cooling of trapped atoms". In *Advances in atomic, molecular and optical physics*, volume 37, edited by B. Bederson and H. Walther, pages 181–236, Academic Press (1996).

[146] O. J. Luiten, M. W. Reynolds and J. T. M. Walraven, "Kinetic theory of the evaporative cooling of a trapped gas". *Phys. Rev. A* **53**, 381–389 (Jan 1996).

[147] Daniel Steck, "Rubidium 87 D Line Data" (01 2003).

[148] W. Ketterle, D.S Durfee and D.M Stamper-Kurn, "Making, probing and understanding Bose-Einstein condensates". In *Proceedings of the International School of Physics "Enrico Fermi", Course CXL*, edited by M. Inguscio, S. Stringari and C.E. Wieman, pages 67–176, IOS Press Ohmsha (1999).

[149] R. Grimm, M. Weidemüller and Yu.B. Ovchinnikov, "Optical dipole traps for neutral atoms". *Adv. At. Mol. Opt. Phys.* **42**, 95–170 (2000).

[150] M.R Andrews, M.O. Mewes, N.J. van Druten, D.S. Durfee, D.M. Kurn and W. Ketterle, "Direct, Nondestructive Observation of a Bose Condensate". *Science* **273** (5271), 84–87 (1996).

[151] M Pappa, P C Condylis, G O Konstantinidis, V Bolpasi, A Lazoudis, O Morizot, D Sahagun, M Baker and W von Klitzing, "Ultra-sensitive atom imaging for matter-wave optics". *New Journal of Physics* **13** (11), 115 012 (nov 2011).

[152] Aaron Reinhard, Jean-Félix Riou, Laura A. Zundel and David S. Weiss, "Dark-ground imaging of high optical thickness atom clouds". *Optics Communications* **324**, 30–33 (2014).

[153] M. R. Andrews, D. M. Kurn, H.-J. Miesner, D. S. Durfee, C. G. Townsend, S. Inouye and W. Ketterle, "Propagation of Sound in a Bose-Einstein Condensate". *Phys. Rev. Lett.* **79**, 553–556 (Jul 1997).

[154] R. Meppelink, R. A. Rozendaal, S. B. Koller, J. M. Vogels and P. van der Straten, "Thermodynamics of Bose-Einstein-condensed clouds using phase-contrast imaging". *Phys. Rev. A* **81**, 053 632 (May 2010).

[155] Miroslav Gajdacz, Poul L. Pedersen, Troels Mørch, Andrew J. Hilliard, Jan Arlt and Jacob F. Sherson, "Non-destructive Faraday imaging of dynamically controlled ultracold atoms". *Review of Scientific Instruments* **84** (8), 083 105 (08 2013). `https://pubs.aip.org/aip/rsi/article-pdf/doi/10.1063/1.4818913/14781030/083105_1_online.pdf`.

[156] J. M. Higbie, L. E. Sadler, S. Inouye, A. P. Chikkatur, S. R. Leslie, K. L. Moore, V. Savalli and D. M. Stamper-Kurn, "Direct Nondestructive Imaging of Magnetization in a Spin-1 Bose-Einstein Gas". *Phys. Rev. Lett.* **95**, 050 401 (Jul 2005).

[157] S Franke-Arnold, M Arndt and A Zeilinger, "Magneto-optical effects with cold lithium atoms". *Journal of Physics B: Atomic, Molecular and Optical Physics* **34** (12), 2527 (jun 2001).

[158] R. Hooke, *Of a New Property in the Air*. In Micrographia (1665).

[159] Max Langer, Peter Cloetens, Jean-Pierre Guigay and Françoise Peyrin, "Quantitative comparison of direct phase retrieval algorithms in in-line phase tomography". *Medical Physics* **35** (10), 4556–4566 (2008). `https://aapm.onlinelibrary.wiley.com/doi/pdf/10.1118/1.2975224`.

[160] Chao Zuo, Qian Chen, Weijuan Qu and Anand Asundi, "Direct continuous phase demodulation in digital holography with use of the transport-of-intensity equation". *Optics Communications* **309**, 221–226 (2013).

[161] Gael Reinaudi, *Manipulation et refroidissement par évaporation forcée d'ensembles atomiques ultra- froids pour la production d'un jet intense dans le régime de dégénérescence quantique : vers l'obtention d'un laser à atomes continu*. PhD thesis, Université Paris 6 (2008).

[162] Carmelo Mordini, *Measurement of the density profile of quantized vortices and of the equation of state in a 3D interacting Bose gas*. PhD thesis, University of Trento (2019).

[163] H Terças, J P A Martins and J T Mendonça, "Rossby waves in rapidly rotating Bose–Einstein condensates". *New Journal of Physics* **12** (9), 093 001 (2010).

[164] S. Nazarenko, *Wave Turbulence*. Springer Berlin Heidelberg (2011).

[165] Guillaume Gauthier, Matthew T. Reeves, Xiaoquan Yu, Ashton S. Bradley, Mark A. Baker, Thomas A. Bell, Halina Rubinsztein-Dunlop, Matthew J. Davis and Tyler W. Neely, "Giant vortex clusters in a two-dimensional quantum fluid". *Science* **364** (6447), 1264–1267 (2019). `https://www.science.org/doi/pdf/10.1126/science.aat5718`.

## Résumé

Cette thèse présente la production d'un gaz quantique dégénéré de rubidium 87 dans le régime tridimensionnel (3D) ainsi que dans le régime quasi bidimensionnel (2D). Nous montrons que la géométrie du piège final dans l'expérience, le piège en forme de bulle, offre une plateforme pour étudier la dynamique d'un superfluide quasi-2D en rotation rapide. Le point de départ de cette étude est un superfluide confiné au fond du piège bulle, formé par l'habillage des atomes dans un champ magnétique quadrupolaire avec un champ radiofréquence. Nous montrons qu'une fréquence de rotation élevée peut être atteinte dans ce piège en raison de sa nature anharmonique. Nous étudions le scénario de fusion, très bien expliqué par la théorie de Kosterlitz, Thouless, Halperin, Nelson et Young (KTHNY), dans un superfluide quasi-2D en rotation. Nous montrons la présence de la transition de la phase hexatique à la phase liquide à mesure que la fréquence de rotation du superfluide augmented.

Afin de produire un superfluide, un condensat de Bose-Einstein est d'abord créé dans un piège hybride constitué d'un champ magnétique quadrupolaire et d'un faisceau laser très désaccordé vers le rouge, dont la position est optimisée pour rendre le transfert des atomes vers le piège bulle adiabatique. Nous présentons également une nouvelle technique d'imagerie non destructive mise en œuvre dans notre expérience afin de prendre plusieurs images in situ d'un superfluide au cours d'une séquence expérimentale.

**Mots-clefs :** Condensat de Bose-Einstein, potentiels adiabatiques, réseau de vortex, rotations rapides, superfluide quasi-2D.

## Abstract

This thesis presents the production of a degenerate quantum gas of rubidium 87 in both the three-dimensional (3D) and quasi-two-dimensional (2D) regimes. We show that the geometry of the final trap in the experiment, i.e., the bubble trap, provides a platform for studying the dynamics of a rapidly rotating quasi-2D superfluid. The starting point of this study is a superfluid confined at the bottom of the bubble trap, which is formed by dressing atoms in a quadrupole magnetic field with a radio-frequency field. We show that a high rotation rate can be achieved in this bubble trap due to its anharmonic nature. We explore the melting scenario, which is well explained by the Kosterlitz-Thouless-Halperin-Nelson-Young (KTHNY) theory, in a quasi-2D rotating superfluid. We demonstrate the presence of a transition from the hexatic to the liquid phase as the rotation rate of the superfluid increases.

To produce a superfluid, a Bose-Einstein condensate is first created in a hybrid dimple trap, composed of a quadrupole magnetic field and a red-detuned laser beam. The position of the laser is optimized to ensure the adiabatic transfer of atoms to the bubble trap. Additionally, we present a new non-destructive imaging technique implemented in our experiment to capture multiple in-trap images of the superfluid during an experimental sequence.

**Keywords:** Bose-Einstein condensate, adiabatic potentials, vortex lattice, fast rotations, quasi-2D superfluid